Annual Report 2019

Physik-Department

Lehrstuhl für Funktionelle Materialien

mit dem

Fachgebiet Physik Weicher Materie

Technische Universität München

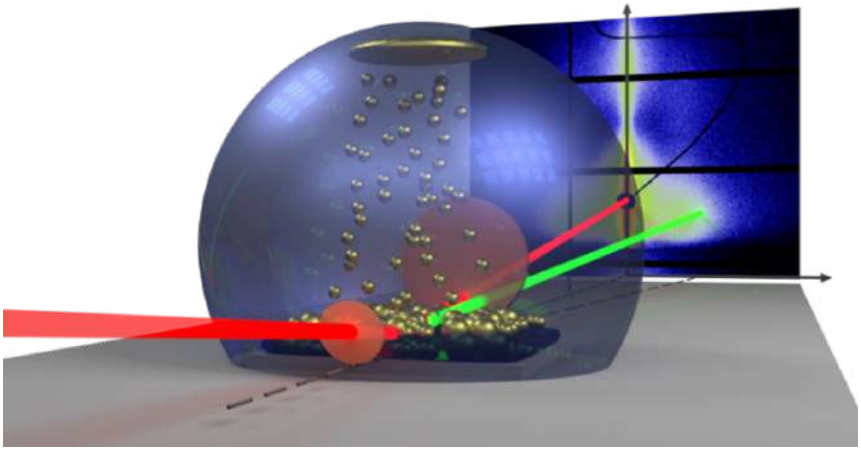

Prof. Dr. Peter Müller-Buschbaum
Chair of Functional Materials
muellerb@ph.tum.de
www.functmat.ph.tum.de
www.polymer.ph.tum.de

Prof. Dr. Christine M. Papadakis
Soft Matter Physics Group
papadakis@tum.de
www.softmatter.ph.tum.de

Physik-Department
Technische Universität München
James-Franck-Straße 1
85748 Garching

Secretaries/Administration:
Marion Waletzki: marion.waletzki@ph.tum.de
Carola Kappauf: carola.kappauf@ph.tum.de

Tel.: +49(0)89 289-12452
Fax: +49(0)89 289-12473

Cover-page picture:

In-operando GISAXS measurement of the sputter deposition
of gold particles on a polymer thin film.

Editor: Florian Jung

Preface

It is a great pleasure to present the annual report for the year 2019 in the name of the staff of the Chair of Functional Materials and the Soft Matter Physics Group. It provides an overview of our teaching, research, and development activities. Our research activities are focused on functional materials and cover a broad range from soft matter physics to developments of methods and instrumentation. We examine the fundamental physics of material properties using mainly scattering methods (neutron, x-ray and light scattering). The general goal of our research is to explain the functional characteristics of soft condensed matter from the knowledge of the molecular dynamics and nanostructure as well as their kinetics.

In 2019, the chair activities covered the specific areas of polymer solutions and gels, responsive thin films, functional thin films, photovoltaics, polymer-hybrid systems, real-time characterizations and instrumentation and new materials. The activities in the fields of polymer films for application in photovoltaics and polymer-hybrid systems have been successfully continued. With *"TUM.solar"*, the keylab in the network in the Bavarian Collaborative Research Project *"Solar Technologies go Hybrid"* (SolTec) headed by Prof. Müller-Buschbaum is running in its eighth year of funding. Research activities cover a broad area of next generation solar cells, such as organic solar cells, dye sensitized solar cells, hybrid solar cells and organometal halide perovskite solar cells. Moreover, thermoelectric materials and energy storage materials with focus on the lithium ion battery technology are actively researched. We investigated polymers with complex architecture, novel responsive polymers, self-assembling polymers in solution, multiresponsive and orthogonally switchable polymers as well as polymers for medical applications. Special focus was on the influence of pressure on the phase behavior, self-assembly, dynamics and switching behavior of responsive polymers in solution. Major reviews on schizophrenic behavior of all thermoresponsive UCST-LCST diblock copolymers as well as on the role of polarity for multiresponsive polymers were published.

The in-house experiments available in the laboratories of the chair were supplemented by the lively activities at numerous large scale facilities, comprising synchrotron radiation and neutron scattering experiments, also at the FRM II. In particular, the in-house x-ray scattering experiments were operated with full time schedule. Importantly, we started the general renovation of the laboratories including a reorganization of the instrument floorplan. In collaboration with our guest, Prof. Alfons Schulte, the sample environment for high-pressure research was substantially improved, now allowing for dynamic light scattering investigations as well as rapid pressure changes in combination with time-resolved measurements of the light transmittance.

In 2019, the Chair of Functional Materials comprised 8 fellows, 54 PhD students, 30 master students, 16 bachelor students, 3 student assistants and 6 administrative and technical staff members. 8 PhD theses were accomplished; moreover, 15 master theses as well as 15 bachelor theses were finished. As all the years before, we had the pleasure to host numerous guests from abroad, which stimulated a lively and inspiring scientific atmosphere. Prof Alfons Schulte, University of Central Florida, spent again two months in the Soft Matter Physics Group to continue the high-pressure research.

In general, all members of the chair were very active at conferences and workshops, participating with both, talks and posters. We organized the "4th internal biennial science meeting of the MLZ" in Grainau, during which there was an intensive exchange with the MLZ members. Moreover, important conferences were organized by members of the chair: Prof. Peter Müller-Buschbaum co-organized the MLZ Conference *" Neutrons for Information and Quantum Technologies"*, the 9th MSE Colloquium *" Shaping a Sustainable Energy Future"* and the international workshop*"GISAXS2019"*. Again, two Edgar-Lüscher seminars were organized by Prof. Peter Müller-Buschbaum, this year on the subjects *"Erneuerbare Energien"* and *"Quantenphysik"*.

Regarding teaching activities of the chair, we offered lectures in general physics for the TUM elite engineers in the Munich School of Engineering (MSE) (Müller-Buschbaum) and lectures in advanced physics to future teachers in vocational schools (Papadakis). Specialized lectures comprised *"Polymer physics"* (Papadakis) and *"Nanostructured soft materials"* (Müller-Buschbaum). Prof. Papadakis acted again as a deputy women's representative of the Physics Department. Moreover, Prof. Müller-Buschbaum heads the activities in the *"Network Renewable Energies (NRG)"* in the MSE.

As a service to the community, Prof. Papadakis acted as one of the Editors-in-Chief of *"Colloid and Polymer Science"* and Prof. Müller-Buschbaum served as Associate Editor at *"ACS Applied Materials & Interfaces"*.

This annual report comprises a selection of the different research topics and projects carried out in the individual groups of the chair. It highlights the dedicated and successful research activities and collaborations with other groups and large-scale facilities. We wish all chair members a fruitful continuation and a very successful year 2020.

Peter Müller-Buschbaum and Christine M. Papadakis March 2020

Contents

1 Polymer solutions and gels

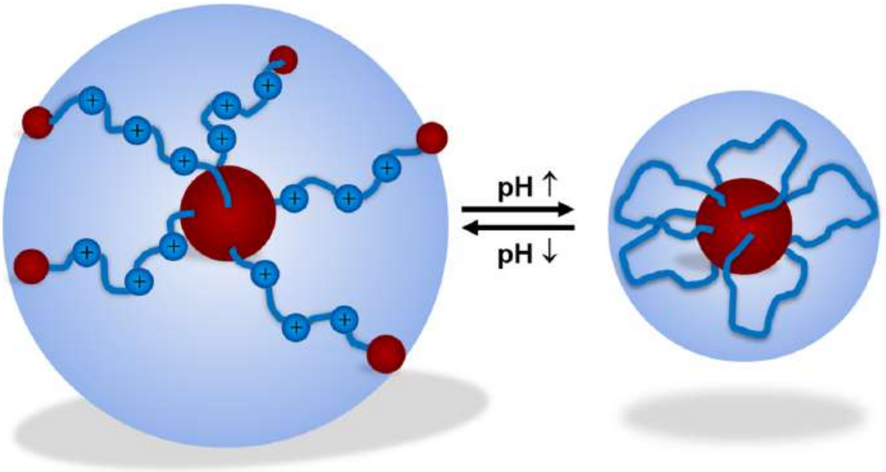

1.1 Structural properties of micelles formed by telechelic pentablock quaterpolymers with pH-responsive midblocks and thermoresponsive end blocks in aqueous solution

F. A. Jung, P. A. Panteli[1], C.-H. Ko, J.-J. Kang, L. C. Barnsley[2], C. Tsitsilianis[3],
C. S. Patrickios[1], C. M. Papadakis

[1] University of Cyprus, Nicosia, Cyprus
[2] JCNS at MLZ, Garching, Germany
[3] University of Patras, Greece

Stimuli-responsive physical hydrogels change their properties upon a small change of the environment and may be used as fast sensors, for drug delivery or for tissue engineering [1]. We previously studied hydrogels formed by a multi-responsive, telechelic triblock terpolymer with thermoresponsive random copolymer end blocks, which act as crosslinkers, and a polyelectrolyte midblock [2]. We found that its mechanical properties vary strongly with temperature, changing from a weak hydrogel at low temperatures to a strong hydrogel at high temperatures. This was attributed to a slowdown of the exchange dynamics of the end blocks owing to their increased hydrophobicity.

In the present work, we investigate the structural properties of micelles formed by a pentablock quaterpolymer of similar architecture using a combination of scattering methods [3]. The end blocks are statistical copolymers of hydrophobic *n*-butyl methacrylate (*n*BuMA) units and thermoresponsive triethylene glycol methyl ether methacrylate (TEGMA) units (lower critical solution temperature, LCST, ∼50 °C). The midblock consists of the two poly(2-(dimethylamino)ethyl methacrylate) (PDMAEMA) blocks and a central poly(ethylene glycol) (PEG) block. PDMAEMA is a weak cationic polyelectrolyte, that is, it is positively charged at pH values below its $\mathrm{p}K_\mathrm{a}$ of ∼7.5.

The hydrodynamic radius, R_h, of the micelles measured with dynamic light scattering (DLS) at various pD and temperature values is shown Fig. 1.1a. At pD values below the $\mathrm{p}K_\mathrm{a}$, R_h is larger than at higher pD values, which is attributed to a stretching of the PDMAEMA blocks due to electrostatic interactions. With increasing temperature, R_h is constant at the low pD values, whereas it decreases at high pD values.

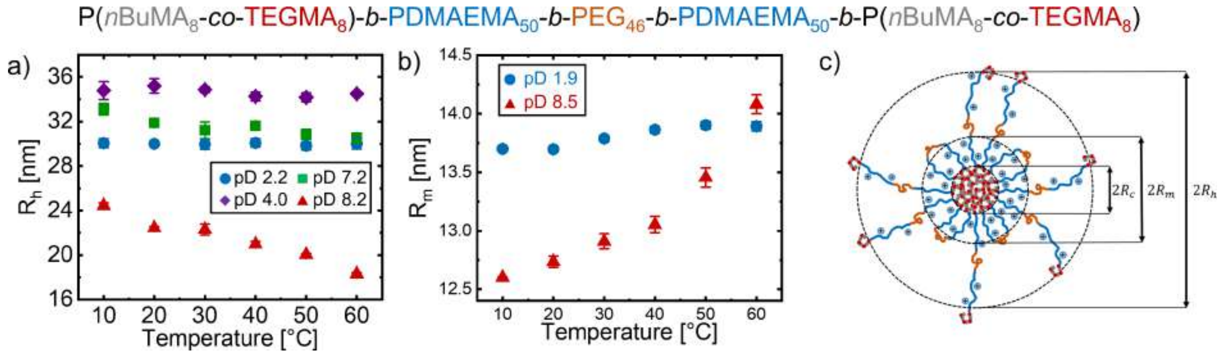

Figure 1.1:
(a) Temperature dependence of the hydrodynamic radius, R_h, of micelles in a 1 wt% D_2O solution measured with DLS at the pD values indicated. (b) Temperature dependence of the micellar radius, R_m, of a 2 wt% D_2O solution measured with SANS at the indicated pD values. (c) Schematic representation of a micelle formed by the telechelic pentablock quaterpolymer in aqueous solution at low pD and temperature values. R_h, R_m and the core radius, R_c, are indicated and drawn to scale. Adapted with permission from [3]. Copyright 2019 American Chemical Society.

Information about the inner structure of the micelles was obtained from small-angle neutron scattering (SANS) experiments at instrument KWS-1 at MLZ, Garching. The data are well described by a spherical core-shell micelle model [4], yielding, among other parameters, the radius of the core, R_c, the water content in the core and the micellar radius, R_m (Fig. 1.1b). Similar to R_h, the latter is larger at low pD values, but the absolute values are significantly smaller than the corresponding R_h values. With increasing temperature, R_m is higher at the highest pD value, which is in contrast to the behavior of R_h. We also find that water is expelled from the core, that is, its hydrophobicity increases.

From these findings, the micellar structure is deduced as shown in Fig. 1.1c for the case of low pD and temperature values: The core is formed by the end blocks, and it is rather hydrated due to the hydrophilic TEGMA units. Dangling ends are present, that is, not all chains form loops, which is evident from the significantly larger R_h compared to R_m. Due to low scattering contrast, R_m is mostly sensitive to the denser areas formed by the loops.

The change of structure in response to a change in pD or temperature is summarized in Fig. 1.2. Increasing the temperature at low pD values increases the hydrophobicity of the end blocks, but dangling ends are still observed, that is, they are stabilized by electrostatic interactions which prevent backfolding into loops. At high pD values, the increased hydrophobicity of the end blocks induces a transition from dangling ends to loops, which explains the opposite behavior of R_h and R_m shown in Fig. 1.1a,b. R_h decreases due to absence of dangling ends and R_m increases due to higher chain density, leading to both steric effects and a larger scattering contrast.

The results show that, in these kind of multi-responsive systems, the responses to different stimuli are not independent from each other but are strongly correlated. These findings may help improving the design of such polymers for potential applications as micelles or hydrogels.

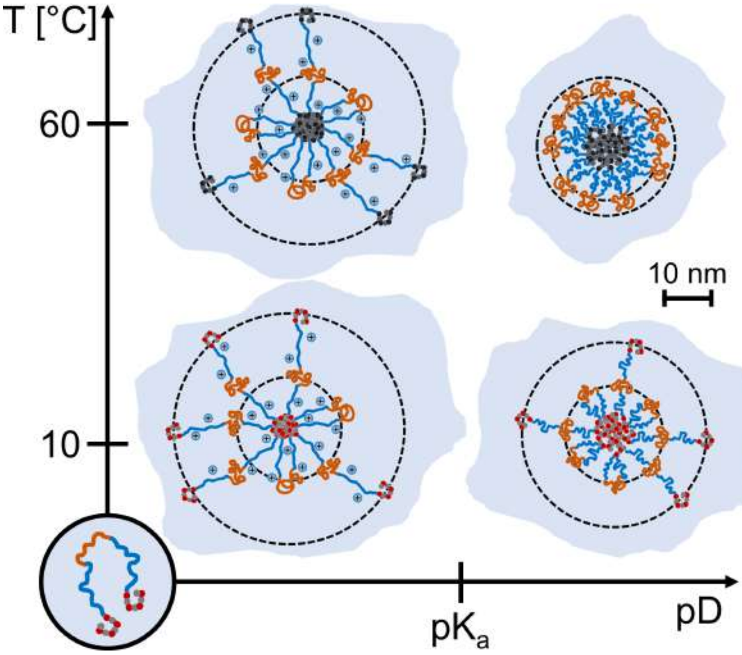

Figure 1.2:
Schematic structures of the micelles formed by the pentablock quaterpolymer in aqueous solution at different pD and temperature conditions. Circles represent R_h (outer circle) and R_m (inner circle). All dimensions are drawn to scale. Colors represent TEGMA (red), nBuMA (gray), DMAEMA (blue), and EG (brown). The grayed out core at high temperatures indicates higher hydrophobicity. The scale bar gives a length scale. Reprinted with permission from [3]. Copyright 2019 American Chemical Society.

The project is funded by Deutsche Forschungsgemeinschaft (DFG) (Pa771/19-1).

[1] C. Tsitsilianis, *Soft Matter* **6**, 2372-2388 (2010)

[2] C. Tsitsilianis, G. Serras, C.-H. Ko, F. Jung, C. M. Papadakis, M. Rikkou-Kalourkoti, C. S. Patrickios, R. Schweins, C. Chassenieux, *Macromolecules* **51**, 2169-2179 (2018)

[3] F. A. Jung, P. A. Panteli, C.-H. Ko, J.-J. Kang, L. C. Barnsley, C. Tsitsilianis, C. S. Patrickios, C. M. Papadakis, *Macromolecules* **52**, 9746-9758 (2019)

[4] T. Zinn, L. Willner, K. D. Knudsen, R. Lund, *Macromolecules* **50**, 7321-7332 (2017)

1.2 Self-assembled physical hydrogels from telechelic polyampholytes: Effect of co-solvent

Y. Li, M. A. Dyakonova, C.-H. Ko, J.-J. Kang, I. Grillo[1], G. Gotzamanis[2],
C. Tsitsilianis[2], C. M. Papadakis

[1] Institut Laue-Langevin, Grenoble, France
[2] University of Patras, Greece

Triblock polyampholytes feature hydrophobic end blocks and a polyampholytic middle block. In aqueous solution, they form a micellar network with the associating hydrophobic blocks forming the cross-links. Gel formation even at low polymer concentration is promoted by a highly charged midblock, which is expanded and can thus easily bridge the micelles formed. However, systems with long hydrophobic end blocks are prone to non-equilibrium states, and a so-called "frozen gel" is formed. Adding a co-solvent which dissolves these blocks may promote equilibration.

Here, we investigate the triblock polyampholyte $PMMA_{86}$-*b*-P(DEA_{190}-*co*-MAA_{96})-*b*-$PMMA_{86}$, where PMMA stands for poly(methyl methacrylate) and P(DEA-*co*-MAA for poly(2-(diethylamino)ethyl methacrylate-*co*-methacrylic acid) [1,2]. At pH 3, the midblock is positively charged, and at a polymer concentration of 3 wt% in water, a micellar gel is formed [2]. Acetone is chosen as a good solvent for the PMMA blocks. Apart from plasticizing the PMMA cross-links, this solvent also reduces the dielectric permittivity of the solvent and screens the ionic interactions.

Using small-angle neutron scattering (SANS), we determine the gel structures in dependence on acetone content, using fully deuterated solvents to enhance the scattering contrast. The polymers were dissolved in $(CD_3)_2CO$, centrifuged and stirred, D_2O was added, and pD 3 was installed by adding HCl inD_2O. The fraction of $(CD_3)_2CO$ was varied between 0 and 30 wt%. SANS measurements were carried out at room temperature at instrument D22 at ILL, Grenoble, using a wavelength of 0.5 nm and sample-detector distances of 2.0 and 12.5 m. The background from the empty cell was subtracted. Model fitting was carried out using the software SasView.

Fig. 1.3 shows the SANS data. For fractions of $(CD_3)_2CO$ of 1 wt%, the shape of the curve

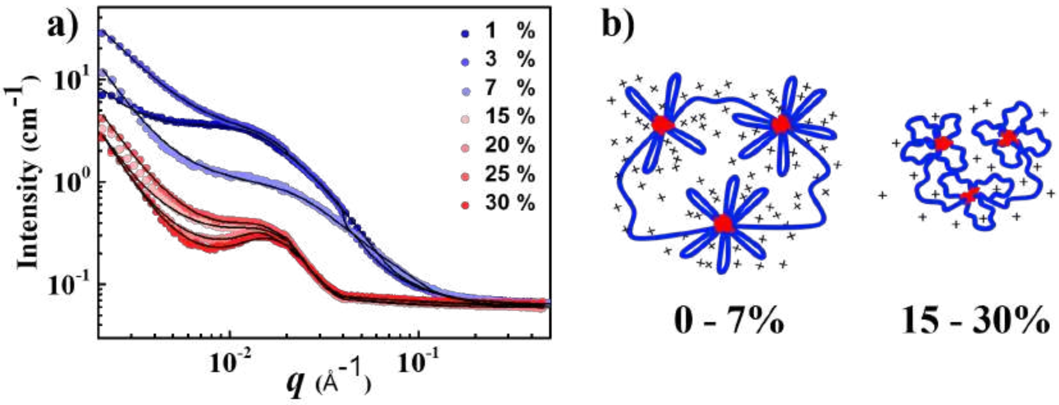

Figure 1.3:
(a) SANS data of 0.5 wt% solutions of $PMMA_{86}$-*b*-P(DEA_{190}-*co*-MAA_{96})-*b*-$PMMA_{86}$ solutions in the solvent mixtures D_2O/ $(CD_3)_2CO$ with fractions of $(CD_3)_2CO$ given in the graph. Symbols represent the data, solid lines the fits. (b) Schematics of the structures at the fractions of $(CD_3)_2CO$ given below the images. Blue: mid-block, red: PMMA end block.

is characteristic of the one for a micellar network [2], but at 3 wt%, significant additional forward scattering is observed. This indicates that the infinite network breaks up into clusters, as depicted schematically in Fig. 1.3, which is probably due to the lower degree of stretching of the mid-blocks, resulting in more back folded mid-blocks. At a fraction of $(CD_3)_2CO$ of 7 wt%, a shoulder of low intensity along with strong aggregate scattering is observed. When the ratio of $(CD_3)_2CO$ in solvent between 15 and 30 wt%, the curves feature a distinct maximum along with aggregate scattering and are similar to each other, indicating that the gel structure is unchanged in this range.

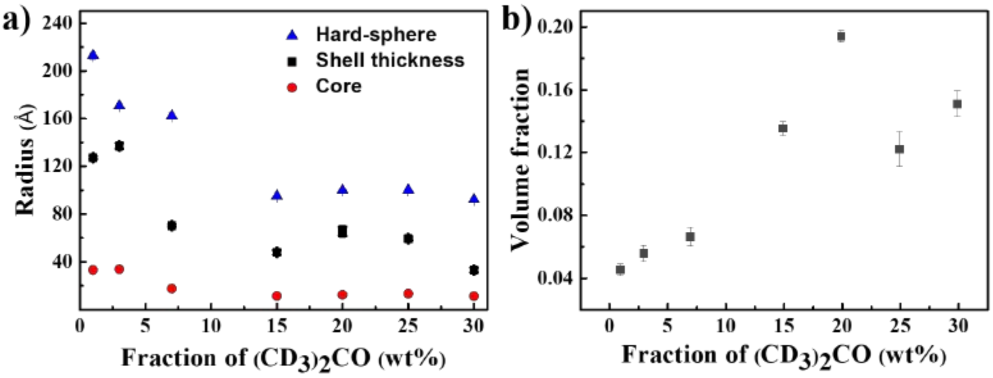

Figure 1.4:
Structural parameters from model fitting in dependence of the fraction of $(CD_3)_2CO$. (a) Core radius, shell thickness and hard-sphere radius. (b) Volume fraction of correlated micelles.

A model for spherical core-shell micelles correlated by a hard-sphere structure, along with Ornstein-Zernike structure factor and a Porod term to model the forward scattering was used to fit the data. Fig. 1.4 shows the resulting micellar sizes: When the fraction of $(CD_3)_2CO$ increases from 1 to 15 wt%, the core radius and the shell thickness decrease. The hard-sphere radius, i.e. half the average distance between the micelles, decreases as well. This means that the mid-blocks contract, and the resulting increased space demand causes the aggregation number of the core to decrease as shown in Fig. 1.3. At the same time, the volume fraction of correlated micelles increases shown in Fig. 1.4, which may be due to the fact that, upon addition of $(CD_3)_2CO$, the PMMA blocks are mobile, which leads to an improved correlation between the micelles. From 15 to 30 wt%, no more changes in the gel structure are observed.

We conclude that the addition of an organic solvent, acetone, to a hydrogel from triblock polyampholytes leads to a complex interplay between the contraction of the mid-blocks forming the bridges and the mobilization of the end blocks forming the cores. These concern the size and distance of the micelles as well as the homogeneity of the network on larger length scales.

[1] C. Tsitsilianis, G. Gotzamanis, Z. Iatridi, *Eur. Polym. J.* **47**, 497-510 (2011)

[2] M. A. Dyakonova, G. Gotzamanis, B.-J. Niebuur, N. S. Vishnevetskaya, K. N. Raftopoulos, Z. Di, S. K. Filippov, C, Tsitsilianis, C. M. Papadakis, *Soft Matter* **13**, 3568-3579 (2017)

1.3 Drug-loaded poly(2-oxazoline) molecular brushes: A structural investigation

J.-J. Kang, D. Gieseler[1], C.-H. Ko, L. C. Barnsley[2], R. Jordan[1], C. M. Papadakis

[1] Technische Universität Dresden, Germany
[2] JCNS at MLZ, Garching, Germany

Molecular brushes (MBs) are polymers which are densely grafted with polymeric side chains. When the side chains are amphiphilic block copolymers with the hydrophobic segment attached directly to the backbone and hydrophilic segment at the periphery, the MBs are unimolecular micelles with a hydrophobic core and a hydrophilic shell, which is a desired structure for nano-carriers to transport hydrophobic drugs in the human body [1]. In the present work, poly(2-oxazoline) (POx)-based MBs with amphiphilic block copolymer side chains are investigated in aqueous solution, to characterize their structural changes upon drug loading.

The MBs under study are composed of a poly(methacrylic acid) (PMA) backbone and P*n*BuOx-*b*-PMeOx side chains [2], where poly(2-*n*-butyl-2-oxazoline) (P*n*BuOx) is hydrophobic and poly(2-methyl-2-oxazoline) (PMeOx) is hydrophilic. The P*n*BuOx block is attached to the backbone. Three MBs with different backbone and side chain lengths are investigated: PMA_{29}-*g*-(P*n*$BuOx_{10}$-*b*-$PMeOx_{37}$), PMA_{62}-*g*-(P*n*$BuOx_{10}$-*b*-$PMeOx_{37}$) and PMA_{210}-*g*-(P*n*$BuOx_{3}$-*b*-$PMeOx_{12}$), named P29, P62 and P210, respectively. As an anticancer drug, Paclitaxel (PTX), which has low water solubility was loaded. The MBs are dissolved in D_2O at 10 g/L, and the PTX/MB weight ratio was chosen in the range from 0 to 0.1. The solutions were studied at 37 °C, the human body temperature.

The inner structure of the MBs is resolved by small-angle neutron scattering (SANS), and the measurements were performed at KWS-1 at Heinz Maier-Leibnitz-Zentrum. The neutron wavelength was 5 Å, and the sample-to-detector distances (SDD) were 1.9 m, 8.0 m and 20 m, with the exposure times 8 min, 15 min and 30 min, respectively. Fig. 1.5 shows the SANS data of the MB solutions at different amounts of PTX. The scattering curves of both P29 and P62 show one decay at 0.03 $Å^{-1}$, indicating a spherical or ellipsoidal shape; while that of P120 has two decays with different slopes at 0.01 and 0.06 $Å^{-1}$, which is the feature of a rod-like particle. Considering the MBs to have a polymer-rich inner part and a water-rich outer part, the SANS data without PTX loading are modeled by a core-shell ellipsoid structure for P29 and P62, resulting in good fits (Fig. 1.5a,b). In contrast, P210 has a cylindrical shape (Fig. 1.5c).

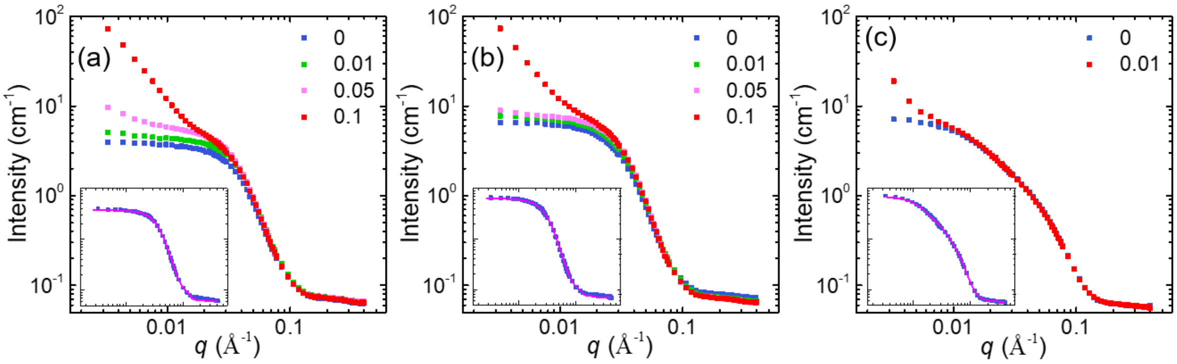

Figure 1.5:
SANS data of 10 g/L MB solutions in D_2O: (a) P29 (b) P62 and (c) P210, with different PTX/MB weight ratios as indicated. Shown in the insets are model fits for MB without PTX, where the core-shell ellipsoid model was used for P29 and P62, and the cylinder model for P210.

The SANS data of P29 and P62 with different PTX/MB ratios are modeled by the core-shell ellipsoid form factor, revealing the structural dependence on the drug loading amounts. The results show that both P29 and P62 are elongated particles (Fig. 1.6a,b). Upon PTX loading, for P29, the polar radius increases from 6.5 to 8.0 nm as the PTX/MB ratio reaches 0.05, with the other parameters staying nearly constant. The extension of P29 is presumably due to the spatial limit in the core region. On the contrary, for P62, the polar radius decreases from 10 to 8.5 nm, showing a contraction upon PTX loading. This might be attributed to the increasing overall hydrophobicity caused by the addition of the hydrophobic PTX. The structural changes upon PTX loading are sketched in Fig. 1.6c and d for P29 and P62, respectively.

From the strong forward scattering (Fig. 1.5), it is seen that aggregates form as the PTX/MB weight ratio reaches 0.1 for both P29 and P62, while in P210 aggregates already appear at a PTX/MB weight ratio as low as 0.01. This implies that P210 cannot accommodate the hydrophobic drug, which explains why it aggregates upon loading with a very small amount of PTX. Possibly, the very short P*n*BuOx block in P210 limits its drug-loading capacity. In contrast, P29 and P62, which have longer P*n*BuOx blocks, are able to take up PTX in amounts up to a weight fraction of 5%.

To summarize, it is found that the hydrophobic segment in MB must be sufficiently long so that a core-shell structure is established, which allows storage of the hydrophobic drug. Besides, two factors are influencing the structure of MB upon drug uptake: the spatial limitation of the hydrophobic core and the overall hydrophobicity. By resolving the structure of MB, the present study can provide hints to a rational design of MBs as drug carriers.

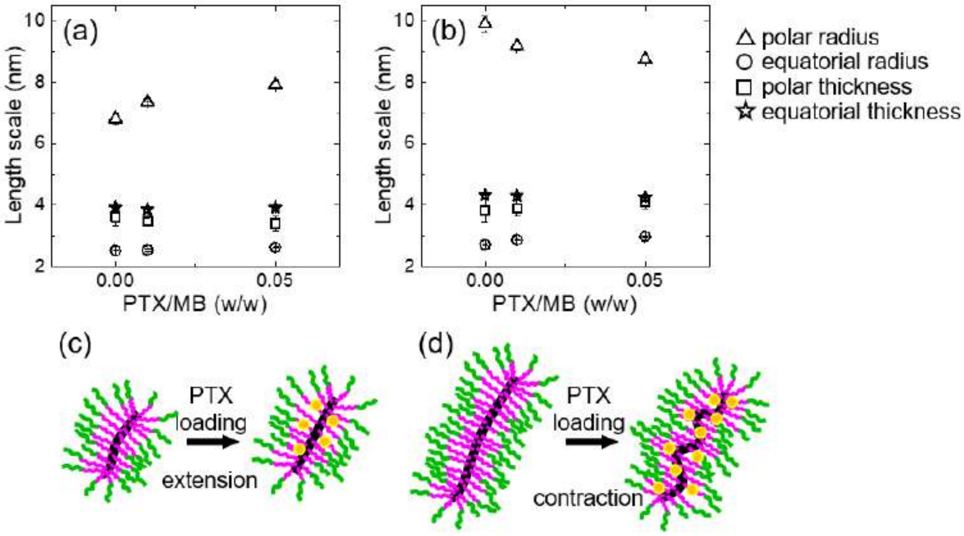

Figure 1.6:
Structural parameters from the core-shell ellipsoid model for (a) P29 and (b) P62 in dependence on the PTX/MB ratio. Schematic representations for (c) P29 and (d) P62 upon PTX uptake, where PTX is shown as yellow spheres.

[1] J. A. Johnson, Y. Y. Lu, A. O. Burts, Y. Xia, A. C. Durrell, D. A. Tirrell, R.H. Grubbs, *Macromolecules* **43**, 10326-10335 (2010)

[2] D. Gieseler, R. Jordan, *Polym. Chem.* **6**, 4678-4689 (2015)

1.4 Thermal Behavior of the Thermoresponsive Diblock Copolymer PMMA-*b*-PNIPAM in Aqueous Solution

C.-H. Ko, C. Henschel[1], G. P. Meledam, M. Schroer[2], P. Müller-Buschbaum,
A. Laschewsky[1,3] and C. M. Papadakis

[1] Universität Potsdam, Potsdam-Golm, Germany
[2] European Molecular Biology Laboratory, Hamburg, Germany
[3] Fraunhofer IAP, Potsdam-Golm, Germany

Amphiphilic block copolymers having a hydrophobic poly(methyl methacrylate) (PMMA) block and a thermo-responsive poly(*N*-isopropylacrylamide) (PNIPAM) block form core-shell micelles in aqueous solution. The shell of the micelles collapses at the transition temperature of the PNIPAM block, and the collapsed micelles further form aggregates. We aim at investigating the structure of self-assembled micelles and the changes upon collapse and aggregation with increasing temperature in water. We investigate the temperature-dependent phase behavior of PMMA-*b*-PNIPAM in D_2O using turbidimetry to determine the cloud point, dynamic light scattering (DLS) to reveal the hydrodynamic radius of micelles and small-angle X-ray scattering (SAXS) to characterize the inner structure and correlations of the micelles.

$PMMA_{22}$-*b*-$PNIPAM_{260}$ with molar mass 32 000 g/mol was synthesized by the reversible addition fragmentation chain transfer (RAFT) method. The polymers were dissolved in D_2O at a concentration of 10 g L^{-1}. The cloud point T_{CP} of this sample is 31.2 ^{o}C, as determined by turbidimetry. DLS results show that, below T_{CP}, the hydrodynamic radius R_h of the micelles stays constant at 27 nm and increases from 27 nm to 32 nm above (Fig. 1.7b).

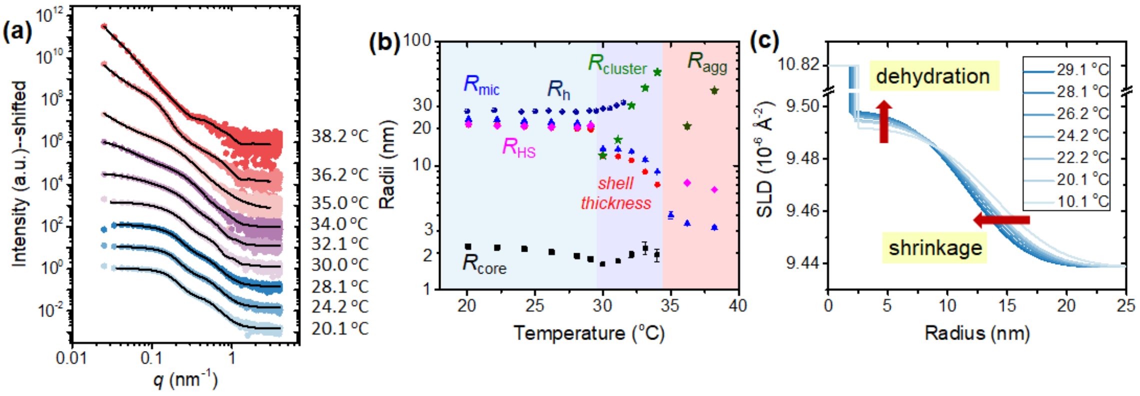

Figure 1.7:
a) SAXS data and model fits curves of 10 g L^{-1} $PMMA_{22}$-*b*-$PNIPAM_{260}$ in D_2O in dependence on temperature. b) Corresponding fitting results. c) The SLD profile along the radius.

The inner structure and correlations of the micelles are characterized by SAXS. Fig. 1.7a shows the SAXS data of $PMMA_{22}$-*b*-$PNIPAM_{260}$ at 10 g L^{-1} in pure D_2O in dependence on temperature, measured at beamline P12, EMBL. The wavelength of incident X-ray was 0.124 nm, the sample-detector distances was 3 m, and the measurement time of each curve was 0.045 s. Below T_{CP}, the scattering curves feature two shoulders. The SAXS curves below 30 ^{o}C are modelled by a form factor for spherical core-shell particles, in which the shell SLD profile is a continuous error function along the radius of the particles. A sticky hard sphere structure factor describes the correlations between the micelles. Above 30 ^{o}C, the scattering in the low-q region increases significantly with increasing temperature, which may be attributed to the clusters formed by collapsed micelles. Therefore, the previous model was replaced by a model, which describes the clusters as fractal aggregates formed by spherical core-shell micelles. Above 34 ^{o}C, the forward scattering in the low-q region becomes very strong, due to the presence of large aggregates. Therefore, the SAXS curves above 34 ^{o}C are fitted by a model comprised of a Porod term, a Guinier term, and a sphere form factor with a hard sphere structure factor, which describes the surface roughness of aggregates, the size of the aggregates, and the collapsed micelles, respectively.

At 20 ^{o}C, the fitting results (Fig. 1.7b) shows that the micellar radius R_{mic} is 23 nm, the core radius R_{core} 2.2 nm and the shell thickness 20.5 nm. Besides, the hard sphere radius R_{HS} is 20 nm, which is 2-3 nm smaller than R_{mic}, meaning that the micelles are densely packed, and overlap with each other. Below 30 ^{o}C, R_{core} slightly decreases upon heating, which can be attributed to a decreasing aggregation number upon heating. R_{mic} is also slightly reduced with increasing temperature, indicating a weak shrinkage of the micelles. The SLD profiles (Fig. 1.7c) reflect the core without water content, the slightly collapsed micelles and the dehydration of the shell upon heating. Above 30 ^{o}C, R_{mic} abruptly decreases to 13 nm, thus, the shell drastically collapses. Upon further increase of temperature, R_{mic} continuously decreases to 9 nm. In addition, fractal-like clusters that are formed by the collapsed micelles, appear and grow. The cluster size drastically increases from 15 nm to 55 nm with increasing temperature. However, above 34 ^{o}C, the collapsed micelles become even smaller upon heating, and the fractal-like clusters become more compact and turn into compact aggregates.

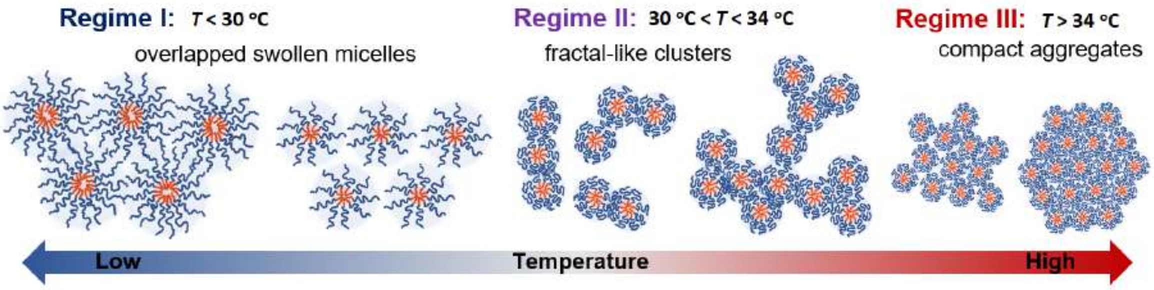

Figure 1.8:
Schematic structures of of a 10 g L^{-1} solution of $PMMA_{22}$-*b*-$PNIPAM_{260}$ in D_2O in dependence on temperature.

In summary, the structure of self-assembled micelles and their changes upon collapse and aggregation with increasing temperature in D_2O is elucidated by synchrotron SAXS. The resulting structures are summarized in Fig. 1.8. In regime I, spherical micelles are formed and overlapped with each other. In regime II, the micelles collapse and form fractal-like clusters. The clusters become compact aggregates in regime III.

The project is funded by Deutsche Forschungsgemeinschaft (DFG).

1.5 Water dynamics in a concentrated poly(*N*-isopropylacrylamide) solution at variable pressure

B.-J. Niebuur, W. Lohstroh[1], M.-S. Appavou[2], A. Schulte[3], C. M. Papadakis

[1] MLZ, Garching, Germany
[2] JCNS at MLZ, Garching, Germany
[3] University of Central Florida, Orlando, U.S.A.

Hydration water is of fundamental importance for the structure and functionality of responsive polymers in aqueous solution. Here, we address the water dynamics in a concentrated aqueous solution of the thermoresponsive polymer poly(*N*-isopropylacrylamide) (PNIPAM). At atmospheric pressure, PNIPAM shows lower critical solution temperature (LCST) behavior with a critical temperature of 32 °C. In the one-phase region, both hydrophilic and hydrophobic groups are hydrated, and the polymer is soluble. Above the cloud point T_{cp}, cooperative dehydration of hydrophobic groups causes the chains to collapse and to aggregate, while the hydrophilic groups retain a substantial amount of hydration [1]. At high pressure, the chains do not dehydrate as strongly at T_{cp}. In the present study, we use quasi-elastic neutron scattering (QENS) to investigate the role of hydration water in a concentrated aqueous PNIPAM solution at temperatures around T_{cp} at both atmospheric and at high pressure [2].
Poly(*N*-isopropylacrylamide) with a molar mass of 36 kg mol^{-1} was dissolved in deionized H_2O at a polymer concentration of 25 wt%. At this concentration, a large fraction of water is in contact with the polymer as hydration water. QENS measurements were conducted at the time-of-flight spectrometer TOFTOF at the FRM II, Garching, Germany. A wavelength of the incident neutron beam of 6 Å along with an elastic energy resolution of ca. 0.03 meV (HWHM) were selected. The sample was mounted in an aluminum pressure cell. Heating scans around the cloud points ($T_{cp} = 31.4 \pm 0.1$ °C and 34.1 ± 0.1 °C for 0.1 and 130 MPa, resp.) were performed at atmospheric pressure (0.1 MPa) and at 130 MPa with measuring times of 60-120 min. The spectra were normalized to the incoming neutron flux and a vanadium standard measurement, and the empty cell scattering was subtracted.

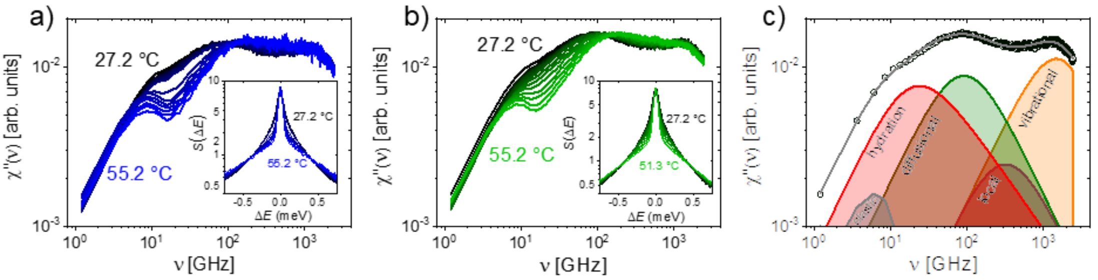

Figure 1.9:
(a,b) Dynamic susceptibilities in dependence on frequency ν at a momentum transfer $q = 1.65$ Å^{-1} at (a) 0.1 and (b) 130 MPa in dependence for temperatures across the cloud point. The insets show the corresponding dynamic structure factors $S(\Delta E)$ in dependence on energy transfer. (c) Example fit (dark grey line) and its deconvolution into the individual components (colored lines) at 130 MPa, 27.2 °C and 1.65 Å^{-1}.

The insets in Fig. 1.9a and b show dynamic structure factors $S(\Delta E)$ at a momentum transfer $q = 1.65$ Å^{-1} in dependence on temperature at 0.1 MPa and 130 MPa. These are transformed into susceptibility spectra (Fig. 1.9a and b). In the latter, a strong relaxation peak at low frequencies (ca. 30 GHz) is observed at temperatures below T_{cp}. We attribute this peak to the relaxation of the hydration water. At T_{cp}, this contribution decreases sharply in intensity at atmospheric pressure, suggesting that the dehydration process is abrupt. At 130 MPa, in contrast, the decrease is gradual. At both pressures, a weak contribution at low frequencies remains above T_{cp}, which is attributed to scattering from very slowly moving moieties. At higher frequencies, the well-known relaxation process of water are observed, namely the diffusional process at ca. 80 GHz, the local process at ca. 400 GHz and the vibrational process at ca. 2000 GHz.

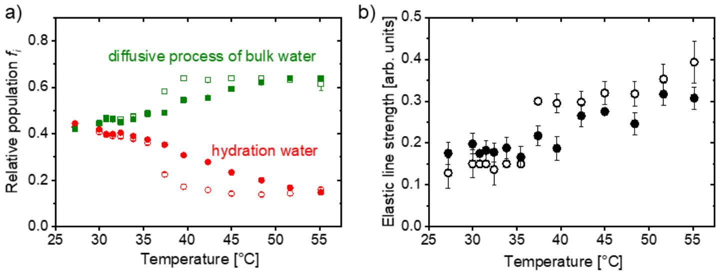

Figure 1.10:
(a) Relative populations f_i of hydration and bulk water and (b) elastic line strength, both in dependence on temperature at $q = 1.65$ Å^{-1}. Open symbols: 0.1 MPa, closed symbols: 130 MPa.

The susceptibility spectra of the PNIPAM solution are modelled with Debye functions (diffusional and local process), a damped harmonic oscillator (vibrational process) and a Cole-Davidson process (hydration water), see Fig. 1.9c. The resulting relative populations of the hydration water and the bulk water are determined (Figure 1.10a). At atmospheric pressure, the relative population of the hydration water far below T_{cp} is 0.45, in consistency with the calculated ratio of bound to free water molecules. Near T_{cp}, the ratio decreases sharply to 0.2, i.e. the chains dehydrate partially. The remaining water may be due to persisting hydrogen bonds of the hydrophilic amide groups with water, and the dehydration is mainly related to the release of water from the hydrophobic groups. In the one-phase region at 130 MPa, the relative population of hydration water is similar to the one at atmospheric pressure. However, at T_{cp}, no sharp transition is observed, but a smooth decay of the relative population of hydration water. Thus, the change of the hydration behavior at T_{cp} depends significantly on pressure, in accordance with results from Raman spectroscopy [3]. The relative population of bulk water increases sharply at atmospheric pressure and gradually at 130 MPa. Thus, the hydration water that is released from the chains at T_{cp} adds to the bulk water phase. Moreover, the amplitude of the elastic line increases with temperature at both pressures (Fig. 1.10b). Thus, above T_{cp}, the hydration water either stays close to the chains or joins the bulk water phase.

The analysis of the q-behavior of the relaxation frequency of the hydration water (not shown) reveals that it can described by jump diffusion, both below and above T_{cp}. At both pressures, the residence time of H_2O on the chain increases at T_{cp}, which may be attributed to an increased hindrance of the motion of H_2O along the chain and/or to trapping of water. The residence time is overall lower at high pressure, which reflects a weaker constraint of hydration water motion than at atmospheric pressure. This may be due to the lower degree of dehydration of the amide groups in favor of the hydrophobic groups, which are more hydrated at high pressure.

To summarize, QENS in a wide range of energy and momentum transfers at high pressure allows distinguishing the relaxation of hydration water around PNIPAM chains from the relaxation processes in bulk water. The findings concerning the dynamics of hydration water in this model responsive polymer point to new opportunities for studies of more complex systems using QENS.

[1] M. Philipp, K. Kyriakos, L. Silvi, W. Lohstroh, W. Petry, J. K. Krüger, C. M. Papadakis, P. Müller-Buschbaum, *J. Phys. Chem. B* **118**, 4253 (2014)

[2] B.-J. Niebuur, W. Lohstroh, M.-S. Appavou, A. Schulte, C. M. Papadakis, *Macromolecules* **52**, 1942 (2019)

[3] B.-J. Niebuur, V. Pipich, M.-S. Appavou, A. Schulte, C. M. Papadakis et al., *ACS Macro Lett.* **6**, 1180 (2017).

1.6 Kinetics of mesoglobule formation and growth in aqueous poly(*N*-isopropylacrylamide) solutions: role of the target pressure

B.-J. Niebuur, L. Chiappisi[1,2], F. A. Jung, X. Zhang, A. Schulte[3], C. M. Papadakis

[1] ILL, Grenoble, France
[2] TU Berlin, Institut für Chemie, Germany
[3] University of Central Florida, Orlando, U.S.A.

The mechanisms of growth in aggregating systems and interactions stabilizing the aggregates are of great importance in a wide variety of research areas, such as the study of proteins, and are of relevance to gain insights that may be needed to design smart materials. The aggregate formation of stimuli-responsive polymers is of special interest, since their solubility can be drastically altered by external stimuli, such as temperature or pressure, resulting in collapse and aggregation. Aqueous solutions of the thermoresponsive polymer poly(*N*-isopropylacrylamide) (PNIPAM) feature lower critical solution temperature (LCST) behavior. At the cloud point T_{cp}, which is ca. 32 °C, hydration water is released, leading to a sharp coil-to-globule transition of the individual chains and subsequent formation of long-lived aggregates in the mesoscopic size range, termed mesoglobules. Several mechanisms have been proposed to contribute to their stability, among them the viscoelastic effect, which is due to fact that the chain entanglement time is much longer than the time during which two mesoglobules are in contact. This reduces the probability of coalescence and prevents macrophase separation in the solution. Since the chains strongly dehydrate when T_{cp} is crossed, the chain mobility in the mesoglobules is low, which leads to a strong viscoelastic effect at atmospheric pressure. Rapid changes of pressure across the coexistence line in the temperature-pressure frame can be applied to induce phase separation. In the present study, we combine fast pressure jumps to initiate phase separation in an aqueous solution of PNIPAM and kinetic small-angle neutron scattering (SANS) to investigate the kinetics of mesoglobule formation [1,2]. Pressure jumps were initiated by opening a pneumatically driven valve between the pressure cell and a reservoir, in which underpressure was applied, resulting in a time resolution better than 0.1 s. Starting in the one-phase region at 31 MPa and at 35.1 °C, the pressure was rapidly lowered by values Δp between -11 and -31 MPa. This way, the coexistence line, which is at 22 MPa at this temperature, is crossed, and the target pressure lies in the two-phase region.

A 3 wt% solution of PNIPAM (molar mass 36 kg/mol) in D_2O was investigated using time-resolved small-angle neutron scattering (TR-SANS) at the instrument D11 at ILL. A neutron wavelength of 0.6 nm was selected along with sample-detector distances of 1.5, 8.0 and 34.0 m. The pressure cell and the separator were connected to the pressure generator by a pneumatically driven valve (PDV). Before each pressure jump, the pressure was set to the initial value, and a static SANS measurement (pre-jump measurement) with a measuring time of 1 min was carried out. The PDV was closed, and the pressure in the external system was set to a lower value. When the PDV was rapidly opened, data acquisition was started automatically. After each pressure jump, 85 frames of a duration of $0.05 - 30$ s were recorded for on total 1650 s.

The pre-jump SANS data (red curve in Fig. 1.11a) show a decay above a momentum transfer $q > 0.1$ nm^{-1}, characteristic of the concentration fluctuations in semi-dilute polymer solutions in the one-phase region. The data are fitted using the Ornstein-Zernike structure factor. The resulting correlation length is $\xi = 15.2 \pm 0.1$ nm. The SANS data following the jumps with $\Delta p = -11$, -15 and -31 MPa are exemplarily shown in Fig. 1.11. Three growth regimes are observed for $\Delta p = -15$ MPa (Fig. 1.11b): (i) Only concentration fluctuations are present during the first 1 s, (ii) forward scattering appears at $q < 0.1$ nm^{-1} and changes shape, and (iii), the forward scattering hardly changes shape anymore after ca. 100 s. This contribution was fitted by the Guinier-Porod form factor to determine the radius of gyration of the aggregates. At

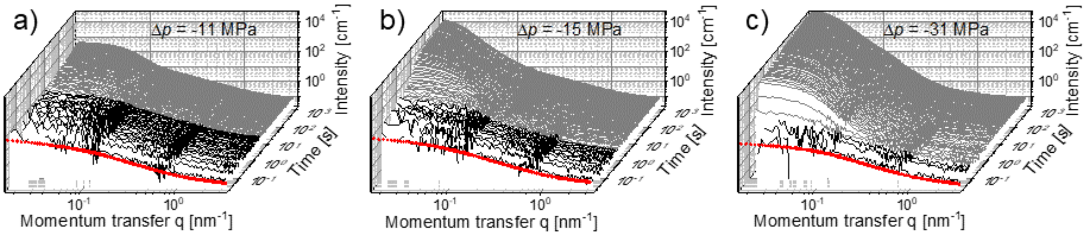

Figure 1.11:
(a,b) SANS data after jumps with $\Delta p = -11$ MPa (a), -15 MPa (b) and -31 MPa (c). Red symbols: pre-jump measurements, black and grey lines indicate the data that do not/do contain a contribution from aggregates, respectively.

$\Delta p = -11$ MPa (Fig. 1.11a), the growth of the forward scattering is much weaker and slower, whereas it occurs abruptly after ca. 0.1 s for $\Delta p = -31$ MPa.

The correlation lengths of the chains, ξ, and the radii of gyration of the aggregates, R_g are shown in dependence on time in Fig. 1.12a for all 4 pressure jumps. For $\Delta p = -15$ and -21 MPa, ξ increases slowly, respectively, as expected when approaching the phase transition. The aggregates appear after 0.1 or 1 s, respectively, and grow first as $R_g \propto t^{1/3}$, i.e. by diffusion-limited coalescence. At later times, the growth of R_g slows down, and a detailed analysis reveals that an energy barrier is present. We attribute this barrier to the dehydration of the aggregates, which leads to the formation of a rigid shell that hinders further coalescence. For $\Delta p = -11$ MPa, aggregates appear only after 10 s, and they grow very slowly, which we attribute to the low thermodynamic driving force for phase separation. For $\Delta p = -31$ MPa, aggregates appear already after 0.17 s and grow abruptly. Very soon, however, the slow growth regime is entered, i.e. the strong dehydration leads to large, but rigid mesoglobules, which can hardly coalesce with each other. For all Δp values, the aggregates still contain water, as evident from the finite values of ξ (Fig. 1.12b).

To summarize, the influence of the target pressure on the kinetics of mesoglobules formation in aqueous PNIPAM solutions has been investigated with time-resolved SANS following fast pressure changes across the coexistence line, starting in the one-phase state and ending in the two-phase state. The time resolution amounts to ca. 0.05 s, and a size range of ca. 1-100 nm was covered, which allows unprecedented information on the aggregate sizes, their inner structure, and the growth processes. Our experiments allow identifying the roles of the thermodynamic driving force and of kinetic effects and this way to contribute to the understanding of mesoglobule formation and their extraordinary stability observed at atmospheric pressure.

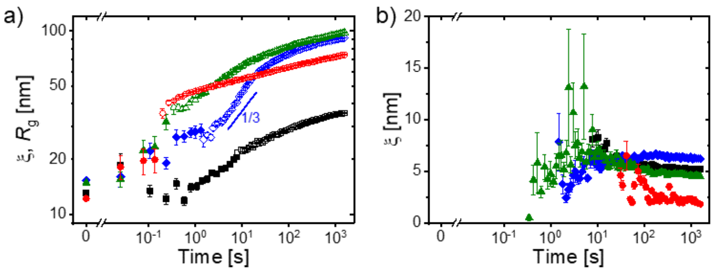

Figure 1.12:
(a) Resulting correlation length of concentration fluctuations, ξ (closed symbols), and radius of gyration of the aggregates, R_g (open symbols). (b) ξ values within the aggregates. Black squares: $\Delta p = -11$ MPa, blue diamonds: -15 MPa, green triangles: -21 MPa, red circles: -31 MPa.

[1] B.-J. Niebuur, L. Chiappisi, X. Zhang, F. Jung, A. Schulte, C. M. Papadakis, *ACS Macro Lett.* **7**, 1155 (2018)

[2] B.-J. Niebuur, L. Chiappisi, F. Jung, X. Zhang, A. Schulte, C. M. Papadakis, *Macromolecules* **52**, 6416 (2019)

1.7 Temperature- and Pressure-Dependent Phase Behavior of PS-*b*-PNIPAM Diblock Copolymers in Aqueous Solution

S.-H. Huang, C.-H. Ko, G. P. Meledam, M. Schroer[1], A. Miasnikova[2],
A. Laschewsky[2,3] and C. M. Papadakis

[1] European Molecular Biology Laboratory, Hamburg, Germany
[2] Universität Potsdam, Potsdam-Golm, Germany
[3] Fraunhofer IAP, Potsdam-Golm, Germany

Polystyrene-*b*-poly(*N*-isopropylacrylamide) (PS-*b*-PNIPAM) is a diblock copolymer, which is able to self-assemble into micelles in aqueous solution and which exhibits the thermoresponsive behavior. Due to its hydrophobicity, the PS block forms the core, and the thermoresponsive PNIPAM block forms the shell [1]. The responsive properties of micelles formed by PS-*b*-PNIPAM are due to the PNIPAM block, which is a lower critical solution temperature (LCST) type thermoresponsive polymer with a cloud point T_{CP} at 32 ^{o}C in aqueous solution [2]. It makes PS-*b*-PNIPAM a potential material for biomedical applications. In addition to the temperature, the cloud point of PNIPAM can also be triggered by pressure.

We investigate the phase behavior of PS-*b*-PNIPAM in D_2O in dependence on temperature and pressure by turbidimetry to determine the coexistence line in the temperature-pressure frame of PS-*b*-PNIPAM in D_2O. Besides, small-angle X-ray scattering (SAXS) measurements are carried out to characterize the micellar structure and its transition in dependence on temperature at atmospheric pressure.

PS_{11}-*b*-$PNIPAM_{230}$ with a molar mass 25 760 g/mol was synthesized by the reversible addition fragmentation chain transfer (RAFT) method. The polymers were dissolved in D_2O at a concentration of 15 mg/ml.

The turbidimetry results are shown in Fig. 1.13. The coexistence line is an ellipse in the temperature-pressure frame. For the 15 mg/ml solution, T_{CP} is 30.5 ^{o}C at atmospheric pressure. It increases to 31.1 ^{o}C at 40.0 MPa and decreases as pressure further increases. The data can be fitted by an ellipse. The shape of the coexistence curves from PS_{11}-*b*-$PNIPAM_{230}$ is similar to the one of PNIPAM homopolymer. However, the overall T_{CP} of PS_{11}-*b*-$PNIPAM_{230}$ are ca. 5 K lower than those of the PNIPAM homopolymer. This could be attributed to the fact that the self-assembled micellar structure of the PS_{11}-*b*-$PNIPAM_{230}$ hinders the collapse of the PNIPAM chain.

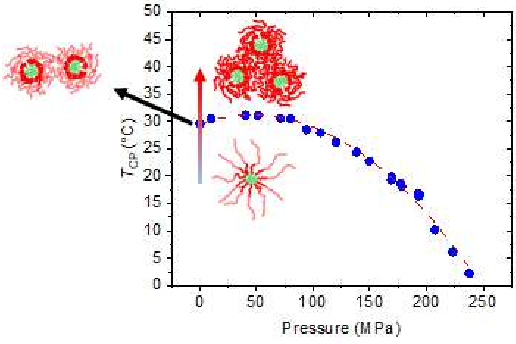

Figure 1.13:
Phase diagram of the PS_{11}-*b*-$PNIPAM_{230}$ in D_2O in dependence on temperature and pressure and its micellar structure evolution at ambient pressure. Blue circles: data from turbidimetry, dashed red line: fit of an ellipse. The arrows indicate the scans carried out by SAXS.

To characterize the inner structure of the micelles, SAXS measurements were performed in dependence on temperature at ambient pressure at beamline, measured at beamline P12, EMBL at DESY, Hamburg. The wavelength of the incident X-ray was 0.124 nm, the sample-detector distance was 3 m, and the measurement time of each curve was 0.045 s. The SAXS data of PS_{11}-*b*-$PNIPAM_{230}$ at 15 mg/ml in D_2O are shown in Fig. 1.14a. Due to the similarity of the scattering length densities (SLDs) of PS and PNIPAM, the core-shell structure of the micelles could not be resolved. Instead, the form factor of homogeneous spheres was applied. At 20 ^{o}C, the micellar radius (R_m) is 6.6 nm, and the hard-sphere radius (R_{HS}) is 14.5 nm. On account of the SLD contrast issue, R_m reveals the size of the PS core and the inner, less hydrated PNIPAM shell rather than the overall size of micelles as shown in Fig. 1.13. Below T_{CP}, both R_m and R_{HS} have decreased as temperature increases, indicating that the micelles collapse and get closer to each other upon heating. Above T_{CP}, R_m is around 5.0 nm and R_{HS} decreases to about 8 nm. This may be attributed to small clusters formed by several collapsed micelles. Above 35 ^{o}C, R_m is dramatically increased, which indicates that the small clusters grow and form larger aggregates. The dehydration of the PNIPAM shell is also confirmed by the increasing SLD values of the micelles in Fig. 1.14c.

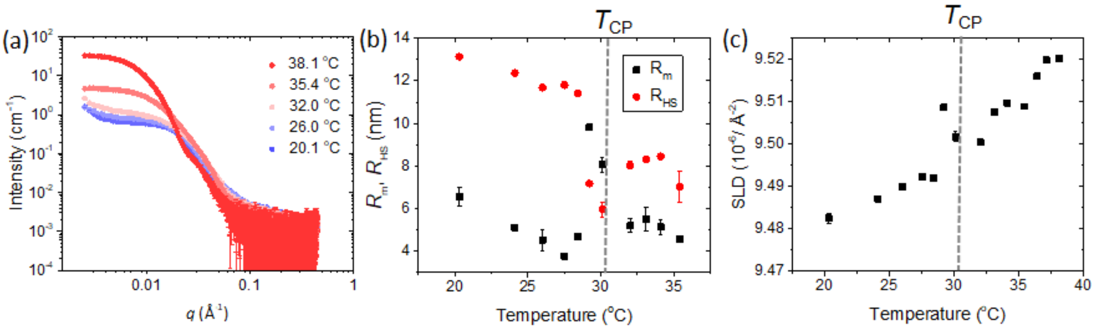

Figure 1.14:
a) SAXS data of PS_{11}-*b*-$PNIPAM_{230}$ at 15 mg/ml in D_2O at ambient pressure at the temperatures given, b, c) resulting structural parameters.

To conclude, the coexistence line of PS_{11}-*b*-$PNIPAM_{230}$ in the temperature-pressure frame is determined. In addition, the micellar structure and its transition behavior of this diblock copolymer is elucidated using synchrotron SAXS. The resulting structures are shown in Fig. 1.13. However, the overall size of the micelles cannot be quantitatively characterized due to the SLD contrast problem. The overall micellar size decreases as the cloud point is approached, while above, the collapsed micelles form small aggregates. The dehydration behavior is evident from the overall increase of the scattering length density.

[1] J. Adelsberger, A. Meier-Koll, A. M. Bivigou-Koumba, P. Busch, O. Holderer, A. Laschewsky, P. Müller-Buschbaum, C. M. Papadakis, *Colloid Polym. Sci.* **289**, 711-720 (2011)

[2] A. Halperin, M. Kröger, and F.M. Winnik, *Angew. Chem. Int. Ed.* **54**, 15342-15367 (2015)

1.8 Small-angle neutron scattering investigations on the phase behavior and structural modifications of PMMA-*b*-PNIPAM micelles in aqueous solutions

G. P. Meledam, C.-H. Ko, S.-H. Huang, B.-J. Niebuur, L. Chiappisi[1], C. Henschel[2],
A. Laschewsky[2,3], A. Schulte[4], and C. M. Papadakis

[1] ILL, Grenoble, France
[2] Universität Potsdam, Potsdam-Golm, Germany
[3] Fraunhofer IAP, Potsdam-Golm, Germany
[4] University of Central Florida, Orlando, U.S.A.

Amphiphilic block copolymers are known to exhibit rich phase behavior with the intriguing associated structural transitions [1,2]. Poly(methyl methacrylate)-*b*-poly(*N*-isopropylacrylamide) (PMMA-*b*-PNIPAM), a special category of amphiphilic diblock copolymers, consists of a hydrophobic PMMA block and a thermoresponsive PNIPAM block. In aqueous solution, PMMA-*b*-PNIPAM self-assembles to form core-shell micelles. PNIPAM in aqueous solution shows a lower critical solution temperature (LCST) behavior where the polymer changes its configuration from an extended coil to a collapsed globule. The LCST transition in PNIPAM is mostly controlled by competing forces such as hydrogen bonding between water molecules and polymer chains and the hydrophobic interactions of hydrophobic entities of PNIPAM with the water molecules. It has been reported that the water molecules which are in the vicinity of the hydrophobic groups in the polymer exhibits very different properties compared to the water molecules in the bulk water. For instance, they display an increased compressibility as well as an ordered clathrate-like structure [3,4]. Owing to these properties, it is possible to affect the hydration state of the thermoresponsive PNIPAM block and thereby the phase behavior of the block copolymer micelle in aqueous solution by applying pressure [3,5].

In this work, the macroscopic phase behavior and the underlying microscopic structural modifications of the diblock copolymer PMMA-*b*-PNIPAM in aqueous solutions have been investigated using turbidimetry in combination with small-angle neutron scattering (SANS) experiments across the phase boundary. Turbidimetry experiments were carried out on a 50 mg/ml solution of PMMA$_{22}$-*b*-PNIPAM$_{260}$ ($M_n = 32000$ g/mol) in D_2O by varying temperature between 10 and 40 °C. The normalized transmittance as a function of temperature measured at different pressures is shown in Fig. 1.15 (a). The cloud point is identified as the temperature at which the normalized transmittance shows a sharp decrease. The temperature-pressure phase diagram is given in Fig. 1.15 (b). The red line in Fig. 1.15 (b) indicates an elliptical fit to the data. The elliptical shape of the co-existence line observed for PMMA-*b*-PNIPAM is similar to the phase diagram observed for PNIPAM homopolymers [5]. Further, the structural changes of PMMA-*b*-PNIPAM in aqueous solution during the LCST transition is monitored using SANS at D11, ILL by performing temperature scans across the phase boundary. The scattering profiles together with the fits at different temperatures measured at two pressures (0.1 MPa and 75 MPa) are shown in Fig. 1.15 (c) and (d) respectively. The scattering profiles at low and high pressure differ markedly, especially above the cloud point, which indicates the strong influence of pressure on the structure of aggregates formed by PMMA-*b*-PNIPAM micelles. At both pressures, the intensity of forward scattering increases with temperature which indicates the formation of larger PMMA-*b*-PNIPAM micellar aggregates. The SANS profiles are modeled using a spherical micelle form factor together with a sticky hard-sphere structure factor to represent the scattering contribution from PMMA-*b*-PNIPAM micelles. Further, a Porod form factor is used to model the scattering contribution from micellar aggregates. From the fits, it is evident that at low pressures the PNIPAM shell collapses and form micellar aggregates above the cloud point. On the other hand at high pressure, the micellar aggregates are rather hydrated even above the cloud point.

A schematic representation of PMMA-*b*-PNIPAM micelles and micellar aggregates, below and above the cloud point, at low pressure and high pressure are indicated in Fig. 1.15 (b). Thus, pressure has a strong influence on the aggregation behavior of thermoresponsive micelles.

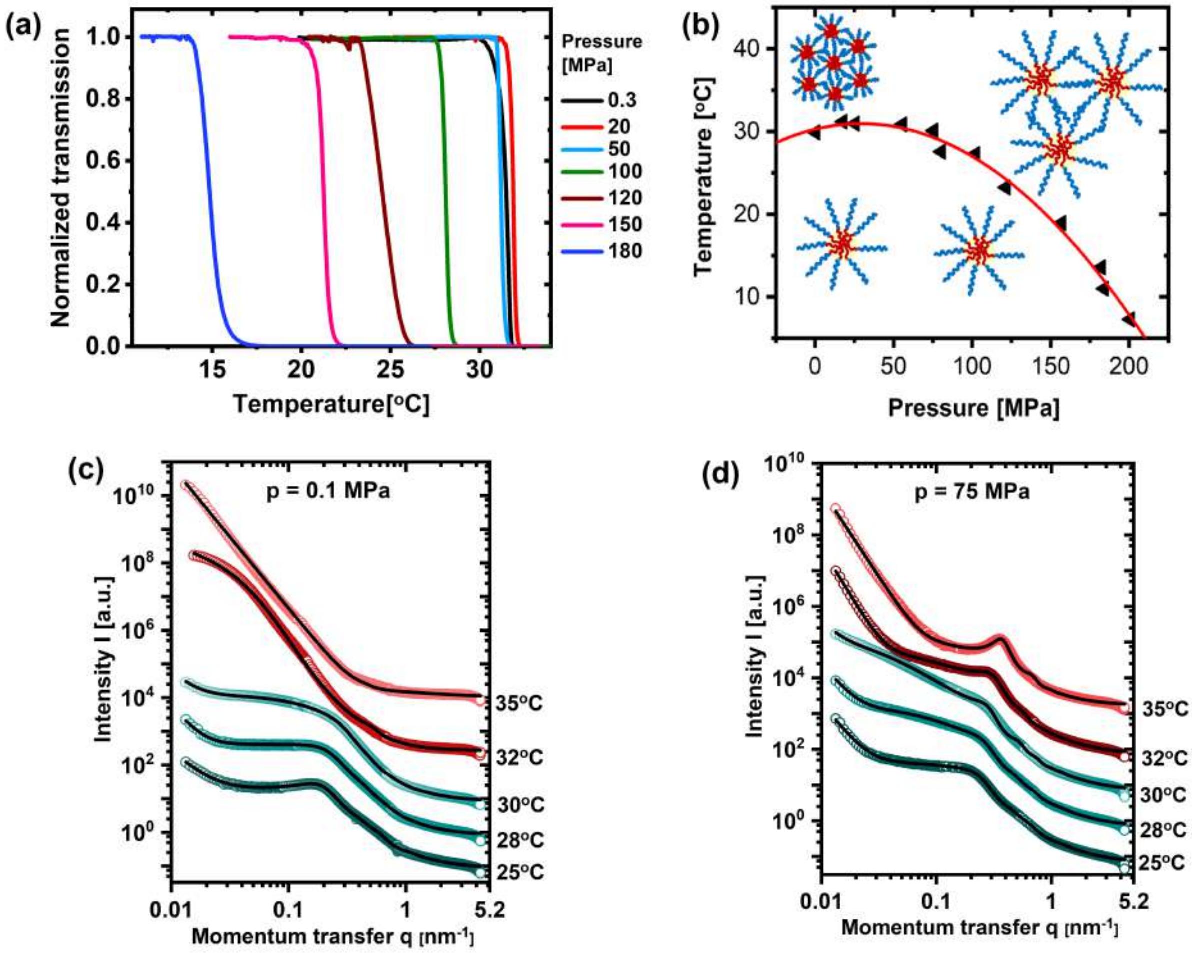

Figure 1.15:
(a) Normalized transmission as a function of temperature measured at different pressures for PMMA-*b*-PNIPAM in D_2O with a concentration of 50 mg/ml. (b) Temperature-pressure phase diagram where the symbols represent measured cloud points, and the red curve indicates an elliptical fit to the data points. SANS profiles together with the fits as described in the text at various temperatures for PMMA-*b*-PNIPAM in D_2O at a concentration of 50 mg/ml measured at pressures of (c) $\mathrm{p} = 0.1\,\mathrm{MPa}$ and at (d) $\mathrm{p} = 75\,\mathrm{MPa}$.

[1] J. Adelsberger, E. Metwalli, A. Diethert, I. Grillo, A. M. Bivigou-Koumba, A. Laschewsky, P. Müller-Buschbaum, and C. M. Papadakis, *Macromolecular Rapid communications*, **33**, 254 (2012).

[2] J. Adelsberger, I. Grillo, A. Kulkarni, M. Sharp, A. M. Bivigou-Koumba, A. Laschewsky, P. Müller-Buschbaum, and C. M. Papadakis, *Soft Matter*, **9**, 5 (2013).

[3] B.-J. Niebuur, K.-L. Claude, S. Pinzek, C. Cariker, K. N. Raftopoulos, V. Pipich, M.-S. Appavou, A. Schulte, and C. M. Papadakis, *ACS Macro Lett.*, **6**, 1180 (2017).

[4] S. Sarupria and S. Garde, *Phys. Rev. Lett.*, **103**, 037803 (2009).

[5] B.-J. Niebuur, L. Chiappisi, X. Zhang, F. Jung, A. Schulte, and C. M. Papadakis, *ACS Macro Lett.*, **7**, 1155 (2018).

2 Responsive thin films

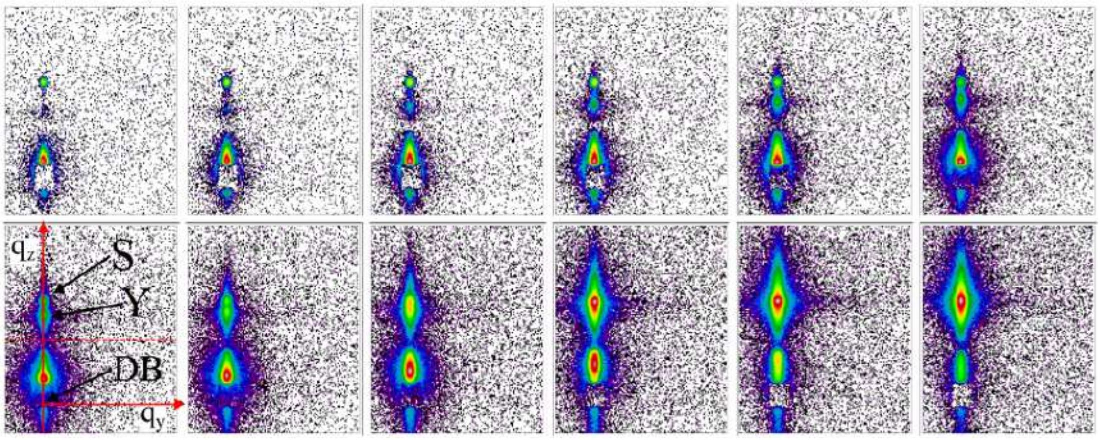

2.1 Time-resolved TOF-NR investigation of the cononsolvency effect of PMMA-*b*-PNIPAM thin films

C. Geiger, L. P. Kreuzer, T. Widmann, R. Cubitt[1], C. Henschel[2], A. Laschewsky[2],
C. M. Papadakis, P. Müller-Buschbaum

[1] ILL, Grenoble, France
[2] Universität Potsdam, Potsdam-Golm, Germany

The amphiphilic diblock copolymer PMMA-*b*-PNIPAM forms micelles in aqueous solution that feature a permanently hydrophobic core of PMMA (poly(methyl methacrylate)) and a thermo-responsive shell of PNIPAM (poly(*N*-isopropylacrylamide)). These micelles exhibit a typical reversible shell collapse transition at the lower critical solution temperature (LCST). Apart from a temperature stimulus, the PNIPAM block is sensitive to the solvent composition, e.g. of water-alcohol or water-acetone mixtures. While water and organic cosolvents each act as good solvents individually, a collapse can be induced in a certain composition range due to the competitive attachment and detachment of water and cosolvent to the PNIPAM chains. Essentially, the LCST shifts to lower temperatures as a function of molar fraction of the cosolvent. [1]

We demonstrate using PMMA-*b*-PNIPAM, that cononsolvency induced collapse transitions are transferrable from polymer solutions to thin films in contact with mixed saturated vapors. In order to design catalysts, sensors and actuators in thin film geometry using thermo-responsive functional polymers, it is essential to get a deeper understanding what differences are to be expected in the cononsolvency behavior of polymers moving from solutions to thin films.

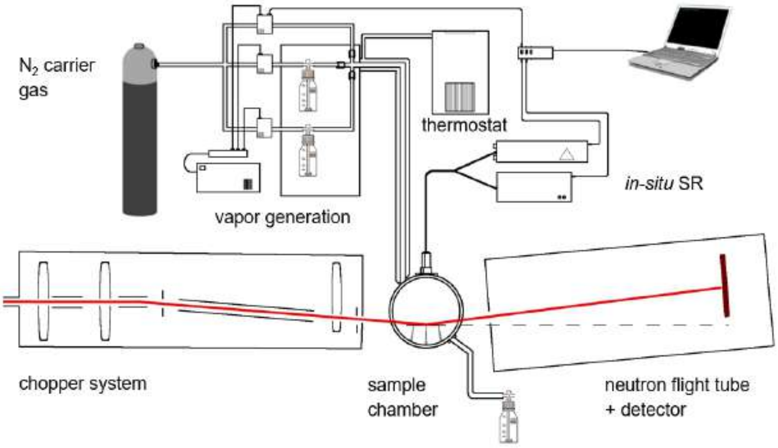

Figure 2.1:
Gasflow setup and sample environment (schematic). N_2 acts as drying gas and carrier gas for vapor generation. Thermal equilibrium across the vapor generation chamber, feed tube and sample environment is achieved via a single thermostat cycle. The setup allows simultaneous collection of SR, TOF-NR, and sample environment (temperature, gasflow status) data. NR layout adopted from [2].

Thin films are prepared by spincoating PMMA$_{22}$-*b*-PNIPAM$_{260}$ (DP_n according to ^{1}H-NMR) from 1,4-dioxane solutions onto precleaned Si wafers. To ensure a consistent quality and eliminate possible influences of the spin-coating agent on the responsive behavior, the films then are thermally annealed at 150 °C.

Film swelling and collapse kinetics are measured combining *in-situ* spectral reflectance (SR) with a time resolution of 10 s and time-of-flight neutron reflectometry (TOF-NR) achieving a time resolution of up to 5 s (D17 reflectometer, ILL). Fig. 2.1 displays the gasflow setup and sample environment used for such an experiment. In general, the measurement protocol consists of a drying phase in N_2, a swelling phase in water vapor and a final phase during which the atmosphere is exchanged to a mix of water and cosolvent. Sequential contrasting experiments using protonated and deuterated compounds allow to differentiate between the distributions of water and cosolvent within the polymer films.

Results obtained from measuring the contrast dataset D_2O/MeOH are displayed in Fig. 2.2. TOF-NR data was collected at the D17 instrument at ILL. Divergent beam reflectometry data reduction was performed using the algorithm presented in [3].

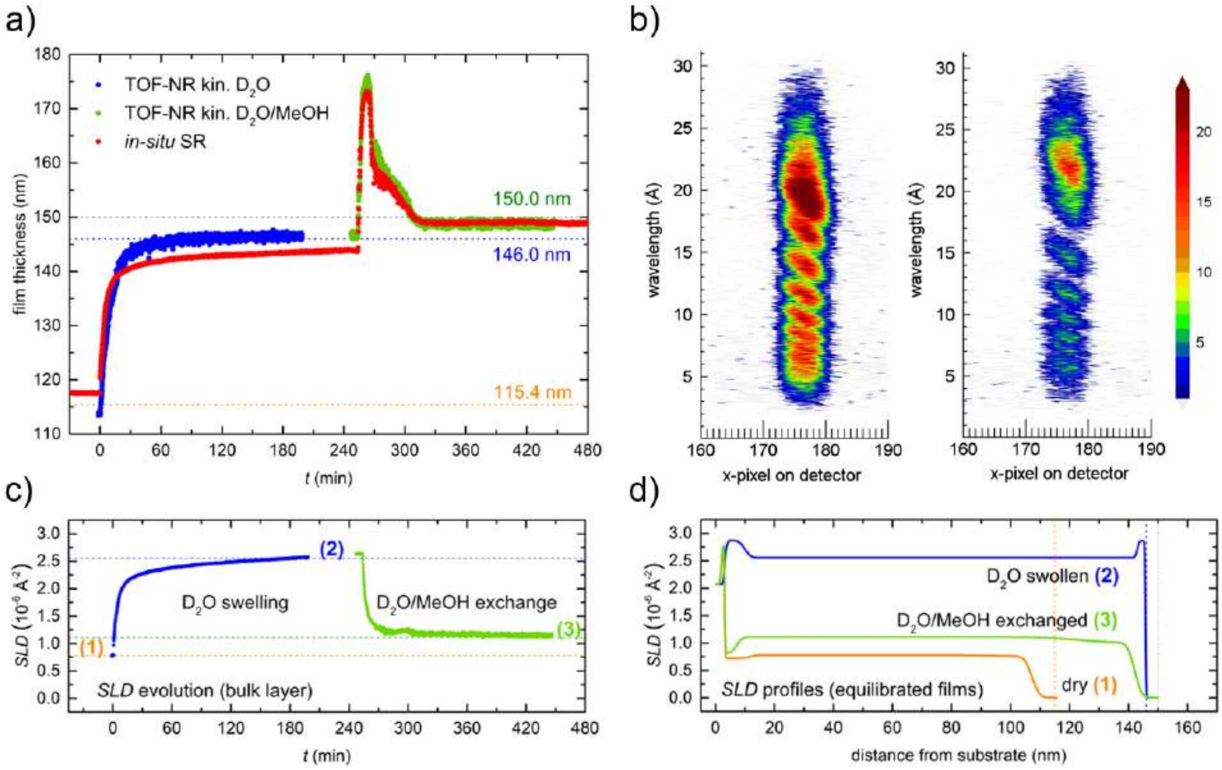

Figure 2.2:
a) Film thickness evolution obtained during swelling in D_2O vapor and exchange to mixed D_2O/MeOH vapor. Dotted lines mark the polymer-air interface in dry, swollen and exchanged equilibrium. b) Reflected intensity (counting time 5 s, contour plot excerpts) collected during kinetic measurements (left: D_2O swollen film, at $t = 245$ min; right: D_2O/MeOH exchanged film, at $t = 485$ min). c) SLD evolution during swelling and exchange processes. Dotted lines mark SLD value of the bulk layer in dry, swollen and exchanged equilibrium. d) Detailed SLD profiles stretching the equilbrated films' vertical. Obtained from multilayer model derived from static measurements. Dotted lines mark the polymer-air interface in dry, swollen and exchanged equilibrium.

At the exposure to D_2O vapor, the dried film rapidly swells due to the incorporation of water into the polymer layer, and reaches a equilibrium thickness after ca. 200 min. A slow increase of SLD at equilibrium film thickness marks the slow ongoing deuteration of the amide functional groups of PNIPAM [4]. Then, at the continuous exchange of the fully humidified environment to a saturated mixed atmosphere generated from D_2O and MeOH vapor streams, a swelling and subsequent collapse transition is observed at the steady exchange of water and methanol species within the film, as confirmed by the continuous decrease of the SLD of the bulk. Detailed SLD profiles of the film in its equilibrium stages reveal solvent enrichment at both the air-polymer and polymer-substrate interfaces. Notably, a decrease in SLD close to the polymer-substrate interface reveals methanol has fully penetrated the film's bulk in the exchanged state.

[1] F. M. Winnik, H. Ringsdorf, J. Venzmer, *Macromolecules* **23**, 2415-2416 (1990)

[2] J.-F. Moulin, M. Haese, *J. Large-Scale Res. Facil.* **1**, 9 (2015)

[3] R. Cubitt, T. Saerbeck, R. A. Campbell, R. Barker, P. Gutfreund, *J. Appl. Cryst.* **48**, 2006-2011 (2015)

[4] T. Widmann, L. P. Kreuzer, N. Hohn, L. Bießmann, K. Wang, S. Rinner, J. F. Moulin, A. J. Schmid, Y. Hannappel, O. Wrede, M. Kühnhammer, T. Hellweg, R. von Klitzing, P. Müller-Buschbaum, *Langmuir* **35**, 16341-16352 (2019)

2.2 Phase transition kinetics of doubly thermo-responsive poly(sulfobetaine)-based diblock copolymer thin films

L. P. Kreuzer, T. Widmann, L. Bießmann, N. Hohn, J. Pantle, J.-F. Moulin[1],
V. Hildebrand[2], A. Laschewsky[2], C. M. Papadakis, P. Müller-Buschbaum

[1] MLZ, Garching, Germany
[2] Universität Potsdam, Potsdam-Golm, Germany

Poly(sulfobetaine)s (PSB) are zwitter-ionic polymers, that contain both, an anionic and a cationic group within their repeating units. [1] Due to their similar structure to phospholipids, the independence of their zwitterionic character towards pH and the high chemical stability they are widely used as antifouling materials and biocompatible lubrication. In addition, PSB show an upper critical solution temperature (UCST) in aqueous solution, which means they undergo a coil-to-globule transition upon cooling. This behavior is highly unusual, since UCST behavior is rather known to occur in organic solvents. Furthermore, other zwitterionic polymers, such as poly(carboxybetaine)s and poly(phosphatidylcholine)s show no thermo-responsive behavior at all. In comparison, non-ionic polymers, such as poly(N-isopropylmethacrylamide) (PNIPMAM), show lower critical solution temperature (LCST) behavior in aqueous solution. By combining both, an UCST-type and an LCST-type polymer, a block copolymer (BCP) is generated (Fig. 2.3a), that shows unique solution behavior: micelles with a hydrophobic PSB core and a hyd rophilic PNIPMAM shell are formed at temperatures below UCST and LCST. Their structure can be inversed by increasing the temperature above the UCST and LCST. Now, PNIPMAM is the hydrophobic core, while PSB is the hydrophilic shell. This behavior is called schizophrenic micellar self-assembly. Dependent on the relative positions of the UCST and LCST, the phase diagram shows either a fully hydrophilic (UCST $<$ LCST) or fully hydrophobic intermediate regime (UCST $>$ LCST) (Fig.2.3b). Especially PSB is strongly sensitive towards polymer concentration (UCST increases) and salt additives (UCST decreases).[2] Therefore, it is even possible to switch from a systems with a fully hydrophobic regime to a system with a fully hydrophilic regime and vice versa.

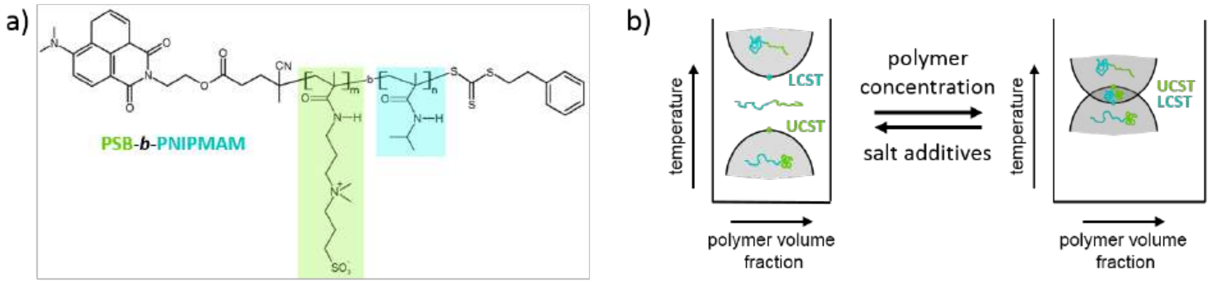

Figure 2.3:
a) chemical structure of PSPP-b-PNIPAM with typical end groups. The PSPP block is colored green, whereas the PNIPMAM block is colored blue. b) The schizophrenic micellar self-assembly of a doubly thermo-responsive BCP is shown schematically. By varying parameters such as polymer concentration or salt additives, respectively, it is possible to change the relative positions of the UCST and the LCST.

While the doubly thermo-responsive BCPs are relatively well understood in aqueous solution, rather less is known about these BCPs in thin film geometry.[3-4] In our recent work, we focus on the phase transition kinetics upon temperature change in a doubly thermo-responsive BCP thin film, that consists of a PSB and a PNIPMAM block. A custom-made sample environment enables control about key parameters, such as temperature and relative humidity. First, we induce a swelling process with heavy water of the thin film by increasing the relative humidity at a temperature below the UCST and LCST. Subsequent, two temperature jumps, the first one to the intermediate regime, above the UCST but still below the LCST, and the second one to high temperatures, above both, the UCST and LCST, are performed. The kinetic processes are followed in-situ with time-of-flight neutron reflectometry (ToF-NR) since this method is capable to distinguish between relaxed polymer chains (swollen polymer thin film) and coiled polymer chains (collapsed polymer thin film). In order to get insights in the dynamic processes on a molecular level, Fourier Transform Infrared (FTIR) spectroscopy is applied. Here, details about the interaction between the polymer and water are obtained. Furthermore, the role of characteristic groups such as the anionic SO_3^- group at the end of the PSPP side chain, and the polar amide groups at both blocks, during water uptake and temperature change, is revealed.

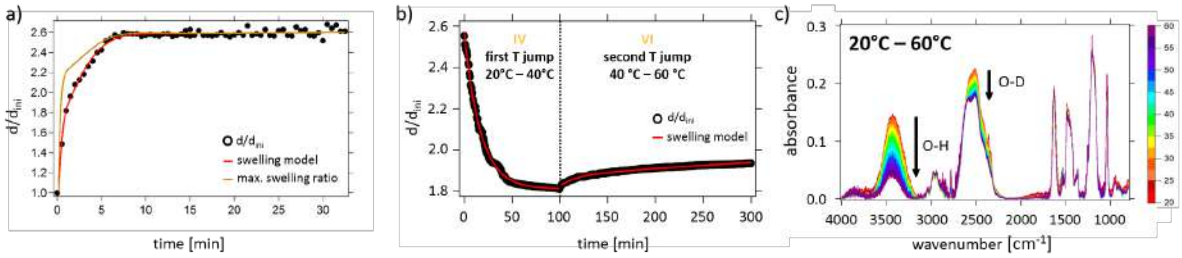

Figure 2.4:
in-situ ToF-NR measurements during D2O swelling (a) and temperature change (b). c) FTIR measurements upon increasing temperature. d) change in thin film morphology determined with ToF-GISANS.

In-situ ToF-NR experiments reveal one major phase transition during the first temperature jump: an LCST-type transition at lower temperature as compared to aqueous solution. Upon the second temperature jump, only slight re-swelling of the BCP thin film was detected. This indicates a strong shift of the UCST (of the PSB block) above the LCST (of the PNIPMAM block) in thin film geometry as compared to the corresponding aqueous solution. Detailed analysis of FTIR spectra yields information about the interaction between D_2O molecules and the polymer and reveals how functional groups such as the amide group (present in both blocks) and the SO_3^- group (present at the end of the PSB side chain) affect the swelling and collapse mechanism. In addition, information about deuteration of the polymer chain is obtained, which reveal a complex interplay between different water species.

In summary, we introduced a complementary in-situ study of the phase transition kinetics in a doubly thermo-responsive PSB-b-PNIPMAM thin film. Major differences were found in the temperature-dependent behavior of the thin film when compared to its counterpart in aqueous solution. This study, demonstrates the strong potential of in-situ measurements for the understanding of the mechanisms behind the kinetic phase transitions.

[1] A. Laschewsky *Polymers* **6**, 1544-1601 (2014)

[2] N. S. Vishnevetskaya, V. Hildebrand, B.-J. Niebuur, I. Grillo, S. K. Filippov, A. Laschewsky, P. Müller-Buschbaum, C. M. Papadakis *Macromolecules* **50**, 3985-3999 (2017)

[3] B.-J. Niebuur, J. Puchmayr, C. Herold, L. P. Kreuzer, V. Hildebrand, A. Laschewsky, P. Müller-Buschbaum, C. M.Papadakis *Materials* **11**, 850 (2018)

[4] L. P. Kreuzer, T. Widmann, N. Hohn, K. Wang, L. Bießmann, L. Peis, J.-F. Moulin, V. Hildebrand, A. Laschewsky, C. M.Papadakis, P. Müller-Buschbaum *Materials* **52**, 3486-3498 (2019)

2.3 Co-Nonsolvency transition of PNIPMAM-based block copolymer thin films in a series of binary mixtures

P. Wang, C. Geiger, L. P. Kreuzer, T. Widmann, S. Liang, C. M. Papadakis,
R. Cubitt[1], A. Laschewsky[2], P. Müller-Buschbaum

[1] ILL, Grenoble, France
[2] Universität Potsdam, Potsdam-Golm, Germany

Co-nonsolvency occurs if a mixture of two good solvents causes the collapse or demixing of polymers into a polymer-rich phase in a certain range of compositions of these two solvents [1]. The nonionic thermo-responsive polymer, poly(isopropylmethacrylamide) (PNIPMAM), which features a lower critical solution temperature (LCST) in aqueous solution, has been widely used to investigate its collapse transition behavior in a mixture of two competing good solvents. However, the co-nonsolvency response of its block copolymer containing a zwitterionic poly(sulfobetaine), such as poly(4-((3-methacrylamidopropyl)dimethylammonio)butane-1-sulfonate)) (PSBP),which exhibits an lower upper critical solution temperature (UCST) and shows a strong swelling transition in aqueous media, is newly studied. We focus on the co-nonsolvency behavior of PSBP-*b*-PNIPMAM thin films in a series of deuterated binary mixtures by using time-of-flight neutron reflectometry (TOF-NR).

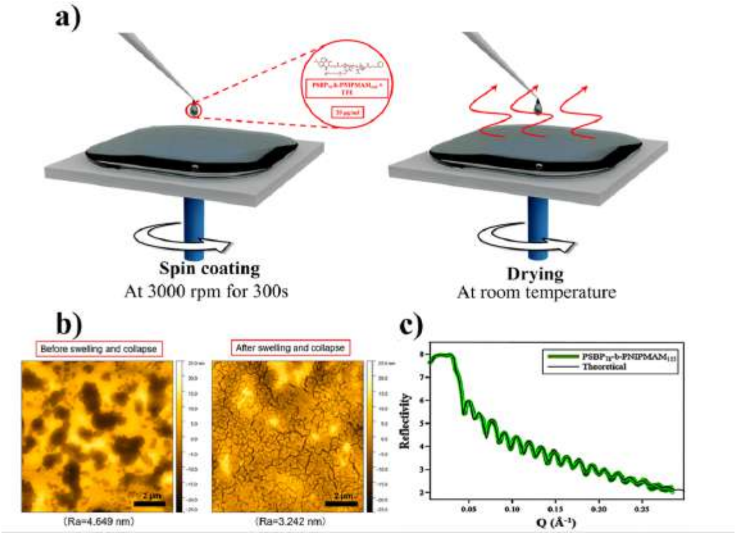

Figure 2.5:
(a) Spin coating schematic. (b) AFM height images (10×10 μm^2) of the polymer films before and after swelling. (c) XRR data of the PSBP-*b*-PNIPMAM thin film.

In our research system, the polymer PSBP-*b*-PNIPMAM is dissolved in tetrafluoroethylene (TFE, with a boiling point at 76.3 °C) firstly under stirring for 24 h to form a yellowish and transparent solution, to make sure that it yields homogeneous films. Fig.2.5a displays the process of samples preparation with appropriate spin-coating parameters. Due to a lower boiling point of TFE, we can get the films with a consistent quality at room temperature overnight after spin-coating. Then, the polymer film with a thickness around 50 nm was characterized by XRR, as shown in the Fig.2.5b.The XRR curve is perfectly modelled using Igor pro software. In order to further investigate the effect of co-nonsolvency on the surface morphology from a relatively macro scopic perspective, AFM is adopted to detect this change. From Fig.2.5a, We can observe a very significant change between before and after swelling in the surface morphology, from agglomerated particles to dispersed, uniform and wrinkled thin films. This change is as expected and can also be explained by the expected conformational change of PSBP-*b*-PNIPMAM polymer chains in aqueous solution [2]. Besides, the surface roughness Ra decreases from 4.6 nm to 3.2 nm, which also confirms this surface change trend.

The co-nonsolvency transition of PNIPMAM-based block copolymer thin films in a series of binary mixtures is investigated by neutron scattering and white light spectral reflectance. As shown in Fig.2.6a, neutron scattering measurements are performed using the D17 reflectometer at ILL Grenoble in time-of-flight (TOF) mode; sample thickness and optical properties (refractive index n) are measured with the Filmetrics F20 ThinFilm Measurement System (Filmetrics Inc., San Diego) [3]. The entire testing process is divided into 5 stages: N_2 drying; N_2 drying static; H_2O swelling kinetic; H_2O swelling static; acetone-d6 collapsed kinetic and acetone-d6 collapsed static. The static result is shown in the Fig.2.6b. From the fitting, the value of the film thickness changes from 67 nm to 123 nm. After collapse, the thickness changes to 100nm. All of the changes match with the results from white light spectroscopic reflectometry in Fig.2.6c.

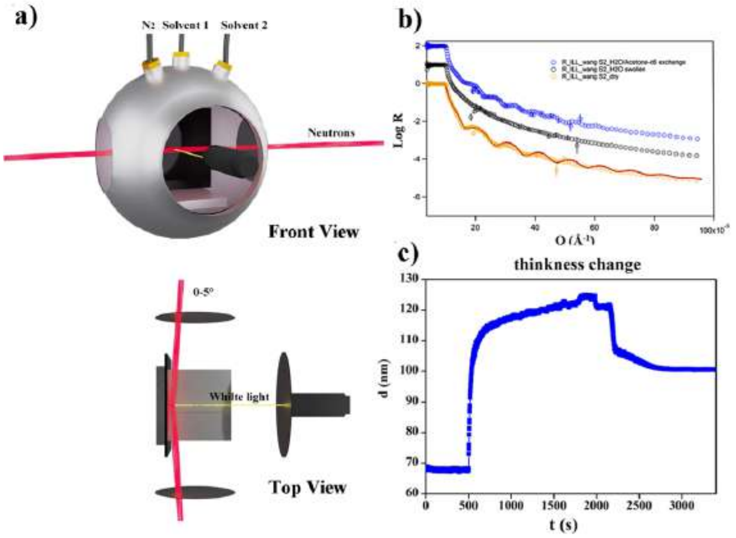

Figure 2.6:
(a) Neutron scattering and white light spectral reflectance setup. (b) Static results of dry, swollen and collapse films caused by H_2O/ Acetone-d6 mixture. (c) Plot of the thickness change versus time.

In this work, we preliminary study the co-nonsolvency behavior of PSBP-*b*-PNIPAM thin films in H_2O/Acetone-d6 mixture. A pronounced sensitive switching behavior (observed as a 100% increase in thickness during momentary swelling and a 35% decrease during collapse) of thin films is found. We believe the co-nonsolvency behavior of PSBP-*b*-PNIPAM thin films would make a contribution to many potential applications, like designing smart polymers for thermo sensors, in modeling size controlled nanoparticle precipitation and realizing others functional applications of smart polymers.

[1] S. Keßler, F. Schmid, K. Drese, *Soft Matter.* **12**, 7231-7240 (2016)

[2] N. S. Vishnevetskaya, V. Hildebr, B-J. Niebuur, I. Grillo, S. K. Filippov, A. Laschewsky, P. Müller-Buschbaum, C. M. Papadakis *Macromolecules* **17**, 6655-6668 (2016)

[3] Q. Zhong, E. Metwalli, G. Kaune, M. Rawolle, A. M. Bivigou-Koumba, A. Laschewsky, C. M. Papadakis, R. Cubittd, P. Müller-Buschbaum *Soft Matter* **8**, 5241-5249 (2012)

2.4 Cononsolvency induced collapse of diblock copolymer thin films

J. Reitenbach, C. Geiger, C. Henschel[1], L. P. Kreuzer, T. Widmann, A. Laschewsky[1], C. M. Papadakis, P. Müller-Buschbaum

[1] Universität Potsdam, Potsdam-Golm, Germany

The chemical constitution of polymers determines their chemical and physical properties. Different functional groups enable the polymer to become responsive to a specific stimulus. Those stimuli include – among others – light, temperature, pH, ionic strength, mechanical impact, solvation and pressure. Today, stimuli responsive polymers are of special interest for functional material research because of their switchable properties depending on the surrounding environment. Poly(*N*-isopropyl acrylamide) (PNIPAM) is a prime example for a thermoresponsive homopolymer, which possesses a lower critical solution temperature (LCST) in water at 32°C. As the PNIPAM homopolymer dissolves in water, the amide groups form intermolecular hydrogen bonds to the water molecules resulting in a layer of highly organized water molecules around the polymer. This phenomenon causes a decrease of entropy but sightly increases the enthalpy of mixing. As the temperature increases, the polymer bound water is released, which leads to a preference of polymer-polymer interactions and as a consequence of that to a coil-to-globule transition in solution. On top of that, the entropic term becomes dominant with higher temperatures leading to a positive free energy of mixing, which is the explanation for the existence of the LCST. It was found in the 1990s, that PNIPAM exhibits a cosolvent dependent behavior of the LCST in water for cosolvents like short chained alcohols such as methanol and ethanol, acetone and dimethyl sulfoxide. At a certain mixing ratio of originally good solvents at ambient temperature PNIPAM becomes insoluble in the cosolvent system, a phenomenon which is called cononsolvency. To date, different models exist to explain the cononsolvency effect. First, cononsolvency is explained by cluster formation of water and cosolvent molecules by hydrogen bonding. Secondly, by concentration fluctuations in the close vicinity to the polymer. Thirdly, by selective solvent absorption due to competitive polymer-water and polymer-cosolvent hydrogen bonding.[1]

To further elucidate the phenomenon of cononsolvency we compare two similar thermoresponsive diblock copolymer thin film systems. To investigate the influence of the chemical structure onto the swelling behavior in mixed atmospheres of water and volatile organic compounds, thin films of $PMMA_{22}$-*b*-$PNIPAM_{260}$ and $PMMA_{23}$-*b*-$PNIPMAM_{200}$ (DP_n according to ^1H NMR) are prepared via spin-coating with 1,4-dioxane as solvent and subsequent thermal annealing. The chemical structures of the diblock copolymers are shown in Fig. 2.7. It is evident, that the structures of NIPAM (*N*-isopropylacrylamide) and NIPMAM (*N*-isopropylmethacrylamide) differ only by an additional methyl functional group in the polymer backbone, which causes steric hindrance and weakens the intramolecular interactions. This also increases the LCST to 43°C and influences the film collapse kinetics on a macroscopic scale.[2]

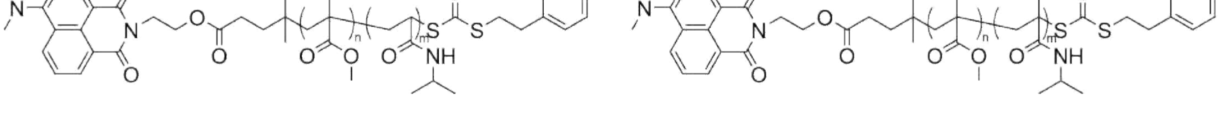

Figure 2.7:
Chemical structures of PMMA-*b*-PNIPAM (left) and PMMA-*b*-PNIPMAM (right).

Employing spectral reflectance (SR) the evolution of the film thickness and the refractive index is measured during swelling experiments. Automated measurements allow for time resolved data as the mixed vapor atmosphere builds up to an equilibrium to observe the volume phase transition.[3] The latter has already been demonstrated for PMMA-*b*-PNIPAM thin films and is now investigated for the PMMA-*b*-PNIPMAM diblock copolymer. Preliminary SR measurements for the solvent systems water/acetone (left) and water/methanol (right) have been performed and the response of the thin films is shown in the graphs below (Fig. 2.8).

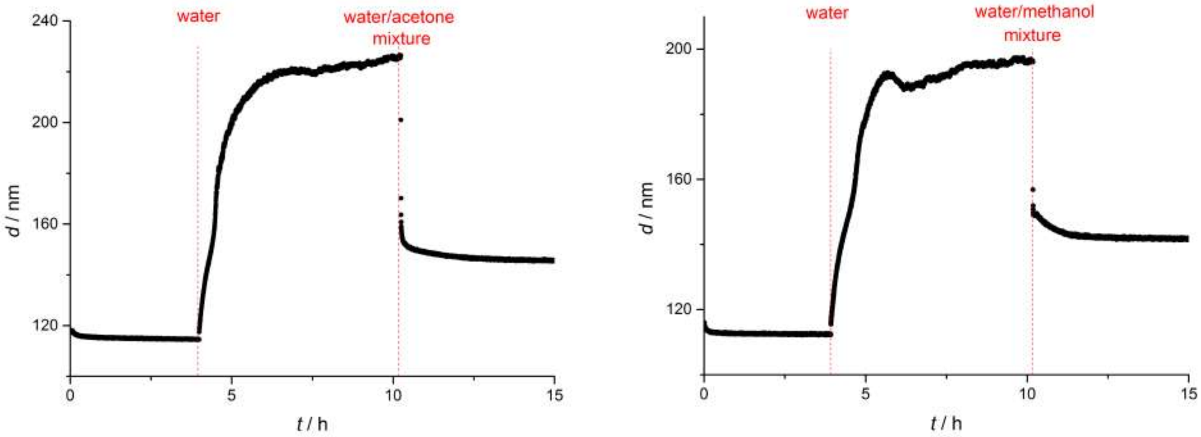

Figure 2.8:
Results of the SR measurements for PMMA-*b*-PNIPMAM thin films for the cosolvent systems water/acetone (left) and water/methanol (right).

After drying the films with anhydrous nitrogen gas, swelling is induced by flooding the measurement chamber with saturated water vapor. Once swollen, the cosolvent (acetone or methanol) is fed into the chamber in a specific water-to-cosolvent ratio as determined by previous measurements of PMMA-*b*-PNIPAM. The films immediately collapse and show a volume phase transition like previously observed for the PMMA-*b*-PNIPAM thin films.

In the future, we will reveal the solvent/cosolvent exchange taking place at the polymer functional groups with FT-IR and attribute key changes in the local chemical environment to the macroscopic film collapse stages. To gain further insights about inner morphology changes, selectivity to solvents and cosolvents and diffusion rates, the thin films will be characterized by neutron reflectometry.

[1] K. Kyriakos, M. Philipp, C. Lin, M. Dyakonova, N. Vishnevetskaya, I. Grillo, A. Zaccone, A. Miasnikova, A. Laschewsky, P. Müller-Buschbaum, C. M. Papadakis, *Macromol. rapid commun.*, **37** (5), 420-425 (2016)

[2] K. Kubota, K. Hamano, N. Kuwahara, S. Fujishige, I. Ando, *Polymer Journal*, **22**, 1051-1057 (1990)

[3] T. Widmann, L. P. Kreuzer, N. Hohn, L. Bießmann, K. Wang, S. Rinner, J.-F. Moulin, A. J. Schmid, Y. Hannappel, O. Wrede, M. Kuhnhammer, T. Hellweg, R. von Klitzing, P. Müller-Buschbaum, *Langmuir* **35** (49), 16341-16352 (2019)

2.5 Neutron reflectivity studies on metal-coated PNIPAM microgel thin films for potential use as humidity sensors

T. Widmann, L. P. Kreuzer, P. Müller-Buschbaum

The presence of water vapor in the atmosphere has a significant role for life, industry and science. Observing humidity is important for weather forecast, optimization of industrial or experimental processes and relevant for human physiology. Various types of humidity sensors are commercially available and some of these use polymers as humidity sensitive material. Hygrometers on polymer basis typically register a change in electrical parameters due to a changing humidity [1]. While resistive humidity sensors measure the resistivity and require conducting polymers, capacitive polymeric humidity sensors measure the capacity of a polymer-metal capacitor and also work with non-conductive polymers.

The thermo-responsive polymer poly(N-isopropylacrylamide) (PNIPAM) is a non-conducting smart polymer that shows highly hygroscopic behavior depending on temperature and offers interesting features to humidity sensing applications. PNIPAM shows a LCST-type phase transition around T_c = 32 °C below which it becomes affine to water. Cross-linking the PNIPAM chains with N,N′-methylenebisacrylamide (BIS) to a microgel, achieves an spherical interconnected network with good stability. The microgel retains the smart behavior of the homo-polymer and can be used as a nano-agent to sense changes in surrounding humidity. As schematically shown in Figure 2.9a, depending on temperature and humidity, the microgel undergoes a collective volume phase transition (VPT) from a collapsed to a swollen state and vice versa.

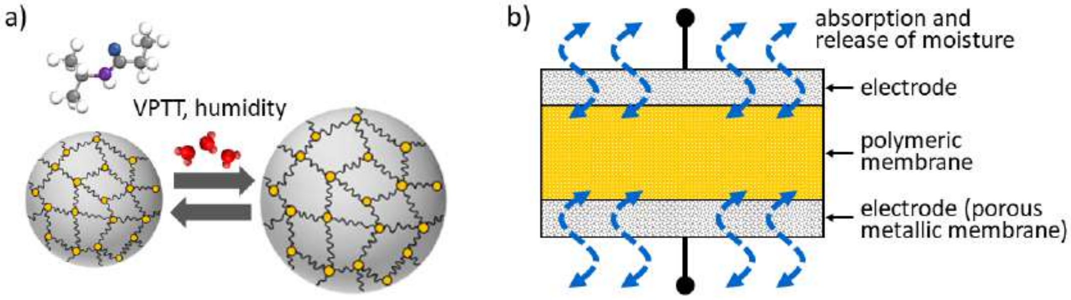

Figure 2.9:
a) Volume phase transition of a PNIPAM/BIS microgel: for high humidity and temperatures below the LCST the microgel will increase in volume while it will shrink at lower humidity and temperatures above the LCST. b) Layout of a capacitive humidity sensor. A water sensitive polymer is sandwiched between two porous electrodes to form a capacitor. Measured changes in capacity are translated into humidity values.

To realize a capacitive polymeric humidity sensor, a hygroscopic polymer is placed in-between two electrodes as indicated in Figure 2.9b. As the surrounding humidity changes, the water vapor can penetrate through the porous electrodes and bond to the polymeric membrane. This changes the polymers permittivity and thereby its capacity which is measured. To keep the sensor as thin and small as possible, the electrodes can be coated directly onto the polymer. It must be assured that the electrodes are porous enough to allow the transport of water molecules but also stable enough to not break upon slight deformations of the polymer due to water uptake or release.

We aim to realize such capacitive humidity sensors, using a PNIPAM/BIS microgel with a PNIPAM:BIS molar ratio of 10:1 of which we already investigated the swelling behavior with H_2O and D_2O and proved to be able to produce compact films of high homogeneity [2]. We spin-coat homogeneous monolayers of the microgel before we thermally evaporate very thin metal layers of gold, copper and aluminum on top of the polymer film. The thin film layer stack is then subjected to varying humidity while we observe the films response with in-situ time-of-flight neutron reflectometry (TOF NR) to learn about the diffusion capabilities of the different metal electrodes.

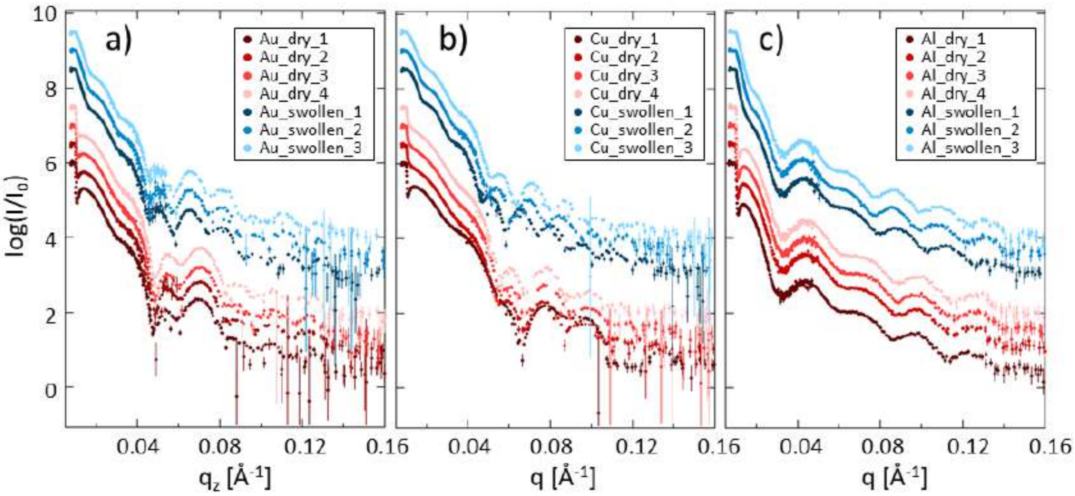

Figure 2.10:
Static TOF NR data of PNIPAM/BIS microgel monolayers coated with a thin metal film of (a) gold, (b) copper and (c) aluminum. Starting from an initially dried film (dry_1), three cycles of swelling (reds) and subsequent re-drying (blues) are performed.

We performed three cycles of humidification and drying of the polymer film, using a custom made sample chamber with a connected gas-flow system, that provides a range from 0 % up to over 95 % relative humidity. The temperature around the sample is kept below T_c, as the microgel shows the greatest sensitivity to humidity in that regime. Figure 2.10a-c shows the static TOF NR data of three cycles of humidification and drying of different polymer layers coated with thin layers of gold (a), copper (b) and aluminum (c). We see clear shifts in the fringes towards lower q-values upon humidification, which indicate the successful swelling of the polymer, confirming the porosity of our films. Also we find the films fringe pattern to be mostly reproducible upon re-swelling or re-drying. The strongest changes occur after the first swelling cycle, which can be accounted to some degree of restructuring within the polymer chain network upon reaching a fully relaxed state. After the first cycle hardly any changes occur between the second and third cycle. Moreover, we find the film with the copper electrode to exhibit the strongest shift after the first cycle, which may hint towards a better water uptake through the copper electrode. In conclusion, we can say that usage of directly linked polymer/metal layer stacks looks promising as humidity sensors with a nanoscale thickness.

[1] Z. Chen, C. Lu, *Sensor letters* **3(4)**, 274-295 (2005)

[2] T. Widmann, L. P. Kreuzer, N. Hohn, L. Bießmann, K. Wang, S. Rinner, J.-F. Moulin, A. J. Schmid, Y. Hannappel, O. Wrede, M. Kühnhammer, T. Hellweg, R. v. Klitzing, P. Müller-Buschbaum *Langmuir* **35**, 16341-16352 (2019)

3 Functional thin films

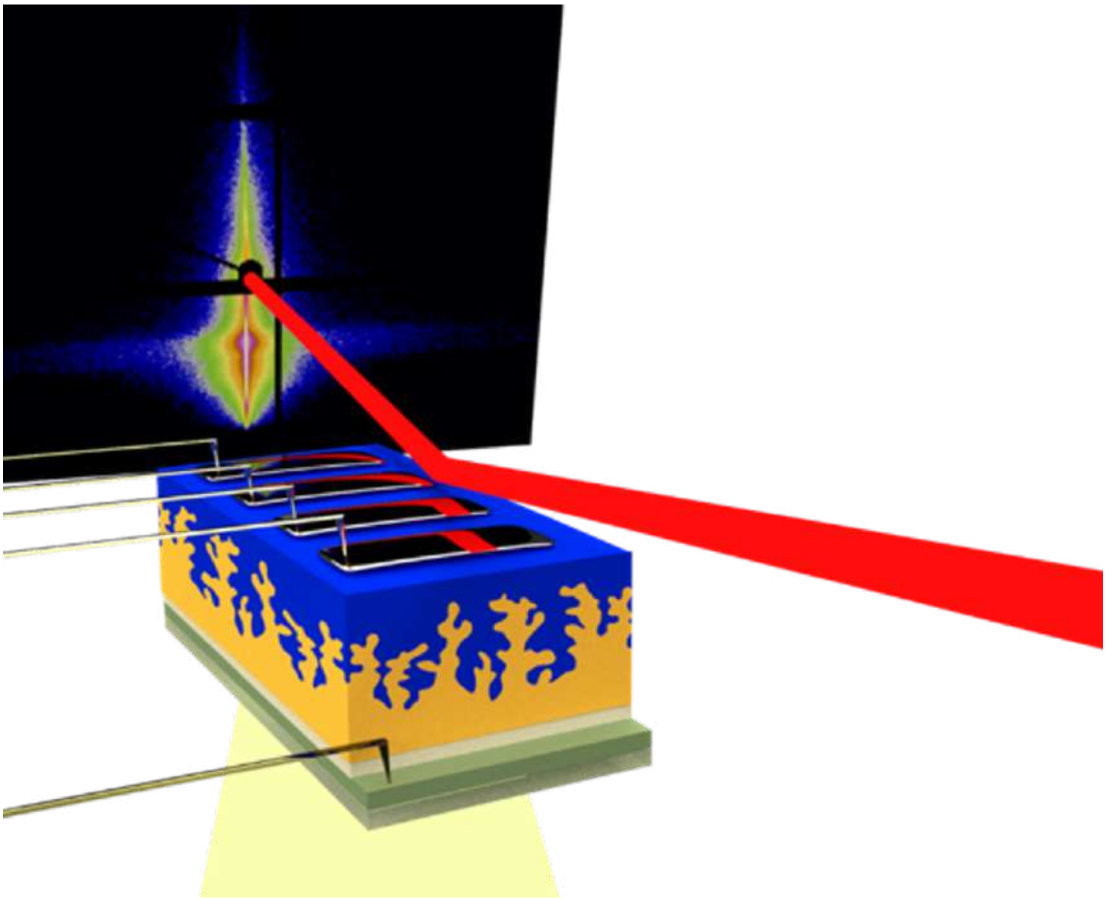

3.1 Interfaces between Polymer Electrolyte, Electrodes and Metal Current Collectors of Thin Film Lithium-Ion Batteries

G. Glänzer, S. J. Schaper, P. Müller-Buschbaum

With the rising importance of renewable energies comes a demand for convenient and reliable energy storage. The safety hazards connected to lithium-ion batteries (LIBs) stem from the liquid electrolites that are usually used. Polymer based solid state electrolytes may be a safer alternative with higher energy densities, better lifetimes and possibly easier ways to produce thus lowering costs. Especially their advantages in energy density determines them as auspicious for different fields of application, from electric mobility to medical application such as implants and pacemakers.

Polystyreneblock-polyethylene oxide (PS-*b*-PEO) diblock copolymer (DBC) in combination with bis(trifluoromethane)sulfonimide lithium salt (LiTFSI) is investigated in this study as perhaps the most promising material to be used as electrolyte. PEO offers a pathway to guarantee the mobility of lithium ions while the PS block ensures the necessary mechanical stability. The formation of dentrides and the short circuits caused by them are prevented by the covalent bond between the hydrophobic PS block and the hydrophilic PEO block.

A solution of $10\frac{mg}{ml}$ PS-*b*-PEO was produced with $CHCl_3$ as solvent and mixed with LiTFSI. The extremly hygroscopic nature of LiTFSI made it necessary to produce the samples in a glove box with pure nitrogen atmosphere. 0.1 has been found to be a good ratio for Li/Eo by Metwalli et al [1] and was also unsed in this study. At this ratio PEO is kept from crystallizing while self assembled microstructures are stable for all relevant temperatures. The solution has been spincoated onto silicium and then annealed with $CHCl_3$ for 5 minutes.

The same process has been repeated with only PEO instead of PS-*b*-PEO, keeping the ratio of Li/Eo at 0.1.

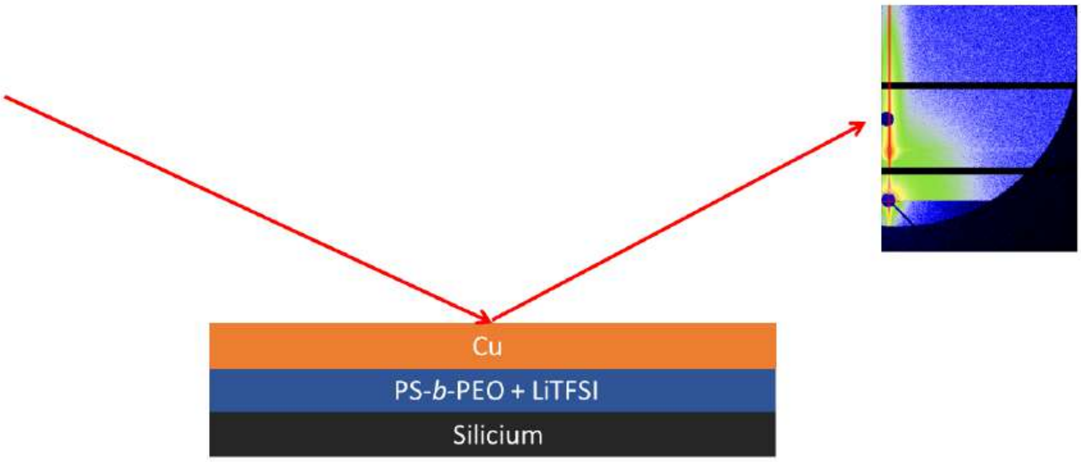

Figure 3.1:
Schematic example of one of the GISAXS experiments performed during this study. A solution consisting of either PEO or PS-*b*-PEO was mixed with LiTFSI and spin coated onto Si. For the GISAXS a monochromatic x-ray source with a wavelength of 0.964 Å was used.

To further investigate PEO and PS-*b*-PEO not only as electrolyte but also as part of the electrodes, further solutions of the polymer and DBC respectively were produced with LiTFSI and with carbon black (CB) in addition to either lithium-nickel-cobalt-aluminum-oxide (NCA), lithium-iron-phosphate (LFP) or graphite as active material. The ratio of the active material

(LFP, NCA or graphite) to CB and the polymer were kept at 60:8:32, which has been noticed as a good ratio by Bouchet et al. [2]

Copper had been sputtered on pure Si and on some samples with PS-*b*-PEO and LiTFSI. Aluminum has been sputtered on pure Si and on all types of samples produced. Those samples have then been investigated using grazing incidence small-angle x-ray scattering (GISAXS), x-ray reflectivity (XRR) and x-ray diffraction (XRD).
GISAXS is useful to determine morphological properties such as the form factor and the structure factor.

XRD and XRR is used to determine thickness and homogenity of different layers without damaging the samples.

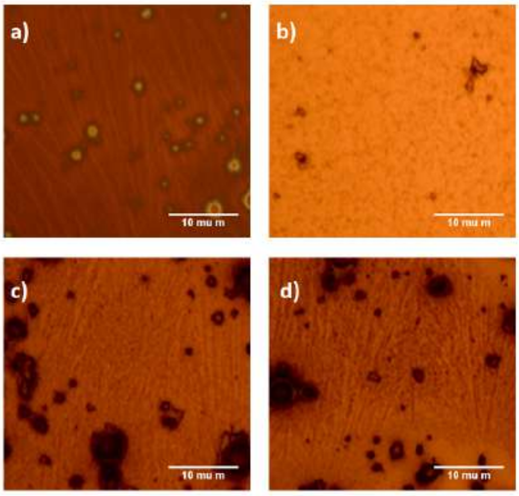

Figure 3.2:
This figure shows light microscopy images of different samples produced for further investigation with GISAXS, XRR and XRD. a) The first image consits of a simple PEO layer on Si. b) A layer of PEO mixed with LiTFSI. c) LFP an carbon black have been added as active material to a mixture of PEO an LiTFSI, creating an electrode. d) Another active material, NCA, has been mixed with PEO, LiTFSI and carbon black.

SAXS experiments had already been conducted e.g. by Möhl [3], using a capillary geometry for polymer based batteries. To tackle the lower ion conductivity of solid electrolytes compared to their liquid counterparts, a thin film geometry was deemed desireable, as it would result in short ion paths. For thin film layers, GISAXS is a more appropriate methode than transmission SAXS. Figure 3.1 shows the schematic design of a GISAXS experiment. Here a multi layer sample with the PS-*b*-PEO and LiTFSI solution is covered by a layer of copper. A monochromatic x-ray source with a wavelength of 0.964 Å was used for this experiment.

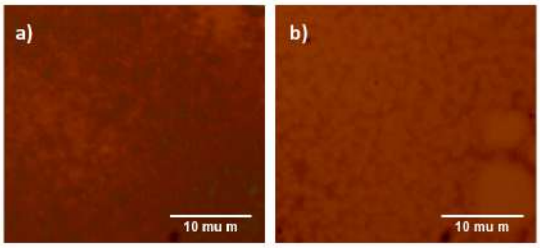

Figure 3.3:
This figure shows light microscopy images of different samples produced for further investigation with GISAXS, XRR and XRD. a) The first Sample consists of a layer of PS-*b*-PEO mixed with LiTFSI spin coated on Si substrate. b) A layer of PS-*b*-PEO mixed with LiTFSI, Carbon Black and Graphite.

[1] E. Metwalli, M. Rasool, S. Brunner, P. Muller-Buschbaum, *Chem. Phys. Chem.* **13**, 2882-2889 (2015)

[2] R. Bouchet, S. Maria, R. Meziane, et al, *Single-ion BAB triblock copolymers as highly efficient electrolytes for lithium-metal batteries.* Nature Mater **12**, 452–457 (2013)

[3] G. E. Möhl, E. Metwalli, P. Muller-Buschbaum,*In Operando Small-Angle X-ray Scattering Investigation of Nanostructured Polymer Electrolyte for Lithium-Ion Batteries* ACS Energy Letters **2018** 3(7), 1525-1530 (2018)

3.2 Improvement of the thermoelectric properties of PEDOT:PSS thin films by post-treatment with ionic liquids

A. L. Oechsle, P. Müller-Buschbaum

The primary energy consumption of the world is steadily increasing. In the past main energy sources had been oil, gas, coal, nuclear and hydro power. Nowadays and in the future an increasing part of the primary energy will be delivered by more sustainable sources like wind or solar power. Therefore, a lot of current research is focusing on developing and improving these renewable energy techniques. However beneath that, it is of immense importance to also consider ways of energy waste reduction. As nearly every industrial process, every car, our mobiles or even the human body is producing heat, which mostly just dissipates unused into the environment, like that in total around 66% of the produced primary energy is just lost as so called waste heat [1]. Therefore it would be crucial to be able to recover the low-quality energy heat back into a high-quailty energy form like electrical power. As shown in Fig.3.4 exactly for that termoelectric materials are providing a very promising way as they enable the direct conversion of a temperature gradient into electrical voltage.

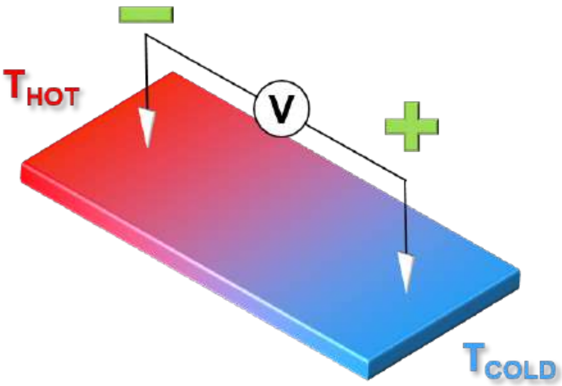

Figure 3.4:
Thermoelectric material with applied temperature gradient and the arising thermovoltage.

Thermoelectric generators are nowadays already in conventional use with mostly containing inorganic semiconductors like the bulk alloy material Bi_2Te_3. These inorganic thermoelectric systems are already well developed and can reach high efficiencies. However they are usually difficult and expensive to process, and furthermore contain rare and toxic elements like bismuth, tellurium, lead and antimony. Therefore current research is strongly focusing on the investigation of alternative organic thermoelectric materials as these provide several advantages. First they normally are more environmetal-friedly as they are low or non toxic. On the other hand organic semiconductors usually can be processed from solution allowing a large scale, low cost fabrication of lightweight, flexible and sometimes even transparent thin film devices [2]. A huge research interest is lying on the conductive polymerblend PEDOT:PSS consisting of poly(3,4-ethylene dioxythiophene) and poly(styrene sulfonate). In this work we are investigating PEDOT:PSS for the use as thermoelectric material and try to imporve its thermoelectric properties. Herefore we further investigate the research attempt of ionic liquid treatment, which is expected to simultaneously improve the Seebeck coefficient (S) and the conductivity (σ) of the PEDOT:PSS thin films [3,4]. Therefore we first fabricate PEDOT:PSS thin films by spin-coating on cleaned glass substrates, then following we did a post-treatment step using three different ionic liquids with varying concentrations. The chosen and tested ionic liquids are 1-ethyl-3-methylimidazolium tetracyanoborate (EMIM-TCB), 1-ethyl-3-methylimidazolium dicyanamide (EMIM-DCA) and 1-allyl-3-methylimidazolium dicyanamide (AMIM-DCA), the respective structural formulas are shown in Fig.3.5.

After the samples were prepared we measured the Seebeck coefficients and the conductivities of the respective polymer films. With these values we were able to calculate the so called power factor $PF = S^2\sigma$ which is an often used parameter to evaluate the properties of a thermoelectric material. The results are shown in Fig.3.5.

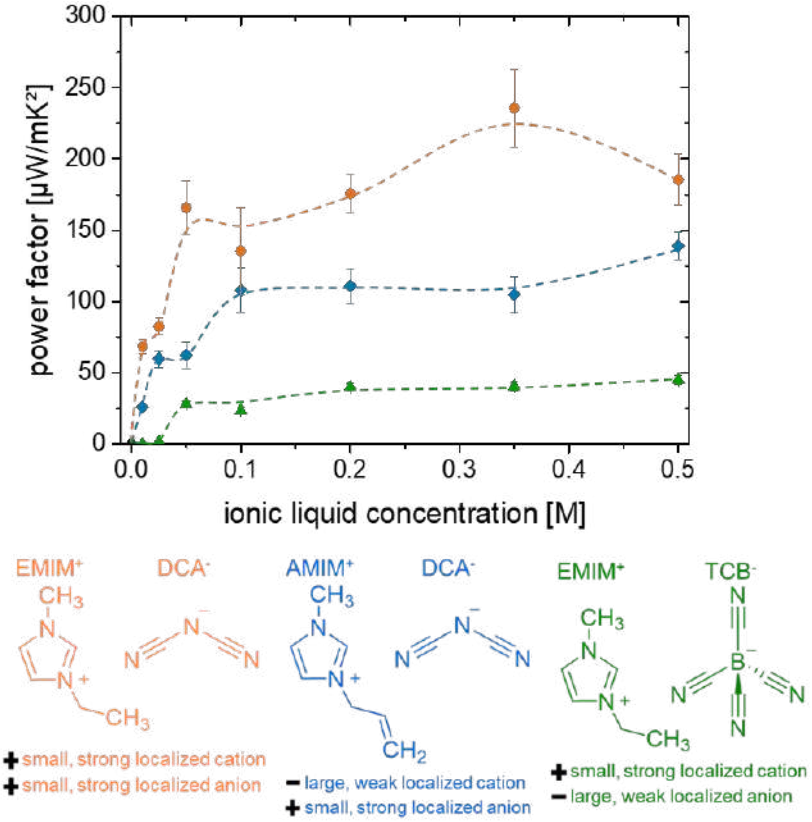

Figure 3.5:
Seebeck coefficients of PEDOT:PSS thin films treated with different concentrations of three different ionic liquids, EMIM-TCB (green ▲), AMIM-DCA (blue ■) and EMIM-DCA (orange •). The dotted lines act as guides to the eye. Shown below are the structural formula of the tested ionic liquids.

Upon ionic liquid post-treatment of the PEDOT:PSS thin films, we can observe a strong initial increase in the power factors for all three tested ionic liquids. With further increase in the ionic liquid concentration the power factors seem to reach a plateau. The highest value of $\approx$*230* $\mu W/mK^2$ can be reached for a post-treatment of PEDOT:PSS thin films with EMIM-DCA of a concentration *0.35 M*. Looking at the structure formulas of the ionic liquids we can see that EMIM-DCA is containing small cation and anion molecules with strongly localized charges. This renders the ions very reactive and could explain why we reach the highest increase in thermoelectric properties for this type of ionic liquid. As compared to EMIM-DCA the other two ionic liquids EMIM-TCB and AMIM-DCA just contain either a small and strongly localized cation or anion their reactivity and therefore their positive effect on the power factors of PEDOT:PSS is lower. With further investigation techniques like GISAXS, GIWAXS, UV-Vis, conductive AFM or FTIR we are now aiming to get more information about the morphological and electronical changes of the PEDOT:PSS due to the ionic liquid treatment.

[1] Fitriani, R. Ovik, B. D. Long, M. C. Barma, M. Riaz, M. F. M. Sabri, S. M. Said, R. Saidur, *Renew. Sustain. Energy Rev.* **64**, 635-659 (2016)

[2] Q. Zhang, Y. Sun, W. Xu, D. Zhu, *Adv. Mater.*, (2014)

[3] N. Saxena, B. Pretzl, X. Lamprecht, L. Bießmann, D. Yang, N. Li, C. Bilko, S. Bernstorff, P. Müller-Buschbaum, *ACS Appl. Mater. Interfaces* **11**, 8060-8071 (2019)

[4] H. Shi, C. Liu, Q. Jiang, J. Xu, *Adv. Electron. Mater.*, 1500017 (2015)

3.3 Investigation of molecular dynamics of a PTB7:PCBM polymer blend with quasielastic neutron scattering

D. Schwaiger, W. Lohstroh[1], P. Müller-Buschbaum

[1] MLZ, Garching, Germany

In organic photovoltaics, donor - acceptor bulk heterojunctions are often used as active materials due to their superior performance compared to e.g. planar layered devices.[1] After the absorption of a photon and the creation of an exciton, this intermixed structure provides an interface for the dissipation of the exciton that can be reached within its lifetime. Subsequently, the separated charge carriers can be extracted at the respective electrodes. A well studied model system is the combination of P3HT as donor and PCBM as acceptor material. There are lots of studies on structure and morphology of such systems, but only a very limited number of publications, dealing with the molecular dynamics, which have been prooven to also have a major influence on electronic properties and thus device performance.[2] Such studies on molecular dynamics, based on quasielastic neutron scattering have been performed on the system P3HT:PCBM [3] but not on any other bulk heterojunction materials. In our experiment, we try to determine molecular dynamics in the system PTB7:PCBM, which excels previounsly mentioned materials by e.g. higher power conversion efficiencies in photovoltaic applications.

For the present experiment, we prepared eight thick films of the sample material by dropcasting from a Chlorobenzene solution on aluminum foils to stack them on top of each other in order to ensure sufficient scattering intensity in the neutron measurement. This measurement was performed at the cold neutron time of flight spectrometer TOFTOF at MLZ (Garching). This instrument measures the energy transfer between neutrons and the sample by measuring the time, they need from the sample position to the detector in four meters distance. This energy transfer can be attributed to motions of hydrogen atoms within the sample. In the analysis, we can draw conclusions about type and intensity of these motions on a molecular level.

To be able to evaluate the effect of blending on the material properties, we produced three samples: pure PCBM, pure PTB7 and a 1:1 (wt.) blend. Since we could not observe any motions within the energy window of the instrument for the PCBM sample, we only analyzed the data of the PTB7 and the blend sample. Analyzing the scattering cross sections of the individual materials, treated in this study, shows, that in all samples, containing PTB7, mainly the alkyl side chains contribute to the incoherent scattering, which is analyzed.

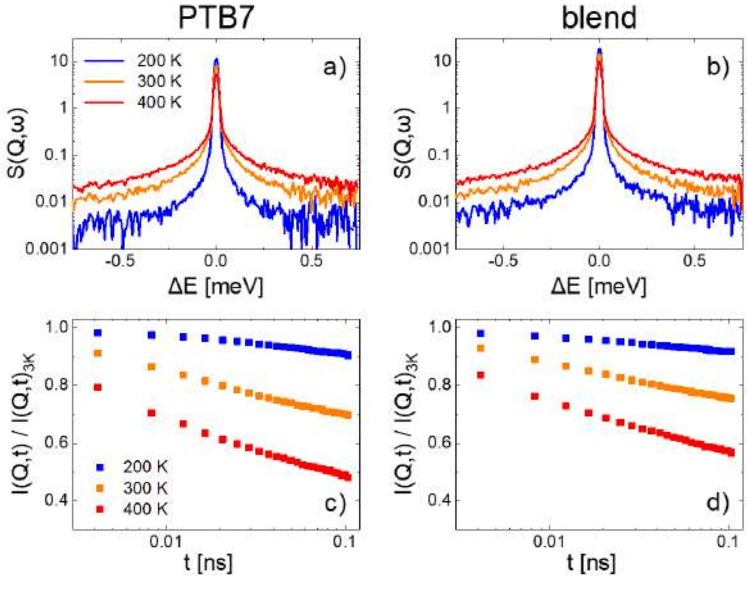

Figure 3.6:
Dynamic structure factor S(Q,ω) for the PTB7 (a) and blend (b) sample as well as intermediate scattering function I(Q,t) (c & d). The spectra represent data at a Q-value of 1.05 $\AA^{-1}$

Figures 3.6a) and 3.6b) show the measured and corrected scattering function S(Q,ω) of PTB7 and the blend, respectively. The S(Q,ω) spectra reveal the intensity of scattered neutrons according to their energy gain and loss. For both samples, it is clearly evident, that with increasing temperature the intensity in the quasielastic region (˜0.03 meV – 0.6 meV) increases on cost of the intensity of the elastic line (central peak). As expected, this indicates higher mobility of the polymer at elevated temperatures. A distinct difference between the spectra in figure 3.6a) and 3.6b) is not directly visible from the present plot.

A Fourier transformation of S(Q,ω) in time gives the intermediate scattering function I(Q,t) which is displayed in the lower two diagrams of figure 3.6 for the two samples. Figure 3.6c) shows PTB7 and 3.6d) shows the blend sample. From this representation, a difference in the decay of intensity over the investigated timescales is visible. It appears that PTB7 shows faster relaxation behavior than the blend sample. The data of S(Q,ω), as well as I(Q,t), can be fitted by various models, describing different kinds of motions. In this study, a jump diffusion model was applied, which delivers residence times and a diffusion coefficient for the polymer side chains.

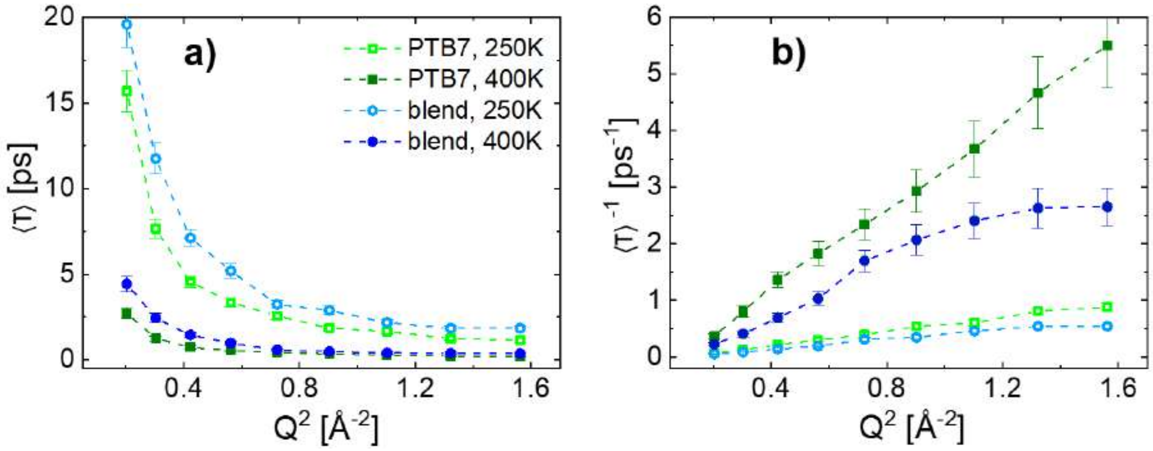

Figure 3.7:
a) Average residence times for the two samples PTB7 and blend at temperatures of 250 K and 400 K, respectively. b) Corresponding inverse average residence times. Dashed lines do not follow a mathematical relation, but are only a guide to the eye.

Figure 3.7a shows the extracted residence times for two different temperatures. 250 K was chosen as a low temperature example, whereas 400 K represents a high temperature measurement with a lot more thermal motion. Increasing Q values do in principle represent a higher scattering angle of the detected neutrons. It is clearly visible that pure PTB7 shows lower residence times compared to the blend sample at both temperatures over the entire Q range. This indicates a loss of flexibility and molecular dynamics of PTB7 side chains upon blending with PCBM. Figure 3.7b displays the inverse residence times against Q^2, which can be fitted with a diffusional model in order to extract a diffusion coefficient.

[1] G. Dennler, M. C. Scharber, C. J. Brabec, *Adv. Mater.* 21, 1323 - 1338 (2009)

[2] J. Obrzut, K. A. Page, *Phys. Rev. B* 80, 195211 (2009)

[3] A. A. Y. Guilbert, M. Zbiri, M. V. C. Jenart, C. B. Nielsen, J. Nelson, *J. Phys. Chem. Lett.* 7, 2252 - 2257 (2016)

3.4 Thermoelectric thin hybrid films based on PEDOT:PSS and inorganic nanoparticles

S. Tu, N. Saxena, P. Müller-Buschbaum

Thermoelectric (TE) materials, which convert heat into electricity and vice versa, facilitate electric power generation as well as refrigeration without any liquid coolants[1]. The energy conversion efficiency of a TE material is evaluated by a dimensionless figure of merit ZT and defined as $ZT= S^2\sigma T/k$ where S is the Seebeck coefficient, σ is the electrical conductivity, T is the absolute temperature, k is the thermal conductivity, and $S^2\sigma$ is defined as the power factor. Organic semiconductors have attracted intense attention because of their potential use in mechanically flexible, lightweight, and inexpensive electronic devices. In particular, PEDOT:PSS is the most studied conducting polymer system due to their intrinsically high electrical conductivity, low thermal conductivity, and high mechanical flexibility in thermoelectric devices[2]. However, it is generally considered that it is difficult to obtain a high ZT value of TE materials, due to the fact that the parameters S, σ, and k are interdependence as a function of carrier concentration and hard to be optimized simultaneously. In generally, several strategies such as additive technique, post-treatment and forming inorganic-organic nanocomposites, and etc are applied to overcome the conflicting relationship between S and σ. Especially, synthesizing inorganic-organic nanocomposites is regarded as a promising and simple technique in which S and σ are decoupled through energy filtering effect at interfaces of components in a composite. The nanocomposites may take the advantages of both the low thermal conductivity of the polymer and high power factor of inorganic TE fillers. Herein, PEDOT:PSS thin films nanostructured with inorganic nanoparticles as a function of Si-NPs content and doped with organic solvents is deeply investigated.

Fig. 3.8a shows the evolution of S as function of Si-NPs concentration. From the reference value of PEDOT:PSS only post-treated with EG of approximately $15.3\mu V/K$, an increase is observed with increasing amount of Si-NPs in the film, yielding a maximum value of $24.3\mu V/K$ for 0.5wt% Si-NPs, only to slightly drop to $23.4\mu V/K$ for the highest concentration. From Fig. 3.8b, increasing concentrations of Si-NPs have an adverse effect on σ, since it decreases from 809S/cm for the reference film without Si-NPs to 517S/cm for the highest concentration. Combining both S and σ, the steady increase from values of $16.4WK^{-2}m^{-1}$ for the reference up to $27.6WK^{-2}m^{-1}$ for 0.5wt% Si-NPs concentration is for the most part governed by the changes in S in Fig. 3.8c. The drop which was seen for the latter at Si-NPs concentrations of 0.7wt% is even more prominent for the power factor, due to its square dependence on the Seebeck coefficient. As seen from Fig. 3.8d, k of approximately $1Wm^{-1}K^{-1}$ for PEDOT:PSS post-treated with EG fits well to previous results. A maximum of $1.37Wm^{-1}K^{-1}$ is observed at 0.3wt%, which subsequently drops again to $0.97Wm^{-1}K^{-1}$ for the highest concentration of 0.7wt%. In Fig. 3.8e, the maximum value of 0.008 is found for a 0.5wt% Si-NPs concentration while for the reference film without Si-NPs a ZT value of roughly 0.005 is achieved.The improvement of ZT by a factor of roughly 1.5 renders the hybrid nanostructuring approach feasible regarding improvement of thermoelectric properties. It can be concluded that the enhancement of ZT originates from a combination of three factors: 1) the Seebeck coefficient is enhanced up to intermediate concentrations; 2) while the introduction of Si-NPs with their insulating oxide shell is detrimental to the overall electrical conductivity of the films, it is still sufficiently high; 3) even though the thermal conductivity increases for low amounts of Si-NPs, further addition yields values close to that of the reference film.

Fig. 3.9 shows the schematic illustration of energy filtering effect between PEDOT:PSS and Si.

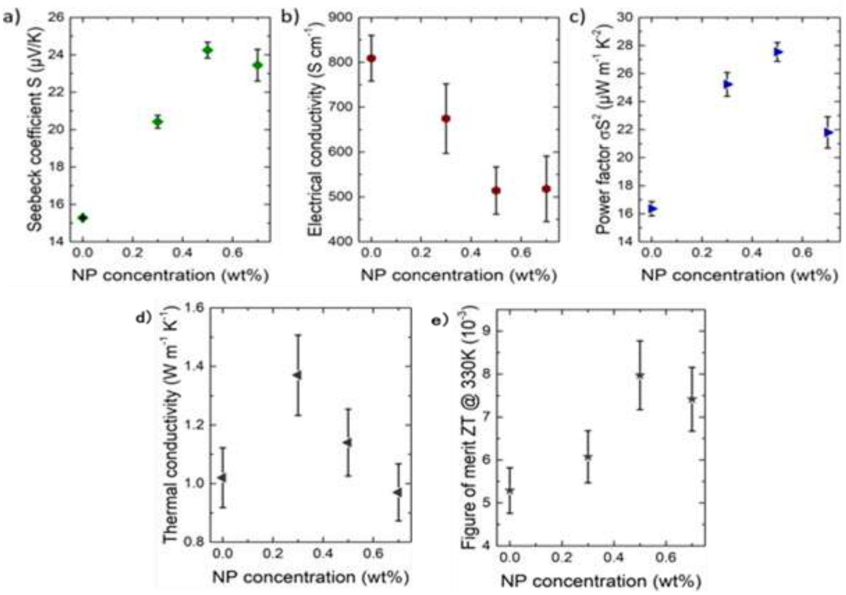

Figure 3.8:
a) Seebeck coefficient, b) electrical conductivity, c) power factor, d) thermal conductivity and e) ZT of PEDOT:PSS films with varying concentrations of Si-NPs. Adapted from [3].

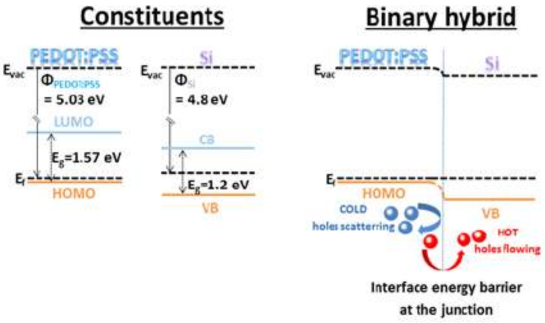

Figure 3.9:
Schematic illustration of the energy-filtering effect: Energy diagram of the PEDOT:PSS/Si heterojunction showing energy filtering at the junction.

Due to different work functions of PEDOT:PSS and Si, an interfacial potential barrier exists. When the carriers transport through the interface, this energy barrier can selectively scatter low-energy carriers and allow high-energy carriers to cross over the barrier. The average energy of the carriers in the material can be enhanced and the effective density of states of composites can be sharpened; therefore, the S is enhanced. Introduction of the Si-NPs could lead to a disruption of the intermolecular order of PEDOT chains or the polymer matrix in general and thus impede charge transport between chains. This may result in increased S. However, the slight drop in S for concentrations of 0.7wt% would then have to be explained in terms of size changes of nanoparticle clusters, namely, S of Si-NPs is inversely correlated to their respective size. This suggests aggregation of Si-NPs which would lead to increased effective sizes and therefore to lower intrinsic S.

[1] Y. Wang, L. Yang, X. L. Shi, L. D. Chen, M. S. Dargusch, J. Zou, Z. G. Chen, *Adv. Mater.* , 1807916 (2019)

[2] S. D. Xu, M. Hong, X. L. Shi, Y. Wang, L. Ge, B. Yang, L. Z. Wang, M. S. Dargusch, J. Zou, Z. G. Chen, *Chem. Mater.* **31**, 5238-5244 (2019)

[3] N. Sexena, Doctoral dissertation, *Technische Universität München* **(**2019)

3.5 Key factors study in amphiphilic block copolymer-oriented porous SnO_2 synthesis process

S. Yin, T. Tian, M. Schwartzkopf[1], S. V. Roth[1,2], P. Müller-Buschbaum

[1] DESY, Hamburg, Germany
[2] KTH, Stockholm, Sweden

SnO_2, as a crucial material in the field of energy storage, has always been the focus of scientific research. Compared with conventional bulk materials, mesoporous SnO_2 thin films afford more advantages during the wide practical applications. In the present work, a novel amphiphilic block copolymer assisted sol-gel chemistry is used for the synthesis of porous SnO_2 nanostructure. Different kinds of solvent, THF or 1,4-dioxane, are used as good solvent for both PS and PEO polymer chains. HCl is a selective poor solvent for PS chains and catalyst for the hydrolytic condensation reaction of $SnCl_4$. The corresponding component phase diagram of the samples prepared with THF or 1,4-dioxane solvent are shown in Fig. 3.10. With the progressive addition of HCl, the stretch of the hydrophobic PS chains is significantly restricted. As a result, different micelle structures of the block polymer are formed in the sol-gel solution, and the simultaneously hydrolysed $(HO)_xSnCl_{4-x}$ species is specifically confined in the PEO domains by hydrogen-bond interaction. For removing the organic polymer template, the composite thin film is calcined at 500^{o}C for two hours with a heating rate of 1^{o}C/min under ambient condition. The obtained nanostructure is visualized by scanning electron microscope (SEM). By correlating different characterization results with the thin film preparation method, the action mechanism governing the film morphology is revealed by the preferential affinity of the utilized solvent mixture.

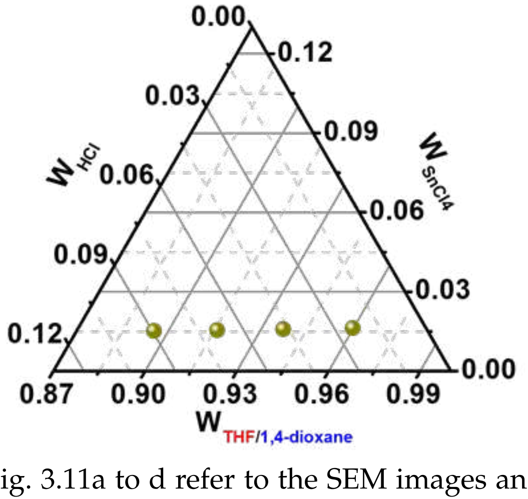

Figure 3.10:
Component phase diagram of the samples prepared with THF or 1,4-dioxane solvent.

Fig. 3.11a to d refer to the SEM images and corresponding FFT patterns of the SnO_2 thin films prepared with THF solvent. The HCl content added in the sol-gel solution are 50ul, 100ul, 150ul and 200ul from Fig. 3.11 a to Fig. 3.11d, respectively. It can be found that all of the thin films prepared with THF solvent exhibit ramdomly distributed porous structures. No obvious structure variation is demonstrated with the progressive HCl addition. The weak ordering of the porous structures can be further revealed by the corresponding blurred ring like FFT patterns of the SEM images. In comparision with the THF system, the SnO_2 thin films prepared with 1,4-dioxane solvent exhibit more intriguing microstructures, such as cylinders and vesicles. Moreover, the FFT pattern of the thin film prepared with 50 ul HCl addition demonstrated conspicuous hexagonal symmetry patterns (Fig. 3.11e), which suggests the existence of hexagonally ordered porous structure of the thin film. In addition, a similar porous structure with that in Fig. 3.11a is obtained when the HCl addition increased to 100ul. However, the relative blurred FFT patterns suggest the smearing of the hexagonally ordered arrangement. With the further

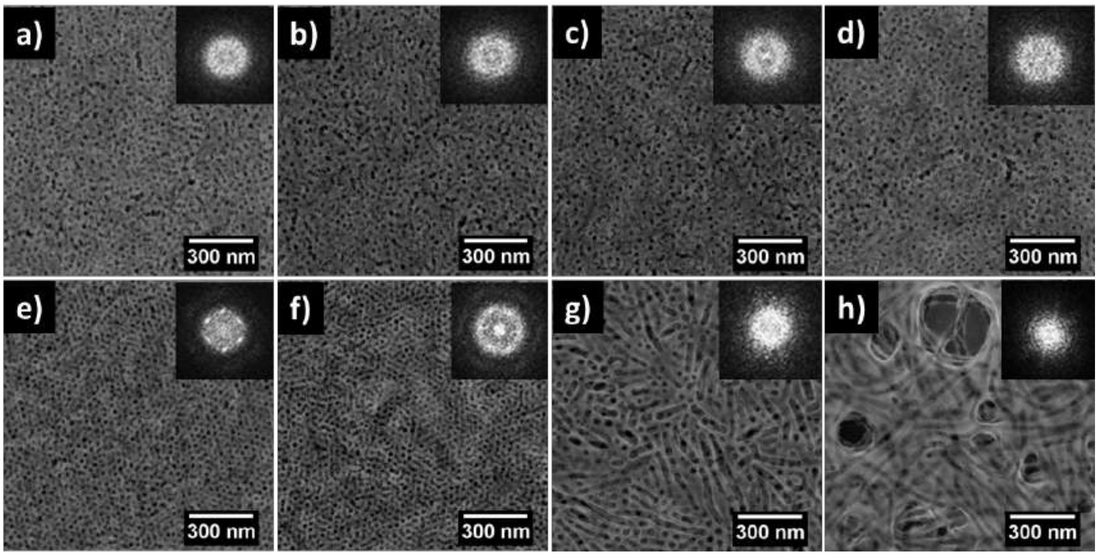

Figure 3.11:
SEM images and corresponding FFT patterns (upper right of the SEM images) of the samples prepared with THF (a to d) and 1,4-dioxane (e to h) solvent. The corresponding HCl content added into the sol-gel solution are 50ul (a and e), 100ul (b and f), 150ul (c and g) 200 ul (d and h), repectively.

HCl addition, a novel hybrid nanostructures consisted with spheres and cylinders are obtained (Fig. 3.11g). The FFT pattern in Fig. 3.11g reveals the random structure arrangement of the thin film. When the HCl content utilized for sol-gel solution preparation is increased to 200 ul, a coexisting nanostructures of cylinders and vesicles are obtained (Fig. 3.11h). Considering the nonionizing properties of the PS and PEO blocks and the low dielectric constant of the solvent (THF: 7.58, 1,4-dioxane: 2.25) utilized in the present work, the repulsion force among the polymer chains provoked by ionization is negligible. Accordingly, the morphology variation of the SnO_2 thin film shown in (Fig. 3.11) can be analyzed from the perspective of the polymer-solvent interaction parameter χ.[1] The polymer-solvent interaction parameter is a measure of the affinity between the polymer chains and the surrounding solvent in the system. The preferential affinity of a solvent for a certain block can be represented by an expression of $\Delta\chi = \chi_{PS-S} - \chi_{PEO-PS}$. As a consequence, the corresponding $\Delta\chi$ values for the thin films shown from Fig. 3.11 a to Fig. 3.11 h are caculated to be 0.04, 0.08, 0.12, 0.15, 0.14, 0.18, 0.21 and 0.25,respectively. It is demonstrated that spherical pore structure is preferred to be formed with relative lower $\Delta\chi$ values ($0.04 \leqslant \Delta\chi \leqslant 0.18$). When the $\Delta\chi$ value reaches 0.21, a hybrid morphology consist of spherical and cylindrical porous structures are observed. Further increasing the $\Delta\chi$ value to 0.25 leads to the appearance of vesicle structures. It's worth noting that, the ordering of the spherical porous structure arrangement obtained with 1,4-dioxane solvent are significantly enhanced compared with that obtained with THF solvent (Fig. 3.11a to Fig. 3.11f), which can be explained by the hydrogen bond interaction between water and the employed organic solvent molecules (THF or 1,4-dioxane).[2] Compared with 1,4-dioxane, the formation of THF/H_2O clusters circumvents the unfavorable interactions between water and hydrophobic PS chains of the block copolymer, which hence leads to a decrease in the ability of the THF/H_2O solvent mixture to stimulate the phase separation of the block copolymer. As a consequence, compared with the hexagonally packed pore arrangement obtained with 1,4-dioxane solvent (Fig.3.11e), a reduction in number and ordering of the pore structure are observed in THF system (Fig. 3.11a to Fig. 3.11d).

[1] L. He, S. Pan, J. Peng,*J. Polym. Sci. Pol. Phys.* **54**, 544-551 (2015)

[2] T. Takamuku, A. Nakamizo,M. Tabata,K. Yoshida, T. Yamaguchi,T. Otomo,*J. Mol. Liq.* **103**, 143-159 (2003)

4 Photovoltaics

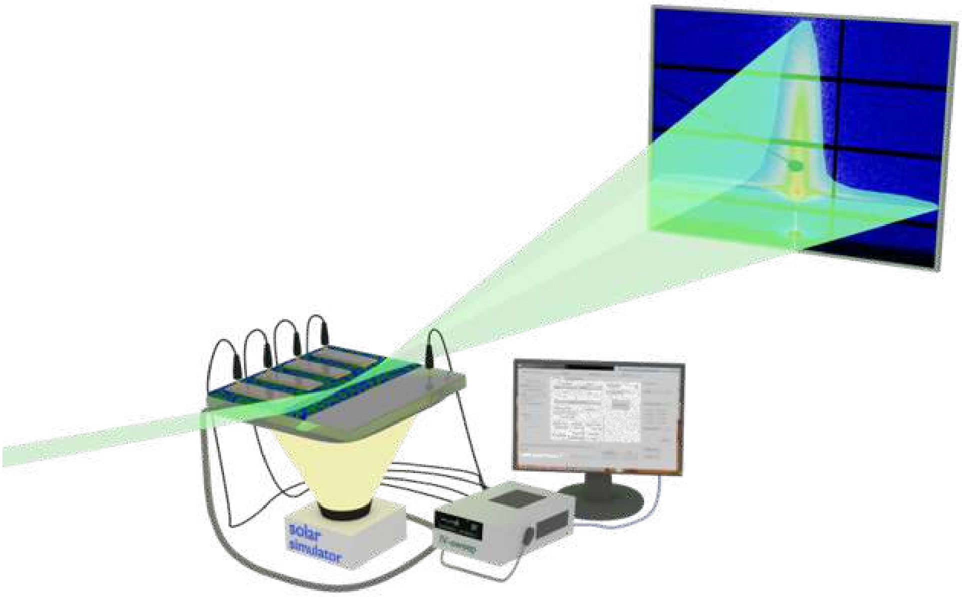

4.1 Quantum dot based novel device architectures

W. Chen, P. Müller-Buschbaum

Colloidal PbS quantum dots (QDs) demonstrate great potentials for various optoelectronic applications, including transistors, photodetectors, and photovoltaics, due to the tunable bandgap property and the solution processability.[1] The monodisperse QDs are normally synthesized in a solvent condition with outer long-chain ligands capping limiting the crystal growth in nanoscale and maintain their solubility. For instance, oleic acid (OA) capped PbS QDs are able to be dissolved in many organic solvents, which make them compatible with currently-used large-scale deposition facilities towards roll-to-roll printing or spray deposition. However, the long-chain ligands act barrier potentials consequently resulting in the weak electronic coupling of as-deposited solids. To functionalize the solids, ligand exchange processes are performed to decrease the inter-dot spacing between neighboring QDs in the solid by replacing their long-chain ligands with short chain-ligands or ions. The ligand exchange process to OA capped QDs is mainly performed in solution (towards ink) or on the solid-state OA-QD film (integrated with a layer-by-layer (LBL) process). The inking technique enables QDs being deposited in a single step, which significantly simplifies the deposition process. However, the ink relies on toxic lead halides, e.g. PbI_2, and metal-coordinate solvent, e.g. butylamine, which leads the ink preparation process complicate and costly. Moreover, the concentrated ink exhibits strong metal affiliation make it less compatible with current large-scale fabrication facilities due to the pipe stoppage problem. Therefore, the deposition strategy based on OA-QDs integrating with an post-ligand-exchange treatment is still promising for current large-scalable and low-cost fabrication techniques, such as printing as indicated in Fig. 4.1, towards optoelectronic applications.

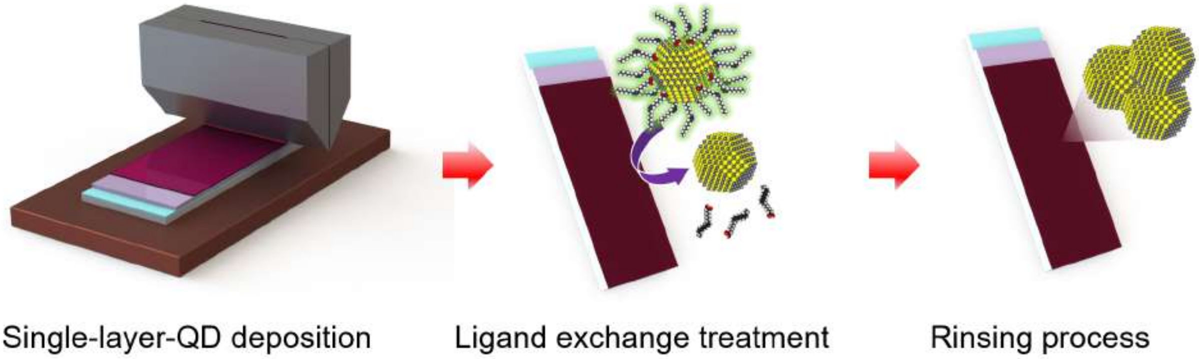

Figure 4.1:
Fabrication process of a printed QD solid with detailed steps: deposition of OA capped QD layer, ligand exchange treatment, and rinsing process.

The charge carrier dynamics in the ligand exchanged QD solid is influenced by the inner particle stacking which determines different dot-to-dot couplings between all neighboring QDs.[2] This means that different deposition methods of QDs may lead to different energy disorder due to different QD stacking behavior. The conventional spin-coated QD solid in literature has well revealed the potentials of QD materials for optoelectronic applications. However, the charge carrier dynamics in QD solid via a large-scaled deposition method, for instance, printing deposition, is rarely studied. In this report, The charge carrier dynamics of ligand exchanged printed QD solid is investigated by time-resolved photoluminescence spectroscopy (TR-PL). The spin-coated QD solid is also prepared as the reference sample. The spectral mapping results are shown in Fig. 4.2 and the energetic disorder is obtained from the overall shift of the radiative recombination center in the measuring scale and the corresponding fitting by a exponential decay function. The exciton hopping rate pre-factors $k_{\Delta E}$ is derived from the fitting parameters. The temporal photon lifetimes for both solids are also provided at the equilibrium state of the exciton indicating a similar exciton lifetime from the fitting parameters based on a bi-exponential decay function. However, the printed solid demonstrates a slightly larger energy shift ΔE of 4.4 meV but slower hoping rate $k_{\Delta E}$ value of 0.056 ps^{-1} than that of spin-coated solid with energy shift of 2.4 meV and $k_{\Delta E}$ of 0.105 ps^{-1}.

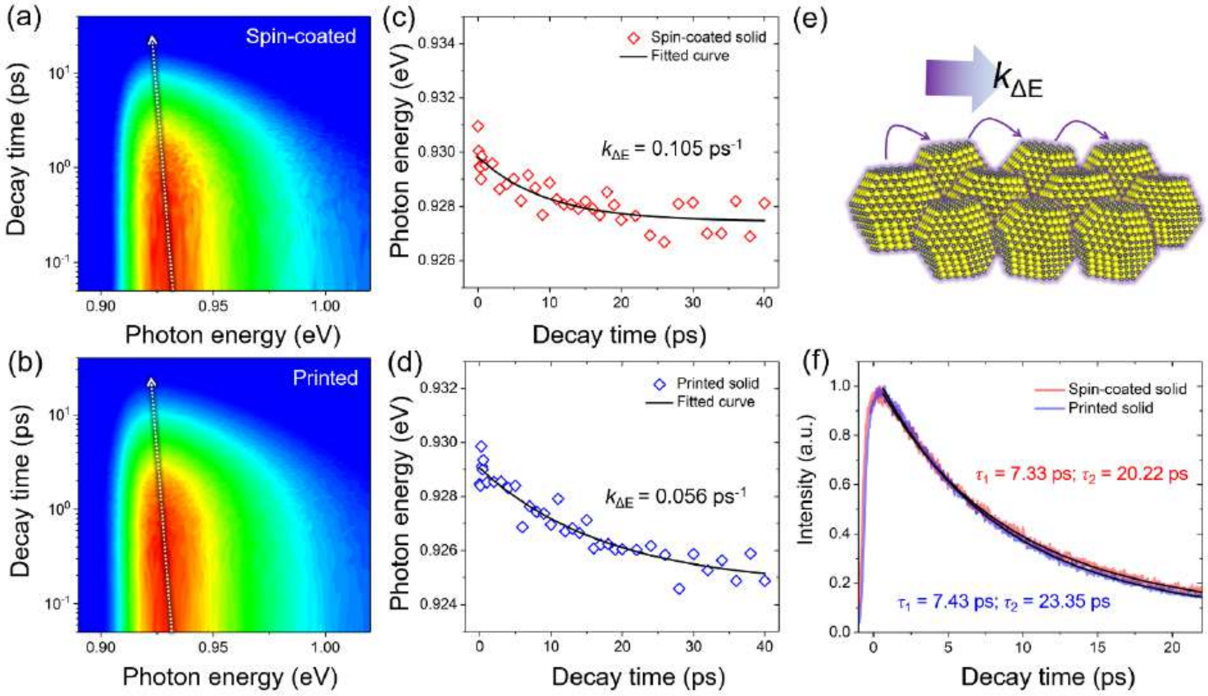

Figure 4.2:
Time-resolved 2D spectral data for QDs solids based on (a)spin-coating and (b) printing. As derived radiative center shifts fitted by a decay function (c-d).(e) Exciton diffusion with a hoping rate pre-factor of $k_{\Delta E}$. (f) Temporal decay of compared QD solids at the equilibrium radiative recombination center.

We assume that the self-organization of QDs during the deposition process is determined not only by the shape (or size) of QDs but also related to the solvent evaporated conditions. The spin-coating deposition is known as a fast drying process, while the printing process brings in a wet condition for QDs to have a slower timescale for the self-organization, even though the heating up the substrate is considered to accelerate the solvent evaporation. The deposition induced structure and energy state distribution in QD solids are still under the investigation.

[1] M. Liu, F. Che, B. Sun, O. Voznyy, A. Proppe, R. Munir, M. Wei, R. Quintero-Bermudez, L. Hu, S. Hoogland, A. Mandelis, A. Amassian, S. O. Kelley, F. P. García de Arquer, E. H. Sargent, *ACS Energy Lett.* **4**, 1225-1230 (2019)

[2] W. Chen, J. Zhong, J. Li, N. Saxena, L. P. Kreuzer, H. Liu, L. Song, B. Su, D. Yang, K. Wang, J. Schlipf, V. Körstgens, T. He, K. Wang, P. Müller-Buschbaum, *J. Phys. Chem. Lett.* **10**, 2058-2065 (2019).

4.2 A morphologic study fullerene-free bulk heterojunction blends for photovoltaic applications

S. Grott, L. Bießmann, N. Saxena, W. Cao, S. Bernstorff[1], P. Müller-Buschbaum

[1] Elettra Sincrotrone, Trieste, Italy

Over the past centuries the energy demand was growing continuously and has driven technology and science to enormous progress concerning energy conversion in a broad field. The growing energy demand as well as the global warming has led science to focus renewable energy technologies. Thereby, photovoltaic applications are one of the most promissing technologies. They are capable of generating energy out of sunlight. The already widely used inorganic solar cells, which are operated to harvest sunlight are one step towards tackeling the energy crisis. However, science has made hugh progress in developing promissing alternatives for the commonly used silicon based solar cells. One promissing alternative are solar cells based on organic compounds and offer advantages, such as being semi-transparent, flexible and light weight. Furthermore, these cells can be produced out of solution, which enables the usage of low-cost and large-scale production methods like printing or spray coating.

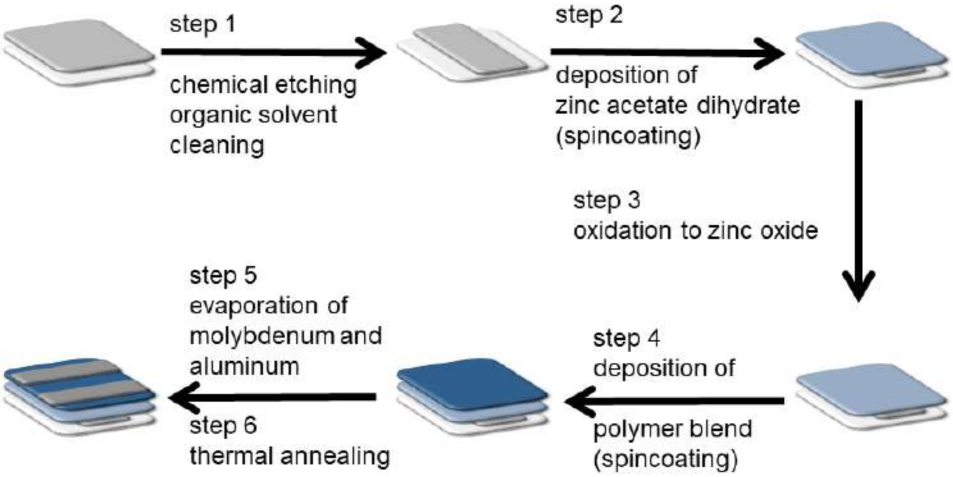

Figure 4.3:
Schematic processing route of an organic solar cell.

Regarding this kind of solar cells, the polymer poly(3-hexylthiophen-2,5-diyl) (P3HT) and the fullerene [6,6]phenyl-C_{61}-butyric acid methyl ester (PCBM) is the most studied donor-acceptor system used as photoactive layer for organic solar cells, which achieved efficiencies of around 4-5 %. In order to increase the efficiency of organic solar cells, one approach is to tune the absorption properties of the used donor-acceptor system to match the solar spectrum in order to optimize the energy generation. Hence, substituting the fullerene by a none-fullerene small molecule and adjusting the absorption of the acceptor molecule is a promising approach to harvest sunlight more efficient. In Fig. 4.3 a schematic route for the processing of such an organic solar cell, based on the donor polymer poly[(2,6-(4,8-bis(5-(2-ethylhexyl)thiophen-2-yl)-benzo[1,2-b:4,5-b′]dithiophene))-alt-(5,5-(1′,3′-di-2-thienyl-5′,7′-bis(2-ethylhexyl)benzo[1′,2′-c:4′,5′-c′]dithiophene-4,8-dione)] (PBDB-T) and the acceptor molecules [6,6]phenyl-C_{71}-butyric acid methyl ester (PC71BM) and 3,9-bis(2-methylene-(3-(1,1-dicyanomethylene)-indanone))-5,5,11,11-tetrakis(4-hexylphenyl)-dithieno[2,3-d:2′,3′-d′]-s-indaceno[1,2-b:5,6-b′]diethiophene(ITIC)is shown. [1]

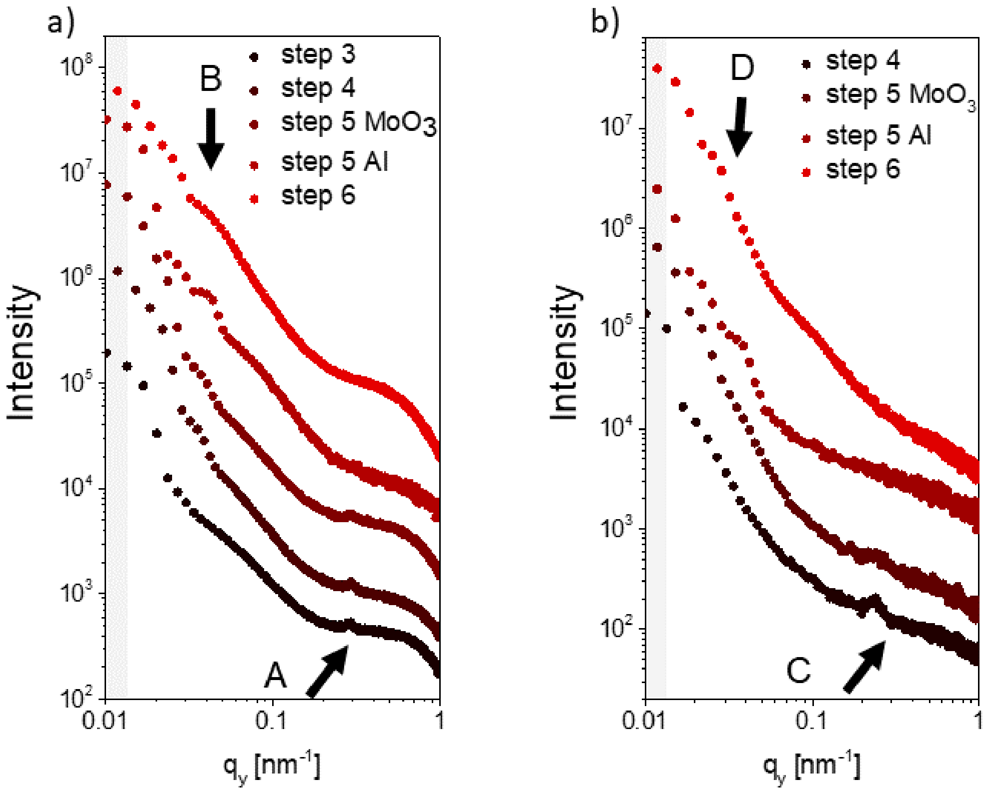

Figure 4.4:
GISAXS horizontal line cuts of the 2D GISAXS data for at different yoneda regions a) ZnO b) PBDB-T.

Tuning the photo-physical properties of the used materials is just one approach, to enhance the efficiency of organic solar cells. Understanding and improving the inner morphology of the donor-acceptor system is as important as the compounds characteristics. To get insight on the morphology formed by PBDB-T:ITIC, grazing-incidence small angle scattering (GISAXS) is used to probe the structures and domain sizes within thin films. [2] Fig. 4.4 shows the obtained horizontal GISAXS line cuts at different Yoneda regions (a)at the ZnO position; b) at the PBDB-T position). Thereby, it can be observed that the processing steps of such a solar cell is influencing the inner morphology of the different layers. Regarding the ZnO layer, a growth of larger domains (B) can be observed as well as a decrease of small domains (A). In case of the PBDB-T layer at the beginning a small domain related to ZnO sublayer (C) are found. Furthermore, a growth of the polymer (D) domains can be observed. Correlating these findings with obtained photo-electric measurements is of major importance to fully understand and further improve the performance of organic photovoltaic devices and their power conversion efficiency.

[1] W. Zhao, D. Qian, S. Zhang, S. Li, O. Inganäs, F. Gao, J. Hou, *Adv. Mater.* **28**, 4734-4739 (2016).

[2] P. Müller-Buschbaum, *Anal. Bioanal. Chem.* **376**, 3-10 (2003).

4.3 Fabrication on Plasmonic Nanostructures in Photovoltaics

T. Guan, P. Müller-Buschbaum

Photovoltaics, the technology to convert sunlight directly into electricity by employing solar cells is one of the most promising ways to harvest solar energy for generating renewable energy. For photovoltaics, light and electric management are essential issues for achieving higher efficiency. Plasmonic includes various aspects of surface plasmons are coherent oscillations, which are electromagnetic surface waves utilize light-metal interactions, which has been demonstrated as a promising approach for enhancing the performance of solar devices. [1] In applications where surface plasmon polaritons (SPPs) and the near field from localized surface plasmon resonance (LSPR) are beneficial to light absorption as well as electrical characteristics of the photovoltaics. It has been shown that the utilization of plasmonic metal nanostructures is frequently proposed as a means to further enhance the light absorption in the broad wavelength range as well as facilitate charge collection and transportation of the devices. In particular, the use of metallic nanostructures has been investigated in almost all types of solar cells, such as organic solar cells (OSCs), perovskite solar cells (PSCs), dye-sensitized solar cells (DSSCs), etc., be they solid-state or solution-processed. [2] Besides, the facile tunability of their optical properties has shown great potential as an optical engineering tool in photovoltaics by modifying their constitution, size, morphology and surrounding materials. Recently, many types of plasmonic nanoparticles (NPs), including Au and Ag nanoparticles with different shapes and structures such as nanosphere, nanorod and nanostar, etc., have been incorporated either between interfaces or in photoactive layers of photovoltaics to improve their efficiency. [3] However, there is still limited effect in terms of a systematical fundamental study and fabrication novelty plasmonic structures in plasmonic enhanced photovoltaics. Therefore, it is of crucial importance to fabricating suitable plasmonic nanostructure and investigated the deep mechanism in solar devices. Herein, we excogitation the precise modulation of metallic nanostructures with tunable plasmonic effects is planned to be achieved based on the self-assembly technique.

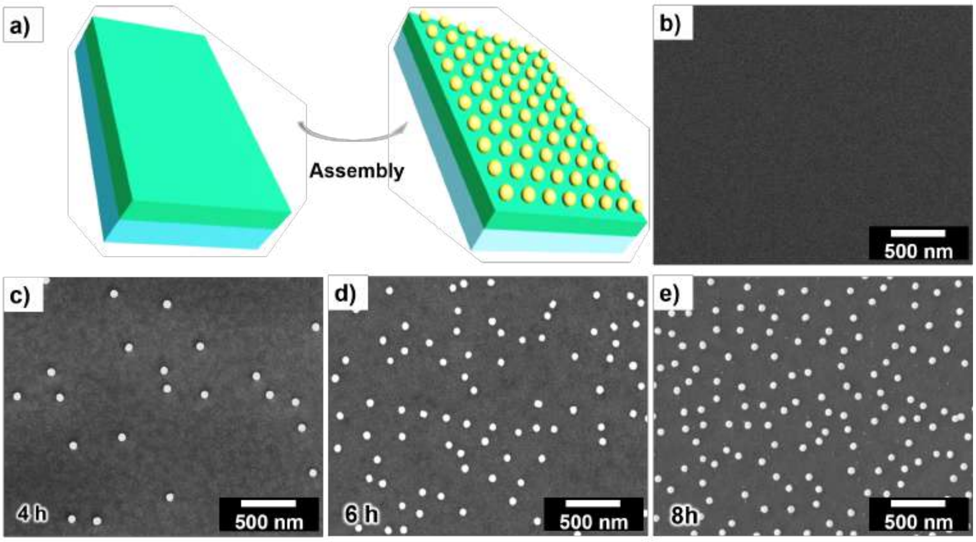

Figure 4.5:
Schematic diagram of Au NPs assembled on the top of TiO_2 film. SEM images of b) pristine TiO_2 film and Au NPs assembled on TiO_2 film with different assembly times c) 4 h d) 6 h e) 8 h.

In this work, we fabricated plasmonic structures through facile and scalable methods,as is shown in Fig. 4.5a, that could enable integrate the highly-dispersed plasmonic metal NPs into photovoltaics. From Fig. 4.5, we can see that the well-dispersed Au NPs array fixing on TiO_2 film by self-assembly method that could effectively avoid the common aggregation problem of plasmonic metallic NPs for their practical application in light-harvesting systems. Fig. 4.5b shows the pristine TiO_2 film with a smooth surface and after assembled Au NPs on the top of TiO_2 film as is shown in Fig. 4.5b-e, we can see that with the increase of assembly times the density distribution of Au NPs is gradually enhanced. In addition, there is almost no agglomeration of Au NPs which might rarely affect device performance to some extent. As we have mentioned above, the optical properties of different sizes of metal NPs were distinctive as well as will impact the performance of photovoltaics. In order to investigate the possible influence of the sizes of Au NPs on subsequent films and device performances, we also have a preliminary morphology exploration of Au NPs assembled on top of silica as is shown in Fig. 4.6, we can see that the well-dispersed Au NPs with different sizes were visibly assembled on the silica surface. To further study the properties of plasmonic structures and their applications in photovoltaics, advanced testing methods, such as grazing incidence wide angle x-ray scattering (GIWAXS) and grazing incidence small angle x-ray and neutron scattering (GISAXS and GISANS) will be used to further investigating the mechanism of plasmonic structure application.

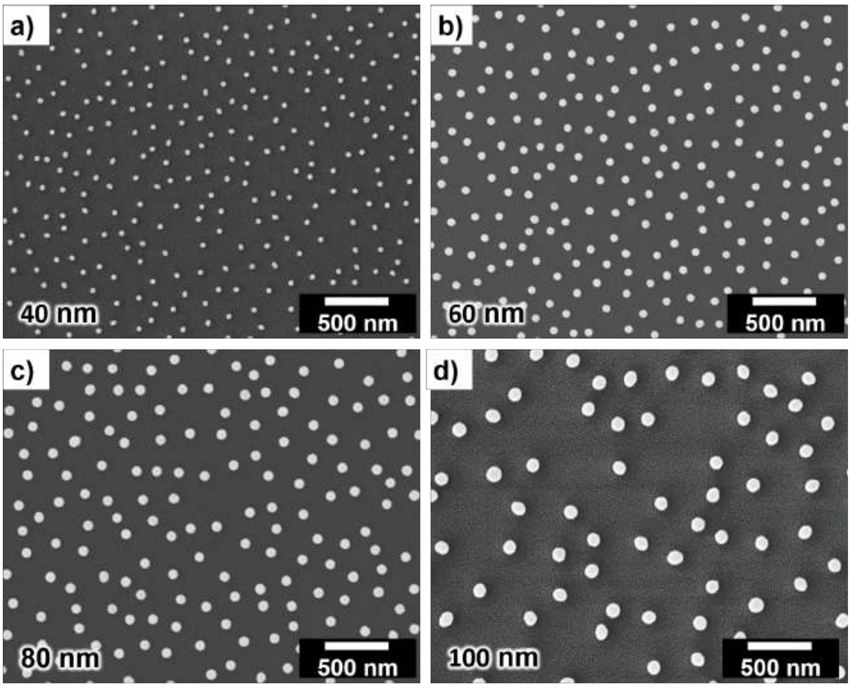

Figure 4.6:
SEM images of Au NPs assembled on the top of silica with different sizes a) 40 nm b) 60 nm c) 80 nm d) 100 nm.

[1] S. Liu, R. Jiang, P. You, X. Zhu, Ji. Wang, F. Yan, *Energy Environ. Sci.* **9**, 898-905 (2016)

[2] K. Chan, M. Wright, N. Elumalai, A. Uddin, S. Pillai, *Adv. Optical Mater.* **5**, 1600698 (2017)

[3] X. Ma, B. Ma, T. Yu, X. Xu, L. Zhang, W. Wang, K. Cao, L. Deng, S. Chen, W. Huang, *ACS Appl. Energy Mater.* **2**, 3605-3613 (2019)

4.4 Stabling α-formamidinium lead iodide ($HC(NH_2)_2PbI_3$ for highly efficient perovskite solar cells

R. Guo, P. Müller-Buschbaum

Perovsktie solar cells (PSCs) have attracted a number of attention in the field of photovoltaic technology. Features like using earth-abundant elements, low fabrication consumption, and excellent optoelectronic properties, make it suitable for terawatt-scale energy harvesting technology with low production costs and low capital expenditure.[1] However, their structural instability limits practical applications.

Figure 4.7 shows that, with broader solar-light absorption through narrower bandgaps, PSCs can increase PCE due to the enhancement of light harvesting.[2] Among lead based PSCs, α-$FAPbI_3$ has narrowest bandgap (1.45 eV) in the films and can improve thermal stability compared with $MAPbI_3$ because of its higher decomposition temperature.[3] However, it is difficult to exploit the full potential of halide perovskites for technological applications. The main barrier is that the best-performing α-$FAPbI_3$ maintains at a hexagonal structure at room temperature, which cannot respond to the solar spectrum (Figure 4.8a).[4] Although several strategies have been tried to stable α-$FAPbI_3$ with adding cations (Cs^+,Rb^+) or halides (Cl^-, Br^-) etc, those additives widen its bandgap and decrease the thermal stability.[5] In addition, adding such additives can cause phase segregation, which induce low current intensity because of the increase of bandgap.[6]

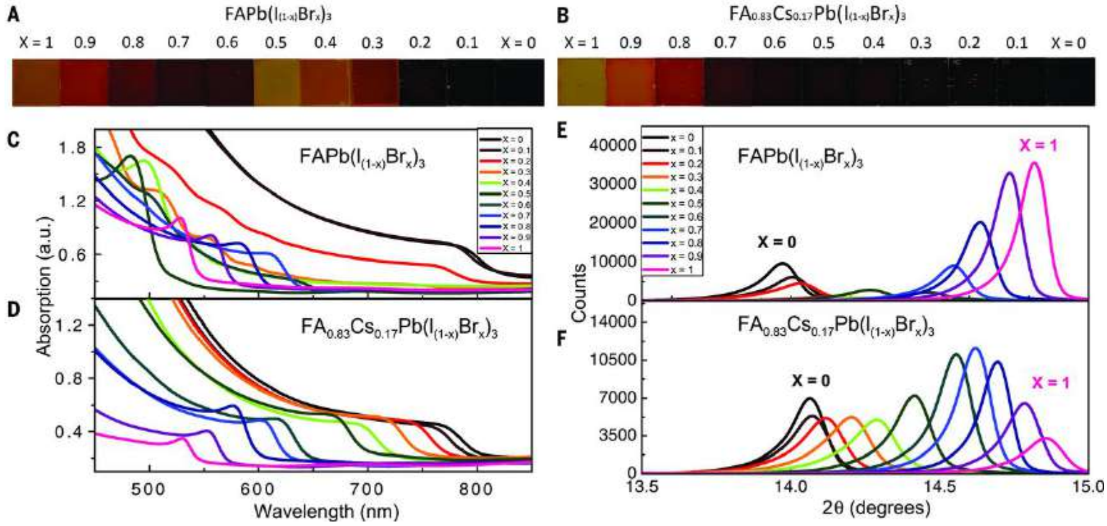

Figure 4.7:
Photographs of perovskite films with Br composition increasing from x = 0 to 1 for (A) $FAPb[I_{(1-x)}Br_x]_3$ and (B) $FA_{0.83}Cs_{0.17}Pb[I_{(1-x)}Br_x]_3$. (C) UV-visible absorbance spectra of films of $FAPb[I_{(1-x)}Br_x]_3$ and (D) $FA_{0.83}Cs_{0.17}Pb[I_{(1-x)}Br_x]_3$. a.u., arbitrary units. (E) XRD pattern of $FAPb[I_{(1-x)}Br_x]_3$ and (F) $FA_{0.83}Cs_{0.17}Pb[I_{(1-x)}Br_x]_3$. The stated compositions are the fractional compositions of the ions in the starting solution, and the actual composition of the crystallized films may vary slightly. Figure adapted with permission from reference [2], Science.

Therefore, a strain engineering was developed to tackle this problem. Chen et al grew crystalline α-FAPbI3 from a solution so that it formed on another more stable halide perovskite (the substrate). The $FAPbI_3$ atoms in the growing crystal align with the cubic structure of the atoms in the substrate, thereby forming a pseudocubic structure themselves (Fig. 4.8b). The epitaxy aligns atoms in different materials and locks α-$FAPbI_3$ into the pseudocubic structure as a result of the strong chemical forces between it and the substrate. This limits the formation of undesirable hexagonal structure, and the pseudocubic structure remains stable for at least a year at room temperature. The α-FAPbI$_3$ films growing on different substrates have different compressive strain because the dimensions of the cubic array of the substrate are different from those of the natural atomic array of α-FAPbI$_3$. Hence, it is possible to control the strain of α-FAPbI$_3$ from 0 to 2.4 percent compressive deformation by growing FAPbI$_3$ on substrates that have different lattice dimensions.

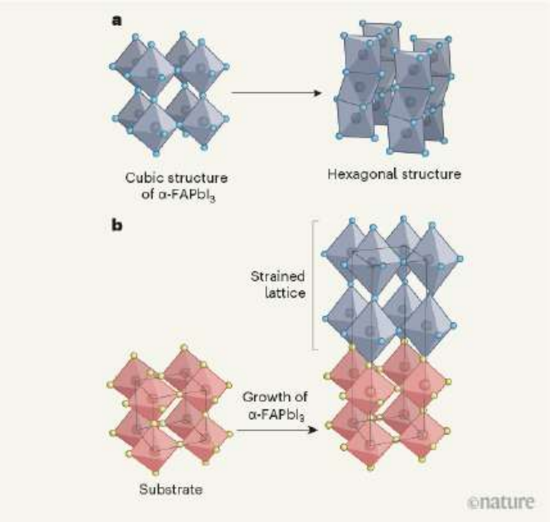

Figure 4.8:
The stabilization and strain engineering of a semiconductor. a, Cubic α-FAPbI$_3$ is unstable, and converts to a hexagonal form that is unsuitable for practical applications. The octahedra represent subunits of the lattices: iodine atoms at the vertices surround a central lead atom; FA$^+$ ions fill the gaps between octahedra, but are not shown. b,The structure of α-FAPbI$_3$ can be stabilized by growing it on a stable halide perovskite (the substrate) that has an analogous structure, so that the atoms in the two lattices align. Because the lattice dimensions of the substrate are smaller than those of α-FAPbI3, the crystal lattice of the latter is squeezed (put under strain). This strain increases the mobility of electrical charge carriers in the material. Figure adapted with permission from reference [4], Nature.

Today, we grow perovskite thin films on electron transporting layers like SnO$_2$ or hole transporting layers like PTAA, which do not have a genuinely epitaxial substrate. The remaining question is that how to apply such a method via the solution based fabrication method.
To conclude, stabling α-FAPbI$_3$ will be one of the most important topic in the field of PSCs. Strain engineering could be one of the most useful strategy to modify the strain of perovskite materials instead of functional additives in the near future. Hence, x-Ray diffraction and grazing incident wide-angle x-Ray scattering would be the crucial technology to analyze the structure and strain information of perovskite phases.

[1] M. Green, A. Ho-Baillie, S. Botta, H. Snaith, *Nat. Photonics* **8**, 506–514 (2014)

[2] D. P. McMeekin, G. Sadoughi, W. Rehman, G. .E. Eperon, M. Saliba, M. T. Hörantner, A. Höghighirad, N. Sakai, L. Korte, B. Rech, M. B. Johnston, L. M. Herz, H. J. Snaith, *Science* **351**, 151–155 (2016)

[3] B. Chen, J. Song, X. Dai, Y. Liu, P. N. Rudd, X. Hong, J.Huang, *Adv. Mater* **31**, 1902413 (2019)

[4] J. Shi, *Nature* **577**, 171–172 (2020)

[5] Q. Jiang, Y. Zhao, X. Zhang, X. Yang, Y. Chen, Z. Ye, Q. Li, X. Yin, J. You *Nat. Photonics* **13**, 460–466 (2019)

[6] D. J. Slotcavege, H. I. Karunadasa, M. D. McGehee, *ACS Energy Lett.* **1**, 1199–1205 (2016)

4.5 Influence of printing temperature on the efficiency of organic solar cells

L. Huber, K. Wienhold, S. V. Roth[1,2], P. Müller-Buschbaum

[1] DESY, Hamburg, Germany
[2] KTH, Stockholm, Sweden

Solar cells have been a front-runner for environmentally friendly energy conversion over the past decades. Organic solar cells have been proven to be advantageous in many ways. They are light-weight, semitransparent , non-toxic and have been proven to have high efficiencies [1]. In order to supply the world with clean energy at reasonable prices, mass production of organic solar cells needs to be enhanced. This can be achieved by decreasing the amount of individual production steps and exploring technologies with high scale-up potential. Printing the active layer instead of spin-coating could lead to easier and faster production cycles and therefore make organic solar cells a more competitive energy conversion method. The effect printing has, on the performance of the solar cell and the molecular structure of the polymer, also needs to be investigated.

PBDB-T-SF:IT-4F solar cell devices use the high efficiency polymer donor material PBDB-T-SF and the acceptor material IT-4F. Fluorine is also introduced to increase chemical stability and obtain higher absorption coefficients. Crystallinity and charge transport can also be increased by the introduction of fluorine [1-3].

Looking at the UV-Vis spectrum of the active layer (Figure 4.9), one can see two distinct peaks. They correspond to the polymer and the acceptor peak. Investigating the different temperatures yields only slight differences in normalized absorption. Higher printing temperature seems to increase absorption slightly compared to room temperature.

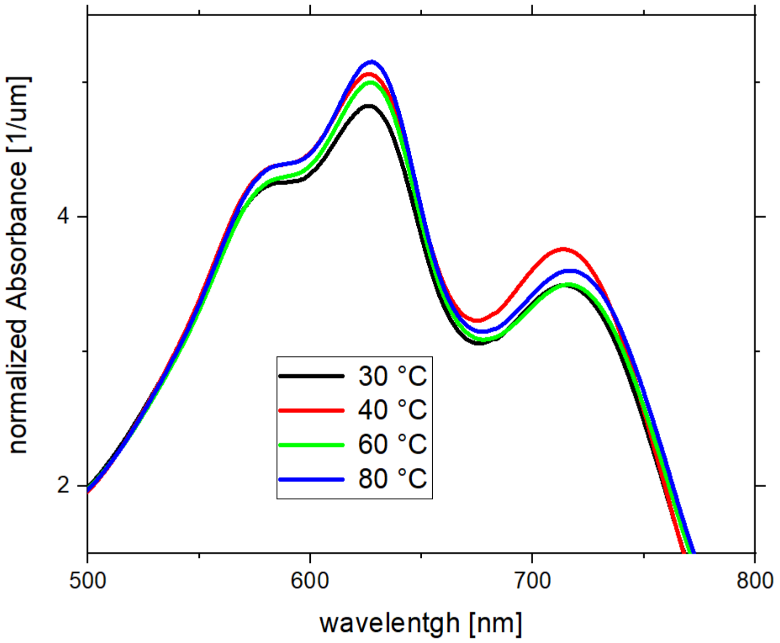

Figure 4.9:
Normalized absorbance spectra for four different printing temperatures.

Our organic solar cells consist of ITO (indium tin oxide)as the bottom electrode, ZnO (zinc-oxide) as our first blocking layer, PBDB-T-SF:IT-4F as our active polymer layer, MbO (molybdenum oxide) as our second blocking layer and silver as the top electrode. The polymer was dissolved in chlorobenzene and stirred for 48 hours at 80 °C. All of the ITO samples were etched and organically cleaned. After a plasma treatment zinc-oxide was spin-coated and they were annealed for 1 hour at 200 °C. After cooling down the active polymer layer was printed at four different temperatures. 30 °C, 40 °C, 60 °C and 80 °C were investigated. Finally molybdenum oxide and silver was evaporated on the substrate.

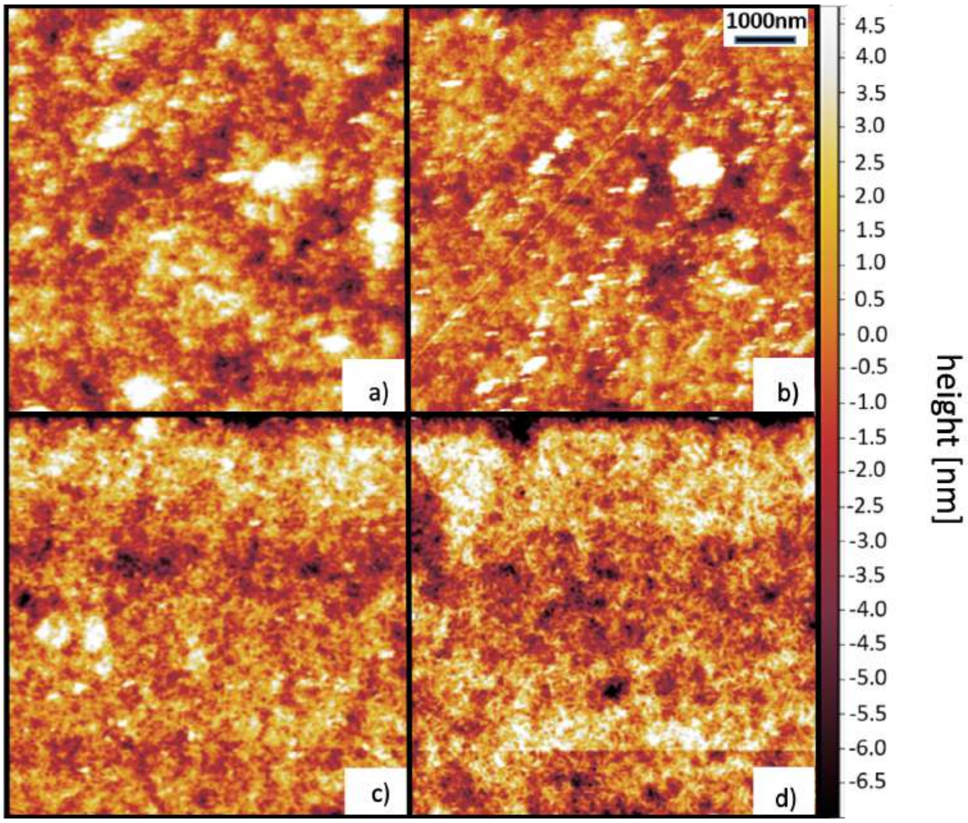

Figure 4.10:
AFM images for four different printing temperatures. a=30 °C, b=40 °C, c=60 °C, d=80 °C.

In the Afm images (Figure 4.10) a trend in structure size and surface roughness can be seen. The more the active layer is heated during printing, the faster is the evaporation of solvent. This faster drying process seems to lead to smaller structure sizes and a higher surface roughness.These parameters play a vital role in organic solar cell efficiency.

[1] W. Zhao, S. Li, H. Yao, S. Zhang, Y. Zhang, B. Yang, J. HouJ., *Am. Chem. Soc.* **139**, 7148-7151 (2017)

[2] S. H. Park, A. Roy, S. Beaupre, S. Chao, N. Coates, J. S. Moon, D. Moses, M. Leclerc, K. Lee, A. J. Heeger *Nat. Photon.* **3**, 297-302 (2009)

[3] Xue, R. Zhang, J. Li. Y., *Small* **14**, 1801793 (2018)

4.6 Perovskite: effects of cesium-incorporation investigated with GIWAXS

L. K. Reb, M. A. Scheel, R. Guo and P. Müller-Buschbaum

Currently, humanity is approaching an age of global warming because of the unsustainable consumption of fossil fuels and greenhouse gas emissions. Considering the continuously growing global power demand, quickly changing towards clean and renewable energy production is essential. For this purpose, sunlight is one of the most promising energy sources. Silicon-based solar cells (SCs) today produce electric power efficiently and are a first step towards a sustainable power generation. However, their resource- and energy-intensive production is cost-intensive. This drives the search for novel material based thin-film SCs to compete with silicon SCs in the near future to substantially decrease the production costs for renewably generated electric power.

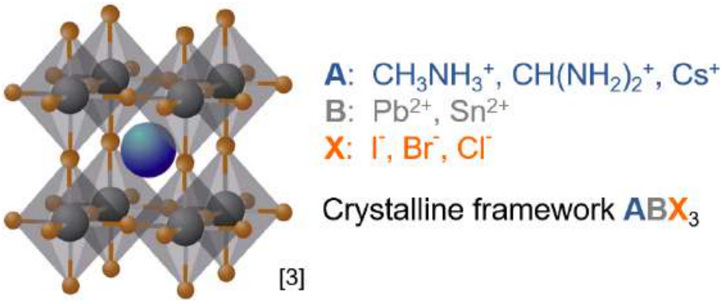

Figure 4.11:
Schematic representation of the cubic perovskite lattice.

Of great interest are perovskite SCs with their impressive increase in efficiency over the last years. Recently, the efficiency surpassed the certified power conversion efficiency of 25 per cent, a value similar to silicon SCs.[1] Additionally, perovskite SCs are easily produced at low temperatures *via* up-scalable and low-cost industrial deposition techniques such as printing or spray casting. The variable chemical composition of the perovskite precursor solution allows optimizing the hybrid crystal structure to benefit from its unique optoelectronic properties. For example, the incorporation of the alkali metal cation cesium (Cs) into the perovskite crystal lattice (cf. Fig. 4.11) has been shown to be advantageous for the perovskite SCs by influencing the crystallization of the perovskite layer.[2] This comprises the crystallite size and orientation in thin-films. By controlling the bulk film morphology the optoelectronic semiconductor properties and also crystal stability can be optimized, essential for highly efficient and long-term durable perovskite SCs.

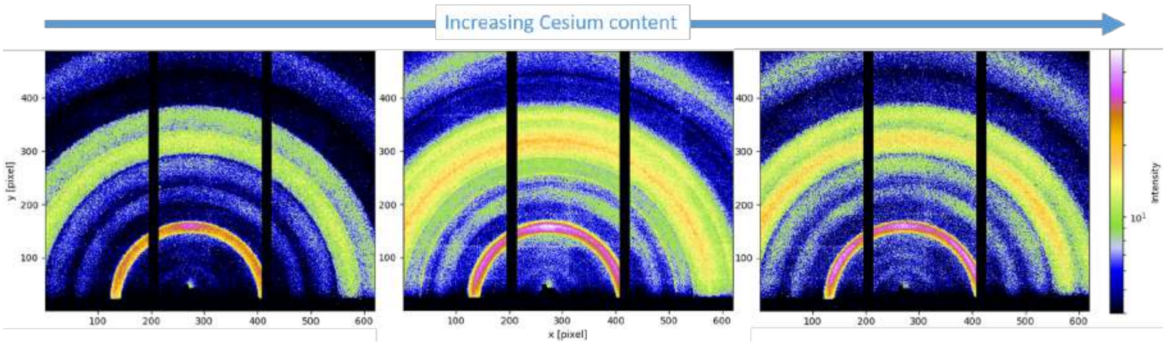

Figure 4.12:
Raw GIWAXS detector images of perovskite for increasing Cs content to the right.

In the present study, we investigate the effect of increasing Cs incorporation for a perovskite composition common in SC-application. We apply statistically relevant grazing-incidence wide-angle X-ray scattering (GIWAXS) to investigate the influence of Cs on the film morphology with focus on the crystallite orientation.

All the three perovskite thin-films are spin-coated onto silicon substrates from a precursor solution of same concentration with the one-step (anti-solvent) method [2] with subsequent annealing. The GIWAXS detector images (measured in-house with an X-ray energy of 8.04 keV) are presented in Fig. 4.11. The face-on lead-iodide (001) peak is hardly visible for any of the films. The intensity close to the center of the rings (i.e. at small q-values), usually attributed to crystalline organic structures, is weak in the present films. These facts together suggest a fairly complete conversion into the perovskite phase after annealing for all different Cs contents. All films show further a strong inner ring, which we attribute to a (001) cubic perovskite reflex, with a slightly preferential face-on orientation. A more-detailed analysis of the intensity reflexes comprises an investigation of the crystallite size and their orientation in dependence of Cs content.

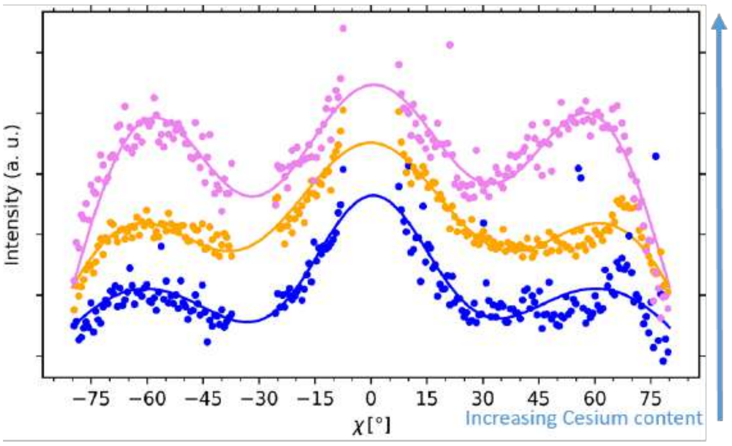

Figure 4.13:
Azimuthal cut of the (001) reflex for the films with different Cs content.

In Fig. 4.13 we focus on the angular distribution of the (001) reflex. By stacking and modeling the intensity distribution for all three films, the differences of crystal orientation become apparent. In particular, there are strong changes visible for the side-peaks, which are attributed to crystallite edge-on orientation. The film of lowest Cs content shows weak side-peaks, and they become more pronounced towards higher Cs contents. For the highest Cs content, the side-peak intensity comes close to the central-peak intensity. In addition, towards higher Cs contents, the side-peak position moves towards smaller angles. These trends indicate a smooth change of crystallite orientation upon Cs incorporation, where the edge-on orientation becomes more favorable for higher Cs contents. The interplay of crystallite size and orientation is known to strongly control the light-harvesting properties of the perovskite layer. Improving our knowledge about perovskite crystal growth is therefore important towards highly efficient perovskite SCs.

[1] NREL. Best Research-Cell Efficiencies.(2020). Available at: https://www.nrel.gov/pv/cell-efficiency.html. (Acessed January 2020)

[2] M. Saliba, J.-P. Correa-Baena, C. M.Wolff, M. Stolterfoht, N. Phung, S. Albrecht, D. Neher, A. Abate, *Chem. Mater.* **30**, 4193-4201 (2018)

[3] M. Grätzel, *Nature Mater.* **13**, 838–842 (2014)

4.7 Influences on the absorption behavior of polythiophene derivatives

R. Schaffrinna[1], M. Schwager[1], P. Müller-Buschbaum

[1] Hochschule München, München, Germany

Polythiophene and derivatives are electrically conductive polymers due to their conjugated π-electron system where electrons are delocalized over the whole backbone resulting in semiconducting properties. The polymers are also flexible, transparent, light weight and have low energy costs per surface compared to inorganic semiconductors. They are used in organic solar cells [1], hybrid solar cells [2], organic light-emitting diodes [3] or field effect transistors [4] and require no heavy metals / heavy metal complexes nor dopants for charge transport and can be easily printed [5], sprayed [6] and deposited via spin-coating [7] from a solution. The synthesis of new air-stable organic semiconductors is therefore essential for further progresses in organic electronics.

The homopolymer poly(3-hexylthiophene) (P3HT) was synthesized from the monomer unit 3-hexylthiophene (3HT) by chemical oxidative polymerization with iron(III) chloride ($FeCl_3$). Poly(3-hexylthiophene-co-3-thiopheneacetic acid) (poly(3HT-co-P3TAA) was synthesized with different molar ratios (1:1, 5:1, 10:1, 20:1) of 3HT and 3-thiophene acetic acid (3TAA). Thiophene acetic acid molecules are compared to hexyl thiophene not soluble in hazardous chlorinated solvents such as chloroform or chlorobenzene but instead in sodium hydroxide (NaOH), acetone or in water, which makes these polymers more environmentally friendly.

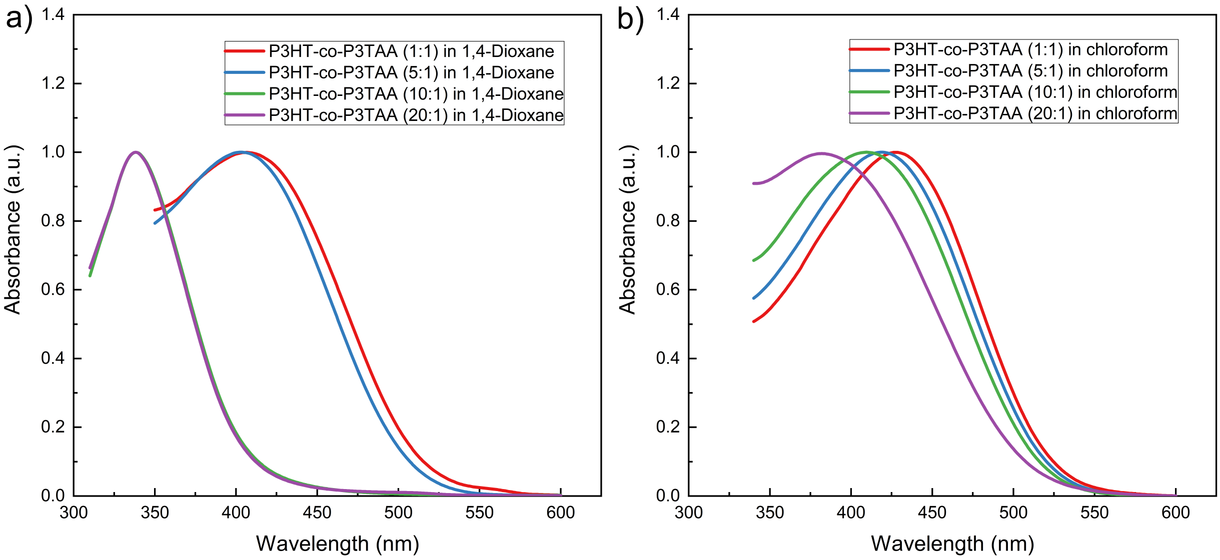

Figure 4.14:
Absorption spectra of poly(3HT-co-P3TAA) with different molar ratios (1:1, 5:1, 10:1, 20:1) dissolved in a) 1,4-Dioxane and b) chloroform. A clear shift to smaller wavelengths with increasing hexyl content is visible in both solvents.

Fig 4.14a shows the absorption spectra of poly(3HT-co-P3TAA) in 1,4-Dioxane with synthesized molar ratios of 1:1, 5:1, 10:1 and 20:1 corresponding to maxima at 414, 403, 338 and 338 nm respectively. Due to the increasing hexyl content the absorption shifts to smaller wavelengths, reaching its wavelength minimum at 338 nm. The same trend is also shown in Fig 4.14b where the polymers are dissolved in chloroform with maxima at 429, 420, 409 and 385 nm. The differences in both spectra result in the different solubility of the copolymer since hexyl and acetic acid molecules are both soluble in 1,4-Dioxane while for chloroform only the hexyl content is soluble.

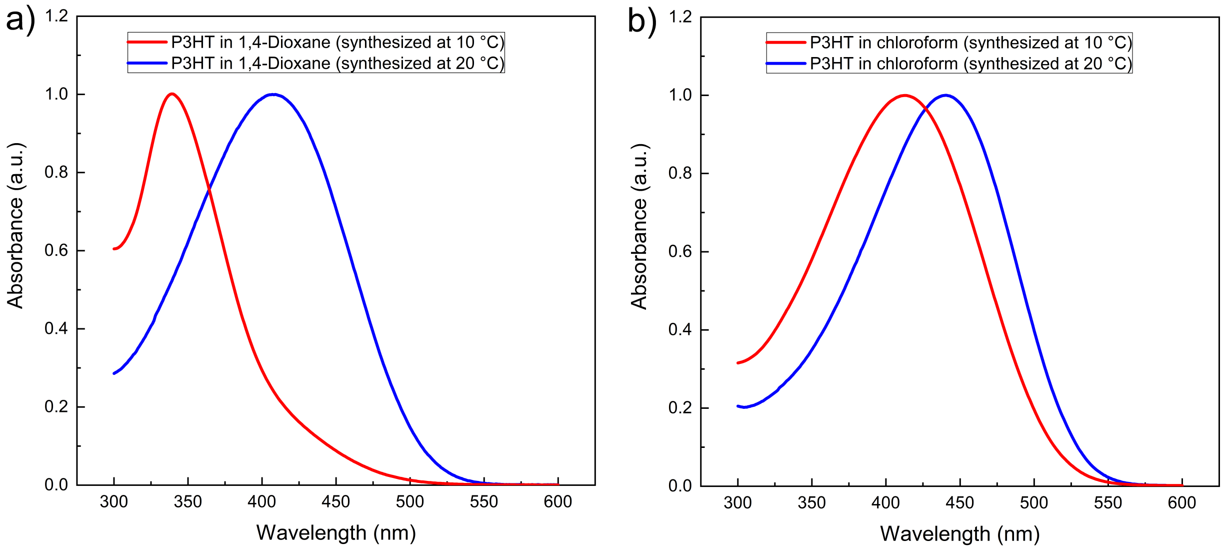

Figure 4.15:
Synthesis temperature influence on the absorption behavior of P3HT dissolved a) in 1,4-Dioxane and b) chloroform at different temperatures. A red shift at higher temperatures is visible for both solvents

Another important parameter to influence the mean conjugation length of the polymer is the synthesis temperature. Fig 4.15 shows two different temperatures the polymerization was carried out. While the maximum at 10°C for P3HT dissolved in 1,4-Dioxane (Fig 4.15a) shifts from 339 nm the maximum at 20°C shifts to 407 nm at 20°C resulting in a strong red shift of 68 nm due to interactions of the polymer with the solvent. P3HT dissolved in chloroform (Fig 4.15b) shows P3HT with maxima at 412 nm (at 10°C) and 441 nm (at 20°C) resulting in a red shift of 29 nm. The different maxima in both solvents are again a result of the separation of shorter and longer conjugated parts of the molecules using 1,4-Dioxane to separate both parts while chloroform only separates hexyl molecules. The band gap of P3HT is determined over the absorption edge, which is extrapolated from the absorption spectrum with an absolute error of around 0.1 eV. For the synthesized molecules dissolved in 1,4-Dioxane the band gap ranges from 2.3 eV for 20°C to 2.9 eV for 10°C. For P3HT dissolved in chloroform values of 2.3 eV at 20°C and 2.2 eV at 10°C are caculated. Varying the monomer ratio in copolymerization process and also the synthesis temperature are therefore both suitable methods to tune the absorption behavior and the band gap of a polymer. Other optical parameters such as the fluorescence or the quantum yield can also be changed with these methods as well as the wetting properties with a variation of hexyl and acetic acid content in the copolymer.

[1] P. R. Berger, M. Kim, *JRSE* **10**, 013508 (2018)

[2] J. Pei, Y. Z. Hao, H. J. Lv, B. Sun, Y. P. Li, Z. M. Guo *Chem. Phys. Lett.* **644**, 127-131 (2016)

[3] T. T. Thao, T. Q. Trung, V.-V. Truong, N. N. Dinh, *J. Nanomater.* **2015**, 463565 (2015)

[4] M. Mas-Torrent, D. den Boer, M. Durkut, P. Hadley, A. P. H. J. Schenning *Nanotechnology* **15**, 265-269 (2004)

[5] A. Lange, M. Wegener, C. Boeffel, B. Fischer, A. Wedel, D. Neher, *Sol. Energy Mater. Sol. Cells* **94**, 1816-1821 (2010)

[6] M. Eslamian, J. E. Newton, *Coatings* **4**, 85-97 (2014)

[7] J. Y. Na, B. Kang, D. H. Sin, K. Cho, Y. D. Park, *Sci. Rep.* **5**, 13288 (2015)

4.8 Influence of different solvents on the properties of PBDB-T-SF:IT-4F basted organic solar cells

D. M. Steger, K. S. Wienhold and P. Müller-Buschbaum

The demand for energy is currently increasing rapidly and considering the huge impacts climate change already has on our planet, the necessity to fulfil this demand in an environmentally friendly way is a great challenge. As the sun is one of the most reliable and cleanest renewable energy sources, ways of harvesting this energy are of great interest in modern research. Inorganic semiconductor based solar cells are by now a well understood technology with great power conversion efficiencies, yet they have several disadvantages, such as high weight and a very high energy demand for production. Thus in recent years attention turns more towards newer generation technologies, such as polymer based organic solar cells, which are lightweight, flexible and can be produces consuming much less energy. In recent years the power conversion efficiency (PCE) of such devices has rapidly improved, with top performing solar cells reaching PCEs of above 16 % [1]. Yet these solar cells still bear some challenges, such as improving the long term stability, or scalability of production to make them commercially viable.

In our work, the promising combination of the polymeric donor material PBDB-T-SF and the non-fullerene small molecule acceptor IT-4F, which has reported efficiencies up to 13 % [2], are being used. In contrast to most other works, the active layer is not produced via spin-coating, but via deposition techniques such as meniscus guided slot-die coating. The main focus thereby lies on studying the effect of different solvents on the morphology of the active layer and the solar cell performance. Therefore the polymer and acceptor material were dissolved in chlorobenzene, chloroform, coluene and 1,2-cichlorobenzene.

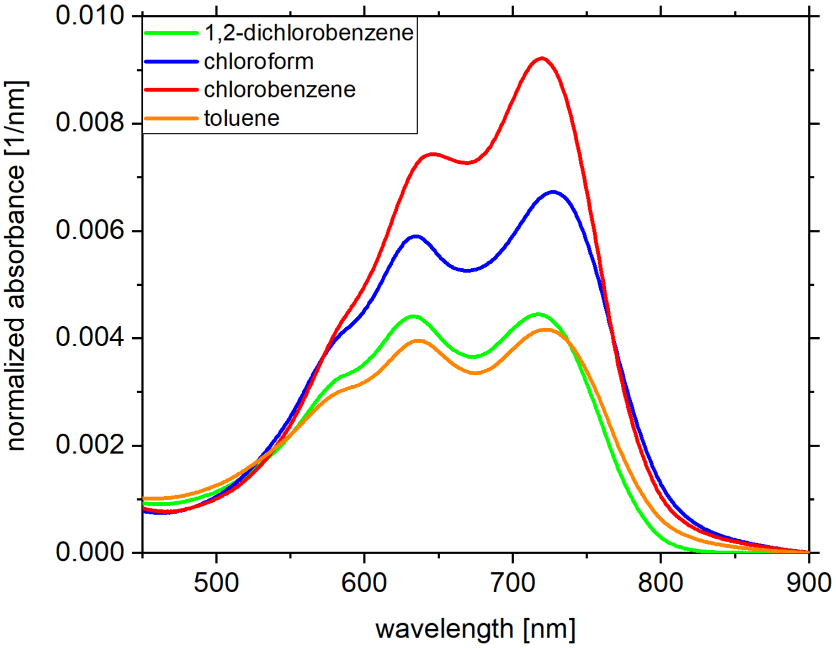

Figure 4.16:
UV/VIS-spectroscopy data for printed thin films of PBDB-T-SF:IT-4F on glass substrates

The optical properties of the active layer can be studied using different techniques, such as

UV/VIS-Spectroscopy, which can be used to investigate the absorption spectrum of the material, which is highly relevant for the performance of a solar cell, as it determines the efficiency with which the material absorbs light. Photoluminescence spectroscopy measurements were done to have a look at the recombination processes. Figure 4.16 shows the absorbance of thin films printed with the four different solvents used, each normalized to the film thickness. The peak at around 720 nm for each solvent mostly originates from the absorbance of the acceptor material, the peak at about 630 nm from the absorbance of the polymer respectively.

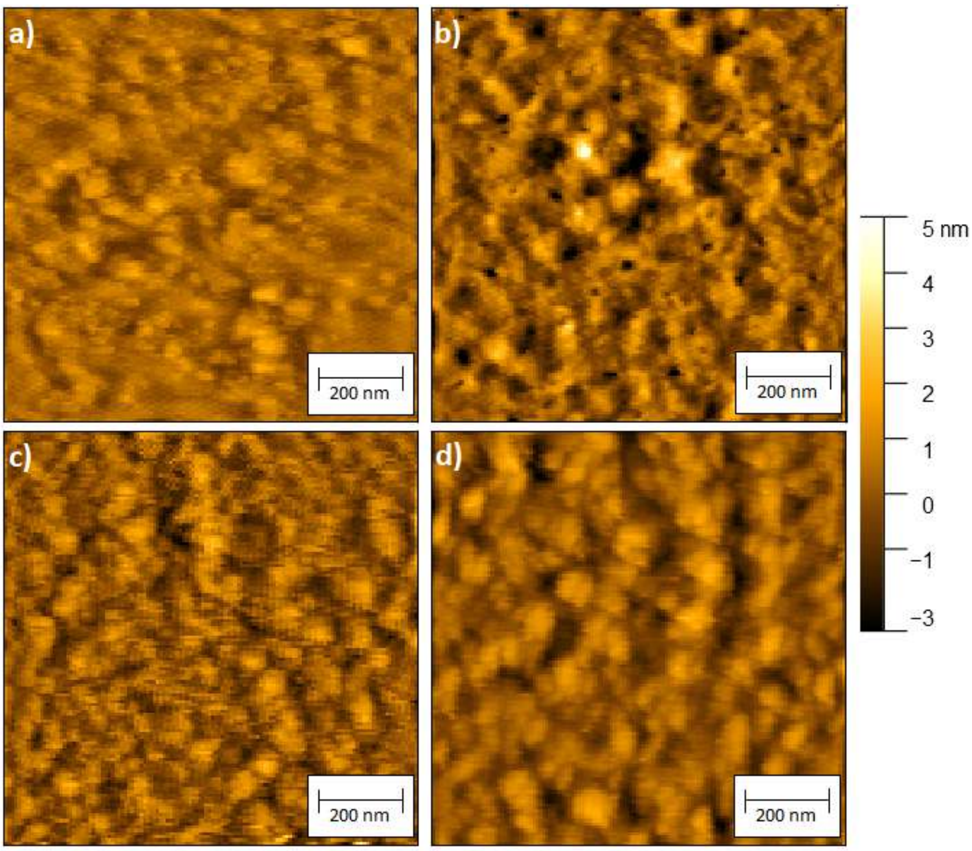

Figure 4.17:
atomic force microscopy images for a) chlorobenzene, b) chloroform, c) toluene and d) 1,2-dichlorobenzene

To further investigate the influence of different solvents on the morphology, techniques such as atomic force microscopy (AFM) to study the surface structure of the active layer, are a great choice, as it has a resolution in the nm-scale, which is sufficiently below the order of magnitude in which we expect our structure sizes to be. As shown in figure 4.17, there are significant differences in the surface structure. Chlorobenzene shows a lower surface roughness compared to the other solvents, which suggest better solving properties of the polymer. For chloroform, there are holes and cracks visible in the surface, which might originate from this solvent evaporating very fast, as it has by far the lowest boiling point of alle the solvents used. 1,2-dichlorobenzene on the other hand shows a surface with quite large but rather smooth structures, as it has the highest boiling point and therefore evaporating the slowest.

[1] B. Fan, D. Zhang, M. Li, W. Zhong, Z. Zeng, L. Ying, F. Huang, Y. Cao, *Sci. China Chem.* **62**, 746 (2019)

[2] W. Zhao, S. Li, H. Yao, S. Zhang, Y. Zhang, B. Yang, J. Hou, *J. Am. Chem. Soc.* **139**, 7148 (2017)

4.9 Effect of Solvent Additives on the Morphology and Device Performance of Organic Solar Cells

K. S. Wienhold, V. Körstgens, S. Grott, X. Jiang, M. Schwartzkopf[1], S. V. Roth[1,2],
P. Müller-Buschbaum

[1] DESY, Hamburg, Germany
[2] KTH, Stockholm, Sweden

Printing of active layers of high efficiency organic solar cells with a meniscus-guided slot-die coater enables up-scaling of the solar cell production. However, an optimization of this thin film deposition is necessary as insights gained from spin-coating cannot simply be transferred to printed photovoltaics. Active layers of the conjugated polymer PBDB-T-SF and the non fullerene small molecule acceptor IT 4F which can reach a power conversion efficiency of 13 % [1] are slot die coated with different concentrations of 1,8-diiodoctane (DIO) and the effect on the inner nano-structure and device performance is studied.[2]

Grazing incidence small angle X-ray scattering (GISAXS) allows to probe the full film thickness of printed active layers and to analyse the inner nano-morphology with high quality and statistical significance. Horizontal line cuts performed at the critical angle of PBDB-T-SF and corresponding modeling results are given in Fig. 4.18 for active layers of PBDB-T-SF:IT-4F printed with different DIO concentrations.

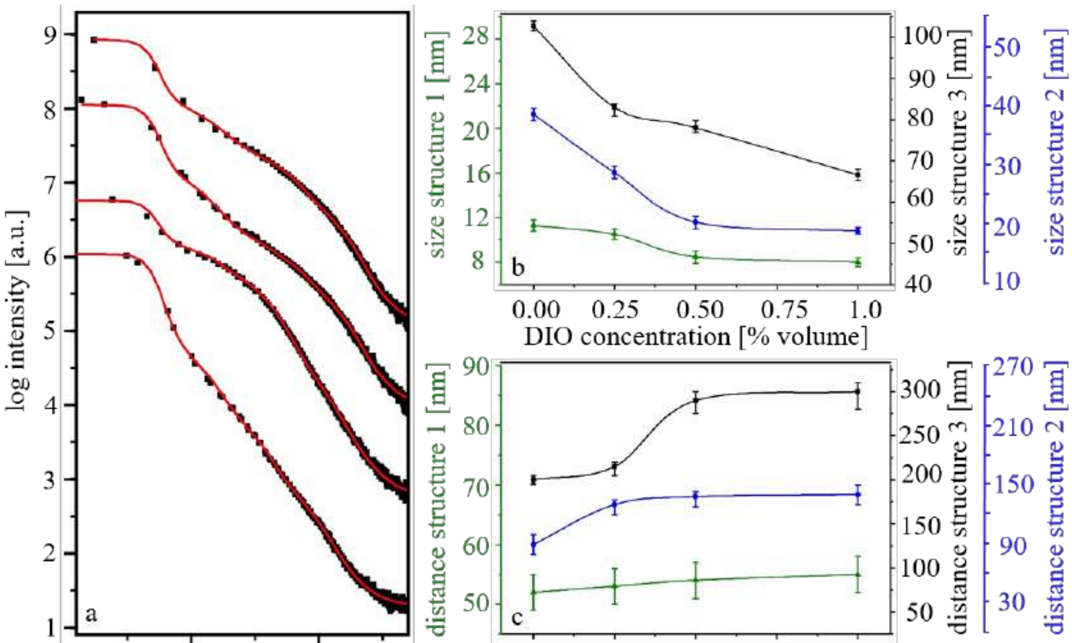

Figure 4.18:
(a) Horizontal line cuts of 2D GISAXS data (black dots) and modelling results (red lines) obtained for printed active layers with different DIO concentrations in chlorobenzene solutions (0.00, 0.25, 0.5 and 1.0 vol % DIO from bottom to top); (b) average domain sizes for different DIO concentrations obtained from modeling; (c) average distances in the BHJ structure for different DIO concentrations. Splines (b and c) are guides to the eye.

The modeling results show reduced average structure sizes and enhanced average distances with increasing solvent additive concentration. Thin films printed without DIO yield average structure sizes of (103 ± 1) nm, (39 ± 1) nm and (11 ± 1) nm, whereas the addition of only 0.25 vol % DIO reduces the average structure sizes to (83 ± 1) nm, (29 ± 1) nm and (10 ± 1) nm. This reduction of the average structure sizes is favorable for the solar cell performance as the charge transfer from the polymer to the small acceptor molecule is facilitated by an increase of interface area. At higher DIO concentrations, the average structure sizes are further reduced to (79 ± 1) nm, (21 ± 1) nm and (9 ± 1) nm for 0.50 vol% and (67 ± 1) nm, (19 ± 1) nm and (8 ± 1) nm for 1.0 vol% DIO which can have a negative effect on the device performance due to a charge trapping assisted recombination mechanism.
The average distances between the polymer domains grow from (200 ± 10) nm, (90 ± 10) nm and (52 ± 8) nm in the case of solvent-additive free thin films to (215 ± 10) nm, (130 ± 10) nm and (53 ± 8) nm for active layers printed with 0.25 vol% DIO. The enlargement of distances between PBDBT-SF and IT-4F domains can provoke charge stabilization and lower the risk of recombination by a reduction of Coulomb forces. Higher solvent additive concentrations of 0.50 vol% and 1.0 vol% form average distances of (290 ± 10) nm, (138 ± 10) nm and (54 ± 10) nm and respectively (300 ± 10) nm, (140 ± 10) nm and (55 ± 8)nm.

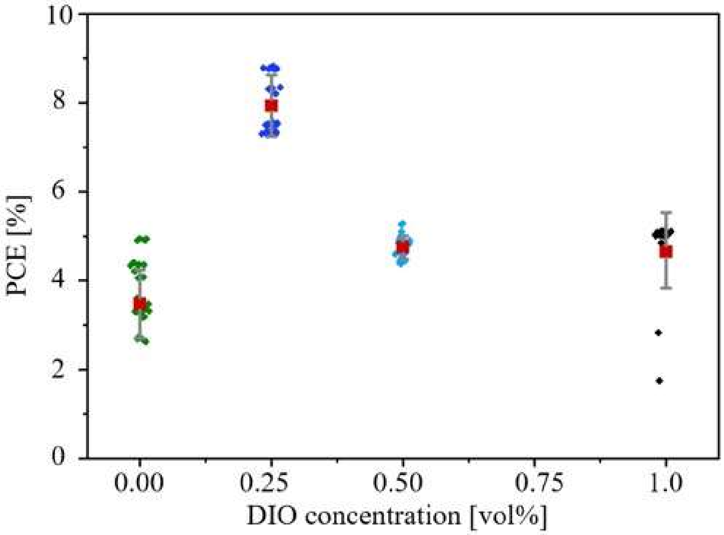

Figure 4.19:
PCE of organic solar cells printed with different DIO concentrations. Efficiencies of measured pixels (small colored dots), the average device performance (red square) and the standard deviation (grey error bar) are given for different solvent additive concentrations.

The PCE achieved for organic solar cells printed with different DIO concentrations is given in Fig. 4.19. Solvent additive free solar cells reach an average PCE of (3.5 ± 0.8)%. The addition of 0.25 vol% DIO improved the average PCE to (7.9 ± 0.7)% with a top device performance of 8.95 %. By further enhancing the solvent additive concentration, average PCE values of (4.6 ± 0.3) % for 0.50 vol% and (4.6 ± 0.9)% for 1.0 vol% of DIO result.

Organic solar cells processed with 0.25 vol% DIO exhibit the best device performance. For a solvent additive concentration of 0.25 vol% DIO, the gain of interface area by decreasing average structure sizes dominate whereas at higher DIO concentrations, the presence of a loss mechanisms due to large distances between domains dominates. The present result give insight into the morphology-device performance relationship of printed photovoltaics and is an important step towards optimization and up-scaling of organic solar cells.

[1] W. Zhao, S. Li, H. Yao, S. Zhang, Y. Zhang, B. Yang, J. Hou *J. Am. Chem. Soc.* **139**, 7148-7151 (2017)

[2] K. S. Wienhold, V. Körstgens, X. Jiang, M. Schwartzkopf, S. V. Roth, P. Müller-Buschbaum, *ACS Appl. Mater. Interfaces* **11**, 42313-42321 (2019)

4.10 Hybrid energy harvester based on solar cell and triboelectric nanogenerator

T. Xiao, W. Cao, W. Chen, S. -J. Wöhnert[1], S. V. Roth[1,2], P. Müller-Buschbaum

[1] DESY, Hamburg, Germany
[2] KTH, Stockholm, Sweden

Developing clean energy techniques plays a central role in the sustainable development of human society [1], in which collecting solar energy is one of the most promising way in replacement of conventional used fossil fuels. However, the daily and seasonal fluctuations limit the continuous electricity generation from the solar cells. Thus, integrating the solar cell with other kinds of energy harvesters in one device is considered as an effective solution to continuously providing energy source [2]. Triboelectric nanogenerator (TENG) originating from Maxwell's displacement current is a new type of energy harvesters. Due to its advantages of light-weight, low-cost, and easily fabricated, TENG attracts worldwide attention in the past years [3].

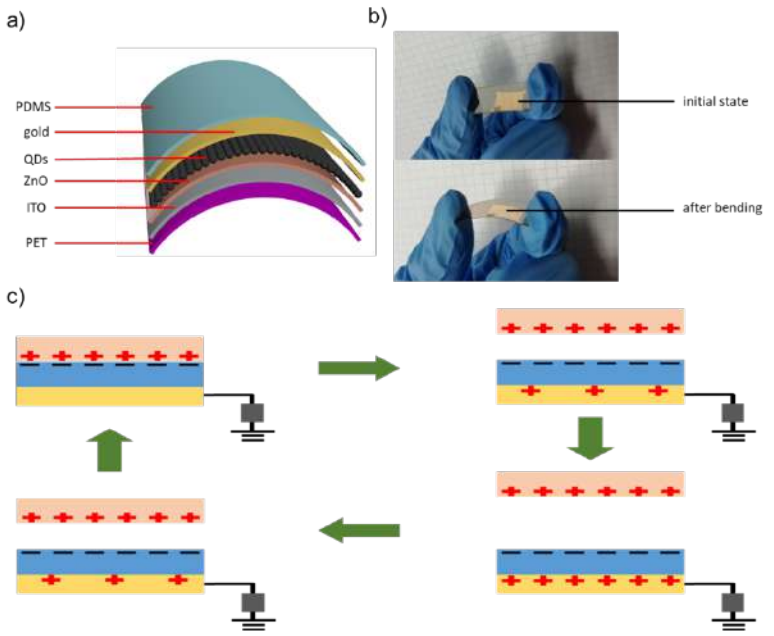

Figure 4.20:
a) Fabricated hybrid energy harvester as sketch and b) in reality. c) The working principle of the TENG part.

In the present work, a flexible hybrid energy harvester has been designed and fabricated based on PbS quantum dots (QDs) as the solar energy convertors. This device consists of a QD solar cell part and a polydimethylsiloxane (PDMS) based TENG part, which can harness both, solar and mechanical energy from ambient environment to generate electricity. The structure of the hybrid energy harvester is schematically shown in Fig. 4.20a. And Fig. 4.20b shows a photograph of as-fabricated energy harvester device at bending state. Fig. 4.20c illustrates the working principle of the TENG part. At the initial state, owing to the different abilities to electron affinities, equal density of positive and negative charges are generated on the external object and PDMS film, respectively. Then, when the external object separates from PDMS film, it drives free electrons flowing from the bottom electrode to the ground, which produces the current until getting the maximum distance. After that, when the external object comes close to PDMS film, free electrons flow back from the ground to the bottom electrode, producing the

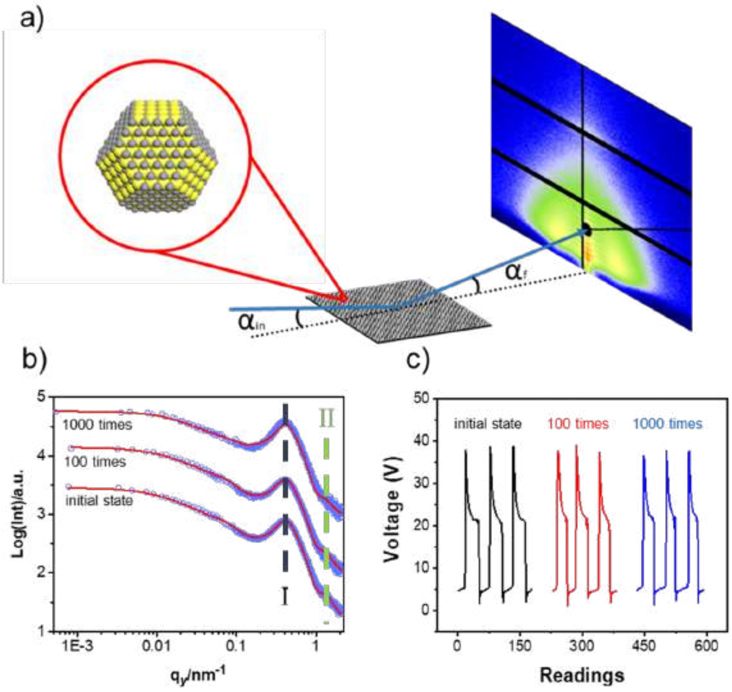

Figure 4.21:
a) GISAXS measurement setup with QD layer. b) GISAXS horizontal-cuts data and corresponding modelling at different states. c) Output performance of the TENG part at different states.

reverse current. Finally, a complete electricity generation cycle has been accomplished after they contact again.

In order to investigate the bending stability of the hybrid energy harvester, grazing-incidence small-angle X-ray scattering (GISAXS) measurements are used to characterize the morphology changes of the mesoscale structure [4]. The GISAXS measurement setup and the principle are presented in Fig. 4.21a. Fig. 4.21b shows the GISAXS horizontal-cuts data and corresponding modelling results of the function layers of the energy harvester device at different states. Here, because of the similar critical angle of ZnO and PbS according to the scattering length density calculations, the peak I is originated from the inter-dot distance between neighboring ZnO nanoparticles (NPs). Besides, the peak II is originated from the inter-dot distance between neighboring PbS QDs. According to the modelling parameters, the inter-dot distances of ZnO NPs and QDs remain stable at 3.8 ± 0.6 nm and 1.5 ± 0.3 nm respectively after bending, which exhibits the high stability of the fabricated hybrid energy harvester. This result can be also demonstrated by the output performance test of TENG part (Fig. 4.21c). After 1000 times bending, TENG part produces roughly the same output voltage (37.8 ± 1.3 V) as that (38.7 ± 0.8 V) in the initial state.

[1] B. O'regan, M. Grätzel, *Nature* **353**, 737 (1991)

[2] Z. L. Wang, *Mater. Today* **20**, 74 (2017)

[3] L. Zheng, Z. Lin, G. Cheng, W. Wu, X. Wen, S. Lee, Z. L. Wang, *Nano Energy* **9**, 291-300 (2014)

[4] P. Müller-Buschbaum, *Adv. Mater.* **46**, 7692-7709 (2014)

4.11 Tailoring morphology compatibility by adding PBDTTPD-COOH as third component to fullerene-based polymer solar cells

D. Yang, B. Cao[1], V. Körstgens, N. Saxena, N. Li, C. Bilko, S. Grott, W. Chen, X. Jiang, J. E. Heger, S. Bernstorff[2], P. Müller-Buschbaum

[1] University of Alberta, Edmonton, Canada

[2] Elettra, Trieste, Italy

Organic solar cells (OSCs) thrive on the prospects of low-cost processing, pliability and large scale fabrication. The new record power conversion efficiency (PCE) of single-junction OSCs is approaching 17 %.[1] However, it is still behind other kind photovoltaic technologies, such as silicon solar cells and perovskite solar cells. It has been demonstrated that further enhancement of the performance of bulk heterojunction (BHJ) OSCs is limited by an approach based on binary components due to the problems in balancing the absorption range, the crystallization and the compatibility of the D/A materials. Thus, ternary OSCs, namely a blend of donor1/donor2/acceptor (D1/D2/A) or donor1/acceptor1/acceptor2 (D1/A1/A2), are proposed to modulate optoelectronic and morphological characteristics of traditional BHJ active layers. In this work, we introduce poly((4,8-bis((2-ethylhexyl)oxy)benzo[1,2-b:4,5-b']dithiophene-2,6-diyl)-alt-((Nethylhexylthieno[3,4-c]pyrrole-4,6-dione)-2,6-diyl)) (PBDTTPD) with a carboxylic acid-based side chain, PBDTTPD-COOH, as a third component in PTB7-Th:PC$_{71}$BM and PffBT4T-2OD:PC$_{71}$BM blends to observe the effects of this third component on the performance of assembled devices and the morphology of BHJ films.

To investigate the performance of solar cells, devices with an architecture of glass/ITO/PEDOT:PSS/BHJ (with or without the third component)/LiF/Al/Mg are fabricated and characterized. The average performance values of each device type are summarized in Table 1. In the PTB7-Th:PC$_{71}$BM series, optimal devices are obtained from a BHJ with 1.5 wt% of PBDTTPD-COOH, which shows a PCE of 10.1 %, owing to the improvement of J_{SC} and FF value. In the PffBT4T-2OD: PC$_{71}$BM series, the best performance is achieved by adding 0.7 wt % PBDTTPD-COOH. It causes a PCE increase from 7.8 % to 8.9 % due to an increase in J_{SC} (17.6 to 18.3 mA/cm^2) and FF (59 to 64 %).

Moreover, grazing incidence wide angle X-ray scattering (GIWAXS) measurements are applied to investigate the influence of the third component on the crystalline structures of the BHJ films.[2] The 2D GIWAXS data are shown in Fig. 4.22a-h and the corresponding sector integrals are displayed in Fig. 4.22i and j. In the PTB7-Th:PC$_{71}$BM series (Fig. 4.22i), the (100) Bragg peak of PTB7-Th appears only in the out-of-plane direction at 0.28 Å^{-1} in case of the BHJ film

	C$_{3rd}$^{a} [%]	J_{SC} [mA/cm^2]	V_{OC} [V]	FF [%]	PCE [%]
a)	0	18.8 ± 0.5	0.781 ± 0.001	55 ± 1	8.3 ± 0.1
	0.7	19.7 ± 0.3	0.783 ± 0.001	56 ± 1	8.8 ± 0.1
	1.5	20.1 ± 0.5	0.790 ± 0.001	59 ± 1	10.1 ± 0.1
	3.0	19.1 ± 0.4	0.783 ± 0.001	50 ± 1	7.5 ± 0.2
b)	0	17.6 ± 0.8	0.754 ± 0.003	59 ± 1	7.8 ± 0.2
	0.7	18.3 ± 0.4	0.765 ± 0.004	64 ± 1	8.9 ± 0.1
	1.5	16.7 ± 0.4	0.766 ± 0.004	65 ± 1	8.3 ± 0.1
	3.0	16.3 ± 0.4	0.754 ± 0.009	60 ± 1	7.3 ± 0.1
	5.0	16.0 ± 0.4	0.753 ± 0.005	57 ± 1	6.8 ± 0.1

Table 1: Mean photovoltaic parameters of devices with different amount of PBDTTPD-COOH. a) PTB7-Th:PC$_{71}$BM series and b) PffBT4T-2OD:PC$_{71}$BM series. ^{a} the concentration of the third component.

without PBDTTPD-COOH addition. In contrast, the (100) Bragg peaks of PTB7-Th are present both in the out-of-plane and in-plane direction at 0.30 Å^{-1} in the samples with 1.5 wt% and 3.0 wt% PBDTTPD-COOH, indicating that face-on oriented crystallites formed in the ternary films. For the PffBT4T-2OD:$PC_{71}BM$ films (Fig. 4.22j), we find that the intensity ratio of in-plane (100) Bragg peak and out-of-plane (100) Bragg peak in the ternary film with 0.7 wt% third component (5.61) is higher than that in the reference film (3.83), which means that more face-on oriented crystallites formed in the ternary film. It has been reported by Sirringhaus et al. that a face-on orientation is more favorable to obtain higher charge mobility than an edge-on orientation in solar cells.[3] Therefore, we claim that the improvement of polymer crystallite orientation benefits for enhancing the J_{SC} value, which is reflected on the device performances.

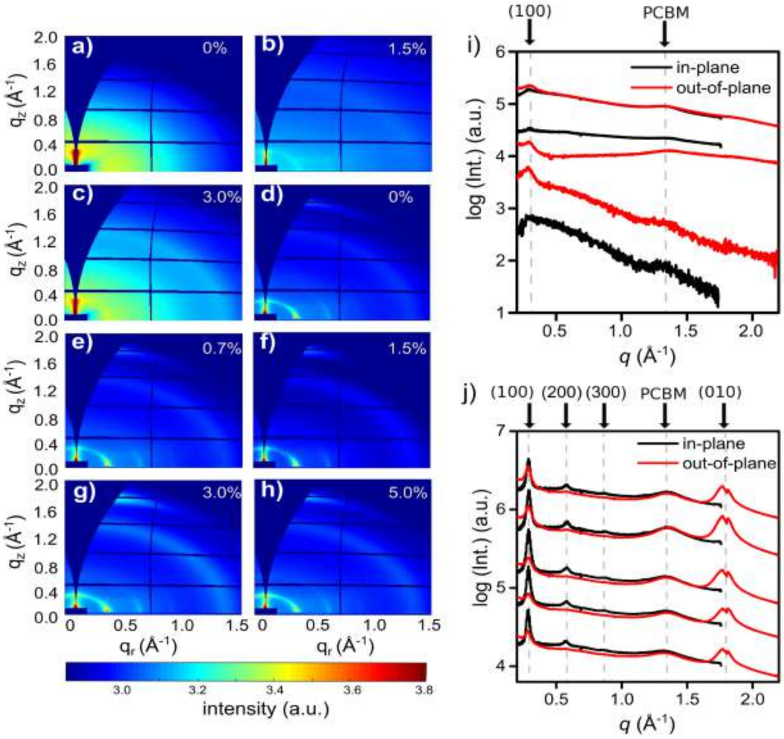

Figure 4.22:
2D GIWAXS data of BHJ films: a)-c) PTB7-Th:$PC_{71}BM$ and d)-h) PffBT4T-2OD:$PC_{71}BM$ films with different ratios of PBDTTPD-COOH. The corespomding horizontal (black curves) and vertical (red curves) sector integrals of 2D GIWAXS data for BHJ films with different blend ratios of PBDTTPD-COOH: i) PTB7-Th:$PC_{71}BM$ samples containing 0 wt%, 1.5 wt% and 3.0 wt% PBDTTPD-COOH from bottom to top; j) PffBT4T-2OD:$PC_{71}BM$ samples containing 0 wt%, 0.7 wt%, 1.5 wt%, 3.0 wt% and 5.0 wt% PBDTTPD-COOH from bottom to top.

Furthermore, we observe that the ternary devices have better stability than the binary reference solar cells, which is attributed to more stable morphology in the BHJ layer. Thus, we conclude that doping the third component, PBDTTPD-COOH, gives an effective approach to optimize the compatibility and morphology of D/A materials in the photovoltaic active layer, which leads to better device performance and stability.

[1] M. -A. Pan, T. -K. Lau, Y. Tang, Y. -C. Wu, T. Liu, K. Li, M. -C. Chen, X. Lu, W. Ma, C. Zhan, *J. Mater. Chem. A* **7**, 20713–20722 (2019)

[2] P. Müller-Buschbaum, *Adv. Mater.* **26**, 7692–7709 (2014)

[3] H. Sirringhaus, P. J. Brown ,R. H. Friend, M. M. Nielsen, K. Bechgaard, B. M. W. Langeveld-Voss, A. J. H. Spiering, R. a. J. Janssen, E. W. Meijer, P. Herwig, D. M. de Leeuw, *Nature* **401**, 685–688 (1999)

4.12 Surfactant for surface-defect passivation of perovskite solar cells

Y. Zou, S. Yin, R. Guo, X. Xiao, P. Müller-Buschbaum

Perovskite films are polycrystalline with large grain boundaries, which are processed at relatively low temperatures, unlike single crystalline silicon typically processed at high temperature. However, polycrystalline films also have a large number of structural defects, which trap photogenerated carriers and cause charge recombination. In addition, the defects (e.g., under-coordinated halide anions I^- and metal cations Pb^{2+}) at surfaces (top and bottom) and bulk (including grain boundaries) of perovskite films could induce serious charge carriers recombination centers and restrict the performance of PSCs. The charge recombination caused by the defect states will lead to loss of free carriers. Those loss of free carriers could cause the decrease of the photo-generated voltage, the reduction of long-term stability and the deterioration of the over all performance [1]. Therefore, passivation defects in perovskite films have become an important way to improve the performance and operational stability of PSCs.

Tailoring functional ligands to passivate the defects in perovskite films and interfacial traps has been demonstrated to effectively reduce the energy offset and thus improve the performance of PSCs. In this work, we add a small amount of sodium dodecyl benzene sulfonate into the perovskite solution to improve the performance of PSCs by the synergistic effect of crystallization control and defect passivation. SDBS which is an anionic surfactant, has the molecular structures as shown in figure 4.23. This material can significantly alter the driving force of the fluid caused by the solvent evaporation to suppress the flows for more uniform perovskite films. Surfactant molecules contain both hydrophilic and hydrophobic functional groups. The hydrophilic functional group points to the inside, resulting in a decrease of surface tension between the electron transport layer and the perovskite layer. This decrease of surface tension could further increase the adhesion. The hydrophobic functional group points to the air to resist the infiltration of external moisture, and improve the stability[2]. In addition, SDBS is electrically conductive and facilitates the carriers extracted timely by ETL/HTL. The negatively charged sulfonic acid group can bind to the uncoordinated Pb2+ and inhibit the formation of morphological defects during the processing of the perovskite film[3]. Two functions of the SDBS surfactant can improve film stability by its surfactant property and passivate perovskite defects by its functional groups.

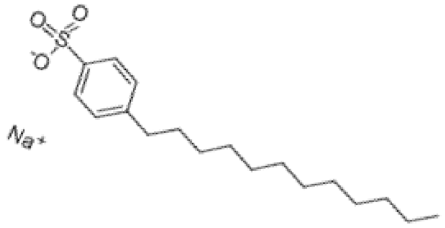

Figure 4.23:
The molecular structures of sodium dodecyl benzene sulfonate (SDBS).

From the SEM images of perovskite thin film (show in figure 4.24), we can observe the particle size has increased. Without adjusting the contrast of SEM images, the surface of the SDBS doped film becomes dark, which could be contributed to the increased conductivity of the perovskite film and a large accumulation of charge.

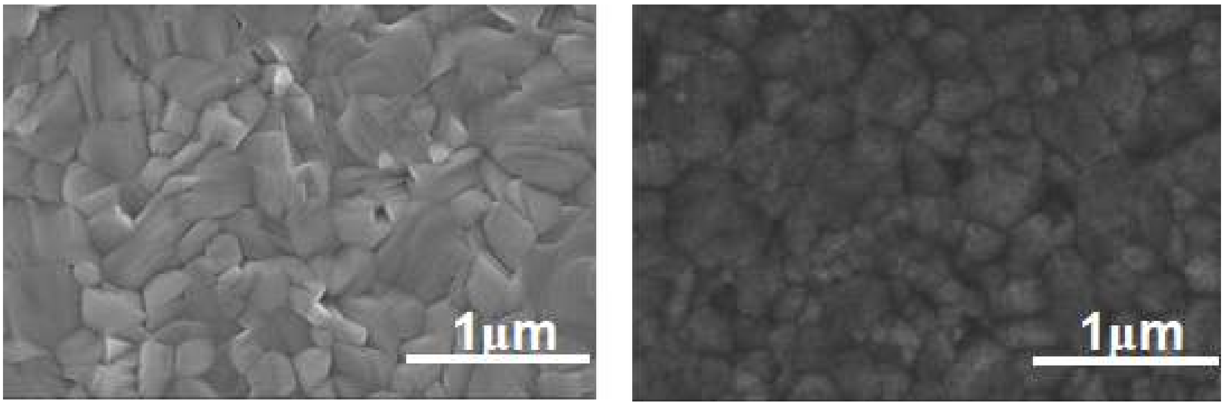

Figure 4.24:
The SEM images of different perovskite thin films: (a) $MAPbI_3$; (b) $MAPbI_3$ with SDBS treated.

In conclusion, SDBS doping can increase the crystal size of the peroskite film and enhance the conductivity of the perovskite films.

[1] X. Zheng Y. Deng B. Chen H. Wei X. Xiao Y. Fang Y. Lin Z. Yu Y. Liu Q. Wang J. Huang *Advanced Materials* **30**, (2018)

[2] Y.o Deng, X. Zheng, Y. Bai, Q. Wang, J. Zhao, J. Huang *Nature Energy* **3**, 560–566(2018)

[3] Y. Lin, B. Chen, Y. Fang, J. Zhao, C. Bao, Z. Yu, Y. Deng, P. Rudd, Y. Yan, Y. Yuan, J. Huang *Nature Communications* **9**, (2018)

5 Polymer-hybrid systems

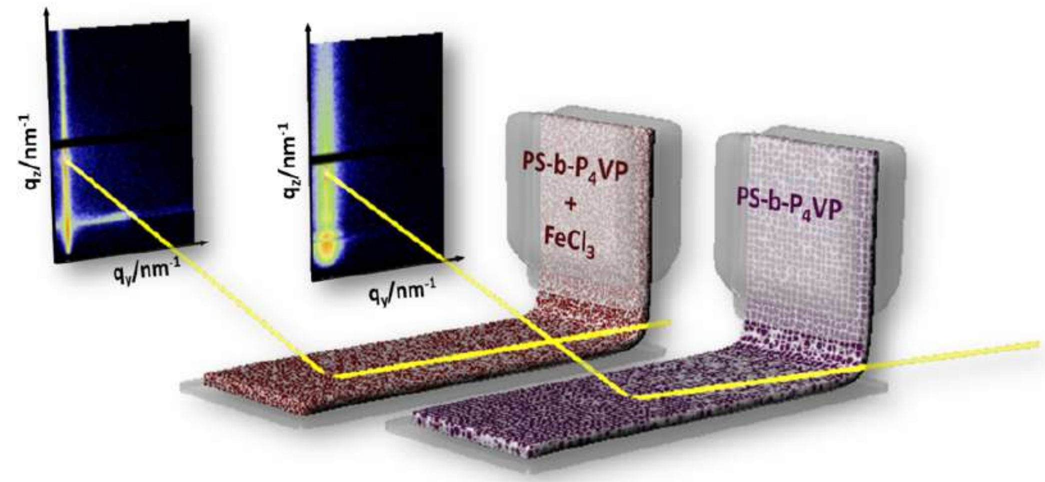

5.1 In situ study of spray deposited ferromagnetic hybrid films containing PS-*b*-PMMA and strontium hexaferrite magnetic nanoplates

W. Cao, S. Yin, M. Plank[1], A. Chumakov[2], C. J. Brett[2], M. Schwartzkopf[2], M. Gallei[3],
S. V. Roth[2,4], P. Müller-Buschbaum

[1] TUD, Darmstadt, Germany
[2] DESY, Hamburg, Germany
[3] UDS, Saarbrücken, Germany
[4] KTH, Stockholm, Sweden

Magnetic hybrid polymer films have attracted increasing research interest for a host of applications that include magnetic sensors and magnetic recording media [1]. Because the hybrid films possess a combined characteristic performance of both (polymers and magnetic nanoparticles), such as light weight, easy fabrication and controllable magnetic properties. In some areas, precise control over the alignment of the magnetic nanoparticles (NPs) is essentially required. Diblock copolymers (DBCs) have proven to be suitable templates for hosting magnetic NPs, due to their ability to form various periodic nanostructures, such as lamellae, cylinders, spheres [2]. So far, most studies have only focused on the superparamagnetic NP-DBC hybrid films, including the final morphology and the formation process of the hybrid films. However, the lack of coercivity in superparamagnetic NPs at room temperature limits their utilization in data storage.

M-type hexaferrite magnetic nanoplates with high magnetic anisotropy and saturation magnetization can be used to obtain high ferromagnetic properties [3]. However, the ferromagnetic properties depend on the alignment of the magnetic nanoplates (magnetic moments). Thus, it is significant to study the kinetic processes during film preparation systematically.

In the present work, spray coating is applied to fabricated ferromagnetic hybrid films from solution precursors containing polystyrene-*block*-poly(methyl methacrylate) (PS-*b*-PMMA) and strontium hexaferrite nanoplates (nanoplates of 50 * 50 * 5 nm^3). The kinetic of the structure evolution during the spray deposition is investigated by in situ small-angle x-ray scattering (GISAXS) measurements.

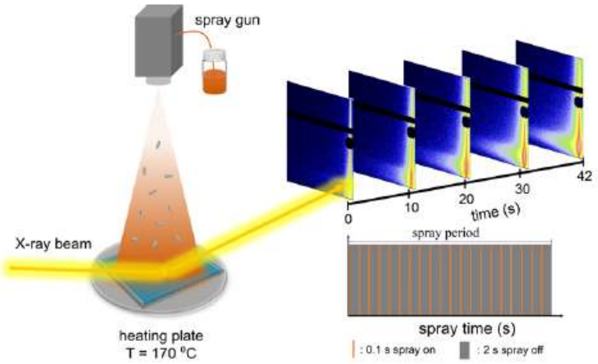

Figure 5.1:
Schematic of the experimental set up used for real-time and in situ GISAXS measurements with simultaneous spray deposition. The spray protocol (0.1 s spray and 2 s wait) is illustrated.

Fig. 5.1 shows the in situ experimental set up used for simultaneous spray coating and GISAXS measurements. The employed spray protocol includes consecutive spray cycles (20 times) and each cycle consists of 0.1 s spray on (spraying) and 2 s spray off (pause). The GISAXS patterns are recorded every 0.1 s during the whole spray process. The substrate is placed on a heating plate with a temperature of 170 °C to ensure rapid drying of the spray-deposited films. As seen from the 2D GISAXS patterns (Fig. 5.1), the overall scattering intensity increases with increasing spray time, which is caused by more magnetic polymer material being deposited on the substrate over time.

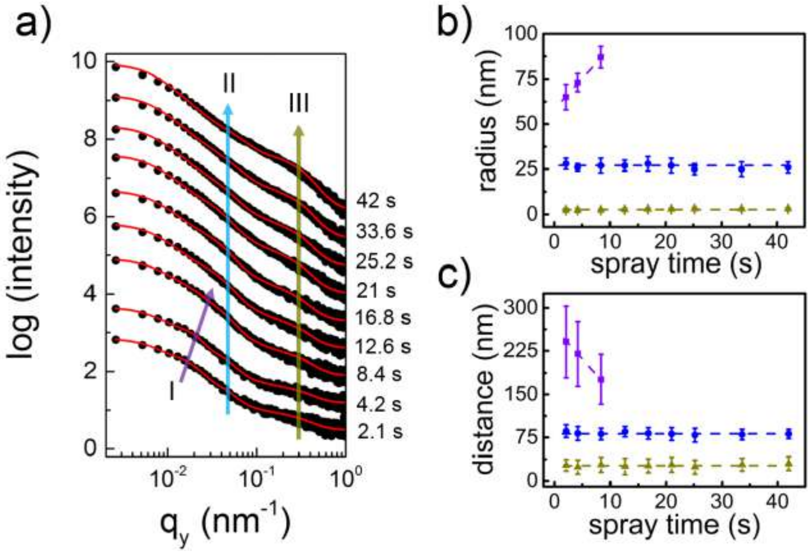

Figure 5.2:
Horizontal line cuts obtained from the 2D GISAXS data for magnetic hybrid films as a function of spray deposition time. The solid red lines represent the fits to the data (black dots). Feature structures extracted from the fits are b) the radius and c) the inter-domain distance of the nanostructures. The dashed lines in b)and c) are guides to the eye.

To gain a quantitative insight into the structure evolution, horizontal line cuts are performed at the Yoneda peak position (2D GISAXS data) and plotted together with the corresponding fits as shown in Fig. 5.2a. Three main characterizations are observed. They are marked with I, II and III, which correspond to the structure of polymer islands, PMMA cylinders (parallel to the substrate according to the AFM measurements) and strontium hexaferrite nanoplates.
In Fig. 5.2a, as the spray time increases, peak I shifts to higher q_y values and vanishes after spray time of 8.4 s. The corresponding average polymer island radius, extracted from peak I, increases from around 65 nm to around 87 nm (Fig. 5.2b), while the inter-domain distance decreases from around 241 nm to around 176 nm (Fig. 5.2c). This indicates a growth of the polymer islands and finally leads to a closed film formation, which is accompanied by more and more material deposition on the substrate. In contrast, peak II, which is ascribed to the structure of PMMA cylinders, stays almost unaltered during the whole spay deposition process. The corresponding average PMMA cylinder radius and inter-domain distance stay constant at around 27 nm (Fig. 5.2b) and 81 nm (Fig. 5.2c), respectively.
Moreover, an additional scattering feature (III) at a high q_y value is seen, which represents the structure factor of the strontium hexaferrite nanoplates. As the spray time increases, peak III stays at a constant q_y value, but becomes more prominent because of an increasing amount of strontium hexaferrite nanoplates on the substrate. The corresponding nanopalte radius stays constant at around 2.8 nm (Fig. 5.2b) and 27 nm (Fig. 5.2c), respectively. This indicates that the nanoplates are arranged in a standing alignment inside the polymer film instead of being randomly distributed. Because GISAXS show the lateral structure inside the film, and the obtained radius (around 2.7 nm) is approximately equal to half the thickness of the nanoplates (around 5 nm). Such alignment of strontium hexaferrite nanoplates can be explained by the unfavorable ratio of PMMA domain size and strontium hexaferrite nanoplate size. The small-sized PMMA cylinders (around 54 nm) do not provide sufficient space for hosting the nanoplates (around 50 nm) in a parallel arrangement.

[1] Y. Zang , F. Zhang , D. Huang , C. Di, D. Zhu, *Adv. Mater.* **27**, 7979-7985 (2015)

[2] S. Xia, L. Song, N. Hohn, K. Wang, S. Grott, M. Opel, M. Schwartzkopf, S. V. Roth, P. Müller-Buschbaum, *Adv. Funct. Mater.* **29**, 1808427 (2019)

[3] L. A. Trusov, A. V. Vasiliev, M. R. Lukatskaya, D. D. Zaytsev, M. Jansend, P. E. Kazin, *Chem. Commun.* **50**, 14581-14584 (2014)

5.2 Morphology investigation of hybrid active layers with TOF-GISANS

V. Körstgens, L. Diaz Piola, C. Geiger, J. Heger, L. Kreuzer, T. Widmann, M. Nuber[1], K. Stallhofer[1], H. Iglev[1], R. Kienberger[1], G. Mangiapia[2], P. Müller-Buschbaum

[1] LS Laser- und Röntgenphysik, TU München, Garching, Germany
[2] MLZ, Garching, Germany

One approach in the emerging field of photovoltaics is the concept of water-processed hybrid solar cells. Here the use of harmful or toxic materials is avoided in the production of devices. The fabrication process is also very efficient in terms of energy demand and costs. These solar cells consist, on the one hand, of a water-soluble, polythiophene which acts as a donor in the active layer. On the other hand TiO_2-nanoparticles are used, which serves as an electron acceptor in the cell. Thus advantages of both organic and inorganic materials are combined. The organic material provides high absorption and flexibility, while the inorganic part provides good conductivity and stability [1]. From the processing perspective, continuous ongoing research is devoted to combine roll-to-roll (R2R) compatible deposition techniques for solution-processed photovoltaics, which allows for fast fabrication of thin films that can be produced at large scales and at a low cost. Therefore, here two different R2R-compatible deposition methods are used: spray and slot die coating [2, 3]. To study the morphology of the active layers produced over large sample areas, Time-of-Flight Grazing Incidence Small Angle Neutron Scattering (TOF-GISANS) is used at the Refsans instrument of MLZ, Garching [4]. The scattering technique allows to obtain statistically relevant information on surfaces and buried structures of thin films. The Time-of-Flight mode, additional to the well-established GISANS technique, allows to obtain scattering patterns at different wavelength bands in one single experiment. Several studies have demonstrated this technique to be a powerful tool to study nanostructured systems for energy applications [2].

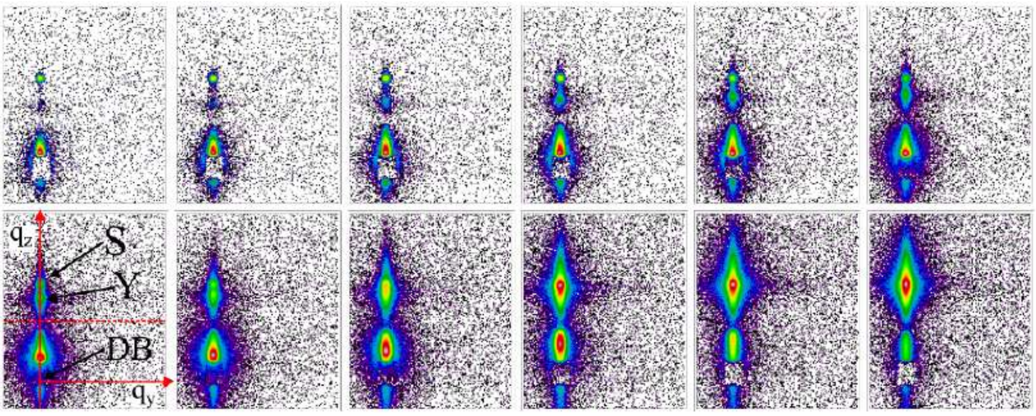

Figure 5.3:
Selected 2D GISANS data of the sprayed TiO2:P3P6T thin film obtained in the TOF-GISANS measurement. From left to right and from top to bottom the wavelengths are: 4.03, 4.45, 4.92, 5.44, 6.01, 6.65, 7.35, 8.12, 8.97, 9.92, 10.96, 12.12 and 13.39 $\AA$. The red arrows show the q_z and q_y directions. The specular peak (S), Yoneda peak (Y) and direct beam (DB) are marked with arrows.

The detector images for the sample prepared via spray coating is shown in Fig.5.3, with the q_z and q_y axis directions shown schematically with red arrows. The main features of the detector images are: the direct beam (DB) shielded by a beam stop to avoid saturation, the material characteristic Yoneda peak (Y) and the specular peak (S) at $\alpha_f = \alpha_i$. In order to obtain information about the film structure in the direction perpendicular to the substrate, in-plane cuts at $q_y = 0$ are performed for selected wavelengths, shown in Fig.5.4.

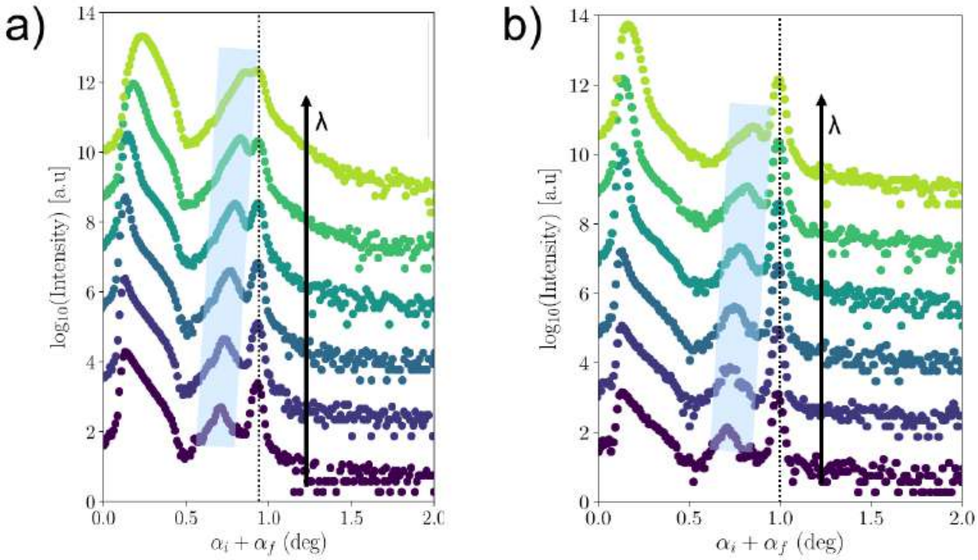

Figure 5.4:
Vertical cuts around $q_y = 0$ for selected wavelengths λ for (a) sprayed sample and (b) slot-die-coated sample.

Between the sample horizon and the specular peak, the Yoneda peak shifting towards the specular peak for increasing wavelength appears, and it is highlighted in a blue region. From these wavelengths the critical angle and consequently the scattering length density (SLD) of the material can be extracted. The Yoneda peaks for the two different samples are clearly seen, making the determination of the material SLD straightforwardly possible from the data. To obtain its value Gaussian fits are performed around the Yoneda region (blue shaded in Fig.5.4). Once the Yoneda peaks are determined consistently, the SLD of the material for the two deposition techniques can be obtained by plotting the critical angle against the wavelength of each TOF-GISANS channel. This allows to compare the obtained SLD of the mixed material with the SLD coming from the polymer P3P6T and titania nanoparticles separately and therefore the mixing ratio can be determined. The experimentally determined SLD yields a volume ratio for the sprayed sample, which is in very good agreement with the initially as-prepared volume ratio. On the other hand, for the slot-die coated sample the experimental value differs significantly from the as-prepared solution value. This difference implies less content of titania nanoparticles within the polymer matrix. To obtain information about lateral structures inside the probed film, horizontal line cuts in q_y direction are performed. Quantitative information about the size of the scattering objects and their nearest neighbor distances is obtained. Here two spherical form factors as scattering objects are used to fit the data, and their center-to-center distances are assumed to be distributed on a 1D paracrystal lattice. The structural sizes obtained for the bulk films are in agreement with the surface morphology observed with SEM.

[1] V. Körstgens, S. Pröller, T. Buchmann, D. Mosegui González, L. Song, Y. Yao, W. Wang, J. Werhahn, G. Santoro, S. V. Roth, H. Iglev, R. Kienberger, P. Müller-Buschbaum, *Nanoscale* **7**, 2900-2904 (2015)

[2] K. Wang, N. Hohn, L. Kreuzer, T. Widmann, M. Haese, J.-F. Moulin, P. Müller-Buschbaum, *ACS Appl. Mater. Interfaces* **11**, 10998-11005 (2019)

[3] K. Wienhold, V. Körstgens, S. Grott, X. Jiang, M. Schwartzkopf, S. V. Roth, P. Müller-Buschbaum, *ACS Appl. Mater. Interfaces* **11**, 42313-42321 (2019)

[4] J.-F. Moulin, M. Haese, *JLSRF* **1**, 1-3 (2015)

5.3 Synthesis of highly ordered mesoporous germanium oxide thin films oriented by amphiphilic diblock copolymer

S. Liang, S. Yin, M. Schwartzkopf[1], S. V. Roth[1,2], P. Müller-Buschbaum

[1] DESY, Hamburg, Germany
[2] KTH, Stockholm, Sweden

Germanium oxide (GeO_2), as a kind of semiconductor material, has been applied in various fields, including electronic, optical, and optoelectronic devices[1]. In recent years, GeO_2 is regarded as a promising alternative anode material for lithium-ion batteries due to its high theoretical capacity (2152 mAh g^{-1}). However, GeO_2 suffer from volume expansion during charge and discharge, leading to a rapid capacity fading. Creating hollow or porous structure is an effective strategy to improve cycling stability of GeO_2 anodes, because it can provide enough void space to accommodate volume changes of GeO_2.

Amphiphilic block copolymers (ABC) have been widely utilized as surface modification agents by constructing nanoscale architectures on various substrates through evaporation induced self-assembly processes[2]. Polymer/inorganic nanocomposites can be obtained via a microphase separation process in mixture solution of mixing block copolymer and precursor of metal oxide. In this work, PS-b-PEO, 1,4-dioxane, and germanium ethoxide are selected as the block copolymer template, solvent, and Ge precursor, respectively. Additionally, concentrated HCl solution acts as a poor solvent for the PS block, leading to the formation of micelles in solution because of increased interfacial energy between the PS block and the solvent. Firstly, PS-b-PEO was dissolved into 1,4-dioxane under continuous stirring. Then, germanium ethoxide and HCl solution were added into the solution successively. After sufficient stirring, hybrid GeO_2/polymer composite thin films were prepared by spin coating the stock solution on silicon wafers. After removing the block copolymer by calcination, mesoporous GeO_2 thin films were obtained. In order to investigate the effect of copolymer concentration on the final morphology, we fabricated four parallel samples with different concentration of PS-b-PEO in 1,4-dioxane.

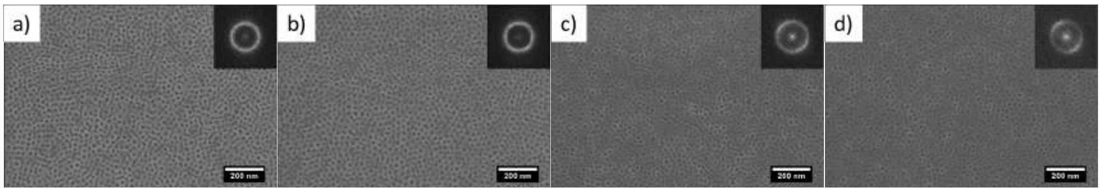

Figure 5.5:
SEM images of the GeO_2 thin films with different concentration of PS-b-PEO in 1,4-dioxane, corresponding to a) 0.125 wt%,b) 0.167 wt%, c) 0.250 wt%, and d) 0.500 wt%, respectively. The up-right insets of the images refer to the corresponding FFT patterns.

Fig.5.5 shows the surface morphologies of the as-prepared GeO_2 thin films with different concentration of PS-b-PEO in 1,4-dioxane. All four samples exhibit porous structure due to the template effect of block copolymer. The second sample (Fig.5.5b) has the most regular porous structure among these samples, which could be attributed to the appropriate concentration of the block copolymer in solvent. The lower concentration can not provide enough micelles to form separated pores, leading to formation of some connected long pores, as presented in Fig.5.5a. However, when the concentration increases, the excess copolymer could form aggregated micelles, leading to bulk structures in the samples (Fig.5.5c and Fig.5.5d). The order degree of porous structures in these samples can also be reflected by the FFT patterns.

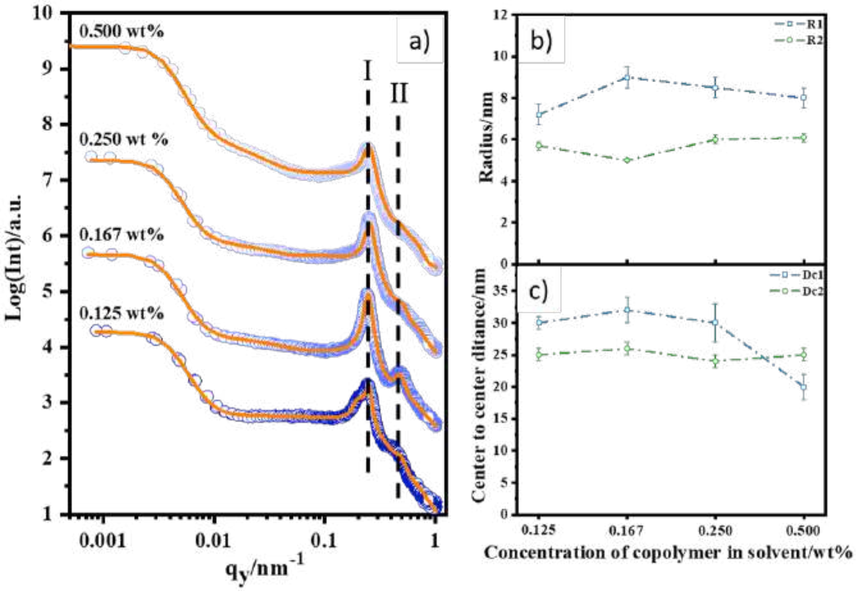

Figure 5.6:
a) Horizontal line cuts of the 2D GISAXS data. The measured data are plotted as hollow circles and the fitting results are shown as solid lines, respectively. All curves are shifted along the intensity axis for clarity of presentation. Extracted structure radius b) and center-to-center distances c) as a function of the concentration of copolymer in solvent. Different color refer to the different size of the structure.

In order to investigate the inner and large-scale morphology, grazing incidence small angle X-ray scattering (GISAXS) were measured for these samples[3]. For quantitative analysis, the horizontal line cuts performed at the Yoneda peak position of GeO_2 as well as the corresponded fitting results are all plotted in Fig.5.6a. Fig.5.6a depicts the peaks marked as I and II by black dash lines. With the strongest intensity, peak I represents the first-order Bragg peak which is originated from the ordered porous structures within GeO_2 thin films. The position of peak I and peak II are observed as q_y = 0.246 nm^{-1} and q_y = 0.481 nm^{-1}, respectively. The ratio of the q_y values is 0.511 (close to $1/\sqrt{3}$), indicating the existent of hexagonally packed structures inside the films. Particularly, the second sample (0.167 wt%) exhibits the highest intensity of peak II among these samples, which means it has the most regular hexagonally packed structure. This is consisted with the results of SEM measurement. All line cuts are fitted within the framework of the Distorted-Wave Born Approximation (DWBA). All data are fitted with two form factors (radius) and two structure factors (center-to-center distance), and extracted results are presented in Fig.5.6b and Fig.5.6c. The peak I (Fig.5.6a) at high q range are well fitted with smaller radius and center-center distances (green circles in Fig.5.6b and 5.6c). As for this smaller structure of all samples, both fitted radius and center-to-center distances are quite close, as about (6 ± 0.5) nm and (25 ± 1) nm, respectively. Besides, the larger radius and center-center distances (blue circles in Fig.5.6b and 5.6c) are related to the peak II at low q range in Fig.5.6a. When the concentration of copolymer in solvent increases to 0.500 wt%, the fitted center-to-center distance decreases to (21 ± 1) nm, which could be attributed to the aggregation inside the sample during sol-gel process.

[1] G. Xiao, Y. Wang, J. Ning, Y. Wei, B. Liu, W. Yu, G. Zou, B. Zou, Q. Zhong, *RSC. Adv.* **22**, 8104-8130 (2013)

[2] Y. Cheng, J. Gutmann, *J. Am. Chem. Soc.* **128**, 4658-4674 (2005)

[3] P. Müller-Buschbaum, *Adv. Mater.* **46**, 7692-7709 (2014)

5.4 Highly ordered titania films with incorporated germanium nanocrystals used as photoanodes

N. Li, J. E. Heger, R. Schaffrinna, P. Müller-Buschbaum

Nanostructured titania films have attracted great attention due to their non-toxicity, low cost and morphology controllability, etc.[1] These advantages enable them successful application in many fields, such as, photocatalysis, lithium-ion batteries and photovoltaics.[2] Especially, anatase titania with interconnected network structures as well as a high surface-to-volume area is desirable as an electron transport layer in solid-state dye-sensitized solar cells (ssDSSCs) and hybrid solar cells. Until now, ssDSSCs based on interpenetrating titania networks can reach up to 11.9%.[3] Also, impressive efficiency of 25.2% has been achieved in the perovskite solar cells.[4] However, these advances all closely depend on the evolution of a superior sensitizer (dye molecules, quantum dots, perovskite-sensitized) or a hole-transporting material. Only a few researches exist targeting whether tailoring the titania could further improve the photovoltaic device performance. For example, Song et al. obtained more efficient titania photoanodes via incorporating with a presyntheised crystalline titania nanoparticles. Duan et al. designed TiO_2/GeO_2 nanocrystallite anodes with an attempt to increase the photogenerated electron density in the conduction band of the titania nanocrystallites and interference light intensity.[5] In this study, we introduce dodecyl functionalized germanium nanocrystals (GeNCs) with a size of about 7-9 nm into the titania films to obtain TiO_2/GeNC composite films for a better solar cell efficiency.

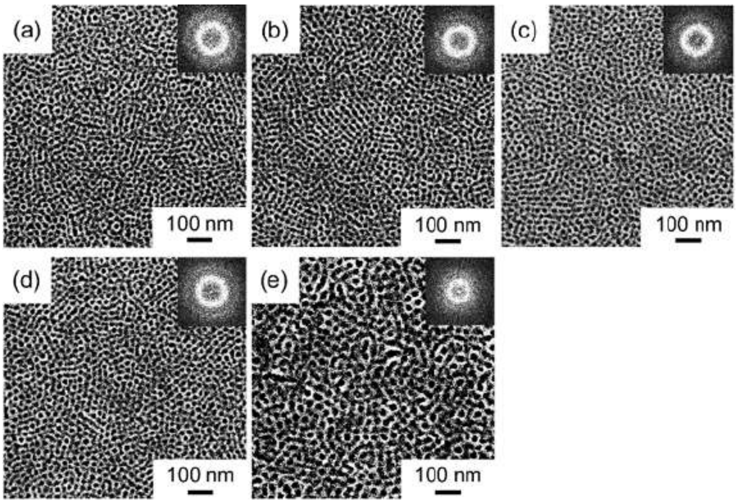

Figure 5.7:
SEM images of the mesoporous TiO_2/GeNCs films after calcination in argon: (a) 0 wt%, (b) 0.5 wt%, (c) 1.0 wt%, (d) 2.5 wt% and (e) 5.0 wt%.

Therefore, different weight percent of GeNCs is employed into the sol-gel solution, which consists of a titania precursor and a diblock copolymer PS-b-PEO template. During calcination in argon, the templating block copolymer is combusted as well as the organic ligands on the surface of GeNCs. Finally, mesoporous TiO_2/GeNC composite films are obtained. Resulting surface and inner morphology changes are investigated by scanning electron microscopy (SEM) and grazing incidence small-angle X-ray scattering (GISAXS), respectively. The crystalline properties and elemental composition of the TiO_2/GeNC composite films are observed via X-ray diffraction (XRD), transmission electron microscopy (TEM) and X-ray photoelectron spectroscopy (XPS), respectively. The optical properties are investigated by ultraviolet–visible spectroscopy (UV-Vis). Through the incorporation of GeNCs with varied weight percent, the optimized morphology and properties of TiO_2/GeNC composite films correlated with the photovoltaic performance will be studied, providing a promising candidate for solar cell photoanodes.

Fig. 5.7 shows the SEM images of TiO_2/GeNC films after calcination in argon. All the films shows foam-like structures, which benefit for the charge carrier transport. The film without GeNCs (0 wt% GeNCs) features ordered titania arrays with a titania wall of about 9 nm and uniform mesopores of around 15 nm in diameter (Fig. 5.7a). With increasing the amount of pre-synthesized nanocrystals, the titania wall-thickness and pore sizes in 0.5 wt% GeNCs, 1.0 wt% GeNCs and 2.5 wt% GeNCs are similar to that in 0 wt% GeNCs. A further increase of the amount of nanocrystals to 5.0 wt% induces an obvious change of the film morphology. The titania nanostructures possess an unchanged wall (9 nm), but with arise in pore sizes up to around 24 nm. To follow the evolution of structural order, two-dimensional fast Fourier transform (2D-FFT) patterns are extracted from the SEM images. A second-order ring appears in FFT pattern for all the samples, except the sample with 5.0 wt% GeNCs. It indicates the loss of order, which might because more GeNCs deteriorate the morphology regularity.

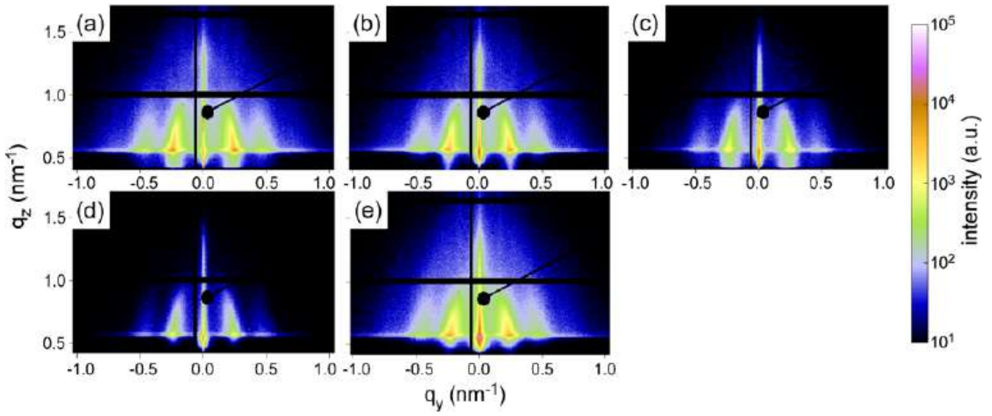

Figure 5.8:
2D GISAXS patterns of the mesoporous TiO_2/GeNCs films after calcination in argon: (a) 0 wt%, (b) 0.5 wt%, (c) 1.0 wt%, (d) 2.5 wt% and (e) 5.0 wt%.

To gain more insights about the inner morphologies, GISAXS measurements are performed to quantify the size of nanostructures and pores inside the TiO_2/GeNC films after calcination in argon. The strong vertical Bragg rods in Fig. 5.8a-e imply highly ordered lateral structures existing in all the films. This result is in good agreement with the corresponding SEM images in Fig. 5.7.

[1] S. Haque, M. J. Mendes, O. Sanchez, H. Águas, E. Fortunato, H. Águas, *Nano Energy* **59**, 91 (2019).

[2] H. Lv, N. Li, H. Zhang, Y. Tian, H. Zhang,X. Zhang, H. Qu, C. Liu, C. Jia, *Sol. Energy Mater. Sol. Cells* **150**, 57 (2016).

[3] Y. Cao, Y. Saygili, A. Ummadisingu, J. Teuscher, J. Luo, N. Pellet,F. Giordano, S.M. Zakeeruddin, *Nat. Commun.* **8**, 1 (2017).

[4] N. Park, *Adv. Energy Mater.* **1903106**, 1 (2019).

[5] Y. Duan, Q. Tang, Z. Chen, B. He, H. Chen, *J. Mater. Chem. A* **12459**, 2 (2014).

5.5 Synthesis of Mesoporous titania by using PS-b-P4VP as template block copolymer: Fabrication and Analysis

M. Spyranti[1], N. Li, S. J. Schaper, P. Müller-Buschbaum
[1] Aristotle University of Thessaloniki, Greece

Because of the chemical and optical stability, excellent photoelectronic and photochemical properties, non-toxicity and low cost, mesoporous titania films have received great research interest in a wide variety of fields, such as photovoltaics, gas sensing, photocatalysis and Li-ion batteries. An optimal mesopore size of the nanostructured titania film plays a significant role in the device efficiency improvement [1-3].

In this work it has been used the bottom up approach of sol-gel synthesis to fabricate titanium oxide films. Diblock copolymer templating combined with sol-gel chemistry is a well known and powerful tool to obtain unique titanium dioxide nanostructures. For the thin film preparation as a template the diblock copolymer polystyrene-b-poly(4-vinylpyridine) (PS-b-P4VP) is used to define the structure and titanium tetra isopropoxide (TTIP) as the precursor. The amphiphilic block copolymer PS-b-P4VP undergoes phase separation and self-assembly due to a good-bad solvent pair, namely N,N-dimethylformamide (DMF) and acetic acid (CH_3COOH). By adjusting the weight ratio of TTIP and annealing time, the mesoporous sponge-like titania films are obtained after template removal by calcination at 550 °C for 2 h. As a result mesoporous titanium dioxide thin films are obtained, which are especially useful for photovoltaic applications.

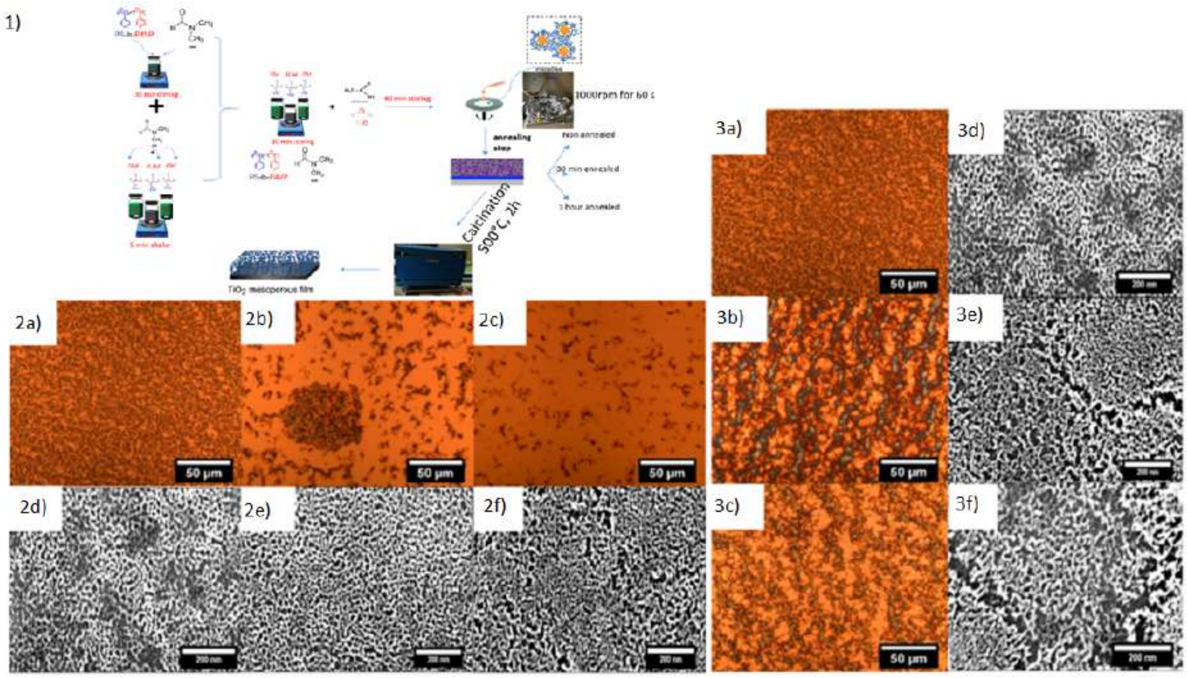

Figure 5.9:
Sol-gel synthesis to fabricate mesoporous titanium dioxide thin films by changing the TTIP weight ratio and annealing time 1). Scanning electron and optical microscopy images of sol-gel synthesized mesoporous titanium dioxide thin films changing the amount of TTIP 2) and changing the annealing time 3). The precursor to template ratio is decreased from left to right and the annealing time is increased up to bottom.

Initial characterization is carried out via scanning electron microscopy (SEM) and optical microscopy (OM) images of the surface morphology can be seen in Figure 5.9. The SEM pictures present promising structure for all different precursor concentrations (Figure 5.9 2d, 2e, 2f). On the other hand there are cracks as the annealing time increases (Figure 5.9 3d, 3e, 3f).

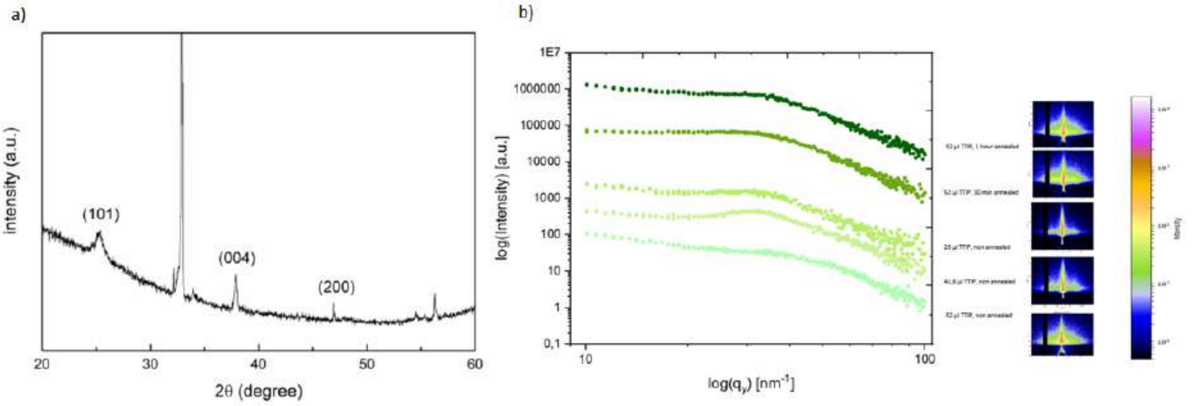

Figure 5.10:
Characterization of mesoporous titanium dioxide thin films via a) X-ray diffraction and b) grazing incidence small angle X-ray scattering.

To confirm if a similar behavior can be found in the bulk of the thin film the inner morphology is explored by grazing incidence small-angle X-ray scattering (GISAXS) [4]. Furthermore, the anatase phase of the crystalline titania films is verified by X-ray diffraction [5]. The measurements have been performed using a Ganesha SAXSLAB instrument with a wavelength of 1.54 Å, a sample-detector distance of 1056.2 mm and an incidence angle of 0.4°. Horizontal cuts have been performed at the material specific Yoneda peak position and the respective cuts are depicted in Figure 5.10. Finally, the mesoporous titanium dioxide thin films have been analyzed via X-ray diffraction (XRD) measurements to ensure suitability for photovoltaic applications. Within this frame an anatase phase has been found as depicted in Figure 5.10a).

In conclusion, it is noticeable that the structure changes with different TTIP amount and not by changing the annealing time, which is in good agreement with the observed surface behavior via SEM and OM. The material is found very promising for photovoltaic applications.

[1] Y. Deng, J. Wei, Z. Sun, D. Zhao, *Chem. Soc. Rev.* **42**, 4054 (2013)

[2] J. Szeifert, D. Fattakhova-Rohlfing, D. Georgiadou, V. Kalousek, J. Rathousky, D. Kuang, S. Wenger, S. Zakeeruddin, M. Gratzel and T. Bein, *Chem. Mater.* **21(7)**, 1260 (2009)

[3] C. Stegelmeier, A. Exner, S. Hauschild, V. Filiz, J. Perlich, S. Roth, V. Abetz, S. Forster, *Macromolecules* **48(5)**, 1524 (2013)

[4] Y. Yoneda, *Phys. Rev.* **131(5)**, 2010 (1963)

[5] R. Lazzari, *J. Appl. Crystallogr.* **35(4)**, 406 (2002)

5.6 Printed ZnO mesostructure templated by amphiphilic diblock copolymer

T. Tian, M. Schwartzkopf[1], S. V. Roth[1,2], P. Müller-Buschbaum

[1] DESY, Hamburg, Germany
[2] KTH, Stockholm, Sweden

ZnO has received much attention over the past few years because it has a wide range of properties, including a range of conductivity from metallic to insulating (including n-type and p-type conductivity), high transparency, piezoelectricity, wide-bandgap semiconductivity, room-temperature ferromagnetism, and chemical-sensing effects.[1] As a n-type semiconductor, ZnO, has several potential advantages over TiO_2 such as better electron mobility and low crystallization temperature. In order to improve the photovoltaic performance of ZnO-based devices, an interconnected mesoporous inorganic nanostructure is favorable, which can provide a high surface-to-volume ratio for exciton separation within their lifetime and a good pathway for charge carrier transport. To fabricate the mesoporous inorganic ZnO semiconductors, various methods can be employed, such as chemical vapor deposition, wet chemical method, hydrothermal synthesis and etc. Among these methods, diblock copolymer assisted sol-gel approach has been corroborated by countless reports to be powerful in morphology tunability. Typically, block polymers can phase separate into different morphologies including cylinderical, spherical, lamellar, and gyroid domains by controlling the characteristic parameters.[2] In this respect, the deposition methods play an important role in producing nanoporous networks as well. Compared to laboratory-scale techniques such as spin coating, industrial-coating process, in particular printing, is more applicable for large scale production.[3] However, the printing process is essentially different due to its complicated kinetics caused by solvent evaporation induced self assembly. For a better understanding of morphology evolution of the involved mesopores formation processes, inner morphology observation is of great importance but also constitute a major experimental challenge in the photovoltaics research. To this end, the amphiphilic diblock copolymer assisted sol-gel method and suitable printing parameters were used to fabricate the nanostructured ZnO films, and the grazing-incidence small-angle X-ray scattering (GISAXS) was applied to probe the inner film morphology without intervening the film formation process or impairing the printed films. Additionally, the investigation of pure diblock copolymer film was conducted to investigate how the template direct the inorganic ZnO nanoparticles assembly.

Panels Fig. 5.11a and Fig. 5.11b show SEM images of the surface of such a printed film after polymer extraction. The ZnO film exhibits a high interconnectivity of the foam-like pores, which suggests the presence of good percolation paths through the 3D ZnO structure. The amphiphilic diblock copolymer PS-b-PEO introduces a micro-phase separation in the sol-gel system and therefore enables control of the ZnO nanostructure and formation of a foam-like structure. As optical microscopy (OM) images demonstrated in Fig. 5.11c and Fig. 5.11d, the surface of printed mesoporous ZnO film appear as homogeneous as the spin coated reference sample. This observation, associated together with the low-magnification SEM images of printed film, indicates that slot die coating can be a promising method for large scale production without destroying specific morphologies.

For the mesoporous ZnO films, not only the surface morphologies are of significance, but also the inner structures need to be probed since they are of especial importance for pore structure investigations. In general, GISAXS is a well-suited method to detect nanostructures within a macroscopic region inside thin films, which gives statistically relevant information. The two-dimensional (2D) GISAXS data of films printed with different solution component are

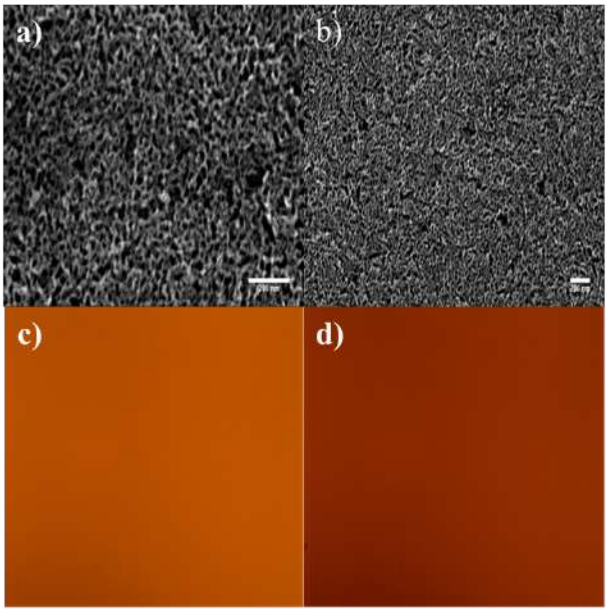

Figure 5.11:
SEM images: a) The high-magnification and b) low-magnification SEM images of printed mesoporous ZnO films after template removal; OM images of mesoporous ZnO films fabricated by different deposition method c) printing d) spin coating.

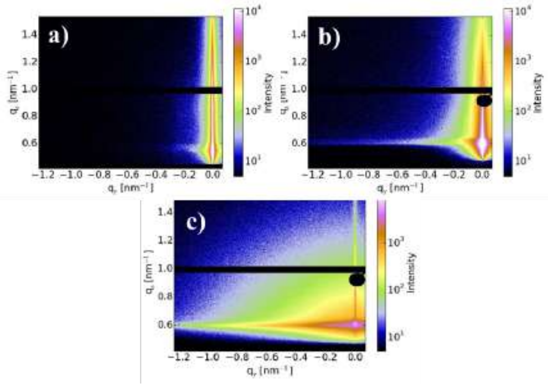

Figure 5.12:
2D GISAXS data a) pure PS-b-PEO polymer film b) PS-b-PEO templated ZnO composite film and c) mesoporous ZnO films after template removal.

shown in Fig. 5.12. As seen in the 2D data, a maximum intensity is observed which originates from the material-dependent Yoneda peak. In the lateral direction, a characteristic scattering signal from the PS-b-PEO nanostructure can be observed in the Fig. 5.12a. As compared to the reference pure polymer film, the hybrid films display a much stronger intensity along the q_y direction, which is caused by the presence of the ZnO. After calcination process, only a characteristic scattering signal from the ZnO nanostructure occurs, indicating that polymer is completely burned off and thus only ZnO nanostructure is reserved.

[1] L. Schmidt-Mende, J. L. MacManus-Driscoll, *Mater. Today.* **10**, 40-48 (2007)

[2] K. Sarkar, M. Rawolle, E. M. Herzig, W. J. Wang, A. Buffet, S. V. Roth, P. Müller-Buschbaum, *Chem. Sus. Chem.* **6**, 1414-1424 (2013)

[3] F. C. Krebs, *Sol. Energ. Mat. Sol. C.* **93**, 394-412 (2009)

5.7 Investigation of polymer templated silicon-germanium nanostructures

C. L. Weindl, M. A. Giebel[1], T. F. Fässler[1], P. Müller-Buschbaum

[1] TUM Chemie, Garching, Germany

Latest research in the field of hybrid photovoltaics focuses on the benefits of inorganic and organic materials. Flexibility, low cost and large-scale production are the most valuable properties of organic components whereas the inorganic components add chemical and physical stability. In this field, two characteristic pathways have formed. One area of interest is hybrid photovoltaics which contain silicon (Si) as light-harvesting material in combination with organic polymers as an electron/hole conducting layer. [1,2] Also multi-junction cells are possible with power conversion efficiencies up to 13 %. [3] Germanium (Ge) and Si are also in the focus of research as anode materials for Li-ion batteries. Even in those materials, these additional elements show their positive effects, like excellent lithium-ion diffusivity for Ge or mechanical support and enhanced electron conductivity for Si. [4,5,6]

For further studies in this field the amphiphilic diblock copolymer polystyrene-block-polyethylene oxide (PS-b-PEO) is used as a structuring agent. The precursor powder, where Si and Ge are bound in a Zintl-phase with Potassium $K_{12}Ge_5Si_{12}$, and the polymer are dissolved in ethylenediamine (en). After stirring for more than 24 hours and filtering the precursor blend, the stock solutions are intermixed. Owing to an aggregation of the Zintl-clusters around the PEO block a microphase separation emerges in the solution. After spin casting and drying overnight the nanostructure is formed. To improve this microphase separation a solvent vapor annealing (SVA) process is followed by this procedure. Here a constant nitrogen flow through the solvents 1-butanol (dissolves the PS block) and toluene (dissolves both blocks) provide a saturated atmosphere for the thin film. As a result, the applied solvent results in a higher degree of phase separation in the thin film (see figure 5.13).

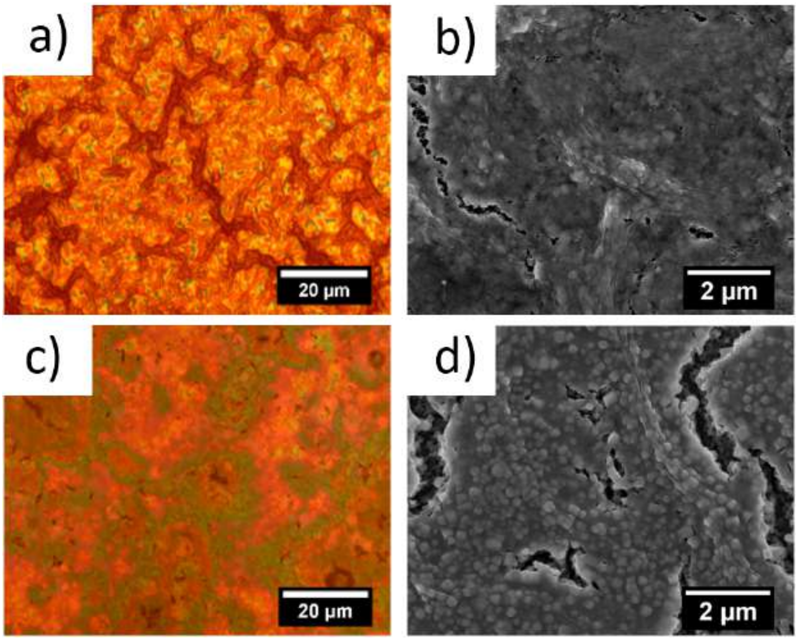

Figure 5.13:
Optical Microscopy images (a,c) and scanning electron microscopy images (b,d) of thin films on silicon without (a,b) and with (c,d) solvent vapor annealing process.

The optical microscopy images of the thin films show for the non-SVA processed substrates an additional surface topography (see figure 5.13). This microstructure is disadvantageous for the Si/Ge tetra-chloride treatment (Si/Ge-Cl_4). Due to the appearance of Potassium (K) there can be more Si or Ge implemented into the nanostructure by forming the salt KCl. During this 12 h treatment $SiCl_4$ or $GeCl_4$ are incorporated over a gas phase into the thin film. This results in the before mentioned salt cubes (see figure 5.13 b), d)). The following step manages the removal of the organic structure agent by calcination. Here the substrates are heated with a constant rate to 600 °C. After removal of all organic materials, the remaining salt KCl can be washed out via tetrahydrofuran (THF) and dimethyl sulfoxide (DMSO) wash successively. Each substrate is immersed for 30 minutes. Finally, a porous foam-like structure is formed as depicted in figure 5.14.

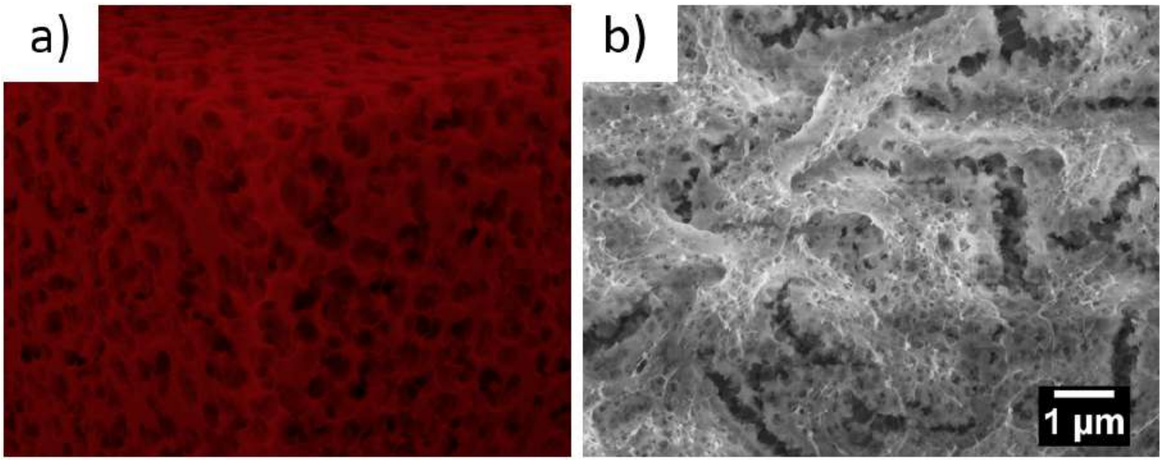

Figure 5.14:
a) Assumed structure after calcination and salt removal as well as b) measured surface morphology of the thin film is probed with SEM

Compared to bulk geometry, this structure shows a significant higher surface to volume ratio, which plays a key role for device performances. Unfortunately, the conductivity of this film is not in the range of the raw Si or Ge. Although the sample preparation is under nitrogen atmosphere SiO_x can be formed during the calcination process which may be the origin of the increased ohmic resistance. To get convincing electronic properties the oxides can be removed by hydrofluoric acid, which is a standard treatment in inorganic semiconductor manufacturing. The final step will be the optimization of the pore sizes, which will be a compromise between the ability of backfilling and exciton diffusion length. With pores of 10 nm, the charge carrier separation of the polymer would be in a reasonable range whereas this size would lead to a poor backfilling efficiency. As a reason, grazing incidence X-ray scattering (GIXS) will be the dominant measurement technique to investigate the inner morphology and receive information about the crystallinity. [7]

[1] S. Avasthi, S. Lee, Y.L. Loo, J.C. Sturm, *Advanced materials* **23(48)**, 5762-5766, (2011)

[2] F. Zhang, B. Sun, T. Song, X. Zhu, S. Lee, *Chemistry of Materials* **23(8)**, 2048-20905,(2011)

[3] H. Tan, A. Furlan, W. Li, K. Arapov, R. Santbergen, M.M. Wienk, R.A. Janssen, *Advanced Materials* **28(11)**, 2170-2177, (2016)

[4] X. Suo, Q. Wu, J. Li, X. Xiao, A. Lott, W. Lu, J. Wu, *Advanced Energy Materials* **4(1)**, 1300882 (2014)

[5] L.F. Cui, Y. Wang, C.M. Hsu, Y. Cui, *Nano letters* **9(9)**,3370-3374, (2009)

[6] G. Cui, L. Gu, L. Zhi, N.V. Kaskhedikar, P.A. van Aken, K. Müllen, J. Maier, *Advanced Materials* **20(16)**, 3079-3083 (2008)

[7] P. Müller-Buschbaum, *A Basic Introduction to Grazing Incidence Small-Angle X-Ray Scattering* in M. Gomez, A. Nogales, M. Garcia-Gutierrez, T. Ezquerra, *Applications of Synchrotron Light to Scattering and Diffraction in Materials and Life Sciences*, *Springer*, **vol 776.**, (2009)

6 Real-time characterizations

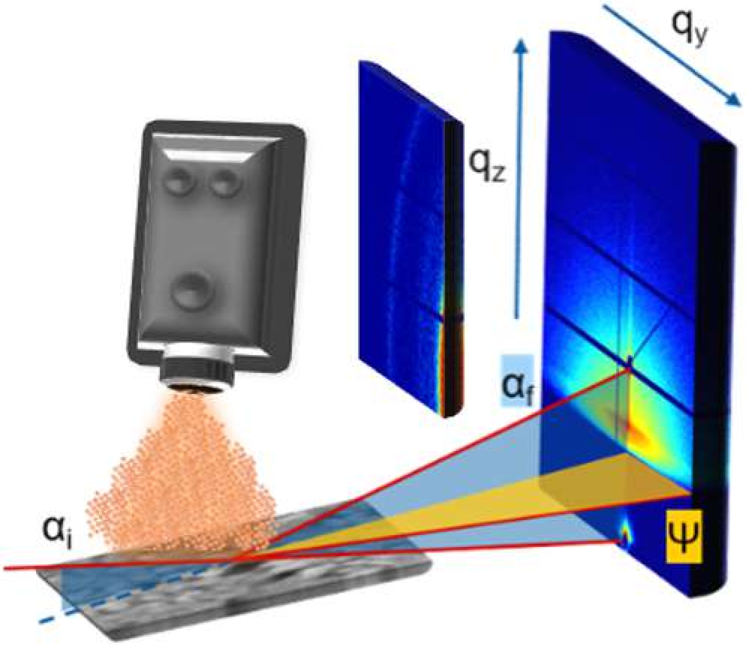

6.1 Investigation during *in situ* slot die coating deposition of TiO_2:P3P6T using grazing incidence X-ray scattering techniques

L. Díaz Piola, V. Körstgens, K. Stallhofer[1], M. Nuber[1], M. Scheel, N. Li, W. Chen, M. Schwartzkopf[2], P. Müller-Buschbaum

[1] Lehrstuhl für Laser- und Röntgenphysik E11 (TUM), Garching, Germany
[2] DESY, Hamburg, Germany

In new generation photovoltaics, not only high efficiencies and long term stability are relevant, but also the sustainability of the overall processing. Following an environmentally friendly pathway, here water is used as the only solvent to process the active layer for hybrid inorganic-organic solar cell applications. As inorganic material, titanium dioxide (TiO_2) nanoparticles treated by laser ablation are used, which are mixed with the water-soluble polymer poly[3-(potassium-6-hexanoate)thiophene-2,5-diyl (P3P6T). From the processing perspective, continuous ongoing research is also devoted to combine roll-to-roll (R2R) compatible deposition techniques for solution-processed photovoltaics, which allows for fast fabrication of thin films that can be produced at large scales and at a low cost. To this end, here slot die coating is used as deposition technique. It is well known that the morphology of the active layer is a key factor that greatly influences the ultimate performance of solar cells [1]. However, less is known about the general picture leading to a final dry film from solution. In order to follow experimentally the film drying process, real space techniques are typically not suited for in situ structural studies. To overcome the inherent challenges of real space characterization, X-ray scattering techniques are commonly used to perform structure investigations during *in situ* drying of thin films.

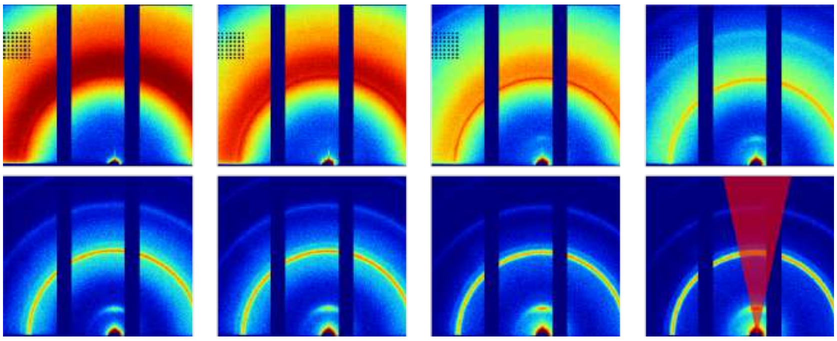

Figure 6.1:
GIWAXS 2D detector images during the drying of TiO_2:P3P6T (1.5:1) at selected times t = 5, 55, 80, 92.5, 105, 155, 205 and 255 s. Time evolves from left to right and from top to bottom.

In particular, *in situ* grazing incidence wide angle X-ray scattering (GIWAXS) is suited to study the crystalline evolution during the transition from liquid solution to a solid dry thin film. In Fig. 6.1 detector images from *in situ* measurements during the drying of a TiO_2:P3P6T active layer (weight ratio 1.5:1) are presented. From the images, several qualitative features can be already identified. At the beginning of the experiment (top left), a bright diffraction ring emerges due to the presence of bulk solvent, namely water, the intensity of which diminishes while the drying takes place to finally vanish in the final stage of a final dry thin film. The inorganic component (titania nanoparticles) is seen through powder diffraction-like rings, meaning that the crystals do not arrange in any preferred orientation. As the crystallinity of titania nanoparticles does not change at the low drying temperature used ($T = 40$ °C), some of the intense diffraction rings can be identified even at the early stages where the active layer is still in solution. The most interesting feature of the sequence is the intensity peak arising in the vertical direction, which corresponds to the crystallization of the polymer P3P6T. At early stages the polymer is completely dissolved in water and no peak is observed, while at the late stages an intensity peak corresponding to the (100) crystal planes is clearly identified.

To quantitatively analyze the drying process, the detector images are remapped into q-space and azimuthal vertical sector cuts are performed (depicted schematically as a red triangle in the last image of the sequence). Moreover, the images are calibrated to provide with an accurate sample detector distance (SDD) because this evolves due to the measurement protocol and to the fact that the thickness of the film changes drastically when transitioning from liquid to solid state. The time sequence is shown in Fig. 6.2, where the solid lines indicate the literature values of anatase and rutile titania reflections and the dashed line at $q_w = 2.05 \pm 0.02$ Å^{-1} corresponds to the scattering signal from water during the early stages. The scattering signal of the emerging P3P6T (100) planes of the polymer are marked with an arrow, and they are analyzed by Gaussian fits. The fits provide the q position of the peak (and therefore the plane lattice constant) and through the Scherrer equation the average crystallite size can be calculated. Together with the intensity evolution of the H_2O and P3P6T peaks and the SDD evolution, these magnitudes allow to identify four different stages during the drying transition. During stage I, the polymer is completely dissolved in water and therefore no peak intensity is observed. Stage II is characterized by the onset of polymer crystallization, and a fast growing of crystal size starts. During these stages the intensity of the water signal decreases moderately until it drops significantly at stage III, where the solvent bulk is removed and the crystal size growth starts to plateau. Regarding the lattice constant, a fast decrease is observed in both stages II and III. In stage IV, the thin film achieves its final dry state and the increase in polymer intensity indicates further growth of crystals. At this final stage all the parameters plateau towards the final dry film state, which is measured a few minutes after the *in situ* experiment.

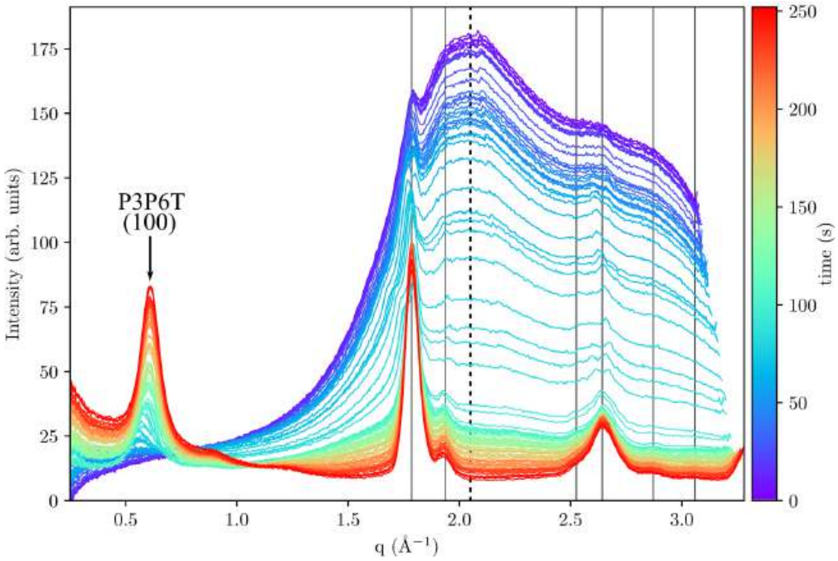

Figure 6.2:
GIWAXS vertical sector plot intensity for the time sequence during the drying process. The dashed line indicates the intensity peak of water and the solid lines the anatase and rutile phases of titania nanoparticles. The Bragg peak for the polymer is marked with an arrow.

[1] P. Müller-Buschbaum, M. Thelakkat, T. F. Fässler, M. Stutzmann, *Adv. Energy Mater.* **7**, 1700248 (2017)

6.2 Correlating nanostructure, optical and electronic properties of nanogranular silver layers during polymer-template assisted sputter deposition

M. Gensch[1,2], P. Müller-Buschbaum, S. V. Roth[1,2]

[1] DESY, Hamburg, Germany
[2] KTH, Stockholm, Sweden

The tailoring of optical and electronic properties by using nanostructured metal-polymer- composites demonstrate great potential for an efficient fabrication of modern organic optical and electronic devices such as flexible electronics [1] or photovoltaics [2]. Self-assembled polymer-metal-nanocomposites offer an excellent perspective for creating hierarchical nanostructures on macroscopic scales by simple bottom-up processes. We investigated in situ the growth processes of nanogranular silver (Ag) layers on diblock copolymer thin film templates during sputter deposition by grazing incidence small angle X-ray scattering (GISAXS) at the DESY beamline P03, PETRA III [3]. The Ag growth is strongly driven by self-assembly and selective wetting on the lamella structure of polystyrene-block-polymethylmethacrylate (PS-b-PMMA).

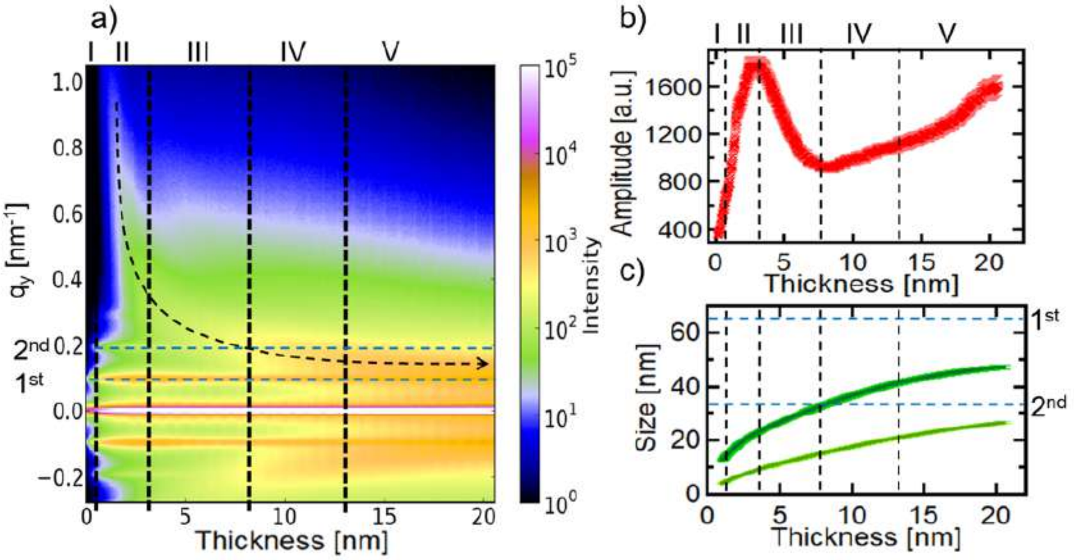

Figure 6.3:
a) Contour plot of Yoneda cuts from the in situ GISAXS data during sputter deposition on PS-b-PMMA as a function of effective deposited Ag thickness. The cluster peak (black dashed arrow) and the lamellar 1st and 2nd order peak (blue dashed lines) at $q_y = 0.096$ nm^{-1} (1st) and $q_y = 0.192$ nm^{-1} (2nd) change due to the Ag deposition. The black dashed vertical lines indicate different growth regions: Nucleation and embedding (I), selective diffusion-mediated cluster growth via coalescence (II), non-selective adsorption-mediated growth (III), partially interconnection between the domains (IV), and percolated regime (V). b) Evolution of the amplitude of the domain peak of PS-b-PMMA during the Ag sputter deposition. The black dashed vertical lines mark the as before mentioned growth regions; the intensity contrast in regions (I) and (II) is increasing due to the selective wetting and decreasing in region (III) due to the limited embedding of Ag clusters in the polymer and the sub-surface growth. c) Evolution of the mean interparticle distance (D, dark green) and the cluster radius (R, bright green) in the different growth regions.

Fig. 6.3a shows the contour plot of the Yoneda cuts from Ag on PS-b-PMMA. The lateral stripes seen as in the Yoneda cut in fig. 6.3a (blue dashed arrow) stem from the polymer domain structure, yielding a domain period of the copolymer template around L = (65 ± 3) nm. The signal of the Ag cluster on the thin copolymer film is clearly visible as a pseudo-Bragg peak (black dashed arrow) moving from high q_y values to nearly reaching the first order domain period.

Due to the ordered lamella copolymer film, a continuous growth on the polymer domains is achieved. The black dashed vertical lines indicate different growth regions: Nucleation and embedding (I), selective diffusion mediated cluster growth via coalescence (II), non selective adsorption-mediated growth (III), partially interconnection between the domains (IV), and percolated regime (V). The decoration of the polymer domains by the metal clusters is clearly visible in fig. 6.3b by the increasing amplitude of the 1st order domain period intensity due to a change in the electron density contrast. From the GISAXS measurements, the average distance and the radii of the clusters were extracted using the established geometrical model from [4]. The results are presented in fig. 6.3c. From fig. 6.4a, the percolation threshold based on this model (2R/D=1) can be determined. fig. 6.4b presents the electrical measurements, where the insulator metal transition (IMT) was determined independently (red solid curves). Both results are compared in fig. 6.4c, where the experimental GISAXS results and the IMT are in good agreement [5].

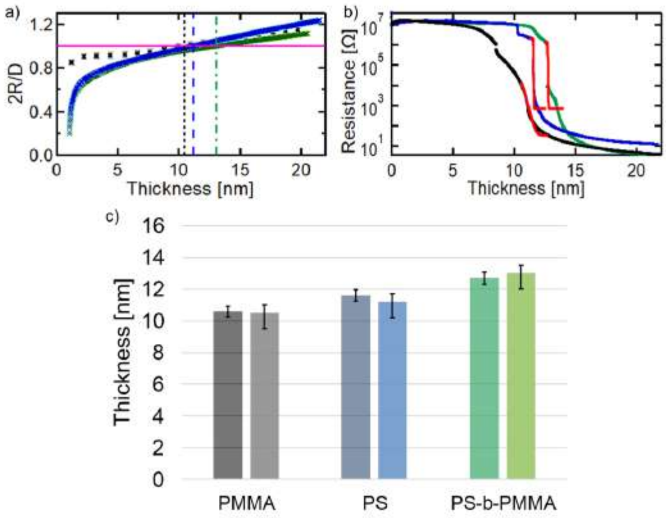

Figure 6.4:
a) Evolution of ratio of average cluster diameter (2R) over the mean interparticle distance (D) for PMMA (black), PS (blue), PS-b-PMMA (green). When 2R/D equals one (pink line) the clusters start to touch each other, which can result in a conductive path. This is indicated by the short-dashed, long-dashed and dash-dotted vertical lines for the PMMA, PS, PS-b-PMMA, respectively. b) In situ 2-point resistance measurements during sputter deposition of Ag on PS, PMMA and PS-b-PMMA thin films. The red line is a fit using the Boltzmann sigmoidal fit function in order to determine the percolation threshold for all samples. c) Comparison of the insulator-to-metal transition (IMT) extracted from resistivity measurements and the percolation threshold p from GISAXS on PS, PMMA and PS-b-PMMA. The IMT is given by a black (PMMA), dark blue (PS) and dark green (PS-b-PMMA) column and the percolation threshold with grey (PMMA), light blue (PS) and light green (PS-b-PMMA).

[1] F. Faupel, V. Zaporojtchenko, T. Strunskus, M. Elbahri, M. *Adv. Eng. Mater.* **12**, 1117−1190 (2010)

[2] G. Kaune, M. A. Ruderer, E. Metwalli, W. Wang, S. Couet, K. Schlage, R. Röhlsberger, S. V. Roth, P. Müller-Buschbaum, *ACS Appl. Mater. Interfaces* **1**, 353−360 (2009)

[3] A. Buffet, A. Rothkirch, R. Döhrmann, V. Körstgens, M. M. A. Kashem, J. Perlich, G. Herzog, M. Schwartzkopf, R. Gehrke, P. Müller-Buschbaum, S. V. Roth *Journal of Synchrotron radiation* **19**, 647−653 (2012)

[4] M. Schwartzkopf, G. Santoro, C. J. Brett, A. Rothkirch, O. Polonskyi, A. Hinz, E. Metwalli, Y. Yao, T. Strunskus, F. Faupel, P. Müller-Buschbaum, S. V. Roth *ACS Appl. Mater. Interfaces* **7(24)**, 13547−13556 (2015)

[5] M. Gensch, M. Schwartzkopf, W. Ohm, C. J. Brett, P. Pandit, S. K. Vayalil, L. Bießmann, L. P. Kreuzer, J. Drewes, O. Polonskyi, T. Strunskus, F. Faupel, A. Stierle, P. Müller-Buschbaum, S. V. Roth, *ACS Appl. Mater. Interfaces* **11** , 32, 29416-29426 (2019)

6.3 In-operando GISAXS investigation of a TiO2:P3HT hybrid photoactive system during heating

J. E. Heger, N. Li, A.-L. Oechsle, S. Yin, S. Bernstorff[1], P. Müller-Buschbaum

[1] ELETTRA, Basovizza, Italy

Hybrid photoactive systems consisting of inorganic and organic materials combine advantages of both classes. This includes long-term stability and solution processability, e.g. by spray coating [1], respectively. Furthermore, these systems can be implemented in hybrid solar cells. A designed morphology is crucial for the device performance [2] and can be achieved by templating of the inorganic phase. Besides well established templating techniques under the use of diblock copolymers, there is an interesting approach to substitute these with water soluble biopolymers [3]. In this work, we want to see the correlation between performance losses and morphology of the organic and inorganic phases. For this, changes in conductance of a photoactive layer consisting of biotemplated TiO2 and P3HT were investigated at elevated temperature and during heating.

The sample was prepared in two main steps. First, nanoporous TiO2 was fabricated by spray deposition of a sol-gel solution. Second, P3HT was filled into the pores by spin coating. To achieve the nanoporous titania film, denatured bovine whey protein ß-lactoglobulin was used as a biotemplate. For this, a 1:2 ratio of ß-lactoglobulin and titanium(IV)isopropoxide (TTIP) was added to a solution of ethanol mixed 1:1 with 10 mM hydrochloric acid. The resulting sol-gel was heated at 60° C under stirring for 225 min. After quenching in cold water, the solution has been spray deposited on cleaned glass substrates at 120° C. Calcination at 500° C was performed to remove the template and to introduce crystallinity into titania. The sample was soaking in chlorobenzene (CB) to enhance backfilling efficiency with P3HT by static spin coating.

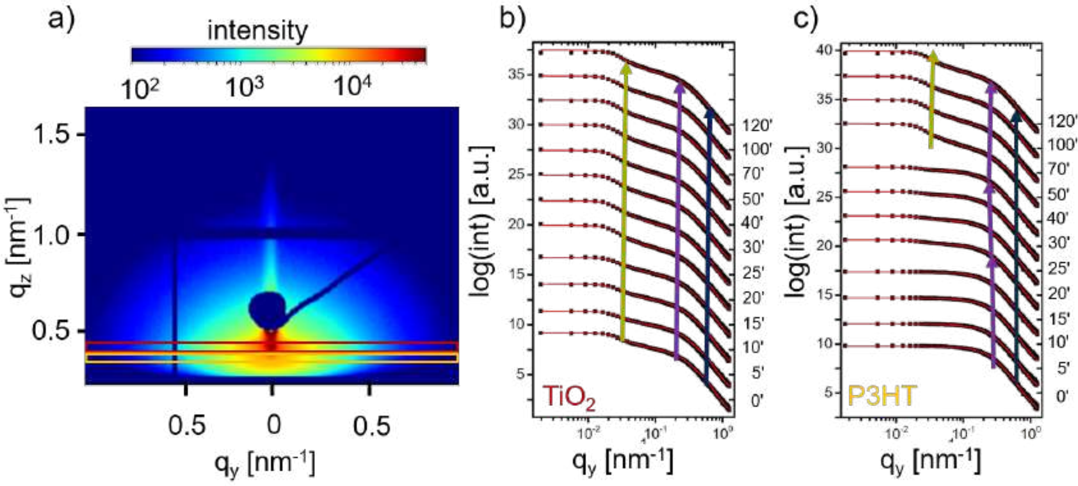

Figure 6.5:
a) 2D GISAXS image with indicated positions of horizontal line cuts for the respective materials TiO2 in red and P3HT in yellow. Applied model shows b) no temporal evolution of TiO2 morphology and c) coarsening of P3HT yielding increased domainsizes

We are interested in investigation of morphological changes in the Ti02:P3HT hybrid system during heating and performing periodic current measurements. For this, in-operando grazing incidence small-angle X-ray scattering (GISAXS) measurements were carried out at the Austria SAXS beamline of ELETTRA synchrotron in Basovizza. To control temperature and applied

voltage, the sample was connected to the respective sources in a custom built chamber and kept under nitrogen atmosphere, to prevent the influence of external chemical degradation. The sample was adjusted in an angle of 0.3° to the impinging beam and placed in a distance of 1.95 m to a Pilatus 1M detector. GISAXS and current measurements were performed in periodical intervals during heating and at constant temperature of 77° C for 120 min.
Figure 6.5 a) shows an exemplary two dimensional detector image of the hybrid system. One dimensional line cuts at the material characteristic q_z values are indicated for Ti02 in red and P3HT in yellow, respectively. By modeling these cuts with a cylindrical form factor on a one dimensional paracrystal for all individual GISAXS measurements, the temporal evolution of the respective materials is revealed. A stacking of selected cuts at different times for TiO2 and P3HT are shown in Figure 6.5a) and b). While no morphological changes are seen in the titania phase, the P3HT phase shows a slight change after 20 min and a prominent change after 50 min.

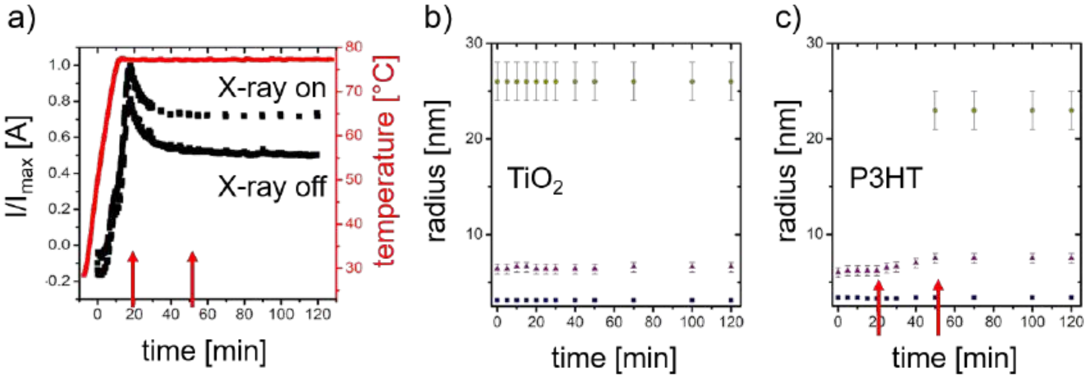

Figure 6.6:
a) Temporal evolution of temperature and normalized current. An increased current during X-ray illumination is observed and an overall drop in current after 20 min. b) Radii of TiO2 form factors remain constant. c) Raddi of P3HT form factors increase after 20 min and coarsening correlates temporal to the drop in current.

In Figure 6.6 a) the normalized current and temperature are plotted against time. A increase in current is seen during preheating. Furthermore, the current of the photoactive system increases during X-ray illumination. The on/off ratio of the final GISAXS measurement shows an current increment of roughly 50 % and the final on-state has a lifetime of 18 s at full width half maximum. After 20 min a current drop followed by a steady decrease appears. The individual form factor radii are plotted against time in Figure 6.6 b) and c). Three different form factor dimensions are found for both materials. The medium dimension of P3HT shows an increase in radius within minute 20 and 50. After this, a third larger dimension appears. This can be attributed to coarsening of the polymer, yielding a reduced exciton separation and hence a drop in current, as seen in the temporal correlation of both. Since, however, there is no change in morphology of the titania phase and hence no obvious correlation with the conductance, the hybrid photoactive system can be understood to show an increased stability due to titania.

[1] N. Hohn, S. J. Schlosser, L. Bießmann, L. Song, S. Grott, S. Xia, K. Wang, M. Schwartzkopf, S. V. Roth, P. Müller-Buschbaum, *ACS Appl. Nano Mater.* **1**, 4227-4235 (2018)

[2] L. Song, W. Wang, S. Pröller, D. Moseguí González, J. Schlipf, C. J. Schaffer, K. Peters, E. M. Herzig, S. Bernstorff, T. Bein, D. Fattakhova-Rohlfing, P. Müller-Buschbaum, *ACS Energy Lett.* **2**, 991-997 (2017)

[3] S. Bolisetty, J. Adamcik, J. Heier, R. Mezzenga, *Adv. Funct. Mater.* **22**, 3424-3428 (2012)

6.4 In-situ tracking the morphology evolution of active layers for non-fullerene organic solar cells

X. Jiang, S. Grott, V. Körstgens, K. Wienhold, M. Schwartzkopf[1], S. V. Roth[1,2],
P. Müller-Buschbaum

[1] DESY, Hamburg, Germany
[2] KTH, Stockholm, Sweden

In the past few decades, organic solar cells (OSCs) have achieved significant advances with the developed novel materials, optimized fabrication routes and applications of new measurement technologies. For instance, owing to the advantages of highly tunable molecular energy levels and light absorption spectra of non-fullerene accepters, OSCs based non-fullerene accepter as active layer reached efficiency values which exceeded 16%.[1] However, despite such progress, the best achieved OSC efficiencies still remain behind that of traditional silicon solar cells. Moreover, most high-performance OSCs are fabricated with the spin coating method under inert atmosphere conditions and through labor-intensive testing on a small scale, which is not compatible with industrial-level large-area mass production demands.Therefore, developing a large-area printing technology is critical for manufacturing energy-efficient, high-throughput, low-cost and low carbon-footprint OSCs. Slot-die coating can be employed in sheet-to-sheet and roll-to-roll (R2R) large-area solution processing with low solution consumption, high film homogeneity and good device performance on a flexible substrate. Thus, this technic has been successfully developed to a fully scalable, robust and reproducible technique in layer deposition.[2] The performance of OSCs is strongly influenced by the morphology of the active layer. Therefore, it is the key to understand the structure formation of the active layer during the drying kinetics for further device optimization.[3] The non-destructive GISAXS technique is capable of providing domain sizes and spatial correlations down to nanometer scales regarding the inner structures of the films, which is desirable for the present work to determine the morphology change during the printing process. Based on these considerations, we use in-situ GISAXS during printing to track the mechanisms of structure formation of polymer domains.In this work, a low bandgap donor polymer (PffBT4T-2OD) and a non-fullerene acceptor (EH-IDTBR) shown in Fig. 6.7a are selected as the active layer materials due to their advantages of being air-stable, thickness insensitive and enabling a high device performance. The corresponding invert geometry of the related organic solar cell device is shown in Fig. 6.7b.As X-rays with high energy are used in combination with an outstanding high time resolution of GISAXS measurments during the thin film printing process, the structure formation and related kinetics can be followed from the liquid state to the final dry film. In total, five regimes of structuere formation are determined. These findings build the foundation for further optimization of the large area photovoltaic device performance.

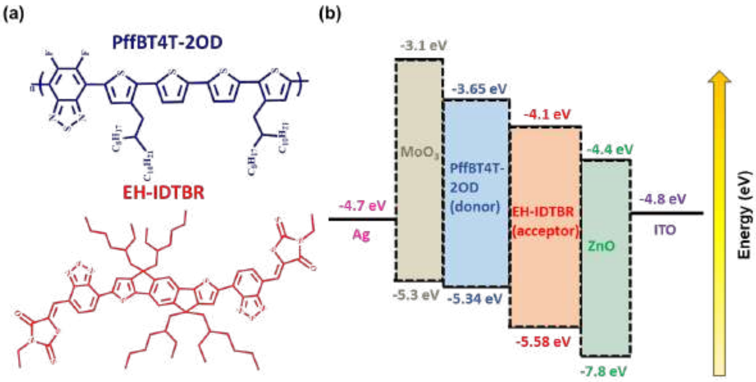

Figure 6.7:
a) Chemical structures of the PffBT4T-2OD donor polymer and EH-IDTBR small molecule accepter, respectively. b) Energy level diagram of the materials in an invert organic solar cell architecture, which contains PffBT4T-2OD:EH-IDTBR as the active layer.

Fig.6.8a shows selected 2D GISAXS data to illustrate the evolution of the active layer during the printing process. Due to the solvent evaporation, the intensity of the Yoneda peak in the qz

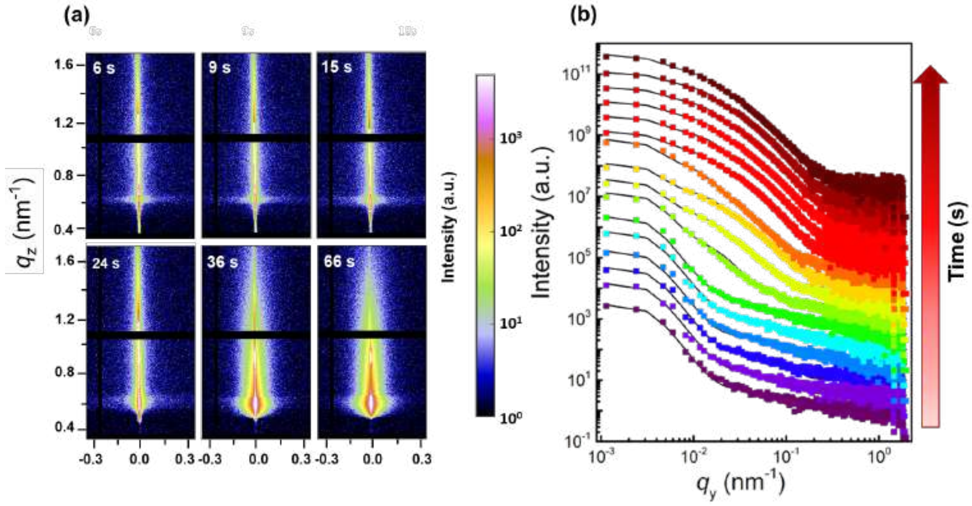

Figure 6.8:
a) Selected 2D GISAXS data during the in-situ printing process at times as indicated. b) Horizontal line cuts extracted from the in-situ GISAXS data, points and lines are data and fits, respectively.

range of 0.5-0.7 nm-1 is increasing with time, which reveals the solidification of the polymer: small molecule blend film in the BHJ morphology. Fig.6.8b shows the horizontal line cuts and the optimal fitting, respectively. In order to gain insights into the thin film formation from the liquid to the solid state over time, we used five states to describe the thin film conditions, which includes the liquid state, the liquid-solid state, the quasi-solid state and the pure solid state. The data molding reveals that the development of the morphology of the polymer donor exhibits five stages independent of the drying conditions. At the first stage, the thin film is in liquid state and no obviously change of morphology occurs. In this regime there is only one domain size with a radius around 10 nm, which refers to the PffBT4T-2OD aggregates in solution. At the second stage, large aggregates of the PffBT4T-2OD polymer are increasing mildly over time and a second structure is appearing with a size around 5 nm, suggesting the phase begins to separate. At the third stage, intense phase separation is observed and PffBT4T-2OD aggregates with the polymer domain radius increasing from around 28 nm to nearly 70 nm. Moreover, the second PffBT4T-2OD strucrure radius changes from 5 nm to 22 nm and a third structure of small PffBT4T-2OD domain sizes is forming, indicating that the liquid-to-solid phase transition starts to occur rapidly inside the thin film. After entering the fourth stage, the phase separation of three structure increases gradually slower, the first structure of PffBT4T-2OD aggregates evolves from around 70 to 100 nm, the second structure increases from around 22 to 38 nm and the third structure grows from around 5 to 10 nm, which reveals the final liquid transfer to a solid state and the morphology reconstruction of the thin film. Finally, all the domain radii remain constant and the final solid state blend film is reached.

[1] B. Fan, D. Zhang, M. Li, W. Zhong, Z. Zeng, L. Ying, F. Huang, Y. Cao, *Sci. Chi. Chem.* **10**, 1007 (2019)

[2] Y. Lin, Y. Jin, S. Dong, W. Zheng, J. Yang, A. Liu, F. Liu, Y. Jiang, T. P. Russell, F. Zhang, F. Huang, L. Hou, *Adv. Energy. Mater.* **8**, 170912(2018)

[3] M. A. Ruderer, E. Metwalli, W. Wang, G. Kaune, S. V. Roth, P. Müller-Buschbaum, *Chem. Phys. Chem.* **10**, 664-671 (2009)

6.5 Following the sputter deposition of gold contacts on thin films of photoactive polymers

F. C. Löhrer, V. Körstgens, G. Semino, M. Schwartzkopf[1], A. Hinz[2], O. Polonskyi[2], T. Strunskus[2], F. Faupel[2], S. V. Roth[1,3], P. Müller-Buschbaum

[1] DESY, Hamburg, Germany
[2] CAU Kiel, Kiel, Germany
[3] KTH, Stockholm, Sweden

With their easy processability, high flexibility and tuneable optical properties, organic electronics (OE) offer a wide range of potential applications. Especially photoactive polymers have received high attention in recent years as candidates for organic photovoltaics (OPV) or light emitting diodes (OLED). Due to their well-known advantages, OPV or OLED devices could combine functionality with design in fields as diverse as mobility, architecture or clothing. Although those devices mainly consist of organic materials, their electrodes are in many cases still made from metals. Thus, polymer-metal interfaces are inherently present in most organic electronic devices. Understanding the growth mechanisms of metal contacts on polymer thin films plays a crucial role in identifying potential ways to enhance the performance of organic electronics. Recent research efforts focus on engineering the optical bandgap of photoactive polymers by tuning their side groups, thereby creating families of polymers with the same backbone, but tunable optoelectronic behavior. Amongst those polymer families, especially PTB7 and its derivatives are interesting. By introducing a thiophene ring into the side-chains, the bandgap of PTB7-Th is significantly decreased, which leads to absorption of less energetic photons and thereby higher solar cell efficiencies.

We investigated the morphological changes during the sputter deposition of gold electrodes onto thin films of both polymers, PTB7 and PTB7-Th, via in-situ grazing incidence small angle X-ray scattering (GISAXS). [1] This technique allows for time-resolved insights into the deposition behavior of the metal on the organic film, which strongly depends on the film structure. Making use of the outstanding time resolution at the P03 instrument at DESY in Hamburg, we compared the deposition behavior of sputtered gold particles on both semi-conducting polymer films. With a mobile sputter chamber, which was implemented directly into the beamline, we followed the creation and growth of gold clusters and the subsequent layer formation. Fig.6.9 schematically illustrates the gold deposition process as well as the in-situ X-ray scattering experiment. The gold particles are created from a gold target via sputtering and impinge on and self-assemble at the polymer substrate.

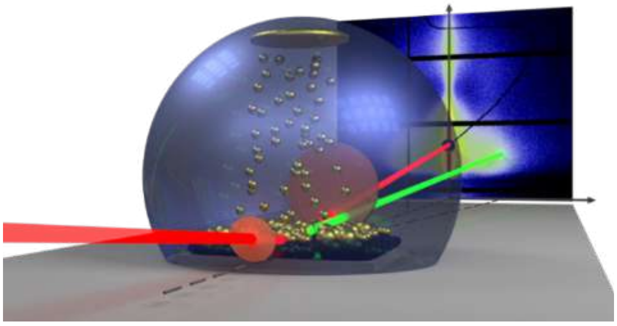

Figure 6.9:
Setup of the in-situ GISAXS measurements during the deposition of gold on a thin film sample in a sputter chamber. Iincoming as well as specularly specularly reflected X-rays are depicted in red; exemplary scattering caused by lateral structures in the forming gold film is shown in green. The grey sphere indicates the sputter chamber, the red circles the entry and exit windows. The sputtered gold atoms are indicated as golden spheres.

The acquired large data sequences were analyzed using the fast data reduction software DPDAK. Hereby, the 2D raw data were cut at specific regions of interest, such as horizontal line cuts, which give information about the lateral film morphology during film growth. Using an appropriate geometrical model, real-space parameters such as the average gold cluster size and distance as well as the surface coverage can be determined. The evolution of the surface coverage over time is shown in Fig. 6.10.

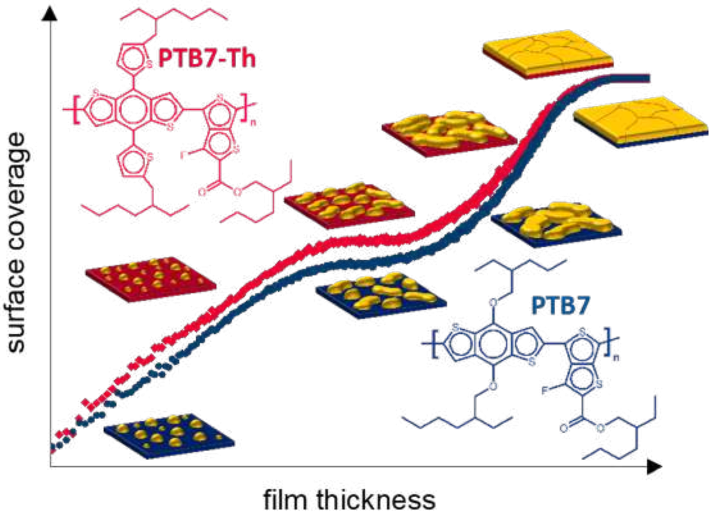

Figure 6.10:
Evolution of the surface coverage of a gold film sputtered on PTB7 (blue) and PTB7-Th (red), showing distinct growth phases for both samples. Differences in terms of cluster size and coverage (PTB7 in blue and PTB7-Th in red) are indicated.

Several growth phases can be distinguished for the gold film growth, in good accordance with a step-like growth shown in other works. [2, 3, 4] However, a distinct difference in surface coverage is visible between the two polymers. Combining these findings with other structural parameters, we can deduce a small, yet significant influence of the type of polymer on the film growth, with PTB7-Th showing a lower gold surface diffusion mobility, leading to a higher amount of smaller gold clusters and higher surface coverage. [5] Even slight differences in the side-chain of polymers can lead to significant changes in the structure of applied gold electrodes, which will be important when optimizing potenial solar cells.

[1] P. Müller-Buschbaum, *Adv. Mater.* **26**, 7692–7709 (2014)

[2] G. Kaune, M. A. Ruderer, E. Metwalli, W. Wang, S. Couet, K. Schlage, R. Röhlsberger, S. V. Roth, P. Müller-Buschbaum, ACS Appl. Mater. Interfaces **1**, 353-360 (2009)

[3] M. Schwartzkopf, G. Santoro, C. J. Brett, A. Rothkirch, O. Polonskyi, A. Hinz, E. Metwalli, Y. Yao, T. Strunskus, F. Faupel, P. Müller-Buschbaum, S. V. Roth, *ACS Appl. Mater. Interfaces* **7**, 13547-13556 (2015)

[4] M. Schwartzkopf, A. Hinz, O. Polonskyi, T. Strunskus, F. C. Löhrer, V. Körstgens, P. Müller-Buschbaum, F. Faupel, S. V. Roth, *ACS Appl. Mater. Interfaces* **9**, 5629-5637 (2017)

[5] F. C. Löhrer, V. Körstgens, G. Semino, M. Schwartzkopf, A. Hinz, O. Polonskyi, T. Strunskus, F. Faupel, S. V. Roth, P. Müller-Buschbaum, *ACS Appl. Mater. Interfaces* **1.12**, 1132-1141 (2020)

6.6 Probing the in-situ dynamics of structure-property evolution in hybrid perovskite thin films spincoated from complex fluids by a custom designed, beamline compatible multimodal measurement chamber

S. Pratap, N. Tamura[1], C. Stan[1], Z. Yuan[2,3], H. Gowdey[4], A. MacDowell[1], T. Song[2], N. Barchi[2], J. Slack[1], C. Sutter-Fella[2], P. Müller-Buschbaum

[1] ALS, Berkeley, USA
[2] JCAP, Berkeley, USA
[3] UC Berkeley, USA
[4] ETA, Berkeley, USA

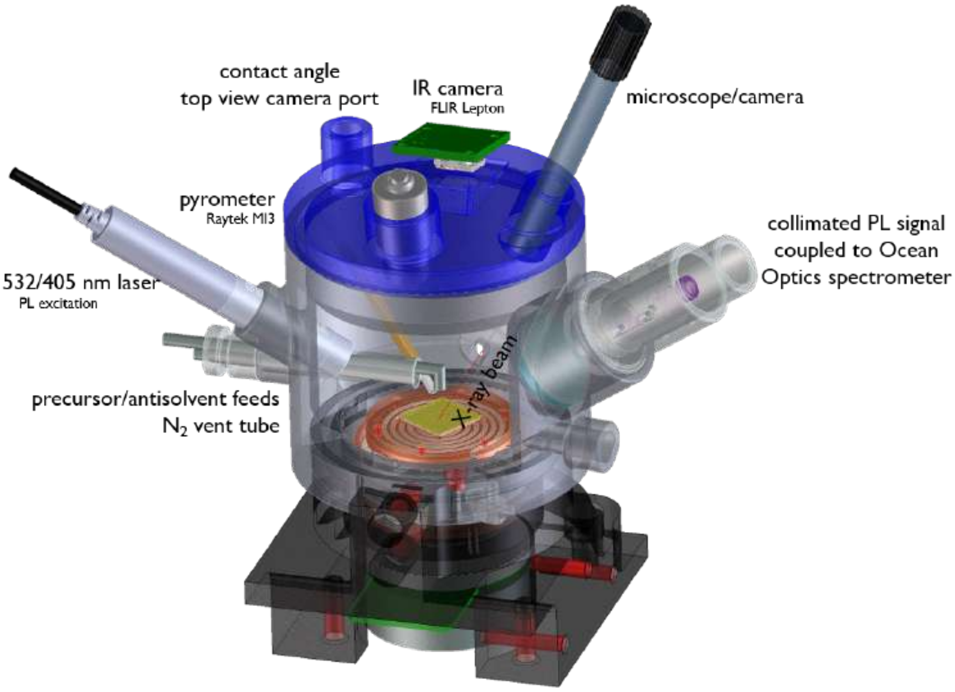

Figure 6.11:
Schematic of the sample environment for processing and investigating solution processed chemical transformations via multimodal measurements

Hybrid perovskite materials and thin-films thereof are processed through chemically complex [1], fluid precursors. The processing occurs throught routes such as spin-coating of the complex fluids, and represents a process far from thermodynamic equilibrium. During the process, the precursor dynamically transforms and experiences non-trivial structural and electronic transformations as it is converted to a final crystalline thin-film. The structural alterations experienced by the film range from the emergence of glassy intermediate states within the drying precursor, to shear-induced morphological instabilities as a response to stresses generated in the film during drying and crystal growth. It is therefore unsurprising that spin-coated thin films display vivid texture, ranging from the crystallographic to the mesoscopic length scales. These morphological and structural heterogeneities within thin films have been linked to avoidable variations in photovoltaic metrics. Finer control over photovoltaic parameters necessitates a better understanding and control over how the non-trivial perovskite crystallization is guided, and what impact do different film transformation methodologies have on the transient and emergent functional properties of the material. Notwithstanding the impact of morphological heterogeneity on photovoltaic performances, the chemical and physical history of the material treatment protocols is reflected within the photovoltaic response of the device. The direct consequence of the above factors gives rise to large variations in photovoltaic properties and diminishes the predictability of the material behavior. It has remained a challenge, until now, to correlate the impact of material structure to its functional properties, due to the absence of appropriate measurement setups that allow the simultaneous resolution of structural and electronic changes during spin-coating, especially when crystallization is enforced through nucleation by using orthogonal solvents.

The premier case of the in-situ evolution of spin-coated hybrid perovskites thin films is presented through multimodal techniques, made possible by a custom-designed measurement chamber, [2] as represented in Fig. 6.11. Grazing incidence wide angle x-ray scattering is utilized to probe the evolving crystalline structure of the spin-coating thin film. Optoelectronic response of the dynamically evolving material is measured through photoluminescence. The film, after spin-coating is annealed and phase transformation of the intermediate state is regulated by temperature, which is controlled through a previously calibrated, spot regulated pyrometer. Local changes in temperature, emissivity of the resultant thin film are characterized by IR radiographic imaging. The simultaneous, highly time-resolved measurements enable unraveling previously inaccessible insights about of the exciting analogue of organic-inorganic lead halide perovskite materials, as well as the kinematic behavior of solution processed soft materials.

In Fig. 6.12, the different structural and electronic states of the MAPI precursor are represented while undergoing spincoating, antisolvent dispersal and subsequent annealing. The data suggests a first order phase transition which occurs, firstly when the antisolvent is introduced to the system. Moreover, as the solvent complexes convert into the perovskite structure, another first order phase transition is observed. The study depicts the correlation betweeen the structure of the various intermediate states with a functional property of photoluminescence.

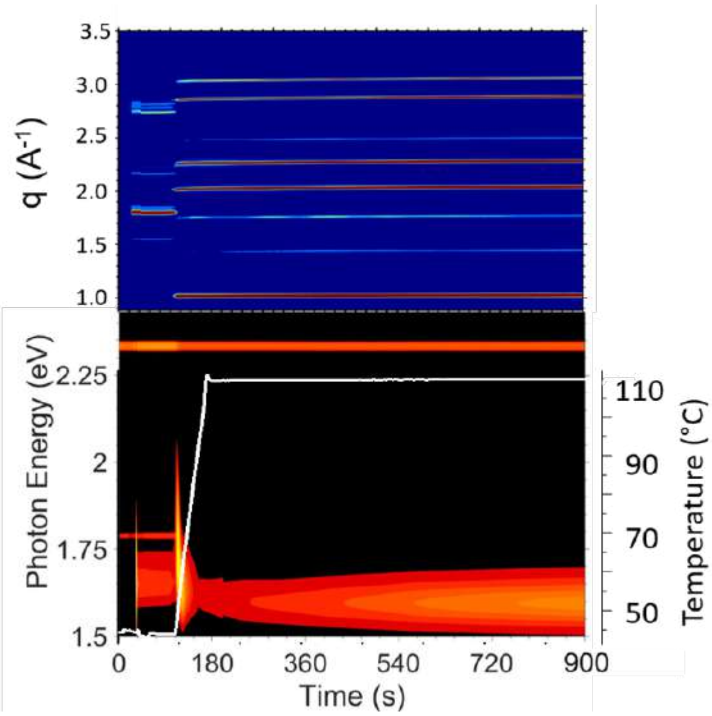

Figure 6.12:
The evolution of a MAPI precursor during the one-step, antisolvent-assisted spincoating

[1] S. Pratap, E. Keller, P. Müller-Buschbaum, *Nanoscale* **11**, 3495 (2019)

[2] S. Pratap, N. Tamura, C. Stan, Z. Yuan, H. Goudey, A. MacDowell, T.-B. Song, N. Barchi, P. Müller-Buschbaum, C. Sutter-Fella, J. Slack, *Acta Cryst.* **A75**, a155-a156 (2019)

6.7 Investigating the growth of sputter deposited copper on diblock copolymer thin films using in-situ GISAXS

S. J. Schaper, F. C. Löhrer, S. Xia, M. Schwartzkopf[1], P. Pandit[1], A. Hinz[2],
O. Polonskyi[2], T. Strunskus[2], F. Faupel[2], S. V. Roth[1,3], P. Müller-Buschbaum

[1] DESY, Hamburg, Germany
[2] CAU, Kiel, Germany
[3] KTH, Stockholm, Sweden

Understanding the interface between metals, commonly used as contacts and current collectors, and (ion-)conducting polymers used in organic electronics, organic photovoltaics and polymer lithium-ion batteries (LIBs) is crucial to develop highly reproducible, low-cost and reliable devices. To address these issues, sputter deposition is the technique of choice to fabricate scalable, reproducible, and controllable nanometer and sub-nanometer metal layers on polymer thin films. The sputter deposition process, being well understood and controlled, offers advantages over chemical methods to tailor metal thin-film morphologies on the nanoscale and offers a superior adhesion of the deposited material.[1] In-situ grazing-incidence small-angle X-ray scattering (GISAXS) is used to investigate the formation, growth, and self-assembled structuring on polymer thin films. To exceed the limits of the polymer LIBs unexploited development the deposition and infiltration of sputtered metals onto the polymer thin film used in composite anodes needs to be understood.

The diblock copolymer (DBC) polystyrene-block-poly(ethylene oxide) (PS-*b*-PEO) is one of the most promising materials for solid state polymer LIBs. The rigid PS block provides mechanical stability while the soft and ion-conducting PEO block enables Li-ion's migration between the electrodes. Due to the covalent bond between the hydrophobic PS and the hydrophilic PEO block of the PS-*b*-PEO DBC undergoes a microphase separation creating a self-assembled structure in the nanoscale, which can prevent the lithium-dendrite's growth leading to a shortcut in LIBs.

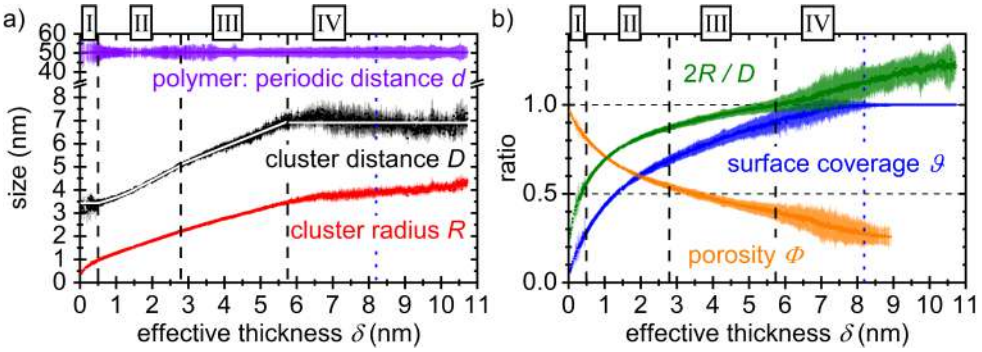

Figure 6.13:
a) evolution of the polymeric periodic distance d, cluster distance D and cluster radius R, and b) calculated ratio of $\frac{2R}{D}$, surface coverage θ and porosity ϕ of the deposited copper with increasing effective film thickness δ, respectively. White lines indicate linear fits of D to distinguish four growth stages (I-IV), devided by dashed lines. At the dotted line (δ = 8.2 nm) of surface coverage of 1 is reached.

The samples under investigation are 90 nm thin, bare PS-*b*-PEO DBC films on acid-cleaned silicon substrates prepared via spin coating at 2000 rpm from 10 mg ml^{-1} solution with CHCl$_3$ as solvent. Subsequently the samples were solvent annealed with CHCl$_3$. The in-situ GISAXS measurements during sputter deposition of copper nanolayers were done at the beamline P03 at DESY in Hamburg using a DC magnetron sputter chamber. In GISAXS measurements the incoming X-rays with an energy of 13 keV impinge on the sample with an incident angel of 0.4°, while the scattered inetsity is collected with a Pilatus 300k detector at a sample-detector distance of 2.305 m. The 2D GISAXS data is analyzed with vertical line cuts at q_y = 0 to extract the effective film thickness δ and horizontal line cuts at the position of the Yoneda peak to extract the copper cluster distance D and the periodic distance of the PS-*b*-PEO DBC d, respectively. The final thickness of the copper layer is calculated to 10.72±0.11 nm from the intensity modulation along the q_z direction, since the metal layer grows with correlated roughness on the polymer film. As the sputter deposition rate is constant, the effective thickness δ is calculated from the final average copper nanolayer thickness and duration of the sputter process. The evolution of D, d, and the cluster radius R during the sputter deposition of copper is shown in Fig. 6.13a. R is calculated using a hemispheroid model with local hexagonal order shown in Fig. 6.14. Using this model the evolution of the ratio of $\frac{2R}{D}$, the surface coverage θ, and porosity ϕ of the deposited copper nanolayer upon increasing effective film thickness δ can be extracted (Fig. 6.13b).

Taking a closer look at the extracted parameters one can distinguish different stages in the growth mechanism of a copper layer on a the PS-*b*-PEO DBC thin film until a completely covered surface is reached at about $\delta = 8.2$ nm: (I) A nucleation phase until $\delta = 0.5$ nm, where the first copper atoms form small metal clusters which are rapidly growing on the polymer surface while their mean distance to each other stays constantly small. (II) A diffusion driven growth (0.5 nm$< \delta < 2.8$ nm) where the single copper clusters merge on the surface increasing their mean distance D faster than their own radius R. (III) A more adsorption-driven growth (2.8 nm$< \delta < 5.75$ nm) of the clusters where the increase in the cluster distance D slows down due to the increasing immobilization of the clusters. (IV) At $\delta = 5.75$ nm the percolation threshold is reached meaning the single copper clusters touch each other forming a percolating network providing paths for electrons over the whole surface. The single clusters serve as grains for the growth of the copper layer while the underlaying lateral structure persists. At an effective thickness $\delta = 8.2$ nm the surface is completely covered according to the applied model. The porosity ϕ still stays at about 26% indicating a rough surface of the copper layer. A sketch of these four growth stages is shown in Fig. 6.14.

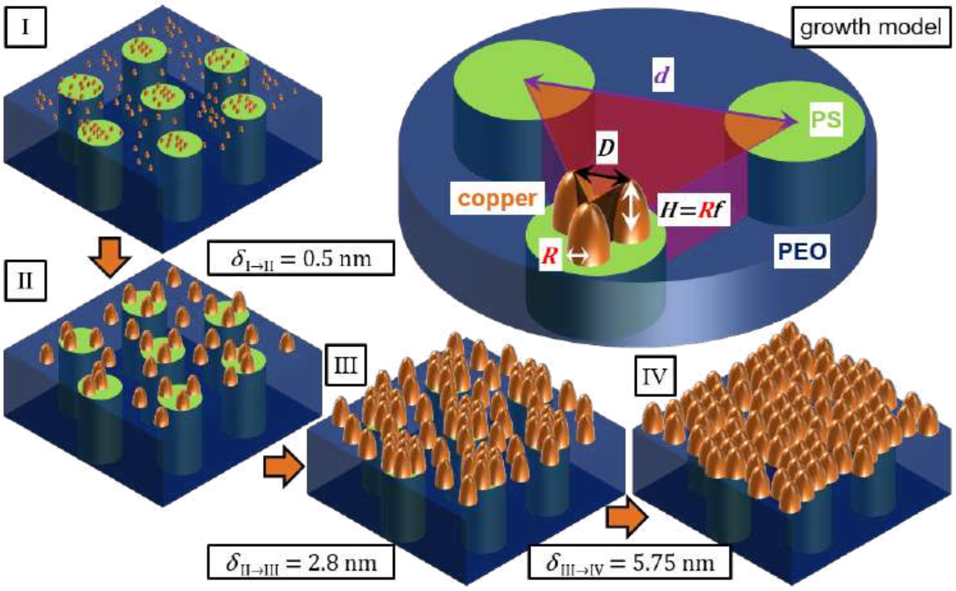

Figure 6.14:
Sketch of the growth model for the formation of a copper nanolayer on a PS-*b*-PEO DBC thin film and the four different growth stages: (I) nucleation phase, (II) diffusion driven growth, (III) adsorption-driven growth, and (IV) grain growth.

[1] F. Faupel, V. Zaporojtchenko, T. Strunskus, M. Elbahri, *Adv. Eng. Mater.* **12**, 1177-1190 (2010)

[2] M. Schwartzkopf, A. Hinz, O. Polonskyi, T. Strunskus, F. C. Löhrer, V. Körstgens, P. Müller-Buschbaum, F. Faupel, S. V. Roth, *ACS Appl. Mater. Interfaces* **9**, 5629-5637 (2017)

6.8 *In-situ* annealing GIWAXS studies of 2-step printed MAPI thin-films

M.A. Scheel, L.K. Reb, R. Guo, T. Xiao, S. Grott, M. Schwartzkopf[1], S.V. Roth[1,2],
P. Müller-Buschbaum

[1] DESY, Hamburg, Germany
[2] KTH, Stockholm, Sweden

Thin-film organic-inorganic metal halide perovskite based solar cells (PSCs) are currently intensely researched for their potential as cheap and flexible next generation solar cells. Reaching module efficiencies of around 17 % in 2018 and 15 % on ultrathin flexible substrates further improvement on the scaling up of organic-inorganic metal halide perovskite based solar cells (PSCs) is needed in order to push PSCs to the commercial market.[1] Especially changing from lab-scale deposition methods as spin-casting to industrial compatible large-area methods requires high research efforts. However, this is worthwhile due to important benefits, e.g. fast and roll-to-roll compatible deposition, low energy consumption and low temperature processing as well as low material waste. Highly crystalline and uniform films with low defect concentrations are paramount in reaching competitive power conversion efficiencies in PSCs. Therefore, a deeper understanding of the formation process of precursor materials to the photoactive perovskite material is beneficial.

In principle, those requirements can be met by roll-to-roll slot-die coating. In order to get deeper insights into the formation kinetics of perovskite films we prepared methylammonium lead iodide (MAPI) thin-films by spin-casting and slot-die printing.

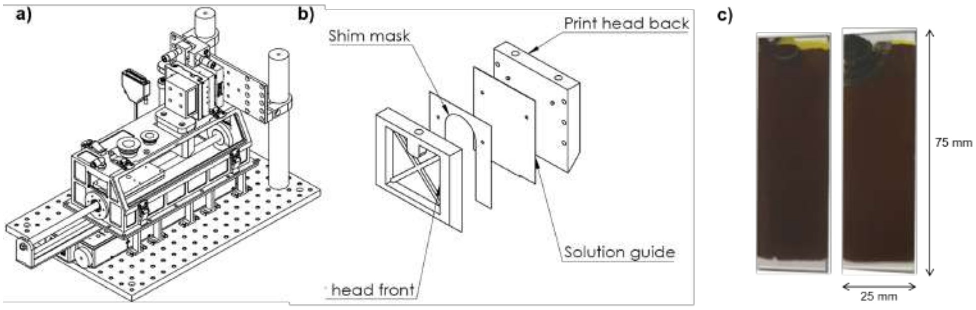

Figure 6.15:
Custom-built slot-die printer (a) with print-head (b) consisting of a front- and back-plate with customizable shim-mask and solution guide for optimal distribution of the printing solution.[2] (c) 2-Step printed MAPI films after the annealing process with PbI_2 visible at the top end of the printed films.

For printing (see fig. 6.15 a) and b) for our custom-built slot-die printer[2]) as well as for spin-casting we used a widely applied deposition procedure consisting of two-steps[3]: Firstly, the precursor lead iodide (PbI_2) is deposited from solution (DMF:DMSO 5:1) onto the substrate and annealed at 70 °C for 2 min. Secondly, methylammonium iodide (MAI) is deposited from solution (isopropanol) onto the PbI_2 layer and annealed at 120 °C. This leads to a thermally driven inter-diffusion of MAI into PbI_2, thus forming MAPI (cf. fig. 6.15 c) for images of two-step printed and annealed MAPI thin-films on glass/PEDOT:PSS).

We applied *in-situ* grazing incidence wide angle x-ray scattering techniques to probe stochastically large sample areas for their crystal structure and preferential orientation evolution during the annealing phase.[4] With high intensity and high brilliance synchrotron radiation it is possible to achieve a time resolution of around 1 s. Corrected 2D-GIWAXS images are shown in fig. 6.16 before and after the second annealing process for spin-cast and slot-die printed MAPI thin-films. PbI_2 obtains a cubic structure and shows a strong face-on (001)-orientation as can be seen from the (001)-reflex. The resulting MAPI crystals obtain a tetragonal structure and show both face-on and corner-up preferential orientation as can be seen from the intensity distribution of the (002)/(110)-reflex. There are distinct differences between spin-casting and printing concerning crystal preferential orientation before and also after the annealing process. For example, printed films show a higher amount of randomly oriented MAPI crystallites and also form less crystals in corner-up orientation.

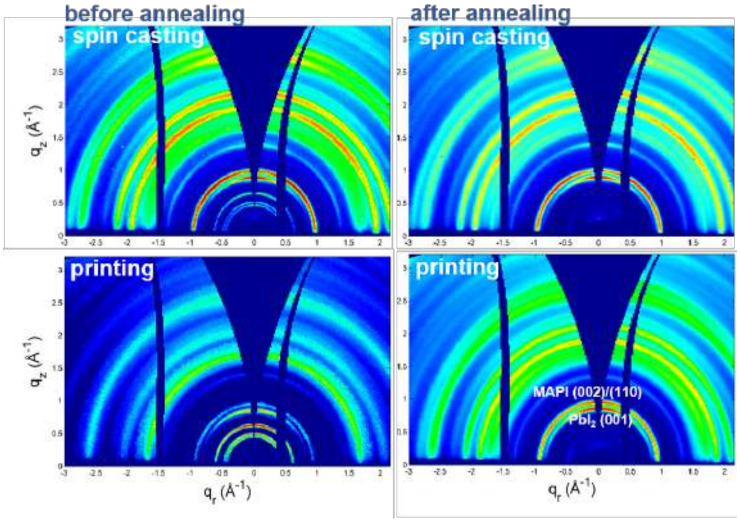

Figure 6.16:
2D-GIWAXS images before and after the annealing process for spin casting and printing deposition. The annealing temperature was raised from RT to 120 °C within less than 200 s.

To visualize the crystal structure time evolution during the annealing process from printed MAI and PbI_2 to MAPI a 2D-plot of azimuthally integrated GIWAXS images are shown in fig. 6.17. Reflexes attributed to MAI in the very low q-range below 0.7 Å^{-1} disappear; whereas the (002)/(110)-reflex of tetragonal MAPI around 0.95 Å^{-1} increases in intensity over time and indicates MAPI formation. The (001)-reflex of cubic PbI_2 is still visible after the annealing process as excess PbI_2 is present in the thin-film. The conversion is completed around 300 s after starting to heat up the sample, i.e. approximately 100 s after the sample reaches thermal equilibrium at 120 °C.

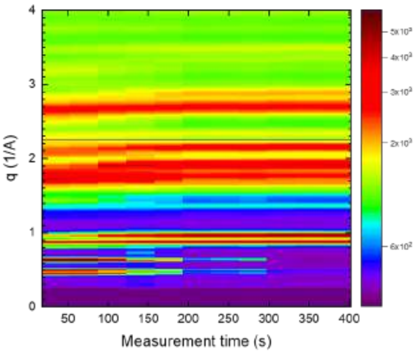

Figure 6.17:
2D-plot of azimuthally integrated GIWAXS images show the time dependent crystal structure evolution during the annealing process of the slot-die printed sample.

[1] M.A. Green, Y. Hishikawa, E.D. Dunlop, D.H. Levi, J. Hohl-Ebinger, M. Yoshita, A.W.Y. Ho-Baillie, Solar cell efficiency tables (Version 53), *Progress in Photovoltaics: Research and Applications*, 27, 3-12, (2019).

[2] K.S. Wienhold, V. Körstgens, S. Grott, X. Jiang, M. Schwartzkopf, S.V. Roth, P. Müller-Buschbaum, *ACS Appl. Mater. Interfaces* 11 (45), 42313-42321, (2019)

[3] H. Chen, *Adv. Funct. Mater.* 27, 1605654, (2017)

[4] L. Oesinghaus, J. Schlipf, N. Giesbrecht, L. Song, Y. Hu, T. Bein, P. Docampo, P. Müller-Buschbaum, *Adv. Mater. Interfaces* 3, 1600403, (2016)

6.9 Monitoring selectivity of gold cluster growth/formation on antifouling-relevant zwitterionic thin block copolymer coatings

A. Vagias[1], S. J. Schaper, L. P. Kreuzer, W. Chen, S. Liang, N. Li, C. Geiger, M. Gensch[2], P. Pandit[2], M. Schwartzkopf[2], S. V. Roth[2,3], B. J. Drewes[4], N. Carstens[4], T. Strunskus[4], F. Faupel[4], A. Laschewsky[5,6], P. Müller-Buschbaum

[1] MLZ, TUM, Garching, Germany
[2] DESY, Hamburg, Germany
[3] KTH Stockholm, Sweden
[4] CAU, Kiel, Germany
[5] Universität Potsdam, Potsdam-Golm, Germany
[6] Fraunhofer IAP, Potsdam-Golm, Germany

Polyzwitterion films exhibit strong potential as antifouling agents, on account of their strong hydrophilicity [1].Moreover, polymer-metal nanocomposites act as promising scaffolds for antibacterial [2] and plasmonic [3,4] applications. Metal sputtering under vacuum offers a versatile and highly controllable approach to construct polymer-metal nanocomposite films with tunable morphologies. Metal layer features such as cluster size, cluster distance and surface coverage, can crucially impact the envisioned application. Gold layers of bulk (μm-range) thickness are notorious for non-specific protein adsorption. However, it remains unexplored if antifouling efficiency gets enhanced when the gold layer thickness is minimized to nm-range. It is intriguing to investigate if the copolymer composition, block length asymmetry and presence (or not) of charges affect metal cluster growth kinetics and metal cluster morphology. Gensch et al.[3] have already shown that metal clusters sputtered on PS-diblock copolymer films exhibit selectivity towards PS comonomers. Films from polysulfobetaine methacrylate–b-poly(N-isopropylmethacrylamide (PSPE-b-PNIPMAM) copolymer and from the respective hopolymers have been prepared by spin coating trifluoroethanol (TFE) polymeric solutions at $c_{polymer}$ = 25 mg/mL onto silicon wafers at 1500 rpm for 15 min, followed by 15 min annealing under TFE vapor. In-situ microfocus μGISAXS experiments were performed at MiNAXS (Petra III, DESY) using an irradiation energy of 13.5 keV at an incident angle $\alpha_i = 0.388°$ inside a magnetron DC sputter chamber (Uni Kiel), Pilatus 1 M detector and sample-detector distance = 2.462 m. Horizontal intensity $I(q_y)$ cuts, at the q_z position of the Yoneda reflection for each material, include information about in-plane correlations of gold clusters, e.g. center-to-center spacing of nearest neighbor clusters. Vertical $I(q_z)$ cuts (at $q_y = 0nm^{-1}$) depict intensity modulations at a given sputter time; the modulation fringe spacing at given times represents the actual metal layer thickness during sputtering, reaching finally a $\sim$10.8 nm thick gold layer. The effective final thickness, δ_{final}, equals the product of (constant) sputter rate with sputter time.
Fig. 6.18 demonstrates 2D color maps of $I(q_y)$ cuts vs. δ which follow the in-plane nanostructural growth of gold clusters on thin (50nm) PSPE-b-PNIPMAM diblock copolymer films as well as to their respective homopolymer analogues.

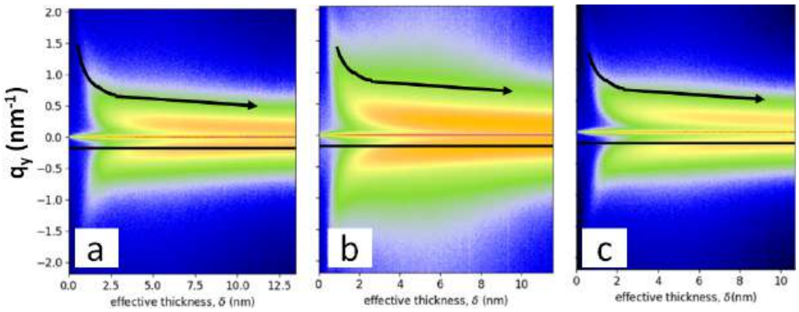

Figure 6.18:
Two-dimensional (2D) color maps from horizontal (q_y, nm^{-1}) intensity cuts vs. effective gold cluster thickness, δ, in nm, on thin ($\sim$ 50 nm) polymer films: (a) PNIPMAM$_{66k}$; (b) PSPE$_{272k}$; (c) PSPE$_{272k}$-b-PNIPMAM$_{61k}$. Intensity scale: [10^{-1} : 2×10^4].

The peak areas (using Lorentzian fits) exhibit distinct differences depending on the polymer employed, with the (larger M_w and more) hydrophilic $PSPE_{272k}$ film displaying the strongest peak intensities. Notably, the block length asymmetry exerts decrease in peak intensity. The peak position q_y^* has been measured and from which, using Bragg's law, the center-to-center distance between nearest neighbor clusters, $d_y^*, cluster$, has been calculated. Assuming hexagonal arrangement of hemispherical gold clusters [4], the calculated cluster radius, $R_{cluster}$, the ratio $2R_{cluster}/d^*_{y,cluster}$ and $d^*_{y,cluster}$ vs. δ are drawn in Fig. 6.19.

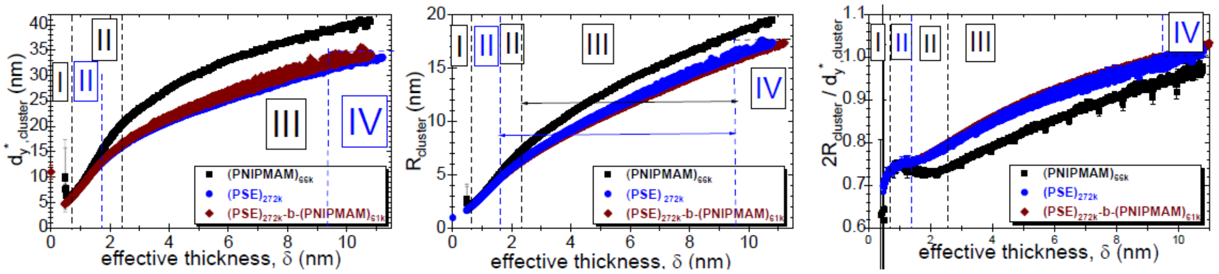

Figure 6.19:
Evolution of $d^*_{y,cluster}$ (left), $R_{cluster}$ (middle) and $2 \times R_{cluster}/\ d^*_{y,cluster}$ (right) vs. the effective gold cluster thickness, δ, on the following thin (50nm) polymer films: (black squares) PNIPAM$_{66k}$; (blue circles) PSPE$_{272k}$; (red rhombi) PSPE$_{272k}$-b-PNIPAM$_{61k}$.Dashed lines are drawn to guide the eye and indicate tentative boundaries between the different regimes.

Although distinct morphological evolution vs. δ was found depending on the (co)polymer structure, all films demonstrate the following similarities: at early sputter times ($\delta \leq$ 1nm), gold nuclei form (regime I,Fig. 6.20) with closest nuclei approach at $d^*_{y,cluster} \sim 5$ nm. Then (1 nm $< \delta <$ 2.5 nm), nuclei diffuse along the film surface and coalesce into larger clusters with $R^*_{y,cluster} \leq$ 3nm. In contrast to earlier studies [3, 4], the examined systems exhibit a rather broad (2.5 $< \delta <$ 9.5 nm, accounting up to 75 % of the δ_{final}) adsorption-driven growth crossing over to grain growth (percolation at $\delta >$ 9.5 nm) only for PNIPMAM films. Hence, rich gold cluster growth kinetics were found raising questions about the impact from charged groups and copolymer block asymmetry.Forthcoming in-situ μGISAXS investigations shall target at the impact of plasma treatment and subsequent sputter rates during either gold or silver sputtering, on the range of the adsorption driven growth.

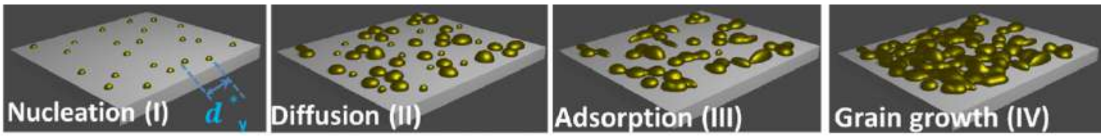

Figure 6.20:
Schematic drawings for the various gold cluster growth regimes: gold nuclei formation (regime I); nuclei coalescence into clusters and diffusion-limited cluster growth (regime II); adsorption-limited cluster growth (regime III); percolation-driven grain growth (regime IV).

[1] A. Laschewsky, A. Rosenhahn, *Langmuir* **35**, 5, 1056-1071 (2019)

[2] J. Ren, P. Han, H. Wei, L. Jia, *ACS Appl. Mater.Interfaces* **35**, 6, 3829-3838 (2014)

[3] M. Gensch, M. Schwartzkopf, W. Ohm, C. J. Brett, P. Pandit, S. K. Vayalil, L. Bießmann, L. P. Kreuzer, J. Drewes, O. Polonskyi, T. Strunskus, F. Faupel, A. Stierle, P. Müller-Buschbaum, S. V. Roth, *ACS Appl. Mater. Interfaces* **11**, 32, 29416-29426 (2019)

[4] M. Schwartzkopf, A. Hinz, O. Polonskyi, T. Strunskus, F. C. Löhrer, V. Körstgens, P. Müller-Buschbaum, F. Faupel, S. V. Roth, *ACS Appl. Mater.Interfaces* **9**, 6, 5629-5637 (2017)

7 Instrumentation and new materials

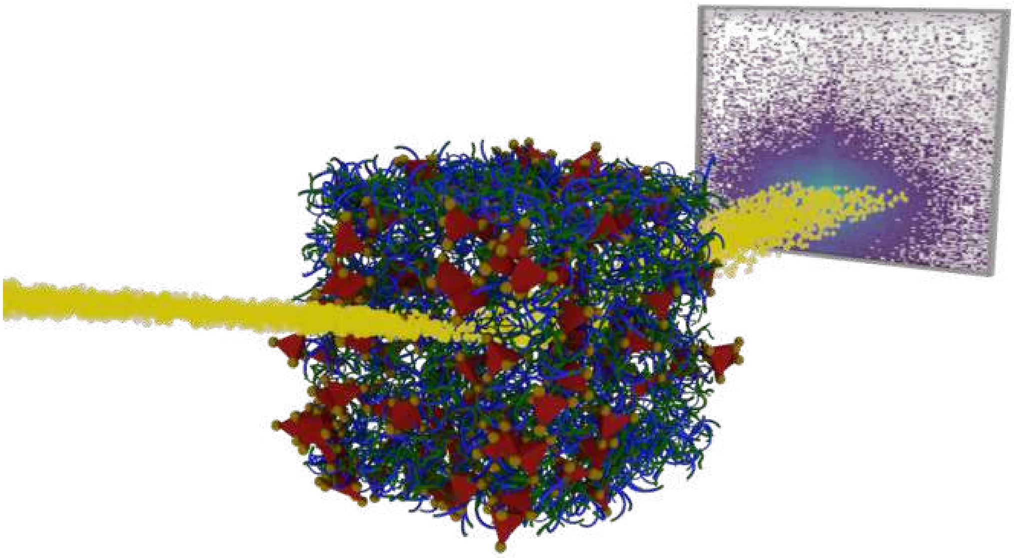

7.1 SANS and QENS investigation of solid state hydrogen storage materials

N. Aslan[1,2], W. Lohstroh[2], S. Busch[1], C. Pistidda[3], K. Pranzas[3], M. Müller[3]

[1] HZG, Garching, Germany
[2] MLZ, Garching, Germany
[3] HZG, Geesthacht, Germany

Complex hydrides like $LiBH_4$, $Mg(NH_2)_2$, $NaAlH_4$ etc. possess high hydrogen densities and are considered as suitable candidates for solid state hydrogen storage. [1] To exploit the full potential of complex hydrides it is crucial to understand the materials behavior and properties at the molecular level. In this context neutron scattering techniques are unique. Compared to X-rays, neutrons can probe hydrogen, because the scattering cross section for hydrogen is similar to other atoms. Moreover, because of the high incoherent scattering length for hydrogen, with neutron spectroscopy the mobility of hydrogen can be measured.

To analyze particle sizes after hydrogen desorption and absorption reactions the small angle neutron scattering of $6Mg(NH_2)_2 + 9LiH + LiBH_4$ was measured at the SANS-1 instrument at MLZ. [2] Furthermore, the molecular motions of $Li_4BH_4(NH_2)_3$ were investigated with quasielastic neutron scattering at the TOFTOF instrument at MLZ.

The hydrogen storage systems are prepared by ball milling to obtain fine powders and a homogenous distribution of the components. Consequently to the increased material surface area and decreased diffusion distances the reaction kinetics are improved. To keep the good reaction properties, the fine particle size should be maintained over absorption/desorption cycling.

The scattering curves from SANS at Q-values $0.005 - 0.2\ \mathring{A}^{-1}$ were fitted with a compostion of a flat background, a power law with the power -4 and a function for spherical particles. The radii of these spheres were analyzed after sample heating and after hydrogen cycling (Fig. 7.1).

The results show that cycling has only a small effect on the particle sizes. Only during sample heating the particles grow to almost triple size of the incident size. After the first hydrogen desorption the fitted spheres shrink again and stay almost constant after each hydrogen absorption and desorption.

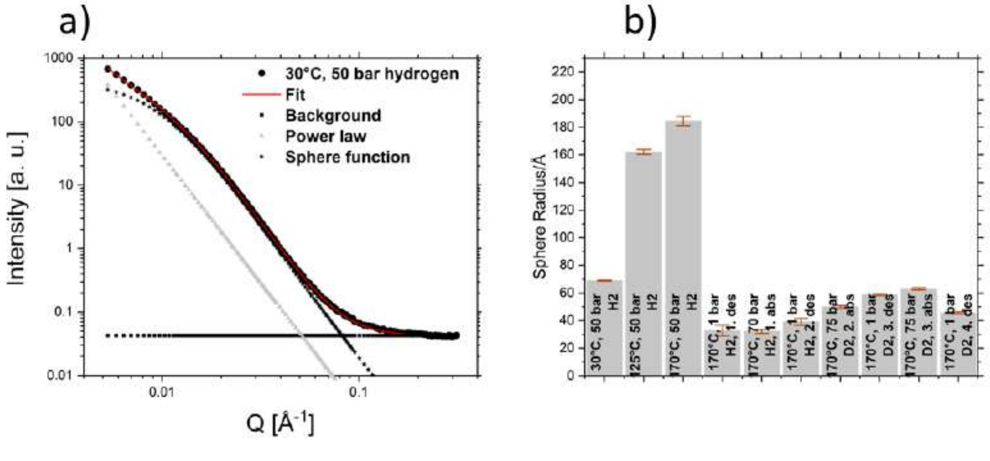

Figure 7.1:
SANS measurement of $6Mg(NH_2)_2 + 9LiH + LiBH_4$: a) Fitting of scattering curves b) Radii of fitted spheres.

Beyond the good reversibility, the metal and complex hydride composites have beneficial thermodynamics with reduced reaction temperature. In general, one problem with these materials is the low reaction kinetics. The mixture of magnesium amide and lithium hydride $2Mg(NH_2)_2 + 4LiH$ has an appealing hydrogen content as well as a low reaction enthalpy,

however, both the desorption and absorption processes take roughly 2 h, respectively. [3] In contrast, the addition of $LiBH_4$ improves the reaction kinetics. As an example, for the system $6Mg(NH_2)_2 + 9LiH + LiBH_4$ full desorption is achieved in 90 min and the absorption is complete within 10 min. [3] (Reaction conditions discussed here: Desorption at $170°C$, 1 bar H_2, Absorption at $170°C$, 70 bar H_2) The reason lying behind the improved kinetics might be that the addition of $LiBH_4$ leads to formation of the intermediate $Li_4BH_4(NH_2)_3$, which reduces the reaction enthalpy for hydrogen desorption. The reversible reaction is:
$6Mg(NH_2)_2 + 9LiH + LiBH_4 \rightleftharpoons 3Li_2Mg_2(NH)_3 + Li_4BH_4(NH_2)_3 + 9H_2$
To investigate the effect of $Li_4BH_4(NH_2)_3$ on the reaction kinetics in relation to the molecular motions, QENS spectroscopy was measured at different temperatures up to 480 K. The scattering functions were fitted with a composition of two Lorentzian, one Delta function and a flat background at different temperatures and Q-values. This composite function was convoluted with the resolution function. In the end, the half-width-at-half-maximum of the narrow Lorenz was investigated depending on Q^2 for stochastic motions (Fig. 7.2).
Indeed, the QENS measurement of $Li_4BH_4(NH_2)_3$ shows high mobility for the molecules. The BH_4 tetrahedron reveals jump-rotations with residence time in the range of 3-13 ps, becoming faster with higher temperature. At 480 K, i.e. even below the melting point, which is at 494 K, a long-range motion with a diffusion constant $0.8 * 10^{-5} \frac{cm^2}{s}$ is detected. The motion of the NH_2 pseudo-tetrahedron are supposed to be even faster. They are so fast, that they are blurred in the background. All in all, the component $Li_4BH_4(NH_2)_3$ has high degrees of mobility and this can be the reason for the fast absorption kinetics of the composite material.

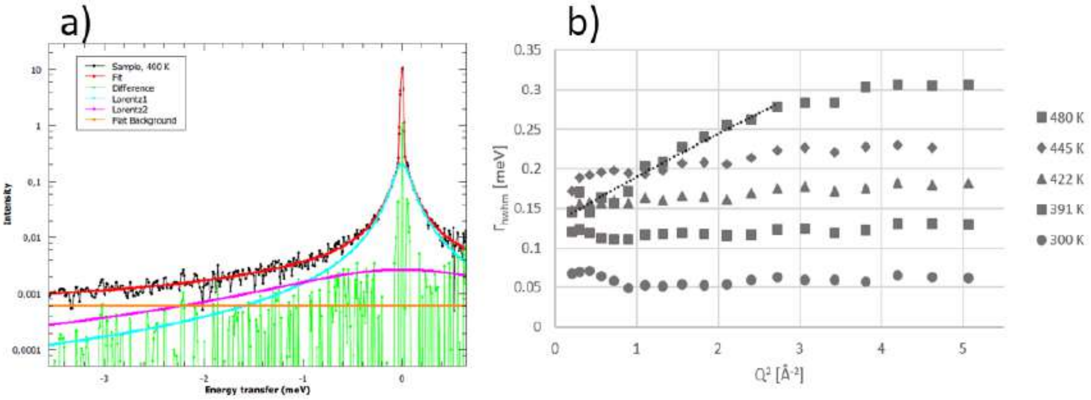

Figure 7.2:
QENS measurement of $Li_4BH_4(NH_2)_3$: a) Fitting of measured scattering functions. b) Half-width-at-half-maximum of the fitted narrow Lorentzian function. Up to 445 K the sample reveals rotational motions. At 480 K on-set of a long-range translational motion is detected.

In view of their possible use, it is mandatory to study the basic properties of complex hydrides. SANS and QENS techniques give important information that is needed to further develop and optimize hydrogen storage materials and to make them appropriate for application.

[1] C. Milanese, T. R. Jensen, B. C. Hauback, C. Pistidda, M. Dornheim, H. Yang, L. Lombardo, A. Zuettel, Y. Filinchuk, P. Ngene, P. E. de Jongh, C. E. Buckley, E. M. Dematteis, M. Baricco, *Int. J. of Hydr. Ener.* **44**, 7860-7874 (2019)

[2] N. Aslan, C. Horstmann, O. Metz, O. Kotlyar, M. Dornheim, C. Pistidda, S. Busch, W. Lohstroh, M. Müller, K. Pranzas, *J. of Neutr. Res.*, (2020), in press

[3] J. Hu, Y. Liu, G. Wu, Z. Xiong, Y. S. Chua, P. Chen, *Chem. Mater.* **20**, 4398-4402 (2008)

7.2 Manufacturing techniques for monolithic U-Mo fuel for high-performance research reactor conversion

B. Baumeister[1], C. Schwarz[1], C. Steyer[1], W. Petry

[1] MLZ Garching, Germany

The high-density fuel working group at the high-performance research reactor FRM II is working actively towards the conversion of FRM II to lower enriched fuel. For this conversion, new high-density fuel is required to compensate the loss of fissile material with a higher uranium density. The most promising candidate for this conversion is a uranium-molybdenum alloy (U-10wt.%Mo) in a monolithic form, e.g. a thin foil of U-Mo. As these fuel foils will be put inside aluminum alloy cover plates, the bare foils need to be coated by an interdiffusion barrier layer to prevent the harmful uranium-aluminum interdiffusion under in-pile irradiation.

The required processes to fabricate this monolithic U-Mo fuel are being developed since more than 10 years, not only by the high-density fuel working group at FRM II but also e.g. within the US research reactor conversion program. In contrast to the processes proposed by the US Laboratories involved, FRM II is focusing its research efforts on the production of uncoated U-Mo foils, the interdiffusion layer application by physical vapor deposition (PVD) and the Framatome-proprietary C2TWP aluminum cladding application process, as shown in Fig. 7.3.

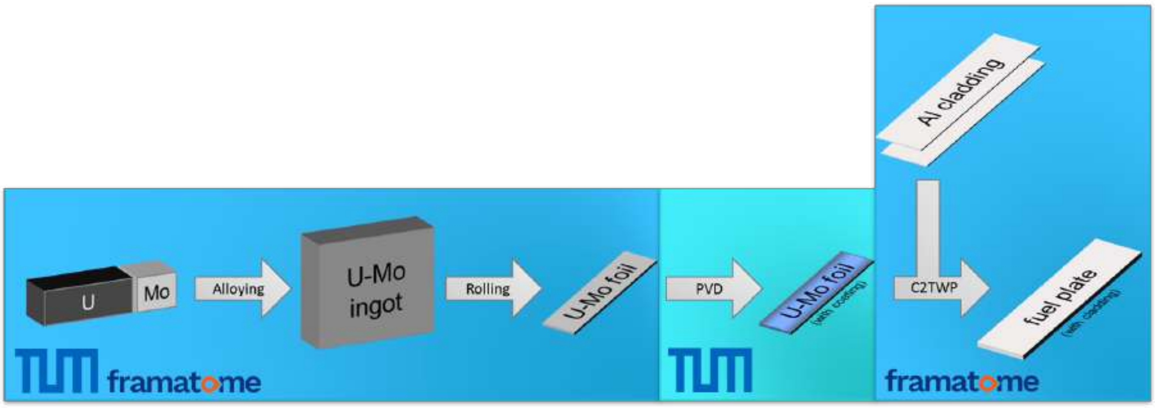

Figure 7.3:
The proposed European fabrication process for monolithic U-Mo fuel.

In 2019, the working group has dealt with the following projects, which are described hereafter:

Optimization of the PVD coating process in mini-size geometry

In the past, the working group has successfully demonstrated the PVD process for monolithic U-Mo fuel using a versatile mini-size device (substrate size 82.5 mm x 19 mm) by coating 7 LEU U-Mo foils for the EMPIrE in-pile irradiation test with 2x25 μm zirconium (Zr) as interdiffusion barrier. The irradiation has been completed successfully in 2018 and the post-irradiation examination (PIE) is currently ongoing at Idaho National Laboratory (INL). Based on this manufacturing experience and first PIE results, the working group has further developed the PVD process also in 2019. The main goals are the improvement of the mechanical coating properties and the compatibility with the C2TWP cladding application process as well as the adaption of the process for alternative coating materials.
Thus, several PVD coating studies were performed using mini-size stainless steel surrogate

foils with (i) a softer and more flexible Zr coating and (ii) a molybdenum (Mo) or tungsten (W) coating. The coating materials Mo and W are being considered as alternative interdiffusion barrier layers which allow thinner layers (less than 2x5 μm) as well as a better irradiation resistance, whereas the softer and more flexible Zr coating can potentially reduce the mechanical coating damage during C2TWP. Both types of samples are currently being processed by C2TWP at Framatome-CERCA.

Upscaling of the PVD coating process

Based on the abovementioned manufacturing experience and irradiation results, the working group has in parallel built a full-size PVD coating device (substrate size 762 mm x 45 mm) for the upcoming in-pile irradiation test FUTURE-MONO-1, which is planned for 2023. This device, which is shown in Fig. 7.4, further incorporates partly industrial PVD components and therefore allows higher coating efficiency and shorter process times. In the last year, the device has been finally commissioned and basically parametrized. A set of process parameters was found which allows the successful application of a 2x5 μm zirconium coating onto stainless steel surrogate foils. A first study of those foils' compatibility with C2TWP is currently ongoing.

Figure 7.4:
The full-size PVD coating device is located inside a high-purity argon glovebox for operator safety and product quality.

Rolling of uncoated U-Mo foils at Framatome-CERCA

Previously, uncoated U-Mo foils for PVD and C2TWP studies have been procured from prototypic production at either US National Laboratories or BWX Technologies Inc., the industrial fuel fabricator for US high-performance research reactors. As the proposed US fuel fabrication process does no longer require uncoated U-Mo foils, those must be procured from another source in the future. Thus, the working group has partnered with FRM II's fuel fabricator, Framatome-CERCA, to develop and put into operation a European U-Mo foil fabrication capability. It is intended to use U-Mo foils from this capability for the FUTURE-MONO-1 irradiation test.

7.3 Simulation of an industrial device for the generation of metal particles by atomization

S. Geara[1,2], S. Adami[3], O. Bonnefoy, S. Martin[1], J. Allenou, B. Stepnik[2], W. Petry

[1] EMSE, France
[2] CERCA, Framatome, France
[3] AER, Garching, Germany

International nuclear non-proliferation agreements gradually lead to the replacement of highly enriched uranium with low enriched uranium (Uranium-Molybdenum alloy). In most cases, the implementation of the UMo alloy is based on powder metallurgy. Thus, it is desirable to generate metal particles having a spherical shape and a well-controlled size distribution in the range of 1 to 100 micrometer. This project focuses on the REP (Rotating Electrode Process) for synthesizing UMo alloy particles to control the shape and size of these particles.

The dynamic of atomization and liquid breakup is mainly dominated by surface tension forces. Because these phenomena occur on small length scales, the development of a proper surface tension model can help greatly in physically developing these applications. However, simulating deforming phase interfaces with strong topological changes is still today a challenging task. For this numerical work, the meshfree Lagrangian numerical method SPH (Smoothed Particle Hydrodynamics) was chosen because it presents the advantage of simulating free surfaces with high deformations. The general idea behind SPH lies in representing the fluid by a series of discretization points/particles each representing a mass of fluid. The continuity of the fluid and its properties are recovered by the spatial convolution of the physical properties of each particle by a kernel or smoothing function, see Fig. 7.5

In our study, we are focusing on the CSF method for modelling surface tension in SPH, origonally proposed by Brackbill [1], because it is a general approach that uses the physical properties of the fluid and does not need to be numerically calibrated for each simulation case. In this approach, the surface tension force is converted to a force per unit volume and is applied only on particles close to the interface. The main challenge of this method is to accurately calculate the normal vectors and the curvature at the interface. Many of the CSF models found in the literature are only valid for fluid-fluid systems. However, for free surfaces, the standard SPH approximations to calculate the normal vector and curvature of the interface suffer from the lack of "full support", i.e. the omitted and therefore missing gas particles. To overcome this problem some correction techniques were proposed in the literature. Many of these correction methods were tested and compared with each other for static and dynamic test cases. For our

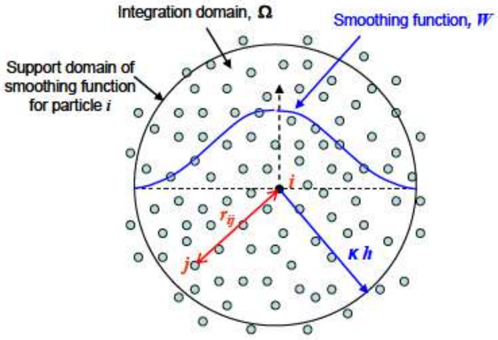

Figure 7.5:
Overview of the SPH method (particle j is one of the neighbors of particle i and kh is the width of the smoothing/kernel function)

application, the most suitable correction method is found to be the correction matrix for the kernel gradient [2] that takes into account the missing gas particles.
Another problem in SPH when simulating free surface flows with a large deformation is the tensile instability. In this case, attractive forces can lead to particle clumping and cluster formation. This instability can lead to unrealistic fluid behavior and sometimes to a complete explosion of the simulation. To avoid this instability, a particle shift position technique, suitable for free surface simulations has been implemented. The particles are shifted according to Fick's diffusion law, this means from high concentration regions towards those of lower concentration [3].
With the initial SPH code implemented in C++ by Dr. Adami and his team and with adding the surface tension model and the necessary corrections we were able to partially reproduce a test case for the fragmentation of a liquid column under the effect of surface tension using the physical properties of water. We tested the fragmentation of a liquid column by applying an initial perturbation in the velocity field. For more details on this test case please refer to [4]. It is worth mentioning that in most of the presented models in the litterature for free surface flows the numerical validation examples were conducted at relatively high fluid viscosities.

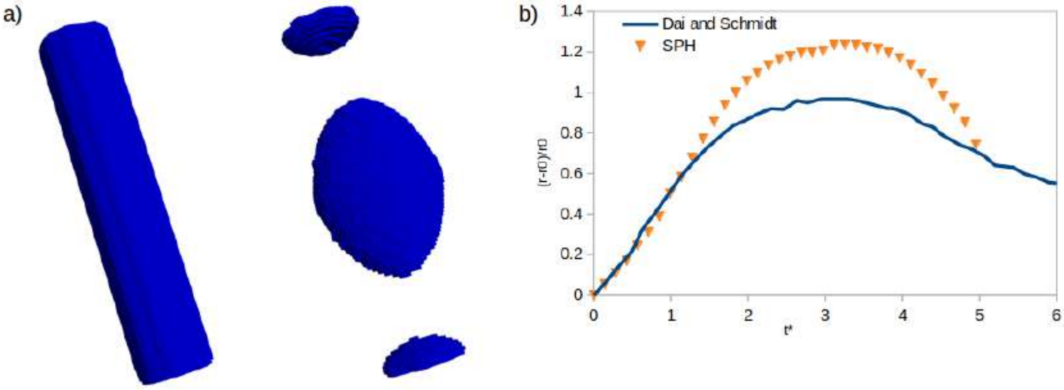

Figure 7.6:
a)Results of the SPH simulation for liquid jet breakup (Re=18 and We=1.4) and b) Disturbance growth (r0 is the initial column radius and r is the maximum distance measured from the axis of symmetry) as a function of non-dimensional time (SPH results compared to Dai and Schmidt FE results)

As shown in Fig 7.6 we were able to conduct a stable simulation for liquid water fragmentation. However, by comparing our results with those presented in the article of Dai and Schmidt, we can see that the dynamic behaviors during the rupture are not the same. It seems that in the SPH simulation there is an excess of energy in the system probably du to the added corrections. We are currently working on fixing this problem and trying to adapt the code to be able to simulate numerically more challenging cases with high density and low viscosity, as it is the case for the UMo. To conclude, the surface tension force is considered to be a major part in modeling the REP, it should be coupled with other aspects (thermal, rotation, ...) in order to obtain a complete model for the REP.

[1] J. Brackbill, D. Kothe, C. Zemach, *J.Comput. Phys.* **100**, 335-354 (1992)

[2] J. Bonnet, T.-S. Lok, G. Kaune,*Comput. Methods Appl. Mech. Eng.* **180**, 97-115 (1999)

[3] X. Xu, P. Yu, *Computational Mechanics* **62**, 963-990 (2018)

[4] M. Dai, S.P. Schmidt *Journal of Computational Physics* **208**, 228-252 (2005)

7.4 Fading of Lithium ion batteries: Combined investigation by neutron diffraction and electrochemistry

D. Petz, A. Senyshyn[1], V. Baran[1], M. Mühlbauer[1], A. Schökel[2], C. Paulmann[2]

[1] MLZ, TUM, Garching, Germany
[2] DESY, Hamburg, Germany

Cycling stability and capacity fading of Li-ion batteries are highly relevant for their application. A variety of mechanisms directly leading to the capacity losses upon cycling are known, e.g. formation of passivation layers, losses of cyclable lithium etc. Typical Li-ion cells are characterized by non-uniform distributions of current and temperature along with gradients in electrolyte and lithium concentrations, but cell fatigue often leads to the further development of heterogeneities [1-3].

Among other techniques, the electrochemical behavior can be studied with electrochemical impedance spectroscopy. By varying the frequency of the an AC signal applied to a battery the electrochemical response reveals the behavior of different processes. Commmercial 18650-type lithium-ion batteries were cycled with high currents with different number of cycles, with a few low current cycles were applied for capacity regeneration. The obtained resistances of the solid-electrolyte-interface layer R_{SEI}, the charge transfer R_{CT} and the diffusion W (Fig. 7.7) increase upon cycling in correspondence to the loss of active material.

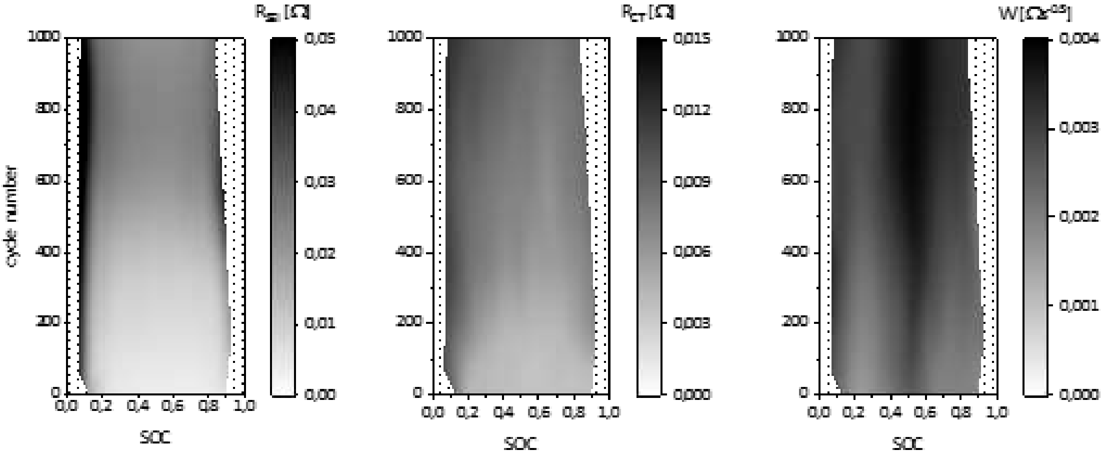

Figure 7.7:
Resistances of the SEI layer R_{SEI} (left), the charge transfer R_{CT} (middle) and diffusion W (right) in dependence of the state-of-charge (SOC) and the cycle number

High-resolution neutron powder diffraction is used for straightforward in-situ quantification of active lithium amount stored in the electrode materials. Experiments were carried out using the instrument SPODI [4] at the FRM II, Munich. The ratio between remaining capacity of differently aged batteries and the remaining active lithium revealed a direct correlation (Fig. 7.8).

X-Ray diffraction radiography has been applied in order to map the local differences in the lithium-concentration. Experiments were carried out ex-situ on the graphite anode in the fully charged state after disassembling of a fresh and a 400 times cycled battery. Experiments with synchrotron radiation were carried out at the P24 beamline for the fresh cell and the P02.1 beamline for the aged cell at Petra III, Hamburg.

The lithium-concentration x in Li_xC_6 in the graphite anode of the fresh cell has been found to be uniformly distributed in first approximation Fig 7.9 (top). The parts with lower lithiation

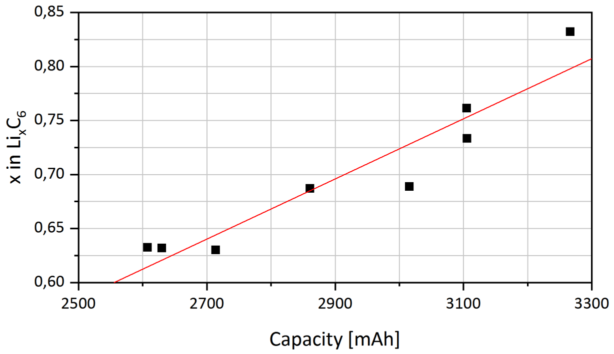

Figure 7.8:
Correlation between the lithium concentration x in Li_xC_6 and the remaining capacity at slow charing rates

correspond to the lacking electrode material at the position of the current tabs and at the beginning and the end of the electrode stripe.

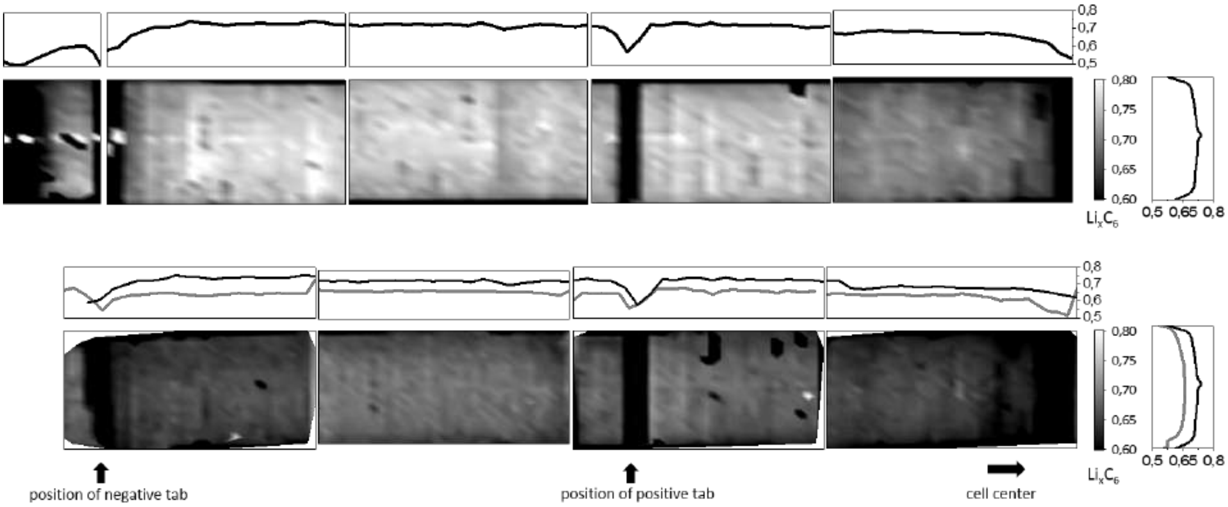

Figure 7.9:
Lithium-concentration x in Li_xC_6 in the fully lithiated graphite anode of a fresh (top) and aged (bottom) 18650-type lithium-ion battery.

The aged graphite anode reveals a non-uniform lithium-distribution towards the cell center and towards the top and the bottom of the stripe Fig. 7.9 (bottom). With increasing cell aging the distribution becomes more inhomogeneous. The loss of lithium is more present towards the cell center and at the top and bottom part of the graphite anode.

In summary, these findings can help to understand the interplay of different fading mechanisms upon cell cycling and further help to build better batteries with improved performances.

[1] G.S. Zhang, C.E. Shaffer, C.Y. Wang, C.D. Rahn, *J Electrochem Soc* **160**, A610-A615 (2013)

[2] P.J. Osswald, S.V. Erhard, A. Rheinfeld, B. Rieger, H.E. Hoster, A. Jossen, *J Electrochem Soc* **329**, 546-552 (2016)

[3] A. Senyshyn, M.J. Muhlbauer, O. Dolotko, M. Hofmann, H. Ehrenberg, *Sci Rep-Uk* **5**,(2015)

[4] Heinz Maier-Leibnitz Zentrum, *Journal of large-scale research facilities* **1**, (2015)

7.5 FRM II core modeling

C. Reiter[1], D. Bonete-Wiese[1], K. Faust[1], M. Kirst[1], J. Mercz[1], R. Schönecker[1],
K. Shehu[1], W. Petry

[1] MLZ Garching, Germany

The reactor physics group at the FRM II actively supports the conversion of the compact fuel element to a uranium enrichment which is significantly lower than the current one of 93%. Even slight changes in the core geometry and the different fuel behavior require a new core design and a re-evaluation of the safety assessments in normal operation as well as in off-normal transients. For developing a new core design several coupled calculations taking into account the neutronics including burnup, hydraulics and the mechanical behavior of the fuel element have to be performed. In order to have possible, compatible core designs available until the end of 2022, a systematic parameter study to identify such designs was launched at the beginning of 2019. In addition to the conversion of the reactor, the reactor-physics group also supports the reactor operations group.

FRM II full-core model As a high-performance research reactor, the FRM II has challenging cooling conditions. To ensure constant cooling in all possible scenarios, the cooling channels in the fuel element are involute shaped to have a constant channel width. Recently, this very special shape could not be modeled by any neutronics code and one had to rely on approximations [1, 2] or subsitutional [3] geometries. In [4], the reactor physics group implemented the exact involute curve in the neutronics code Serpent 2 which is developed by the VTT, Finland. Having a mathematical exact model of the fuel zone, the tank installations like cold and hot source, irradiation positions and the converter plate have been reassessed by means of comparing with technical drawings and CAD models. With all this work completed, a neutronics model of FRM II's core of very high quality is now available.

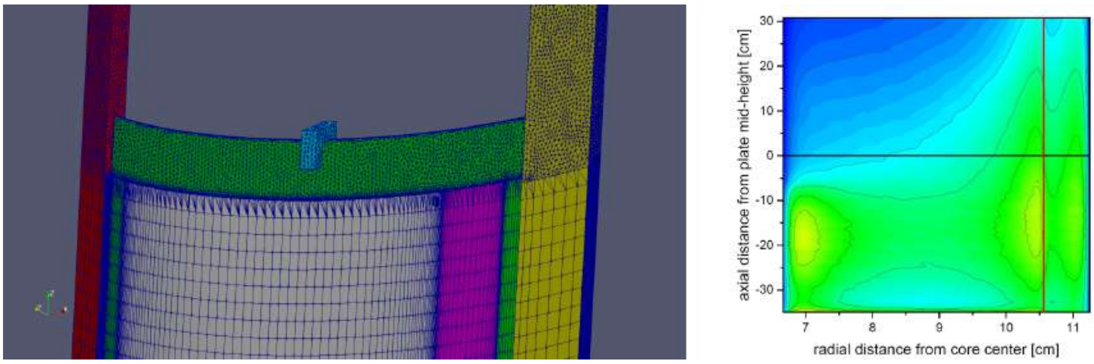

Figure 7.10:
(left) Calculation mesh of a fuel plate used in OpenFOAM. (right) Heat flux in a fuel plate as calculated by pltemp for the current core.

Coupled hydraulic calculations Safety parameters like hot-spot and hot-channel factors will have to be determined in the parameter study. This requires coupled neutronic and hydraulic calculations. Until today, the computational capabilities have been rapidly progressing, so that modern CFD calculations with state-of-the-art codes, like Ansys CFX or OpenFOAM give precise information about the hydraulics even in the thin cooling channels of the fuel element. This could be proved by comparing experimental data of the Gambill test with corresponding CFD

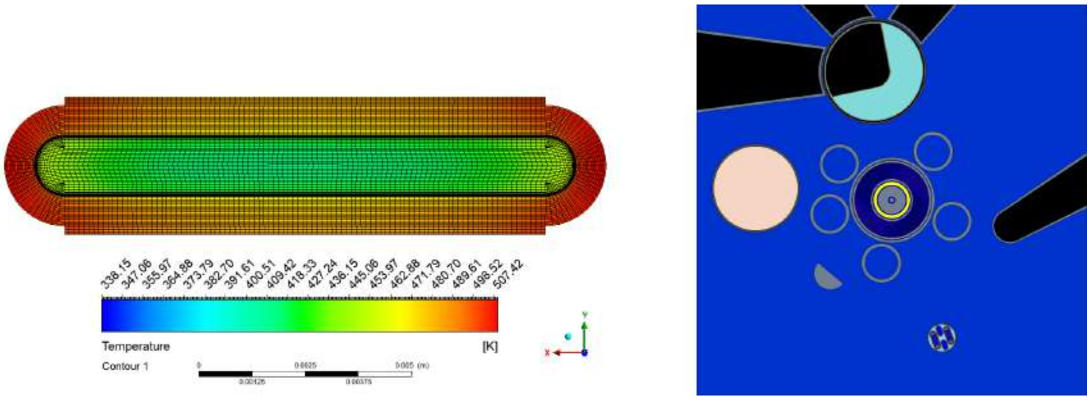

Figure 7.11:
(left) Temperatures as calculated with Ansys CFX for the Gambill test. (right) Sketch of the Serpent 2 full-core model.

calculations. It could be successfully shown that the CFD codes reproduce the turbulent flow in the narrow channel of this experiment very well as well as the heat conduction [5].
The drawback in using these codes is the time consuming mesh generation. Because the number of possible models exceed a hundred, a pre-selection in 1D will be made using pltemp which is developed by the Argonne National Laboratory. First calculations of the current HEU core show very well matching results with previous works, including Siemens during the licensing [6]. The preconnected 1D calculations will exclude most of the investigated models due to non sufficient safety factors. Once the designs are condensed to only few remaining designs, these will be further studied using a CFD code coupled to Serpent 2. Currently, well matching results could be obtained with Ansys CFX and OpenFOAM.

Serpent for medical applications In a recently started collaboration with the VTT, we started to extend Serpent 2 capabilities for medical applications. With the MEDAPP instrument, the FRM II provides optimum conditions to further develop the computational capabilities undergirded with experimental measurements [7]. As a first step a detailed Serpent 2 model of MEDAPP will be created.

[1] A. Röhrmoser, *Nuclear Engineering and Designs* 240, **1417-1432** (2010)

[2] H. Breitkreutz, *Coupled Neutronics and Thermal Hydraulics of High Density Cores for FRM II*, Dissertation (2010)

[3] C. Reiter, H. Breitkreutz, A. Röhrmoser, A. Seubert, W. Petry, *Annals of Nuclear Energy* 131, **1-8** (2019)

[4] K. Faust, H. Breitkreutz, C. Reiter, W. Petry, *RRFM* (2019)

[5] K. Shehu, C. Bojanowski, A. Bergeron, W. Petry, C. Reiter, *PHYSOR* (2020)

[6] R. Schönecker, W. Petry, C. Reiter, *RRFM* (2020)

[7] C. Reiter, T. Chemnitz, W. Petry, V. Valtavirta, J. Leppänen, *RRFM* (2020)

7.6 Heavy ions irradiation in nuclear fuel development

J. Shi[1], S. Matuschik[1], C. Schwarz[1], W. Petry

[1] MLZ, Garching, Germany

The interdiffusion layer problem and heavy ion irradiation

For high density metallic Uranium fuel of research reactors, the growth of an interdiffusion layer (IDL) that forms between U fuel meat and the aluminium matrix and/or the Al cladding during irradiation has been intensively studied. Due to its inferior irradiation properties, the growth of the IDL can lead to exponential fuel swelling and therefore needs to be studied. Furthermore, measures need to be taken to prevent the interdiffusion. Ion irradiation techniques can be effective in simulating fission damage on short laboratory time scales over a large range of experimental conditions in order to develop more detailed scientific understanding and to avoid the complexity and high costs of handling highly radioactive samples. The major source of irradiation damage in fuel assemblies of fission reactors are energetic fission fragments, which are charged particles that also can be produced using 80 MeV Iodine-127 ions at the Maier-Leibnitz Laboratorium (MLL). As a convenient tool, heavy ion irradiation has been used to produce an interdiffusion layer comparable to those occurring during in-pile irradiation.

Microstructural evolution

The microstructure evolution and phase transformation of the interdiffusion layer resulting from the interaction between U-Mo and Al in U-Mo/Al bilayer systems irradiated from 140°C to 275°C are investigated. Scanning and transmission electron microscopy with EDS were performed to determine the nature and the composition of the induced interdiffusion layer. The present analysis reveals that the U-Mo–Al interdiffusion layer is completely amorphous up to an irradiation temperature of 200°C. Nanograins start to form from 220°C from the Al layer to the U-Mo layer (Fig. 7.12:). The γ-U-Mo and the Al layers retain their crystallinity.

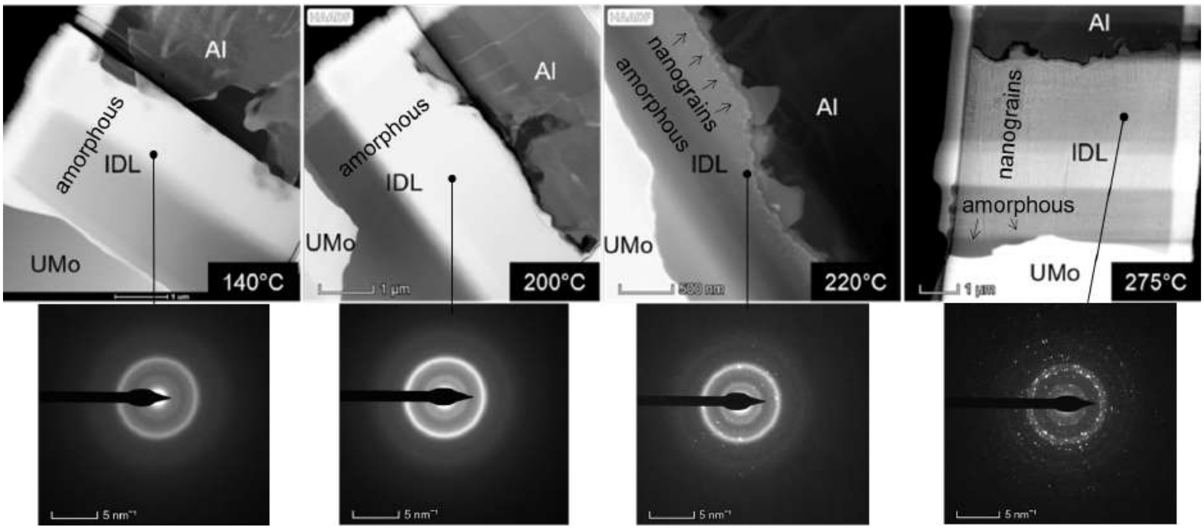

Figure 7.12:
Microstructural evolution of IDL induced in UMo/Al systems by ion irradiation from 140°C to 275°C

W coating as a diffusion barrier

In order to suppress the severe U-Mo-Al interdiffusion reactions, PVD deposited W as a diffusion barrier is applied between the U-Mo and Al. A wide range of coating parameters has been tested to identify optimal sputter parameters for thin W coatings on monolithic U-Mo substrates. Fundamental trails on stainless steel with substrate heating or bias voltage were performed. By using subsequently optical and scanning electron microscopy the resulting layer adhesion, deposition rates, densities and crystal growth structures have been determined. Furthermore bending tests investigated the influence of tensile stress on the applied coating. Emerged from it, substrate heating turns out to be the preferable method for tungsten coating. However, the rough, uneven surface of the U-Mo foil leads to an irregular coating layer thickness across the sample. Therefore a supplementary substrate preparation step has been implemented. Prior to the already necessary chemical cleaning of U-Mo substrates, the surface gets polished and consequently smoothed out. This additional preparation step allows the production of uniformly layer thickness of tungsten coatings on uranium-molybdenum samples. The produced samples (Fig. 7.13:) are utilised for the future heavy ion irradiation test.

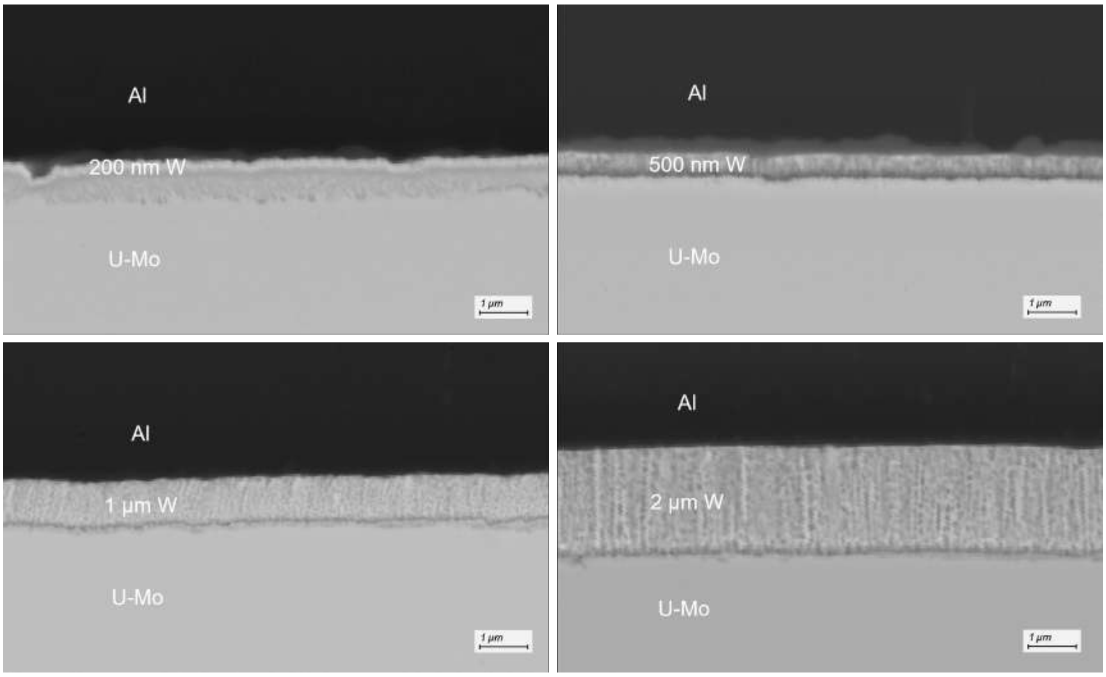

Figure 7.13:
Al/W/U-Mo samples prepared for the future heavy ion irradiation test

7.7 Development of a dry separation technique for the extraction and purification of molybdenum from uranium

R. E. Stene, T. Chemnitz[1], F. Kraus[2], W. Petry

[1] MLZ, Garching, Germany

[2] Philipps-Universität Marburg, Germany

Over the past decade, great international effort has been made to decrease the uranium-235 content in targets for molybdenum-99 production from highly enriched uranium (HEU) to low enriched uranium (LEU). With this change comes many technical and mechanical challenges and problems. The most obvious is that decreased uranium 235 concentrations in targets will be met with decreased molybdenum-99 yields. That is, the switch from HEU to LEU targets will require the irradiation of a higher number of targets to meet world demands for molybdenum-99. The irradiation of more targets, along with the decreased yield per target, will subsequently lead to an increase in solid and liquid radioactive wastes.

Currently, aqueous-based separation techniques are used for the removal and purification of molybdenum from the irradiated targets. Based on these techniques, Lee and coworkers estimate a 200 percent increase in intermediate level liquid wastes (ILWs) per year [1]. To combat these large increases in ILWs, a joint research project between the Philipps University Marburg and FRM II is aimed at developing dry separation techniques for the purification and extraction of molybdenum from uranium. This work focuses on the production of uranium and molybdenum hexafluorides from uranium and molybdenum metals using a fluorination line and the subsequent separation of the hexafluorides from one another using dry-chemical techniques (i.e. without the use of water), see Fig. 7.14. The separation procedure is complicated by the fact that molybdenum-99 only accounts for six percent of the fission products and only for about 0.1 percent of the target mass. All work pertaining to this project is currently conducted at the Philipps University Marburg.

uranium disc before fluorination

uranium hexafluoride recovered from cold trap

Figure 7.14:
Uranium sample before and after fluorination.

During 2019, three dry-chemical processes for the extraction of molybdenum from uranium have been developed. All three of them have been tested for separation efficiency using Inductively Coupled Plasma Mass Spectrometry (ICP-MS) or Microwave Plasma Atomic Emission Spectroscopy (MP-AES).

The first separation technique employs the difference in vapor pressure of molybdenum hexafluoride and uranium hexafluoride for separation. Starting from the elements, both compounds are synthesized using a fluorine containing precursor in a fluorination line and separated in cold traps, which are held at different temperatures. Analysis of this separation technique using MP-AES shows it to be able to remove 95 percent of the uranium while at the same time recovering 80 percent of the molybdenum.

The second separation technique employs a photochemical approach using a gaseous fluorine scavenger. To perform this separation, a mixture of uranium hexafluoride and molybdenum hexafluoride (both volatile chemicals at room temperature) are placed in a transparent reaction vessel. The fluorine scavenger is placed over the sample mixture of uranium hexafluoride and molybdenum hexafluoride and then the mixture is irradiated for a specific time. During this process, the volatile uranium hexafluoride is reduced to a non-volatile species. After a complete reduction of uranium hexafluoride, the volatile and unreacted molybdenum hexafluoride can be pumped away from the reaction vessel. Analysis of this separation technique using ICP-MS shows the technique's effectiveness in removing molybdenum from uranium to be over 98 percent.

The third separation employs the use of a liquid fluorine scavenger and additional UV irradiation to separate molybdenum hexafluoride from uranium hexafluoride. To perform this separation, a mixture of molybdenum hexafluoride and uranium hexafluoride are placed in a reaction vessel. Onto this mixture, the scavenger is condensed and the sample is irradiated. Similar to the first separation technique, uranium hexafluoride is reduced and the volatile molybdenum hexafluoride remains unreacted. After complete reduction of uranium hexafluoride, molybdenum hexafluoride can be removed from the sample via distillation. Analysis using ICP MS shows this techniques effectiveness in removing molybdenum from uranium to be over 98 percent.

Thus, a combination of the different separation procedures should further increase the purity of the deployed uranium and is subject of current investigations.

In addition to the investigation of the dry-chemical separation of molybdenum and uranium, fluorination experiments for the synthesis of high valent platinum metal fluorides have been performed. Thereby, their hexafluorides are of special interest, as they possess a very high oxidation potential. Thus, the first noble gas compound was synthesized using platinum hexafluoride. Using the same line as for the fluorination of uranium and molybdenum, the synthesis of several elements of the sixth period was successful, namely the hexafluorides of rhenium, osmium and iridium as well as the heptafluoride of rhenium, see Fig. 7.15.

osmium powder before fluorination

osmium hexafluoride recovered from cold trap

Figure 7.15:
Osmium sample before and after fluorination.

[1] S. K. Lee, G. J. Beyer, J. S. Lee, *Nucl. Eng. Technol.* **48**, 613-623 (2016)

7.8 Investigation of binary Zr-Ti melts processed by electromagnetic levitation (EML)

S. Szabó[1,2], D. Holland-Moritz[2], F. Yang[2], T. Voigtmann[2], Z. Evenson[1], W. Lohstroh[1], A. Meyer[2] and W. Petry

[1] MLZ, Garching, Germany

[2] DLR, Köln, Germany

Knowledge on the properties of metallic melts is essential to understand the solidification of metals. During the transition from the liquid state to a crystalline state, atoms form a long-range ordered system, emerging from a disordered system. Here, the atomic transport mechanisms in the liquid phases play an essential role. However, processing of some metallic melts is rather challenging, due to the respective temperatures and the chemically highly reactive nature of metallic melts, e.g. sample-container reactions and oxidation. Containerless-processing of melting metallic samples by an inductive coil, so called electromagnetic levitation (EML), became a utile technique to investigate such melts.

Neutrons enable a detailed microscopic probing of structure and dynamics in liquid-state due to their wavelength, which is comparable to typical interatomic spacing of 1-2 Å, and with energies similar to excitation energies in condensed matter. Quasielastic neutron scattering provides simultaneously information on the structure (from the momentum transfer) and dynamics (from the energies gain/loss of the scattered neutrons) of the melt.

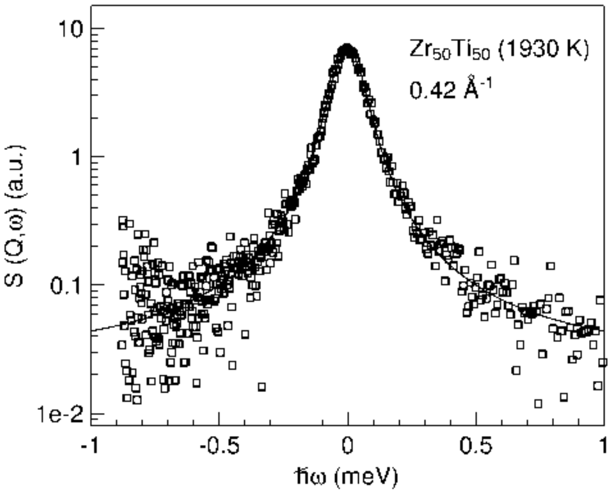

Figure 7.16:
Dynamical structure factor $S(Q, \omega)$ of liquid $Zr_{50}Ti_{50}$ at 1930 K at a momentum transfer of $q = 0.42\ \AA^{-1}$

We investigated binary Zr-Ti melts. Zr and Ti are of the same early-transition metal group in the periodic table. Alloyed they compose a completely miscible system, which is the binary boundary system for many bulk metallic glasses (BMGs), e.g. Zr-Cu-Ti, and stable quasi-crystals, e.g. Zr-Ti-Ni. For these systems a relevant impact of chemical short-range order (CSRO) on the liquid dynamics is reported. Fig. 7.16 shows a dynamical structure factor, $S(Q, \omega)$ of liquid $Zr_{50}Ti_{50}$ at a temperature of 1930 K measured at the multi-disc chopper time-of-flight spectrometer TOFTOF at the Heinz Maier-Leibnitz Zentrum (MLZ) at Garching. The broadening of the elastic line (FWHM) gives direct access to the self-motion of atoms. Since QENS probes atomic motion directly on a pico-second time scale, which is not affected by any convective flow, this allows a determination of the diffusion coefficient on an absolute scale with errors typically

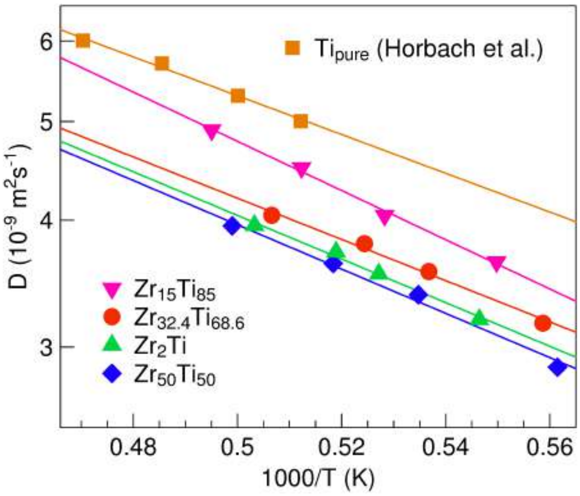

Figure 7.17:
Self-diffusion coefficients of Ti in Zr-Ti melts, measured using electromagnetic levitation (EML) at TOFTOF, MLZ.

smaller than 5 %. Its high neutron flux and very low instrumental background make TOFTOF ideal for carrying out such experiments with small samples.
In Fig. 7.17 self-diffusion coefficients of Zr-Ti melts measured utilizing EML at TOFTOF are depicted. The experimental error bars are on the order of the symbol size. Due to the element specific incoherent scattering cross-sections (σ_{Ti} = 2.87 barn, σ_{Zr} = 0.02 barn) only the motion of Ti-atoms in the melt is measured. The self-diffusivity of Ti follows an Arrhenius behavior over the entire investigated temperature range. At a given temperature the liquid self-diffusion coefficient of the investigated alloys decreases with increasing Ti content. Similar characteristics can be described considering a simple hard-sphere model, where only the topology of atoms is reflected. In-situ neutron diffraction shows that barely any chemical short-range order (CSRO) is present in Zr-Ti melts and the structure is indeed dominated by topological packing. This is in line with our results of the concentration dependent change in diffusivity.

References

[1] J. Horbach, *et al.*, Phy. Rev. B. **80.21**, 212203 (2009).

7.9 Development of a micro peel-stress testing procedure for miniature adhesive joints for MEMS devices

R. Unkelbach[1], J. H. Kuypers[1], C. M. Papadakis

[1] Blickfeld GmbH, München, Germany

In the last decades, traditional bonding techniques have been increasingly replaced by adhesive joints. Applications in highly demanding fields like automotive or aerospace use adhesive joints due to their flexibility, low cost and high performance [1]. Nevertheless, skepticism has prevailed in the past in regards to the longevity of adhesive joints. The performance of an adhesive joint is not only sensitive to numerous process parameters but also the specific joint geometry. Understanding and control of the geometry of the joint is key to understand the stress distribution throughout the joint, often indicating high stress areas which initiate a potential failure. Although standardized testing procedures are very convenient to compare and access the failure limits of different adhesives, they are based on simplified geometries and reference failures to a mean stress. On the other hand, using the actual component to conduct performance tests is often not feasible due to limitation of mounting or challenges applying a well-defined load condition. In particular, the evaluation of yield limits for small adhesive joints, as used in microelectromechanical systems (MEMS), is challenging.
The present work is motivated by a micromechanical mirror structure which needs to withstand a high number of cycles during its service time ($> 10^9$ cycles). Performing adhesive tests with the real component is only possible to a limited extent, as accelerated testing using overstressing is desired. Therefore, we developed a novel approach to identify a micromechanical test that causes comparable stresses as the real structure. The results may be transferred to the real device with the help of finite element modelling and enable to predict the performance throughout the life-time of the micromechanical device.

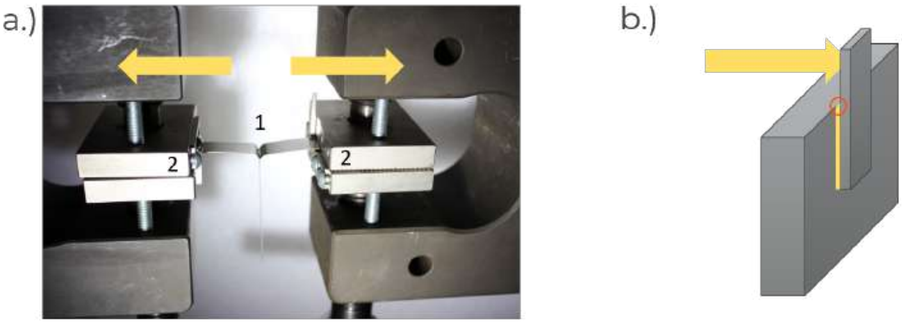

Figure 7.18:
T-Peel setup with specimen (1) and camps (2) (a) in comparison to Micro-Peel design (b). Applied force is indicated with yellow arrows.

A finite element analysis of the micromechanical device revealed that the most critical stress component is the peeling stress. In order to test the limits of the used adhesive resin, a standardized T-Peel test based on DIN EN ISO 11330:2010-06 was performed. The setup is shown in figure 7.18 a.). $200\,\mu\mathrm{m}$ thick steel specimen were prepared to investigate the performance of different epoxy resins as well as one polyurethane acrylate layer, all with a bondline thickness of $(20 \pm 5)\,\mu\mathrm{m}$. The polyurethane acrylate with a Young's modulus below $1\,\mathrm{GPa}$ results in the highest mean force with $(11.0 \pm 0.5)\,\mathrm{N}$. The epoxy resins having a higher Young's modulus result in a significantly smaller mean force, namely between $(0.83 \pm 0.07)\,\mathrm{N}$ and $(3.02 \pm 0.28)\,\mathrm{N}$. No clear correlation of the Young's modulus and the strength was observed. This testing method,

though, has several disadvantages: It is designed for rather large specimens, and therefore, a large amount of adhesive resin is needed to perform this test. In addition, using thin silicon specimens instead of steel is not be possible due to its brittleness, resulting in cracking of the silicon and not a joint failure. A T-Peel test only supports static testing, providing only a mean force. Dynamic loading is not supported with this setup. Another approach is to utilize a Die Shear Test. The shear tool can precisely shear the die off the substrate in a known shear height above the bondline and measure the maximum applied force. This provides the possibility to utilize silicon specimens. However, in the typical operating mode of using a die shear tester, the adhesive layer experiences mostly shear stress rather than the peeling stress, that is of interest in our case.
The proposed testing procedure combines both methods. The setup, which is shown in figure 7.18 b.) can be adapted to most die shear testers by mounting the specimen with a vertical bondline arrangement, versus the common horizontal arrangement of the shear tool. As a result, the adhesive is foremost subjected to peeling stress. Figure 7.19 shows that the test component (orange) experiences a similar stress distribution as the original component (blue), when a force of 10 N at a height of 100 µm above the end of the bondline is applied. The first step is to determine the maximum static load. Next, by reducing the load, dynamic testing can be carried out to evaluate after how many cycles the bond fails. By continuously reducing the load and noting the number of cycles until failure, the Woehler curve can be determined. It describes the fatigue behavior of an adhesive joint due to cyclic loading and can be extrapolated within a reasonable range to estimate whether an adhesive provides the stability to support high cyclic loading [2].

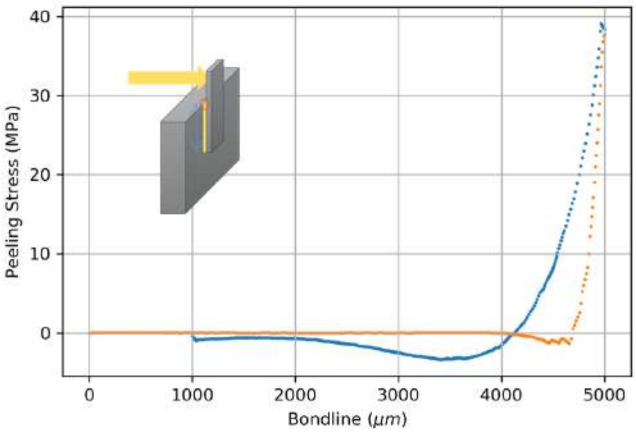

Figure 7.19:
Peeling stress along the bondline for the original (blue) and the test component (orange). Bondline is indicated with light blue arrow.

In summary, testing adhesive joints under conditions as close as possible to the real component is challenging. Existing testing methods are often limited to large joints and simplified structures. Especially when it comes to cyclic loading of micrometer scale components existing standardized methods can not be applied. Here, we present a novel approach of a Micro-Peel test. Obtaining the beginning of Woehler curves provides an effective method to quickly assess the fatigue behavior of adhesives and their suitability for an application that has to endure high-cyclic loading under peel stress.

[1] A. J. Curley, J. K. Jethwa, A. J. Kinloch, A. C. Tayler, *The Journal of Adhesion* **66**, 39-59 (1998)

[2] J. Jeandrau, C. Peyrac, F. Lefebvre, *Procedia Engineering* **133**, 508-517 (2015)

8 Teaching and outreach

8.1 Lectures, seminars and lab courses

Spring Term 2019

Prof. Dr. Christine Papadakis, *Angewandte Physik: Polymerphysik 2*
Prof. Dr. Peter Müller-Buschbaum, Dr. Volker Körstgens,
Nanostructured Soft Materials 2
Dr. Michael Leitner, *Materialphysik auf atomarer Skala 2*
Prof. Dr. Peter Müller-Buschbaum, Prof. Dr. Christian Große, *Mess- und Sensortechnologie*
Prof. Dr. Winfried Petry, *Physics with neutrons 2*
Prof. Dr. Christine Papadakis, *Höhere Physik 2*
Prof. Dr. Peter Müller-Buschbaum, *Seminar: Current problems in organic photovoltaics*
Prof. Dr. Peter Müller-Buschbaum, Prof. Dr. Christine M. Papadakis,
Bachelor-Seminar: Funktionelle weiche Materialien
Prof. Dr. Peter Böni, Dr. Alexandros Koutsioumpas, Dr. Christoph Morkel, Prof. Dr. Peter Müller-Buschbaum, Dr. Markos Skoulatos, *Seminar: Neutronen in Forschung und Industrie*
Prof. Dr. Peter Müller-Buschbaum, Prof. Dr. Christine M. Papadakis,
Seminar: Structure und dynamics of condensed matter
Prof. Dr. Peter Müller-Buschbaum, Prof. Dr. Christine M. Papadakis, *Seminar: Polymers*

Autumn Term 2019/2020

Prof. Dr. Peter Müller-Buschbaum, Dr. Volker Körstgens,
Angewandte Physik: Polymerphysik 1
Prof. Dr. Christine Papadakis, *Nanostructured Soft Materials 1*
Dr. Michael Leitner, *Materialphysik auf atomarer Skala 1*
Prof. Dr. Winfried Petry, *Physics with neutrons 1*
Prof. Dr. Christine Papadakis, *Höhere Physik 1*
Prof. Dr. Peter Müller-Buschbaum, *Seminar: Current problems in organic photovoltaics*
Prof. Dr. Peter Böni, Dr. Alexandros Koutsioumpas, Dr. Christoph Morkel, Prof. Dr. Peter Müller-Buschbaum, Dr. Markos Skoulatos: *Seminar: Neutronen in Forschung und Industrie*
Prof. Dr. Peter Müller-Buschbaum, Prof. Dr. Christine M. Papadakis,
Seminar: Structure und dynamics of condensed matter
Prof. Dr. Peter Müller-Buschbaum, Prof. Dr. Christine M. Papadakis, *Seminar: Polymers*
Prof. Dr. Winfried Petry, *Ferienakademie Sarntal: "Wie funktioniert das? Physikalische Methoden in der Medizin"*, 22 Sep – 4 Oct 2019
Prof. Dr. Winfried Petry, Tobias Chemnitz, *Mastercourse Radiation Biology: Neutrons for medicine*

Lab Courses 2019 (Fortgeschrittenenpraktika)

Rasterkraftmikroskopie
Neutron scattering at FRM II
Darstellung von DNS im Rasterkraftmikroskop
Charakterisierung von Polymeren mittels Dynamischer Differenzkalorimetrie

8.2 Conferences and public outreach

P. Müller-Buschbaum
Lehrerfortbildung "Erneuerbare Energien"
43. Edgar-Lüscher-Seminar
Zwiesel, 22 – 24 Mar 2019

Programm

Freitag, 22. März 2019

13.00 - 14.15	**Einführungsvortrag für Schüler** *Dr. Andreas Kratzer – TUM School of Education*
14.15 - 14.30	Diskussion
14.45 - 15.15	**Begrüßung**
15.15 - 16.30	**Energiemodellierung auf verschiedenen zeitlichen und geographischen Skalen** *Dr.-Ing. Philipp Kuhn – TUM, Lehrstuhl für Erneuerbare und Nachhaltige Energiesysteme*
16.30 - 17.15	Diskussion und Kaffeepause
17.15 - 18.30	**Organische und Hybride Photovoltaik** *Prof. Dr. Peter Müller-Buschbaum – TUM, Lehrstuhl für Funktionelle Materialien*
18.30 - 18.45	Diskussion

Samstag, 23. März 2019

09.00 - 10.15	**Neutronen in der Erforschung von Energiespeicher** *Prof. Dr. Helmut Ehrenberg – KIT Karlsruhe, Institut für Angewandte Materialien*
10.15 - 11.00	Diskussion und Kaffeepause
11.00 - 12.15	**Grundlagen chemischer Energiespeicherung** *Prof. Dr. Hubert Gasteiger – TUM, Lehrstuhl für Elektrochemie*
12.15 -12.30	Diskussion
14.30 - 15.45	**Intelligente Stromnetze** *Prof. Dr.-Ing. Oliver Brückl – OTH Regensburg, Fakultät für Elektro- und Informationstechnik*
15.45 - 16.30	Diskussion und Kaffeepause
16.30 - 17.45	**Biomasse und die Energiewende** *Prof. Dr.-Ing. Matthias Gaderer – TUM Campus Straubing, Lehrstuhl für regenerative Energie Systeme*
17.45 - 18.00	Diskussion

Sonntag, 24. März 2019

09.00 - 10.15	**Rolle der Tiefengeothermie für eine erfolgreiche Energiewende** *Dr. Maximilian Keim – TUM, Projektleitung Geothermie-Allianz Bayern*
10.15 - 11.00	Diskussion und Kaffeepause
11.00 - 12.15	**Windenergie** *Prof. Po Wen Cheng – Universität Stuttgart, Institut für Flugzeugbau*
12.15 - 13.00	Diskussion Thema für 44. Edgar-Lüscher-Seminar

Organisation

Prof. Dr. Peter Müller-Buschbaum
TUM

Prof. Müller-Buschbaum ist Ordinarius am Lehrstuhl für Funktionelle Materialien (E13) des Physik Departments der TU München, Wissenschaftlicher Direktor der Forschungsneutronenquelle Heinz Maier-Leibnitz (FRM II) und des Heinz Maier-Leibnitz Zentrums (MLZ). Er ist Sprecher für das Netzwerk Regenerative Energien (NRG) der TU München, Leiter des bayerischen KeyLabs TUM.solar im Forschungsnetzwerk Solar Technologies Go Hybrid (SolTech). Er befasst sich in seiner Forschungsarbeit mit der Entwicklung neuer Materialien mit speziellem Fokus auf Energiematerialien.

Prof. Dr. Winfried Petry
TUM

Prof. Dr. Winfried Petry war bis März 2018 Ordinarius am Lehrstuhl für Funktionelle Materialien und Wissenschaftlicher Direktor der Forschungsneutronenquelle Heinz Maier-Leibnitz (FRM II). Auch in Zukunft bleibt er der TUM als „Emeritus of Excellence", als Wissenschaftler und Dozent auf dem Gebiet der Materialwissenschaft mit Neutronen sowie als Betreuungsprofessor der Bayerischen Eliteakademie verbunden.

Organisatorische Hinweise

Organisation vor Ort:

OStD Heribert Strunz,	*Gymnasium Zwiesel*
OStR Claus Starke,	*Gymnasium Zwiesel*
OStR Christian Stoiber,	*Gymnasium Zwiesel*
StR Thomas Kufner,	*Gymnasium Zwiesel*

E-Mail: luescherseminar@gymnasium-zwiesel.de

Hinweise:

- Alle Vorträge finden in der Aula des Gymnasiums Zwiesel statt.
- Für 5,- € erhalten die Teilnehmer am Ende des Seminars eine DVD mit sämtlichen freigegebenen Vorträgen und den bisherigen Festschriften.
- In den ausgewiesenen Kaffeepausen wird in der Mensa des Gymnasiums Kaffee und Kuchen gegen eine freiwillige Spende angeboten.
- Am Rande der Aula findet eine Ausstellung verschiedener Lehrmittelausstatter und Verlage statt.

Titelfoto: pixabay©

43. Edgar-Lüscher-Seminar

Erneuerbare Energien

am Gymnasium Zwiesel

Freitag, 22. März 2019 bis Sonntag, 24. März 2019

Schirmherr:
Prof. Dr. Dr. h.c. mult. Wolfgang A. Herrmann, *Präsident der TUM*

Veranstalter:
Ltd. OStD Anselm Räde,
Ministerialbeauftragter für die Gymnasien in Niederbayern

Wissenschaftliche Leitung:
Prof. Dr. Peter Müller-Buschbaum, *TUM*
Prof. Dr. Winfried Petry, *TUM*

Referenten

Dr. Andreas Kratzer
TUM School of Education, München

Dr. Andreas Kratzer ist akademischer Oberrat an der TUM School of Education. Er beschäftigt sich mit Physik-Fachdidaktik und entwickelt Projekte für Schülerinnen und Schüler und Möglichkeiten der Kooperation zwischen Schule und Universität (TUMLab im Deutschen Museum, TUM Science Labs, TUM Schulcluster, Schülerforschungszentrum Berchtesgadener Land). Eines seiner zentralen Interessensgebiete ist „Bildung für nachhaltige Entwicklung".
In seinem Vortrag wird er die vielen Aspekte der Nachhaltigkeit beleuchten. Neben kulturellen und gesellschaftlichen Fragestellung spielen dabei Naturwissenschaft und Technik eine wichtige Rolle. Ein breites Wissen in diesen Bereichen ist entscheidend bei der Entwicklung von Nachhaltigkeitsstrategien.

Dr.-Ing. Philipp Kuhn
TUM, Erneuerbare und Nachhaltige Energiesysteme

Dr.-Ing. Kuhn ist akademischer Rat und stellvertretender Leiter des Lehrstuhls für Erneuerbare und Nachhaltige Energiesysteme an der TUM. In der Forschung beschäftigt er sich mit der Modellierung von Energiesystemen mit besonderem Fokus auf erneuerbaren Energien.
In seinem Vortrag geht er anfangs auf die Klimaziele und die damit einhergehenden Herausforderungen an ein zukünftiges Energiesystem ein. Anschließend erläutert er die wesentliche Rolle von Energiemodellen zur Analyse und Bewertung unterschiedlicher Pfade und Technologieoptionen im Transformationsprozess von Energiesystemen anhand unterschiedlicher Beispiele.

Prof. Dr. Peter Müller-Buschbaum
TUM, Lehrstuhl für Funktionelle Materialien

Prof. Müller-Buschbaum ist Ordinarius am Lehrstuhl für Funktionelle Materialien (E13) des Physik Departments der TU München, Wissenschaftlicher Direktor der Forschungsneutronenquelle Heinz Maier-Leibnitz (FRM II) und des Heinz Maier-Leibnitz Zentrums (MLZ).

In seinem Vortrag berichtet er über die Entwicklungen im Bereich der organischen und hybriden Photovoltaik, also von Solarzellen, die auf leitfähigen Polymeren und kleinen Molekülen basieren. Es werden die Möglichkeiten und Herausforderungen dieser neuen Klasse von Solarzellen aufgezeigt und ein Einblick in den Stand der aktuellen Forschung vermittelt.

Prof. Dr. Helmut Ehrenberg
KIT Karlsruhe, Institut für Angewandte Materialien

Prof. Dr. Helmut Ehrenberg leitet das Institut für Angewandte Materialien – Energiespeichersysteme (IAM-ESS) am Karlsruher Institut für Technologie (KIT) und ist einer der Sprecher des Exzellenzclusters „Energy Storage beyond Lithium" und Koordinator der Batterieforschung in der Helmholtz-Gemeinschaft (HGF).
In seinem Vortrag werden aktuelle Herausforderungen und perspektivische Möglichkeiten von elektrochemischen Energiespeichern diskutiert und dargestellt, welche Rolle bei der Entwicklung von nachhaltigen und sicheren Batterien Großforschungsgeräte an Neutronen- und Synchrotronstrahlungsquellen spielen.

Prof. Dr. Hubert Gasteiger
TUM, Lehrstuhl für Elektrochemie

Prof. Dr. Gasteiger wurde 2010 zum Aufbau des Lehrstuhls Technische Elektrochemie an die Technische Universität München berufen, wo er an der Material- und Elektrodenentwicklung für PEM Brennstoffzellen, PEM Wasserelektrolyseure und Lithiumionen Batterien arbeitet.
In diesem Vortrag soll die großtechnische Erzeugung von Wasserstoff für den Einsatz in Brennstoffzellen oder die Weiterverarbeitung zu Kohlenwasserstoff-basierenden Treibstoffen betrachtet werden. Die technischen, wirtschaftlichen und ökologischen Herausforderungen für eine regenerative Wasserstoffwirtschaft und für den großskaligen Ausbau von Brennstoffzellen, sowie auch deren Vor- und Nachteile im Vergleich zu Batterie-betriebenen Elektroautos, werden im Fokus dieses Vortrags stehen.

Prof. Dr.-Ing. Oliver Brückl
OTH, Fakultät für Elektro- und Informationstechnik

Dr.-Ing. Brückl ist Professor an der Fakultät für Elektro- und Informationstechnik der OTH, Co-Leiter der Forschungsstelle für Energienetze und Energiespeicher (FENES) und Wissenschaftlicher Leiter des Regensburg Center of Energy and Resources (RCER).
In seinem Vortrag will er den Aufbau und die Struktur des deutschen und europäischen Stromnetzes, sowie den Netzausbau (Gründe, Alternativen, Planungsprozess, …) und dessen Unterschied im Übertragungsnetz und Verteilungsnetz aufzeigen. Das Thema Kosten (Netzentgelte, Letztverbraucherabgaben und Tarifierung) ist dabei enorm entscheidend, ob das intelligente Zusammenspiel zwischen Erzeugern, Verbrauchern, Speichern und dem Netz gelingen wird. An einem konkreten Beispiel wird auch der Bereich der Systemstabilität aufgegriffen.

Prof. Dr.-Ing. Matthias Gaderer
TUM, Lehrstuhl für regenerative Energie Systeme

Prof. Dr. Matthias Gaderer leitet den Lehrstuhl Regenerative Energiesysteme am TUM Campus für Biotechnologie und Nachhaltigkeit in Straubing. Hier wird im Rahmen der Bioökonomie an der nachhaltigen energetischen, stofflichen und ökonomischen Nutzung der Biomasse geforscht.
Die Energiewende betrifft insbesondere die Bereiche Wärme, Strom und Kraftstoffe. In allen diesen Bereichen kann die Biomasse Beiträge leisten. Am stärksten ist der Beitrag im Wärme- und Strombereich. Im Vortrag wird daher der aktuelle Stand in diesem Bereich diskutiert und an einem anschaulichen Beispielen ausgearbeitet.

Dr. Maximilian Keim
TUM, Projektleitung Geothermie-Allianz Bayern

Dr. Maximilian Keim ist Projektleiter der Geothermie-Allianz Bayern.
Als Tiefengeothermie bezeichnet man die Nutzung der natürlich in der Erde gespeicherten Wärmenergie aus einem Tiefenbereich von 400 - 5000 m. Mit zunehmender Tiefe nimmt die Temperatur durchschnittlich um 3 °C pro Kilometer zu. Das genutzte Temperatur-Niveau der Tiefengeothermie ist somit höher als das von oberflächennahen Geothermie.
In diesem Vortrag soll ein umfassender Einblick in die Tiefengeothermie ausgehend von den Grundlagen über die Exploration und Umsetzung eines Projekts bis hin zu ihrer Rolle im Energiesystem gegeben werden.

Prof. Po Wen Cheng
Universität Stuttgart, Institut für Flugzeugbau

Po Wen Cheng ist Professor für Windenergie an der Universität Stuttgart. Seine Forschungsgruppe beschäftigt sich mit der Systemmodellierung und der Untersuchung des Windfelds mit Lidar sowie der Regelung und Optimierung von Windenergieanlagen.
In seinem Vortrag gibt er eine kurze Einführung in die Grundlagen der Windenergie und die Auslegung von Rotorblättern nach Betz. Daran schließen sich ein Überblick über den Stand der Forschung bei der Auslegung von Windenergieanlagen und die Besprechung der technischen Herausforderungen in der Hochskalierung von Windenergieanlagen an. Darüber hinaus wird insbesondere die Dynamik von Offshore-Windenergieanlagen und schwimmenden Windenergieanlagen anhand von Forschungsergebnissen aus aktuellen Projekten illustriert.

Heinz Maier-Leibnitz Zentrum, 2DFN
German-French workshop: How will Europe maintain its pole position in neutron science?
Garching, 14 – 16 May 2019

At the end of 2019 two major European neutron sources will stop their operation. With the closure of Orphée, French users will lose their national source, with the closure of the BER2 at HZB, German users will focus even more on the MLZ at Garching. Furthermore, the international users of both facilities will put even more pressure on the availability of beam time at our international source, the Institute Laue Langevin (ILL), and also at the MLZ. However, ESS will come into full operation in the late twenties only. In particular, for the French user community, this means the risk of losing knowledge in neutron science, in the period between the closure of Orphée and the getting into operation of ESS. A first attempt to bridge this gap is made by additional CRG instruments at ILL and SINQ. In the interest of keeping the European leadership in neutron science, French scientists are warmly welcome to become an active partner at MLZ. In this framework, the workshop will discuss opportunities of an enhanced cooperation between French and German neutron scientists covering topics from innovative instrumentation to exploring new fields in neutron science. The Directors of 2FDN and MLZ look forward to welcoming French and German neutron scientists at this workshop.

Participants of the German French Workshop of MLZ and 2DFN in front of the Institut of Advanced Studies in Garching © Björn Pedersen

Heinz Maier-Leibnitz Zentrum Garching

MLZ-Conference "Neutrons for Information and Quantum Technologies"

Lenggries, 4 – 7 Jun 2019

WELCOME

„Grüß Gott", dear colleagues,

We like to welcome you to the MLZ conference **"Neutrons for Information and Quantum Technologies"** in Lenggries.

The conference is the fourth kind of MLZ conferences dealing with the usage and benefits of neutrons science in major areas of science and society. After the MLZ conference "Neutrons for Energy" in 2016, "Neutrons for Health" in 2017 and "Neutrons for Culture and Art" the conference is now devoted to information and quantum technology.

The conference **"Neutrons for Information and Quantum Technologies"** consists of 9 keynote talks, 12 contributed talks and a poster session, and we are proud to welcome numerous renowned speakers from Denmark, France, Korea, India, Japan, Luxembourg, Sweden and Germany joining the conference.

The conference addresses the field of neutron scattering in magnetic and quantum spin systems identifying their complex structure and dynamics. The conference will highlight diverse topics as spin caloritronics, magnon transport, magnetic 2-d van der Waals materials, new trends in spintronics, dynamics of magnetic textures, like skyrmions, domain walls and vortices, high-precision calculations of neutron scattering with the density-matrix renormalization group, and operating quantum states in single molecules. These will hopefully stimulate discussion between the participants, who up-to now have not regularly used neutron scattering as a method and long-standing neutron users. We also hope to offer a discussion platform for experiment and theoretical players in these exciting fields of magnetism. Therefore we have left ample time for discussions and an interesting short excursion in the Bavarian Alps around Lenggries.

The MLZ provides a number of instruments allowing to probe the structure and the dynamics of these systems. DNS, SANS and POLI allow for determining the structure in magnetic systems using neutron spin polarized techniques. The triple axis instruments PUMA, PANDA, MIRA and TRISP can determine the dynamics of these systems. These instruments will be presented in the poster session during the conference.

We look forward to having intense and fruitful discussions on the current status and future perspectives of neutron scattering for information and quantum technologies.

With kind regards and warm welcome

Prof. Dr. Peter Müller-Buschbaum and Prof. Dr. Stephan Förster

Scientific Director of Heinz Maier-Leibnitz Zentrum (MLZ) and
Forschungs-Neutronenquelle FRM II, Technische Universität München (TUM)

Scientific Director of Heinz Maier-Leibnitz Zentrum (MLZ) and
Jülich Centre for Neutron Science (JCNS), Forschungszentrum Jülich GmbH

Credits: MLZ

P. Müller-Buschbaum

4th internal biennial science meeting of the MLZ

Grainau 24 – 27 Jun 2019

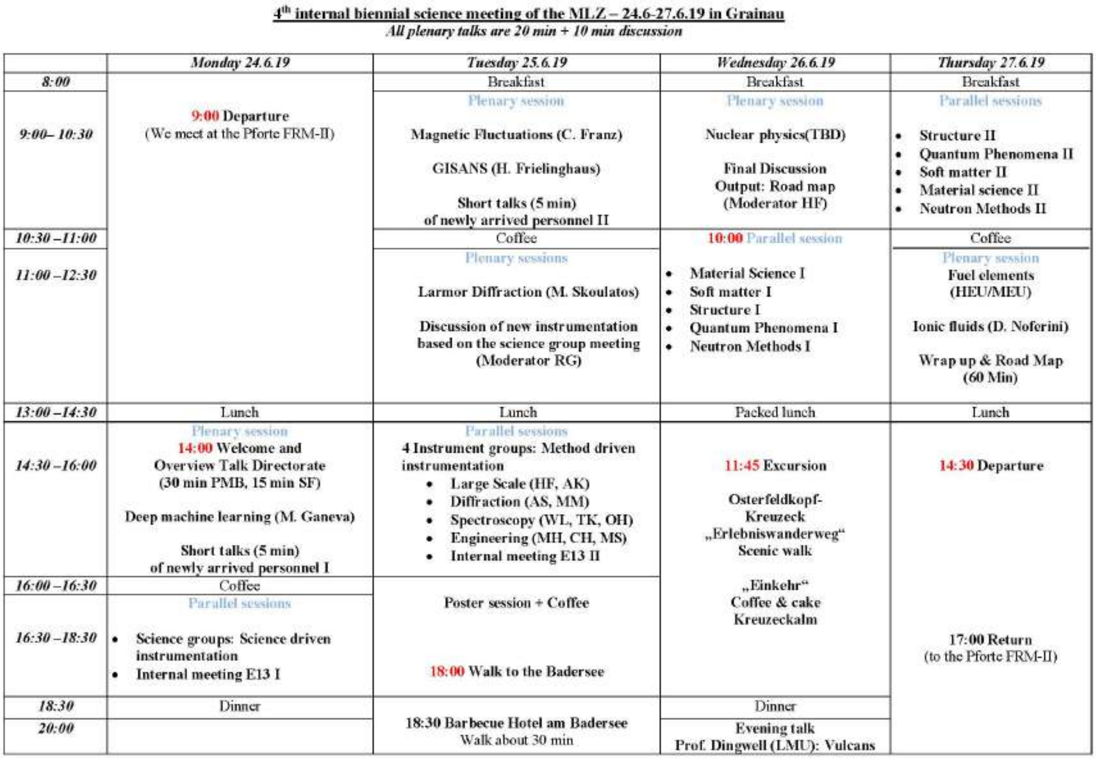

4th internal biennial science meeting of the MLZ – 24.6-27.6.19 in Grainau

All plenary talks are 20 min + 10 min discussion

	Monday 24.6.19	*Tuesday 25.6.19*	*Wednesday 26.6.19*	*Thursday 27.6.19*
8:00	**9:00 Departure** (We meet at the Pforte FRM-II)	Breakfast	Breakfast	Breakfast
9:00– 10:30		Plenary session **Magnetic Fluctuations (C. Franz)** **GISANS (H. Frielinghaus)** **Short talks (5 min) of newly arrived personnel II**	Plenary session **Nuclear physics(TBD)** **Final Discussion Output: Road map (Moderator HF)**	Parallel sessions • **Structure II** • **Quantum Phenomena II** • **Soft matter II** • **Material science II** • **Neutron Methods II**
10:30 –11:00		Coffee	**10:00** Parallel session • **Material Science I** • **Soft matter I** • **Structure I** • **Quantum Phenomena I** • **Neutron Methods I**	Coffee
11:00 –12:30		Plenary sessions **Larmor Diffraction (M. Skoulatos)** **Discussion of new instrumentation based on the science group meeting (Moderator RG)**		Plenary session **Fuel elements (HEU/MEU)** **Ionic fluids (D. Noferini)** **Wrap up & Road Map (60 Min)**
13:00 –14:30	Lunch	Lunch	Packed lunch	Lunch
14:30 –16:00	Plenary session **14:00 Welcome and Overview Talk Directorate (30 min PMB, 15 min SF)** **Deep machine learning (M. Ganeva)** **Short talks (5 min) of newly arrived personnel I**	Parallel sessions **4 Instrument groups: Method driven instrumentation** • **Large Scale (HF, AK)** • **Diffraction (AS, MM)** • **Spectroscopy (WL, TK, OH)** • **Engineering (MH, CH, MS)** • **Internal meeting E13 II**	**11:45 Excursion** **Osterfeldkopf-Kreuzeck „Erlebniswanderweg“ Scenic walk** **„Einkehr“ Coffee & cake Kreuzeckalm**	**14:30 Departure** **17:00 Return** (to the Pforte FRM-II)
16:00 –16:30	Coffee	**Poster session + Coffee** **18:00 Walk to the Badersee**		
16:30 –18:30	Parallel sessions • **Science groups: Science driven instrumentation** • **Internal meeting E13 I**			
18:30	Dinner	**18:30 Barbecue Hotel am Badersee** Walk about 30 min	Dinner	
20:00			**Evening talk** **Prof. Dingwell (LMU): Vulcans**	

Munich School of Engineering (MSE)
9th Colloquium of the Munich School of Engineering: "Shaping a Sustainable Energy Future"
Garching, 1 Aug 2019

Munich School of Engineering
Technische Universität München

9th Energy Colloquium of the Munich School of Engineering

Shaping a Sustainable Energy Future

August 01, 2019 – 8:30 a.m. to 8:00 p.m.
TUM – Quantum, Garching-Hochbrück

8:30 – 9:00 a.m.
Registration

9:00 – 9:15 a.m.
Opening: Prof. Thomas Hamacher
Director, Munich School of Engineering, TUM

9:15 – 9:45 a.m.
Keynote: Challenges and Approaches for a Sustainable and Integrated Energy Transition in Bavaria
Dr. Josef Hochhuber, Bayerisches Wirtschaftsministerium

9:45 – 11:00 a.m.
Energy Material Science: From Heat to Power to Building Applications
Session Chair: **Prof. Peter Müller-Buschbaum**

Development of Salt Hydrate Mixtures for Low-Temperature Latent Heat Storage
Christoph Rathgeber, ZAE Bayern, Energy Storage

A Newly Developed Reference Electrode for In-Situ Impedance Measurements in Sodium-Ion Batteries
Fabian Linsenmann, Chair of Technical Electrochemistry, TUM

Potential Use of Thermo-Responsive Polymers as Smart Window Surface Coatings
Lucas Kreuzer, Chair of Functional Materials, TUM

11:00 – 11:30 a.m.
Poster Presentation and Coffee Break

11:30 – 12:45 p.m.
Future Fuels: Power-to-X
Session Chair: **Prof. Hartmut Spliethoff**

Piping Renewable Energy: Utilizing Methanogen and Organic Waste
Robert Bauer, Deggendorf Institute of Technology

A Comparison of the Energetic Efficiency of the Production of Polyoxymethylene Dimethyl Ethers and other E-Fuels
Yannic Tönges, Chair of Chemical Process Engineering, TUM

Economics of Reversible Power-to-Gas
Gunther Glenk, Chair of Controlling, TUM

12:45 – 2:00 p.m.
Poster Presentation and Lunch Break

Please register: http://www.mse.tum.de

2:00 – 2:30 a.m.
Keynote: Food and Energy – Approaches to a Holistic Vertical Farming Concept
Dr. Petra Liedl, Munich School of Engineering, TUM

2:30 – 3:20 p.m.
Urban Energy Modeling
Session Chair: **Dr. Petra Liedl**

Integrated Urban Energy Modeling: Coupling Urban Growth with Energy Demand
Anahi Molar-Cruz, Chair of Energy Efficient and Sustainable Energy Systems, TUM

Solar Activated Envelopes in District Context – Energy Modeling Tasks
Lea Bogischef, Junior Research Group Cleanvelope, TUM

3:20 – 3:45 p.m.
Poster Presentation and Coffee Break

3:45 – 5:30 p.m.
Trends in Regional Energy Systems: A Bavarian Perspective
Session Chair: **Prof. Thomas Hamacher**

Retrofit Hybridization of Geothermal Binary Cycles in Southern Germany
Davide Toselli, Center of Energy Technology ZET, University of Bayreuth

Assessing Middle and Low Voltage Grid Requirements in Bavaria for the Decades to Come
Luis Ramirez Camargo, Team Geoinformatics, Deggendorf Institute of Technology

Comparison of a Decentralized and Centralized Future Energy System at the Campus Garching
Benedikt Schweiger, Chair of Energy Systems, TUM

How can Prosumer Provide Flexibility to the Local Energy System?
Babu Kumaran Nalini, Chair of Energy Economy and Application Technology, TUM

5:30 – 6:00 p.m.
Keynote: The Antinomies of Climate Policy
PD Dr. Jens Söntgen, WZU Augsburg

6:00 – 6:15 p.m.
Summary and Closing

6:15 – 8:00 p.m.
Poster and Presentation Award with Colloquium Dinner

P. Müller-Buschbaum
Lehrerfortbildung "Quantenphysik"
Edgar-Lüscher Lectures Dillingen, 23 – 25 Sep 2019

EDGAR–LÜSCHER–LECTURES DILLINGEN/DONAU 2019
Thema: Quantenphysik
Datum: Montag, 23. September bis Mittwoch, 25. September 2019
Tagungsort: Akademie für Lehrerfortbildung Dillingen
Veranstalter: Akademie für Lehrerfortbildung Dillingen und TU München
wissenschaftliche Leitung: Prof. Dr. Peter Müller-Buschbaum,
Technische Universität München.

Programm

Montag, 23. 09. 2019
15:00 – 15:30 Begrüßung
StD Werner Ettinger / Prof. Dr. Peter Müller-Buschbaum (Physik-Department, TUM)

15:30 – 17:00 Prof. Dr. Kai Roßnagel [CAU Kiel und DESY]
Herstellung und Charakterisierung von Quantenmaterialien

18:30 – 20:00 Prof. Dr. Kai Müller [Fakultät für Elektrotechnik und Informationstechnik TU München]
Quantenkryptographie

Dienstag, 24. 09. 2019
8:30 – 10:00 Prof. Dr. Stefan Scheel [Institut für Physik, Universität Rostock]
Der Casimir-Effekt Eine Kraft aus Quantenfluktuationen

10:00 – 10.30 Kaffeepause

10:30 – 12:00 Prof. Dr. Thomas Udem [MPI of Quantum Optics, München]
Das Wasserstoffatom und Materiewellen

15:30 – 17:00 Prof. Dr. Stephan V. Roth [KTH Stockholm und DESY
Hamburg] Herstellung von Quantenmaterialien

18:30 – 20:00 Dr. Andreas Reiserer [MPI of Quantum Optics, München]
Quantennetzwerke

Mittwoch, 25. 09. 2019
8:30 – 10:00 Prof. Dr. Friedemann Reinhard [Walter Schottky Institut, TU München]
Quantensensoren

10:00 – 10.30 Kaffeepause

10:30 – 12:00 Dr. Frank Deppe [Walther-Meißner-Institute for Low Temperature
Research, TU München]
Quantencomputer

Ab 12:00 Lehrgangsabschluss
Prof. Dr. Peter Müller-Buschbaum / StD Werner Ettinger

P. Müller-Buschbaum, S.V. Roth, DESY
International Workshop GISAXS 2019
DESY Hamburg, 20 – 22 Nov 2019

Credits: DESY

GISAXS2019 Programme

Nov 20th, 2019

09:00-10:15 Arrival and registration

10:15-10:25 Opening – Welcome

10:25-10:35 Welcome organizers (Stephan Roth, DESY & KTH and Peter Müller-Buschbaum, TUM)

Session 1 – Basic Introduction (Chair: Stephan V. Roth)

10:35-11:20 Moonhor Ree, Pohang University of Science & Technology (POSTECH) (Korea): "**GISAXS on organic electronics**"

11:20-11:55 Peter Müller-Buschbaum: "**Basic Introduction to GISAS**"

11:55-12:30 Gennady Pospelov "**Experiment planning, simulation and fitting for GISAS and reflectometry using BornAgain framework**"

12:30-14:00 Lunch @ DESY / Business lunch

Session 2 – Grazing Incidence Diffraction (Chair: Peter Müller-Buschbaum)

14:00-14:45 Frank Schreiber, Univ. Tübingen (GER): "**Grazing incidence diffraction on organic thin films**"

14:45-15:20 Peter Siffalovic, Slovak Academy of Sciences, Bratislava (SK): "**Real-time tracking of growth of small organic molecules on 2D-substrates by means of GI-SAXS/WAXS**"

15:20-15:30 Group photo

15:30-16:15 Coffee break & Discussion

Session 3 – Future Challenges (Chair: Matthias Schwartzkopf)

16:15-17:00 Alexander Hexemer, ALS, Berkeley (US): "**Big data**"

17:00-17:35 Stephan V. Roth, KTH & DESY (SWE & GER): "**In-situ grazing incidence x-ray scattering for thin film technology”**

Session 4 – GISAS at the air-water interface (Chair: Peter Müller-Buschbaum)

17:35-18:10 Philippe Fontaine, SOLEIL, Gif-Sur-Yvette (FRA): “**Contribution of in-situ GISAXS measurements to the study of semi-fluorinated alkane layers at the air/water interface**”

18:10-18:45 Mark Rutland, KTH Stockholm (SWE): "**Self-assembly structuring of the liquid-air interface in 3D: AFM, VSFG, NR and GISANS - are more acronyms required??**"

19:00-21:00 Poster session with snacks

GISAXS 2019 – Programme

Nov 21st, 2019

Session 5 – GISAS exploiting tender X-rays and neutrons (Chair: Matthias Schwartzkopf)

09:00-09:45 Harald Ade, North Carolina State University (US): "**in-plane and out-of-plane mesoscopic structure of polymer thin films determined by resonant soft x-ray scattering**"

09:45-10:20 Adrien Rennie, Univ. Uppsala (SWE): "**GISANS studies of colloidal thin films**"

10:20-11:00 Coffee break

Session 6 – Advances in GISAS techniques (Chair: Peter Müller-Buschbaum)

11:00-11:35 Emanuel Kentzinger, FZ Jülich (GER): "**3D vector magnetometry by polarised GISANS**"

11:35-12:10 Matthias Schwartzkopf, DESY (GER): "**High-speed GISAXS - current status and future challenges**"

12:10-12:45 Philipp Gutfreund, ILL, Grenoble (FRA): " **The GISANS options at ILL for liquid and polymer interfaces: Recent examples and perspectives**"

12:45-14:00 Lunch @ DESY / Voucher

Session 7 – Towards hands-on training (Chair: Peter Müller-Buschbaum)

14:00-14:20 Introduction to MiNaXS (Matthias Schwartzkopf)

14:20-14:30 General safety training (Stephan V. Roth)

14:30-14:45 Division into training groups A/B/C/D

14:45-15:00 Break

15:00- Training sessions TR1-4 (until Nov 24th, 2019); soft drink available at training stations

15:00-17:00 Training session TR1

DPDAK - A

Bornagain - B

Visit of P03 - C

Break -D

17:00-19:00 Training session TR2

DPDAK - D

Bornagain - A

Visit of P03 - B

Break - C

20:00-22:00 Conference Dinner @ DESY

Nov 22nd, 2019

09:00—11:00 Training session TR3

DPDAK - C

Bornagain - D

Visit of P03 - A

Break – B

11:00-13:00 Training session TR4

DPDAK - B

Bornagain - C

Visit of P03 - D

Break – A

13:00-14:00 Lunch @ DESY

14:00-15:00 Closing remarks (organizers)

15:00 End of Workshop

Heinz Maier-Leibnitz Zentrum
MLZ User Meeting
Marriott Hotel München, 10/11 Dec 2019

We were proud to welcome 243 participants and in particular our Plenary Speakers: Regine von Klitzing, TU Darmstadt, Bella Lake, Helmholtz Zentrum Berlin, and Francesco Grazzi, CNR-IFAC

MLZ USERS2019

Marriott Hotel Munich – December 10th to 11th, 2019

TUESDAY

WEDNESDAY

Instructions:
Just click on the name of the day you like to see.
Tables of the day are linked to the sessions.
Tables of sessions are linked to the abstracts.
By clicking on the icon on the top of each page you will go back to this page.

MLZ is a cooperation between:
JÜLICH
Helmholtz-Zentrum Geesthacht
TUM

TUESDAY

12:00	Lunch						*Marriott Hotel Munich, Berliner Str. 93, 80805 München*
13:00 - 14:30	Materials Science I	Neutron Methods I	Nuclear, Particle, and Astrophysics I	Quantum Phenomena I	Soft Matter I	Structure Research I	Positrons I
14:30	Coffee break						*Marriott Hotel Munich*
15:00 - 16:30	Material Science II	Neutron Methods II		Quantum Phenomena II	Soft Matter II	Structure Research II	Positrons II
16:30	Coffee break						*Marriott Hotel Munich*
17:00 - 18:00	Materials Science III	Neutron Methods III		Quantum Phenomena III	Soft Matter III	Structure Research III	Positrons III
20:00	Dinner						*Zum Franziskaner, Residenzstr. 9, 80333 München*

Credits: MLZ

8.3 Service to the community

Prof. Dr. Peter Müller-Buschbaum:

- Since 4/2019 vice deputy of Association of Chemical Physics and Polymer Physics (CPP) at Deutsche Physikalische Gesellschaft (DPG)
- Since 7/2017 member of the Aptitude Committee of master course Materials Science and Engineering (MSandE) at TUM
- Since 9/2016 spokesman and board member of the Graduate School of "Munich School of Engineering" (MSE) at TUM
- Since 6/2016 member of the doctoral committee of "Munich School of Engineering" (MSE) at TUM
- Since 3/2015 member of "Advanced Light Source (ALS) Review Panel"
- Since 6/2014 member of "Stanford Synchrotron Radiation Lightsource (SSRL) Review Panel"
- Since 9/2012 Associate Editor of journal "ACS Applied Materials & Interfaces" of the American Chemical Society
- Since 3/2012 head of KeyLab "TUM.Solar" at TU Munich
- Since 1/2012 member of the Scientific Selection Panel of the Helmholtz-Zentrum Berlin für Materialien und Energie (HZB)
- Since 2011 member of European Spallation Source (ESS) Scientific Advisory Panel (Reflectivity)
- Since 2011 German representative at the European Polymer Federation (EPF) for polymer physics
- Since 2010 spokesman of the regenerative engergies section (NRG) at the Munich School of Engineering (MSE) of TU Munich
- Since 2010 member of TUM Energie at TU Munich
- Since 2010 German representative at the European Synchrotron User Organization (ESUO)
- Since 2008 chairman of "DESY Photon Science User Committee" at the synchrotron radiation laboratory DESY in Hamburg

Prof. Dr. Christine M. Papadakis:

- Since 4/2015 Editor-in-Chief for Colloid & Polymer Science, Springer-Verlag
- Since 2005 Vice women's representative of the Physics Department at TU München

Prof. Dr. Winfried Petry:

- Since 08/2019 member of the Project Advisory Board (PAC) of the European Spallation Source (ESS)
- Since 10/2018: TUM Emeritus of Excellence
- Since 04/2018: Advisor to the FRM II fuel conversion group
- Since 03/2015 member of the Neutron Scientific Advisory Committee of the National Research Center Kurchatov Institute ″Petersburg Nuclear Physics Institute″ (PNPI, Gatchina)
- Since 2012 member of the Scientific Advisory Board of NaWi Graz
- Since 09/2009 Associate Editor of the Journal “Transactions of Nuclear Science“
- Since 2007 member of the Steering committee of the Laue Langevin Institute

9 Publications, talks, posters and funding

9.1 Publications

- L. Bießmann, N. Saxena, N. Hohn, M. A. Hossain, J. G. C. Veinot, P. Müller-Buschbaum
  Highly conducting, transparent PEDOT:PSS polymer electrodes from post-treatment with weak and strong acids
  Adv. Electronic Mater **5**, 1800654 (2019)

- C. J. Brett, N. Mittal, W. Ohm, M. Gensch, L. P. Kreuzer, V. Körstgens, M. Mansson, H. Frielinghaus, P. Müller-Buschbaum, L. D. Söderberg, S. V. Roth
  Water-induced structural rearrangements on the nanoscale in ultrathin nanocellulose films
  Macromolecules **52**, 4721-4728 (2019)

- W. Cao, S. Xia, M. Appold, N. Saxena, L. Bießmann, S. Grott, M. Gallei, S. Bernstorff, P. Müller-Buschbaum
  Self-Assembly in ultrahigh molecular weight diblock copolymer thin films under strong confinement
  Sci. Rep. **9**, 18269 (2019)

- T. Chemnitz, R. E. Stene, W. Petry, F. Kraus
  A new approach in molybdenum separation
  European Nuclear Society, RRFM (2019)

- W. Chen, J. Zhong, J. Li, N. Saxena, L.P. Kreuzer, H. Liu, L. Song, B. Su, D. Yang, K. Wang, J. Schlipf, V. Körstgens, T. He, K. Wang, P. Müller-Buschbaum
  Structure and the charge carrier dynamics in colloidal PbS quantum dot solids
  J. Phys. Chem. Lett. **10**, 2058-2065 (2019)

- K. Faust, H. Breitkreutz, C. Reiter, W. Petry
  Exact geometrical implementation of involute shaped surfaces in Serpent 2
  European Nuclear Society, RRFM (2019)

- O. Filonik, M. E. Thordardottir, J. Lebert, S. Pröller, S. Weiß, L. J. Haur, A. Priyadarshi, P. Fontaine, P. Müller-Buschbaum, N. Mathews, E. M. Herzig
  Evolution of perovskite crystallization in printed mesoscopic perovskite solar cells
  Energy Technology **7**, 1900343 (2019)

- M. H. Futscher, T. Schultz, J. Frisch, M. Ralaiarisoa, E. Metwalli, M. V. Nardi, P. Müller-Buschbaum, N. Koch
  Electronic properties of hybrid organic/inorganic semiconductor pn junctions
  J. Phys. Condens. Matter **31**, 064002 (2019)

- M. Gensch, M. Schwartzkopf, W. Ohm, C. J. Brett, P. Pandit, S. K. Vayalil, L. Bießmann, L. P. Kreuzer, J. Drewes, O. Polonskyi, T. Strunskus, F. Faupel, A. Stierle, P. Müller-Buschbaum, S. V. Roth
  Correlating Nanostructure, Optical and Electronic Properties of Nanogranular Silver Layers during Polymer-Template Assisted Sputter Deposition
  ACS Appl. Mater. Interfaces **11**, 32, 29416-29426 (2019)

- A. Glensk, B. Grabowski, T. Hickel, J. Neugebauer, J. Neuhaus, K. Hradil, W. Petry, and M. Leitner
  Phonon lifetimes throughout the Brillouin zone at elevated temperatures from experiment and ab initio
  Phys. Rev. Lett. 1, **123**, 23550 (2019)
- P. P. Gu, N. Fan, Y. Wang, J. Wang, P. Müller-Buschbaum, Q. Zhong
  Linear control of moisture permeability and anti-adhesion of bacteria in a broad temperature region realized by cross- ing thermo-responsive microgels onto cotton fabrics
  ACS Appl. Mater. Interfaces **11**, 30269-30277 (2019)
- A. Heldmann, M. Hoelzel, M. Hofmann, W. Gan, W. W. Schmahl, E. Griesshaber, T. Hansen, N. Schellb, W. Petry
  Diffraction-based determination of single-crystal elastic constants of polycrystalline titanium alloys
  J. Appl. Crystallogr. 52, **5**, 1144-1156 (2019)
- N. Hohn, A. E. Hetzenecker, M. A. Giebel, S. Geier, L. Bießmann, V. Körstgens, N. Saxena, J. Schlipf, W. Ohm, P. S. Deimel, F. Allegretti, J. V. Barth, S. V. Roth, T. F. Fässler, P. Müller-Buschbaum
  Amphiphilic diblock copolymer-mediated structure control in nanoporous germanium-based thin films
  Nanoscale **11**, 2048-2055 (2019)
- M. Hruby, P. Štěpánek, J. Pánek, C. M. Papadakis
  Crosstalk between responsivities to various stimuli in multiresponsive polymers: change in polymer chain and external environment polarity as the key factor
  Colloid Polym. Sci. **297**, 1383-1401 (2019)
- S. Jaksch, T. Gutberlet, P. Müller-Buschbaum
  Grazing incidence scattering – status and perspectives in soft matter and biophyiscs
  Curr. Opin. Colloid. Interface Sci. **42**, 73-86 (2019)
- Q. Ji, X. Gao, Q. Zhang, L. Jin, D. Wang, Y. Xia, S. Yin, S. Xia, N. Hohn, X. Zuo, X. Wang, S. Xie, Z. Xu, L. Ma, L. Chen, G. Chen, J. Zhu, B. Hu, P. Müller-Buschbaum, P. G. Bruce, Y. Cheng
  Dental resin monomer enables unique NbO2/carbon lithium-ion battery negative electrode with exceptional performance
  Adv. Funct. Mater. **29**, 1904961 (2019)
- F. A. Jung, P. A. Panteli, C.-H. Ko, J.-J. Kang, L. C. Barnsley, C. Tsitsilianis, C. S. Patrickios, C. M. Papadakis
  Structural properties of micelles formed by telechelic pentablock quaterpolymers with pH-responsive midblocks and thermoresponsive end blocks in aqueous solution
  Macromolecules **52**, 9746-9758 (2019)
- L. P. Kreuzer, T. Widmann, N. Hohn, K. Wang, L. Bießmann, L. Peis, J.-F. Moulin, V. Hildebrand, A. Laschewsky, C. M. Papadakis, P. Müller-Buschbaum
  Swelling and exchange behavior of poly(sulfobetaine)-based block copolymer thin films
  Macromolecules **52**, 3486-3498 (2019)

- A. Leenaers, J. van Eyken, J. Wight, S. van den Berghe, B. Stepnik, J. Allenou et al.
  SEMPER FIDELIS first PIE results
  Argonne National Laboratory, RERTR (2019)
- N. Li, L. Song, L. Bießmann, S. Xia, W. Ohm, C. J. Brett, E. Hadjixenophontos, G. Schmitz, S. V. Roth, P. Müller-Buschbaum
  Morphology phase diagram of printed TiO2 films derived from block copolymer template assisted sol-gel synthesis
  Adv. Mater. Inter. **6**, 1900558 (2019)
- X. Li, J. N. Wagner, A. Stark, R., Kroos, M. Landsberger, M. Hofmann, G. Fan
  Carbon redistribution process in austempered ductile iron (ADI) during heat treatment – APT and synchrotron diffraction study
  Metals **9**, 789 (2019)
- B.-J. Niebuur, L. Chiappisi, F. Jung, X. Zhang, A. Schulte, C. M. Papadakis
  Kinetics of mesoglobule formation and growth in aqueous poly(N-isopropylacrylamide) solutions: pressure jumps at low and at high pressure
  Macromolecules **52**, 6416-6427 (2019)
- B.-J. Niebuur, W. Lohstroh, M.-S. Appavou, A. Schulte, C. M. Papadakis
  Water dynamics in a concentrated poly(N-isopropylacrylamide) solution at variable pressure
  Macromolecules **52**, 1942-1954 (2019)
- S. Nieuwenhuis, Q. Zhong, E. Metwalli, L. Bießmann, M. Philipp, A. Miasnikova, A. Laschewsky, C. M. Papadakis, R. Cubitt, J. Wang, P. Müller-Buschbaum
  Hydration and dehydration kinetics: comparison between poly(N-isopropyl methacrylamide) and poly(methoxy diethylene glycol acrylate) films
  Langmuir **35**, 691-7702 (2019)
- C. M. Papadakis, P. Müller-Buschbaum, A. Laschewsky
  Switch It Inside-Out: "Schizophrenic" behavior of all thermoresponsive UCST-LCST diblock copolymers
  Langmuir **35**, 9660-9676 (2019)
- W. Petry
  Neutrons for research, engineering and medicine in Germany
  ATW-Int. J. Nucl. Power **64**, 10, 455-462 (2019)
- J.-K. Pi, J. Yang, Q. Zhong, M.-B. Wu, H.-C. Yang, M. Schwartzkopf, S. V. Roth, P. Müller-Buschbaum, Z.-K. Xu
  Dual-layer nanofilms via mussel-inspiration and silication for non-iridescent structural color spectrum in flexible displays
  ACS Appl. Nano. Mater. **2**, 4556-4566 (2019)
- V. Pipich, K. Schlenstedt, M. Dickmann, R. Kasher, J. Meier-Haack, C. Hugenschmidt, W. Petry, Y. Orend, D. Schwahn
  Morphology and porous structure of standalone aromatic polyamide films as used in RO membranes–An exploration with SANS, PALS, and SEM
  J. Membrane Sci. **573**, 167-176 (2019)

- S. Pratap, E. Keller, P. Müller-Buschbaum
  Emergence of lead halid perovskite colloidal dispersions through aggregation and fragmentation: Insights from the nanoscale to the mesoscale
  Nanoscale **11**, 3495-3499 (2019)
- S. Pratap, N. Tamura, C. Stan, Z. Yuan, H. Gowdey, A. MacDowell, T. Song, N. Barchi, P. Müller-Buschbaum, C. Sutter-Fella, J. Slack
  Probing the in situ dynamics of structure–property evolution in hybrid perovskite thin films spin-coated from complex fluids by a custom-designed beamline-compatible multimodal measurement chamber
  Acta Cryst. **A75**, a155-a156 (2019)
- K. Rathinam, S. Abraham, Y. Oren, D. Schwahn, W. Petry,, Y. Kaufmann
  Surface–induced silica scaling during brackish water desalination: The role of surface charge and specific chemical groups
  Environ. Sci. Technol. **53**, 5202-5211 (2019)
- C. Reiter, H. Breitkreutz, A. Röhrmoser, W. Petry
  A model system for transient scenarios for FRM II
  European Nuclear Society, RRFM (2019)
- C. Reiter, H. Breitkreutz, A. Röhrmoser, A. Säubert, W. Petry
  Neutronic simulations of the FRM II
  Annals of Nuclear Energy **131**, 1-8 (2019)
- S. Rieger, B. J. Bohn, M. Döblinger, A. F. Richter, Y. Tong, K. Wang, P. Müller-Buschbaum, L. Polavarapu, L. Leppert, J.K. Stolarczyk, J. Feldmann
  Excitons and narrow bands determine the optical properties of cesium bismuth halides
  Phys. Rev **B 100**, 201404 (R) (2019)
- L. Rodrigues, F. Schneider, X. Zhang, E. Larsson, L. W. K. Moodie, H. Dietz, C. M. Papadakis, G. Winter. R. Lundmark, M. Hubert
  Cellular uptake of self-assembled phytantriol-based hexosomes is independent of major endocytic machineries
  J. Colloid Interf. Sci. **553**, 820-833 (2019)
- N. Saxena, B. Pretzl, X. Lamprecht, L. Bießmann, D. Yang, N. Li, C. Bilko, S. Bernstorff, P. Müller-Buschbaum
  Ionic liquids as post-treatment agents for simultaneous improvement of Seebeck coefficient and electrical conductivity in PEDOT:PSS films
  ACS Appl. Mater. Interfaces **11**, 8060-8071 (2019)
- J. Schlipf, Y. Hu, S. Pratap, L. Bießmann, N. Hohn, L. Porcar, T. Bein, P. Docampo, P. Müller-Buschbaum
  Shedding light on the moisture stability of 3D
  2D hybrid perovskite heterojunction thin films
  ACS Appl. Energy Mater. **2**, 1011-1018 (2019)

- L. Silvi, Z. Zhao-Karger, E. Röhm, M. Fichtner, W. Petry, W. Lohstroh
  A quasielastic and inelastic neutron scattering study of the alkaline and alkaline-earth borohydrides LiBH 4 and Mg (BH 4) 2 and the mixture LiBH 4+ Mg (BH 4) 2
  Phys. Chem. Chem. Phys **21**, 718 - 728 (2019)

- L. Song, M. Rawolle, N. Hohn, J. S. Gutmann, H. Frielinghaus, P. Müller-Buschbaum
  In situ monitoring mesoscopic deformation of nanostructured porous titania films caused by water ingression
  ACS Appl. Mater. Interfaces **11**, 32552-32558 (2019)

- L. Song, W. Wang, E. Barabino, D. Yang, V. Körstgens, P. Zhang, S. V. Roth, P. Müller-Buschbaum
  Composition-morphology correlation in PTB7-Th/PC71BM blend films for organic solar cells ACS
  Appl.Mater. Interfaces **11**, 3125-3135 (2019)

- K. Stallhofer, M. Nuber, R. Kienberger, V. Körstgens P. Müller-Buschbaum, H. Iglev
  Dynamics of short-lived polaron pairs and polarons in polythiophene derivatives observed via infrared-activated vibrations
  J. Phys. Chem. C **123**, 28100-28105 (2019)

- R. E. Stene, B. Scheibe, A. J. Karttunen, W. Petry, F. Kraus
  Lewis acid behavior of MoOF4 towards the alkali metal fluorides in anhydrous hydrogen fluoride solutions
  Eur. J. Inorg. Chem **32**, 3672-3682 (2019)

- C. Steyer, B. Baumeister, C. Schwarz, N. Rehms, W. Petry, B. Stepnik, J. Allenou
  Production of monolithic fuel plates with Molybdenum barrier coating
  European Nuclear Society, RRFM (2019)

- H.Tang, J.Zhong, W.Chen, K.Shi, G.Mei, Y.Zhang, Z.Wen, P. Müller-Buschbaum, D.Wu, K.Wang, X.W.Sun
  Lead sulfide quantum dot photodetector with enhanced responsivity through a two-step ligand exchange method
  ACS Appl. Nano Mater. **2**, 6135-6143 (2019)

- P. I. Thro, W. Petry
  Securing the European supply of 19.75 percent enriched Uranium Fuel - a revised assessment
  Euratom Supply Agency (ESA), (2019)

- N. S. Vishnevetskaya, V. Hildebrand, N. M. Nizardo, C.-H. Ko, Z. Di, A. Radulescu, L. C. Barnsley, P. Müller-Buschbaum, A. Laschewsky, C. M. Papadakis
  All-in-one schizophrenic self-assembly of orthogonally tuned thermoresponsive diblock copolymers
  Langmuir **35**, 6441-6452 (2019)

- K. Wang, N. Hohn, L.P. Kreuzer, T. Widmann, M. Haese, J.-F. Moulin, P. Müller-Buschbaum
  Morphology tuning of ZnO/P3HT/P3HT-b-PEO hybrid films deposited via spray or spin coating
  ACS Appl. Mater. Interfaces **11**, 10998-11005 (2019)

- R. Wang, Y. Tong, K. Wang, S. Xia, E. Kentzinger, O. Soltwedel, P. Müller-Buschbaum, H. Frielinghaus
  Monitoring the morphological evolution in mixed-dimensional lead bromide perovskite film with lamellar-stacked perovskite nanoplatelets
  Nanoscale Hor. **4**, 1139-1144 (2019)

- W. Wang, T. Widmann, L. Song, T. Fröschl, N. Hüsing, G. Mo, Z. Wu, P. Zhang, S. V. Roth, H. Fan, P. Müller-Buschbaum
  Aging of low-temperature derived highly flexible nanostructured TiO2/P3HT hybrid films during bending
  J. Mater. Chem. **A 7**,10805-10814 (2019)

- X. Wang, L. Ma, Q. Ji, J.-Q. Meng, S. Liang, Z. Xu, M. Wang, X. Zuo, Y. Xiao, J. Zhu, Y. Xia, P. Müller-Buschbaum, Y. Cheng
  MnO/metal/carbon nanohybrid lithium-ion battery anode with enhanced electrochemical performance: universal facile scalable synthesis and fundamental understanding
  Adv. Mater. Inter. **6**, 1900335 (2019)

- X. Wang, Y. Xia, X. Zuo, S. J. Schaper, S. Yin, Q. Ji, S. Liang, Z. Yang, S. Xia, Y. Xiao, J. Zhu, P. Müller-Buschbaum, Y. Cheng
  Synergistic effects from super-small sized TiO2 and SiOx nanoparticles within TiO2/SiOx/carbon 0nanohybrid lithium-ion battery anode
  Ceram. Int **45**, 14327-14337 (2019)

- X. Wang, D. Zhao, C. Wang, Y. Xia, W. Jiang, S. Xia, S. Yin, X. Zuo, E. Metwalli, Y. Xiao, Z. Sun, J. Zhu, P. Müller-Buschbaum, Y. Cheng
  Role of nickel nanoparticles in high-performance TiO2/Ni/carbon nanohybrid lithium/sodium-ion battery anodes
  Chem. Asian J. **14**, 1557-1569 (2019)

- T. Widmann, L. P. Kreuzer, N. Hohn, L. Bießmann, K. Wang, S. Rinner, J.-F. Moulin, A .J. Schmid, Y. Hannappel, O. Wrede, M. Kühnhammer, T. Hellweg, R. von Klitzing, P. Müller-Buschbaum
  Hydration and solvent exchange induced swelling and deswelling of homogeneous poly(N-isopropylacrylamide) microgel thin films
  Langmuir **35**, 16341-16352 (2019)

- K. S. Wienhold, V. Körstgens, S. Grott, X. Jiang, M. Schwartzkopf, S. V. Roth, P. Müller-Buschbaum
  Effect of solvent additives on the morphology and device performance of printed non-fullerene acceptor based organic solar cells
  ACS Appl. Mater. Interfaces **11**, 42313-42321 (2019)

- X. Wu, A. Surendran, J. Ko, O. Filonik, E. M. Herzig, P. Müller-Buschbaum, W. L. Leong
  Ionic-liquid doping enables high transconductance, fast response time and high ion sensitivity in organic electrochemical transistors
  Adv. Mater **31**, 1805544 (2019)

- S. Xia, L. Song, W. Chen, V. Körstgens, M. Opel, M. Schwartzkopf, S. V. Roth, P. Müller-Buschbaum
  Printed thin diblock copolymer films with dense magnetic nanostructure
  ACS Appl. Mater. Interfaces **11**, 21935-21945 (2019)

- S. Xia, L. Song, N. Hohn, K. Wang, S. Grott, M. Opel, M. Schwartzkopf, S. V. Roth, P. Müller-Buschbaum
  Spray-coating magnetic thin hybrid films of PS-b-PNIPAM and magnetite nanoparticles
  Adv. Funct. Mater. **29**, 1808427 (2019)

- S. Xia, L. Song, W. Chen, V. Körstgens, M. Schwartzkopf, S.V. Roth, P. Müller-Buschbaum,
  Printed Thin Diblock Copolymer Films with Dense Magnetic Nanostructure
  ACS Appl. Mater. Inter. **11**, 21935-21945 (2019)

- D. Yang, F.C. Löhrer, V. Körstgens, A. Schreiber, S. Bernstorff, J. M. Buriak, P. Müller-Buschbaum
  In-operando study of the effects of solvent additives on the stability of organic solar cells based on PTB7-Th:PC71BM
  ACS Energy Lett. **4**, 464-470 (2019)

- Q. Zhong, M. Lu, S. Nieuwenhuis, B.-S. Wu, G.-P. Wu, Z.-K. Xu, P. Müller-Buschbaum, J.-P. Wang
  Enhanced stain removal and comfort control achieved by cross- ing light- and thermo- dual responsive copolymer onto cotton fabrics
  ACS Appl. Mater. Interfaces **11**, 5414-5426 (2019)

- X. Zuo, X. Wang, Y. Xia, S. Yin, Q. Ji, Z. Yang, M. Wang, X. Zheng, B. Qiu, Z. Liu, J. Zhu, P. Müller-Buschbaum, Y.-J. Cheng
  Silicon/carbon lithium-ion battery anode with 3D hierarchical macro-/mesoporous silicon network: self-templating synthesis via magnesiothermic reduction of silica/carbon composite
  J. Power Sources **412**, 93-104 (2019)

9.2 Talks

- N. Aslan, W. Lohstroh, S. Busch, C. Pistidda, K. Pranzas, M. Müller
  6Mg(NH2)/9LiH/LiBH4: Molecular dynamics and hydrogen diffusion
  DPG-Frühjahrstagung, Regensburg, 31 Mar – 5 Apr 2019

- N. Aslan, W. Lohstroh, S. Busch, C. Pistidda, K. Pranzas, M. Müller
  6 Mg(NH2)2 + 9 LiH + LiBH4: QENS investigation and in-siut SANS measurement
  4th internal science meeting of MLZ , Grainau, 24 – 27 June 2019

- A. V. Berezkin, F. Jung, D. Posselt, D.-M. Smilgies, C. M. Papadakis
  Morphologies and Solvent Distribution During Solvent Vapor Annealing of Block Copolymer Thin Films: In situ, Real-time GISAXS Investigations
  National Synchrotron Radiation Research Center, Hsinchu, Taiwan, 22 Apr 2019

- W. Chen, P. Müller-Buschbaum
  Inner structure analysis of quantum dot solids for photo-devices
  DPG-Frühjahrstagung, Regensburg, 31 Mar – 5 Apr 2019

- W. Chen, P. Müller-Buschbaum
  In-situ sputtering deposition of gold on close packed quantum dot solid
  NanoWorkshop 2019, Espoo, Finland, 22 – 24 Jul 2019

- O. Filonik, M. E. Thordardottir, J. Lebert, S. Pröller, S. Weiss, L.J. Haur, A. Priyadarshi, N. Mathews, P. Müller-Buschbaum, E.M. Herzig
  Following the perovskite crystallization in printed mesoscopic organometal halide perovskite solar cells
  DPG-Frühjahrstagung, Regensburg, 31 Mar – 5 Apr 2019

- M. Gensch, M. Schwartzkopf, J. Drewes, O. Polonskyi, T. Strunskus, F. Faupel, P. Müller-Buschbaum, S.F. Roth
  Sputter deposition of Al on nanostructured PMMA-b-P3HT and PS-b-PMMA copolymer thin films
  DPG-Frühjahrstagung, Regensburg, 31 Mar – 5 Apr 2019

- S. Grott, R. Delgado, V. Körstgens, K. Wienhold, X. Jiang, M. Schwartzkopf, S. V. Roth, P. Müller-Buschbaum
  Printed fullerene-free thin films for photovoltaic applications
  DESY Photo Science Users' Meeting, Hamburg, 23 – 25 Jan 2019

- J. E. Heger, P. Müller-Buschbaum
  Directional, hierarchical films by spray coating
  E13 seminar, Garching, 15 Jan 2019

- J. E. Heger, W. Chen, A.-L. Oechsle, N. Li, S. Yin, C. J. Brett, W. Ohm, S. V. Roth, S. Bernstorff, P. Müller-Buschbaum
  Biopolymer templated hierarchical titania films for hybrid solar cells
  4th internal biennial science meeting of the MLZ, Grainau, 24 – 27 Jun 2019

- J. E. Heger, W. Chen, A.-L. Oechsle, N. Li, S. Yin, C. J. Brett, W. Ohm, S. V. Roth, S. Bernstorff, P. Müller-Buschbaum
  Biotemplating of titania nanostructures for hybrid photon sensors
  IFE NPU, Xi'an, China, 9 – 15 Oct 2019

- A. Heldmann
  Diffraction Based Determination of Single Crystalline Elastic Constants on Polycrystalline Alloys
  Euromat 2019, Stockholm, Sweden, 1 – 5 Sep 2019
- S.-H. Huang, C.-H. Ko, G. P. Meledam, M. Schroer, A. Miasnikova, A. Laschewsky and C. M. Papadakis
  Temperature- and pressure-dependent phase behavior of a Polystyrene-b-Poly(N-isopropylacrylamide) diblock copolymer in aqueous solution
  MaMaSELF status meeting, Rigi, Switzerland, 21 – 24 May 2019
- F. A. Jung, P. A. Panteli, D.-M. Smilgies, D. Posselt, C. Tsitsilianis, C. S. Patrickios, C. M. Papadakis
  In situ GISAXS Investigations of Multi-responsive Block Copolymer Thin Films during Solvent Vapor Annealing
  DPG-Frühjahrstagung, Regensburg, 31 Mar – 5 Apr 2019
- F. A. Jung, P. A. Panteli, C.-H. Ko, J.-J. Kang, L. C. Barnsley, C. Tsitsilianis, C. S. Patrickios, C. M. Papadakis
  pH and temperature responsive telechelic pentablock quaterpolymers in aqueous solution
  European Polymer Congress (EPF 2019), Heraklion Crete, Greece, 9 - 14 Jun 2019
- F. A. Jung, P. A. Panteli, D.-M. Smilgies, D. Posselt, C. Tsitsilianis, C. S. Patrickios, C. M. Papadakis
  In situ GISAXS Investigations of Multi-Responsive Block Copolymer Thin Films during Solvent Vapor Annealing
  4th Internal Biannual Science Meeting of the MLZ, Grainau, 24 – 27 Jun 2019
- F. A. Jung, P. A. Panteli, D.-M. Smilgies, D. Posselt, C. Tsitsilianis, C. S. Patrickios, C. M. Papadakis
  In situ GISAXS Investigations of Multi-Responsive Block Copolymer Thin Films during Solvent Vapor Annealing
  FilmSTAR Workshop, Roskilde, 1 – 2 Jul 2019
- F. A. Jung, P. A. Panteli, C.-H. Ko, J.-J. Kang, L. C. Barnsley, C. Tsitsilianis, C. S. Patrickios, C. M. Papadakis
  pH and temperature responsive telechelic pentablock quaterpolymers in aqueous solution
  Kolloid-Tagung "Complex Fluids/49th Conference of the German Colloid Society, Stuttgart, Germany, 23 – 25 Sep 2019
- F. A. Jung, P. A. Panteli, C.-H. Ko, J.-J. Kang, L. C. Barnsley, C. Tsitsilianis, C. S. Patrickios, C. M. Papadakis
  pH and Temperature Responsive Telechelic Pentablock Quaterpolymers in Aqueous Solution
  MLZ User Meeting 2019, München, 10/11 Dec 2019
- J.-J. Kang, J. Zhao, H. Frielinghaus, L. Barnsley, F. Kohler, H. Dietz, S. Pispas, C.M. Papadakis
  Morphology of thermoresponsive molecular brushes with copolymer side arms in aqueous solution
  DPG-Frühjahrstagung, Regensburg, 31 Mar – 5 Apr 2019

- C.-H. Ko, K.-L. Claude, D. Schanzenbach, B.-J. Niebuur, H. Frielinghaus, L. Barnsley, V. Pipich, A. Schulte, P. Müller-Buschbaum, A. Laschewsky, C.M. Papadakis
  The structural and dynamic behavior of the thermoresponsive polymer poly(N-isopropylmethacrylamide)
  DPG-Frühjahrstagung, Regensburg, 31 Mar – 5 Apr 2019

- V. Körstgens, A. Haussmann, F.C. Löhrer, M. Schwartzkopf, A. Hinz, O. Polonskyi, T. Strunskus, H. Iglev, S.V. Roth, R. Kienberger, F. Faupel, P. Müller-Buschbaum
  Growth kinetics of gold electrodes used in hybrid solar cells
  DPG-Frühjahrstagung, Regensburg, 31 Mar – 5 Apr 2019

- V. Körstgens, C. Mayr, F. Buschek, H. Iglev, R. Kienberger, S.V. Roth, P. Müller-Buschbaum
  Spray deposition of water-processed active layers for hybrid solar cells investigated with in situ grazing incidence X-ray scattering techniques
  4th internal biennial science meeting of the MLZ, Grainau, 24 – 27 Jun 2019

- V. Körstgens, A. Haussmann, F. C. Löhrer, M. Schwartzkopf, A. Hinz, O. Polonskyi, T. Strunskus, H. Iglev, S. V. Roth, R. Kienberger, F. Faupel, P. Müller-Buschbaum
  In situ GISAXS sputter deposition of gold contacts onto hybrid solar cells
  SAXS/WAXS satellite workshop of DESY User Meeting, 24/25 Jan 2019

- V. Körstgens, L. Diaz Piola, C. Geiger, J. Heger, L. Kreuzer, T. Widmann, K. Stallhofer, H. Iglev, R. Kienberger, G. Mangiapia, P. Müller-Buschbaum
  Hybrid solar cells with laser-ablated titania: morphology investigation of the active layer with TOF-GISANS
  European Conference on Neutron Scattering, Saint Petersburg, Russia, 1 – 5 Jul 2019

- V. Körstgens, C. Mayr, A. Haussmann, L. Diaz Piola, H. Iglev, S. V. Roth, R. Kienberger, F. Faupel, P. Müller-Buschbaum
  Steps of device fabrication: in situ morphology investigations of hybrid solar cells with grazing incidence x-ray scattering techniques
  8th SolTech Conference, Nürnberg, 30 Sep – 2 Oct 2019

- V. Körstgens, C. Mayr, A. Haussmann, F. C. Löhrer, M. Schwartzkopf, A. Hinz, O. Polonskyi, T. Strunskus, H. Iglev, S. V. Roth, R. Kienberger, F. Faupel, P. Müller-Buschbaum
  Looking into steps of device fabrication of water-processed hybrid solar cells with x-ray scattering methods
  Institute of Flexible Electronics, Northwestern Polytechnical University, Xi'an, China, 11 Oct 2019

- V. Körstgens, L. Diaz Piola, C. Geiger, J. Heger, L. Kreuzer, T. Widmann, K. Stallhofer, H. Iglev, R. Kienberger, G. Mangiapia, P. Müller-Buschbaum
  Morphology investigation of the active layer of hybrid solar cells with TOF-GISANS
  MLZ User Meeting 2019, München, 10/11 Dec 2019

- L. P. Kreuzer, T. Widmann, L. Bießmann, R. Märkl, J.-F. Moulin, V. Hildebrand, A. Laschewsky, C.M. Papadakis, P. Müller-Buschbaum
  Phase transition kinetics in a doubly thermo-responsive block copolymer thin film followed with in-situ neutron reflectometry
  4th internal biennial science meeting of the MLZ, Grainau, 24 – 27 Jun 2019

- L. P. Kreuzer, T. Widmann, L. Bießmann, N. Hohn, J. Pantle, R. Märkl, J.-F. Moulin, V. Hildebrand, A. Laschewsky, C. M. Papadakis, P. Müller-Buschbaum
  Phase transition kinetics in a doubly thermo-responsive block copolymer thin film
  European Conference on Neutron Scattering, St. Petersburg, 30 Jun – 5 Jul 2019

- L. P. Kreuzer, T. Widmann, L. Bießmann, J.-F. Moulin, V. Hildebrand, A. Laschewsky, C. M. Papadakis, P. Müller-Buschbaum
  Potential use of thermo-responsive polymers as self-cooling window surface coatings
  9th MSE Colloquium, Garching, 1 Aug 2019

- L. P. Kreuzer, T. Widmann, L. Bießmann, N. Hohn, J. Pantle, R. Märkl, J.-F. Moulin, V. Hildebrand, A. Laschewsky, C. M. Papadakis, P. Müller-Buschbaum
  Phase transition kinetics in a doubly thermo-responsive block copolymer thin film
  MLZ User Meeting 2019, München, 10/11 Dec 2019

- L. P. Kreuzer, T. Widmann, P. Müller-Buschbaum
  Flexible Sample Environment for the Investigation of Soft Matter for Implementation at the ESS
  Verbundprojekttreffen Flexiprob Meeting, München, 13 Dec 2019

- F. C. Löhrer, V. Körstgens, S. Schaper, M. Schwartzkopf, A. Hinz, O. Polonskyi, T. Strunskus, F. Faupel, S.V. Roth, P. Müller-Buschbaum
  Following the formation of metal electrodes on photoactive polymer thin films
  DPG-Frühjahrstagung, Regensburg, 31 Mar – 5 Apr 2019

- G. P. Meledam, B.-J. Niebuur, L. Chiappisi, C.-H. Ko, S.-H. Huang, A. Schulte, C. M. Papadakis
  Structural evolution of thermoresponsive PMMA-b-PNIPAM micelles in aqueous solution revealed by time-resolved small-angle neutron scattering and rapid pressure jumps
  JCNS Workshop 2019, Tutzing, 7 – 10 October, 2019

- G. P. Meledam, L. Chiappisi, B.-J. Niebuur, C.-H. Ko, S.-H. Huang, A. Schulte, C. M. Papadakis
  Tuning Hydrophobicity and Aggregation Kinetics in Block Copolymer Micelles by Rapid Pressure Jumps: A Time-Resolved Small-Angle Neutron Scattering Investigation
  CompFlu 2019, IISER Bhopal India, 5 – 7 December, 2019

- P. Müller-Buschbaum
  Organic and Hybrid Photovoltaics
  43. Edgar-Lüscher Seminar zu Erneuerbaren Energien, Zwiesel, 22 - 24 Mar 2019

- P. Müller-Buschbaum
  Next-generation solar cells studied with GISANS
  257th American Chemical Society National Meeting in Orlando, USA, 31 Mar – 4 Apr 2019

- P. Müller-Buschbaum
  Grazing Incidence Scattering Methods for Studying Nanostructured Films
  ATUMS Seminar, Garching, 12 Apr 2019

- P. Müller-Buschbaum
  Organic and Hybrid Solar Cells Studied with Neutron Scattering
  Gordon Research Conference on Neutron Scattering, Hongkong, 5 – 10 May 2019

- P. Müller-Buschbaum
  MLZ Vision 2030
  French-German workshop on neutron scattering, Garching, 14 – 16 May 2019

- P. Müller-Buschbaum
  MLZ Conference Neutrons for Information and Quantum Technology - Welcome
  MLZ Conference Neutrons for Information and Quantum Technology, Lenggries, 4 Jun 2019

- P. Müller-Buschbaum
  Polymer and hybrid nanostructures for applications in organic solar cells investigated with advanced scattering techniques
  European Polymer Congress 2019 (EPF 2019), Heraklion, Greece, 9 – 14 Jun 2019

- P. Müller-Buschbaum
  Grainau scope setting
  4th Biannual MLZ Science Meeting, Grainau, 24 – 27 Jun 2019

- P. Müller-Buschbaum
  Heinz Maier-Leibnitz Zentrum (MLZ)
  European Conference on Neutron Scattering ECNS 2019, St. Petersburg, Russia, 30 Jun – 5 Jul 2019

- P. Müller-Buschbaum
  Next-generation solar cells studied with GISANS
  European Conference on Neutron Scattering (ECNS 2019), St. Petersburg, Russia, 30 Jun – 5 Jul 2019

- P. Müller-Buschbaum
  Polymer-Metal Interfaces in Organic Electronics
  9th International Workshop on Polymer-Metal Nanocomposites, Helsinki, Finland, 22 – 24 Jul 2019

- P. Müller-Buschbaum
  Beispiele wissenschaftlicher Untersuchungen am FRM II
  Erörterungstermin zum Antrag auf gehobene wasserechtliche Erlaubnis, Ismaning, 23 Jul 2019

- P. Müller-Buschbaum
  Neutrons for membrane biophysics - welcome
  MLZ School on Neutrons for membrane biophysics, 16 – 20 Sep 2019

- P. Müller-Buschbaum
  MLZ – present status and vision 2030
  ILL Colloquium, Grenoble, France, 20 Sep 2019

- P. Müller-Buschbaum
  MLZ – present status and vision 2030
  Department of Energy, US Visit, Garching, 21 Oct 2019

- P. Müller-Buschbaum
  Nanostructured polymer films for energy harvesting applications
  Seminar „Institute of Flexible Electronics (IFE)“, Northwestern Polytechnical University (NPU) in Xi'an, China, 10 Oct 2019

- P. Müller-Buschbaum
  Nanostructured polymer films for energy harvesting application
  Seminar „School of Materials Science and Engineering“, Northwestern Polytechnical University (NPU) Xi'an, China, 11 Oct 2019

- P. Müller-Buschbaum
  Experts Meeting on Fast Neutron Imaging - welcome
  Experts Meeting on Fast Neutron Imaging, Garching, 21 Oct 2019

- P. Müller-Buschbaum
  A basic introduction to GISAS
  GISAXS 2019, Hamburg, 10 – 22 Nov 2019

- P. Müller-Buschbaum
  Functional materials for energy research and more
  ATUMS annual meeting, Canmore, Canada, 11 – 15 Nov 2019

- P. Müller-Buschbaum
  Morphology–function relationship of hybrid thermoelectric films based on PEDOT:PSS
  MRS Fall Meeting 2019, Boston, USA 1 – 6 Dec 2019

- P. Müller-Buschbaum
  MLZ User Meeting - welcome
  MLZ User Meeting 2019, München, 10/11 Dec 2019

- B.-J. Niebuur, L. Chiappisi, F. Jung, X. Zhang, A. Schulte, C.M. Papadakis
  Formation and growth of mesoglobules in aqueous poly(N-isopropylacrylamide) solutions at low and high pressures revealed with fast pressure jumps
  DPG-Frühjahrstagung, Regensburg, 31 Mar – 5 Apr 2019

- B.-J. Niebuur, A. Schulte, C. M. Papadakis
  High-pressure Experiments on Aqueous PNIPAM Solutions
  Universität Regensburg, 4 June 2019

- B.-J. Niebuur, A. Schulte, C. M. Papadakis
  High-pressure behavior of PNIPAM in aqueous solution: Hydration behavior, segment and water dynamics and the growth of mesoglobules
  JCNS Workshop 2019: Trends and Perspectives in Neutron Instrumentation: Probing Structure and Dynamics in Soft Matter, Tutzing, 7 - 10 Oct 2019

- C. M. Papadakis
  Responsive polymer hydrogels: physical gelling through polyion complexation
  Institute of Polymer Science and Engineering, National Taiwan University, Taipei, Taiwan, 19 Apr 2019

- C. M. Papadakis
  Responsive polymer hydrogels: physical gelling through polyion complexation
  Sino-German Bilateral Forum Polymer Hydrogels and Elastomers, Shanghai, China, 15 -20 May 2019

- C. M. Papadakis, F. Jung, A. V. Berezkin, T. B. Tejsner, D. Posselt, D.-M. Smilgies
  Solvent Vapor Annealing of Diblock Copolymer Thin Films Using a Mixture of Two Solvents
  Roskilde University, Roskilde, Denmark, 1 Jul 2019

- C. M. Papadakis
  All-in-one schizophrenic self-assembly of orthogonally tuned thermoresponsive diblock copolymers
  Max-Planck-Institute for Polymer Research, Mainz, 2 Aug 2019

- W. Petry
  60 Jahre Spitzenforschung mit Neutronen in Garching – Wie Wissenschaft und Politik sich bedingen
  Tech-Histories Alive, eine gemeinsame Veranstaltung der TUM Emeriti of Excellence und des MCTS, 29 Jan 2019

- W. Petry
  Nuclear technology for basic research, industry and medicine
  Scientific workshop "Perspectives for German-Russian Nuclear Safety Science Cooperation", Berlin, 18 Mar 2019

- W. Petry
  French-German opportunities of cooperation to face the European revolution in Neutron Science
  Research Campus of Garching, 15/16 May 2019

- W. Petry
  Neutrons – for what?
  Visit of the European Atomic Energy Society to FRM II, 6 Jun 2019

- W. Petry
  Joint Research at PIK and corresponding education
  PIK-workshop in Jülich, 12 Jun 2019

- W. Petry
  High density fuel for high performance research reactors
  European Neutron Scattering Conference, St. Petersburg, Russia, 1 – 5 Jul 2019

- W. Petry
  Status of Research and Technology, Introduction & Outlook
  Workshop FRM II Conversion – Status and Perspectives, BMBF, Bonn, 19 Nov 2019

- S. Pratap, J. Slack
  A multimodal environment for understanding chemical processing and transformations at the microdiffraction beamline
  ALS Photon Science Group Meeting, ALS Berkeley Lab, USA, 21 Feb 2019

- S. Pratap
  An introduction to the material class of hybrid perovskites for optoelectronic functionality
  Material Science Symposium, UC Berkeley, USA, 21 Mar 2019

- S. Pratap, J. Schlipf, K. John, V. Körstgens, F. Fischer, S. Vema, A. Holleitner, A. Davydok, C. Krywka, P. Müller-Buschbaum
  On the colloidal behaviour of hybrid perovskite precursor dispersion and tracking structural heterogeneties arising from mixed perovskites: insights into the nano and macroscale
  DPG-Frühjahrstagung, Regensburg, 31 Mar – 5 Apr 2019
- S. Pratap, J. Schlipf, L. Bießmann, P. Müller-Buschbaum
  On the Chemical Origins of Crystalline Preferred Orientations in Hybrid Perovskite Thin Films — Microstructures Revisited
  MRS Spring Meeting, Phoenix, USA, 22 – 26 Apr 2019
- S. Pratap, N. Tamura, C. Stan, Z. Yuan, H. Gowdey, A. MacDowell, T. Song, N. Barchi, P. Müller-Buschbaum, C. Sutter-Fella, J. Slack
  Probing the in-situ dynamics of structure-property evolution in hybrid perovskite thin films spin-coated from complex fluids by a custom designed, beamline compatible multimodal measurement chamber
  American Crystallography Association Annual Meeting, Covington, USA, 20 – 24 Jul 2019
- S. Pratap, N. Tamura, C. Stan, Z. Yuan, H. Gowdey, A. MacDowell, T. Song, N. Barchi, P. Müller-Buschbaum, C. Sutter-Fella, J. Slack
  Probing the in-situ dynamics of structure-property evolution in hybrid perovskite solid solutions from complex fluids
  Molecular Foundry User Meeting, Berkeley Lab, USA, 21 – 22 Aug 2019
- S. Pratap
  The fascinating world of soft materials - exploring hybrid perovskites
  Ginsberg Group Symposium, UC Berkeley, USA, 23 Sep 2019
- S. Pratap
  Understanding the crystallization of solution processed alloys of hybrid perovskites by multimodal characterization
  Neville Smith prize talk at ALS User Meeting, ALS Berkeley Lab, USA, 1 – 3 Oct 2019
- S. Pratap, N. Tamura, C. Stan, Z. Yuan, H. Gowdey, A. MacDowell, T. Song, N. Barchi, P. Müller-Buschbaum, C. Sutter-Fella, J. Slack
  Understanding the crystallization of solution processed alloys of hybrid perovskites by multimodal characterization
  ALS User Meeting, ALS Berkeley Lab, USA, 1 – 3 Oct 2019
- R. Schaffrinna, M. Schwager, P. Müller-Buschbaum
  Thiophene based semiconductors for organic solar cells
  2th Ko-op Symposium of the Munich School of Engineering, Garching, 28 Nov 2019
- S. J. Schaper, V. Körstgens, M. Schwartzkopf, P. Pandit, A. Hinz, O. Polonskyi, T. Strunskus, F. Faupel, S.V. Roth, P. Müller-Buschbaum
  In-situ GISAXS during sputter deposition of metal nanolayers on functional polymer thin films for lithium-ion batteries
  DPG-Frühjahrstagung, Regensburg, 31 Mar – 5 Apr 2019

- S. J. Schaper, V. Körstgens, F.C. Löhrer, M. Schwartzkopf, P. Pandit, A. Hinz, O. Polonskyi, T. Strunskus, F. Faupel, S.V. Roth, P. Müller-Buschbaum
  Contacting functional polymer thin films for lithium-ion batteries via sputter deposited metal nanolayers revealing their growth with in-situ GISAXS
  4th internal biennial science meeting of the MLZ, Grainau, 24 – 27 Jun 2019

- S. J. Schaper, F. C. Löhrer, V. Körstgens, S. Xia, M. Schwartzkopf, M. Gensch, P. Pandit, A. Hinz, O. Polonskyi, T. Strunskus, F. Faupel, S. V. Roth, P. Müller-Buschbaum
  Revealing the formation of sputter deposited metal nanolayers on functional polymer thin films for lithium-ion batteries
  9th International Workshop on Polymer-Metal NanoComposites, Helsinki, 21 – 24 July 2019

- S. Szabò, F. Yang, W. Petry
  Self-diffusion in Mercury investigated with quasi-elastic neutron scattering
  17th International conference on liquid and amorphous metals, Lyon, 26 – 30 August 2019

- S. Szabò, D. Holland-Moritz, F. Yang, T. Voigtmann, Z. Evenson and W. Petry
  Short range order in Zr-Ti melts
  XXXVII International Symposium on Dynamical Properties of Solids (DyProSo2019), Ferrara, Italy, 8 – 12 Sep 2019

- N. S. Vishnevetskaya, V. Hildebrand, P. Müller-Buschbaum, A. Laschewsky, C. M. Papadakis
  All-in-One Schizophrenic Self-assembly of Orthogonally Tuned Thermoresponsive Diblock Copolymers
  DPG-Frühjahrstagung, Regensburg, 31 Mar – 5 Apr 2019

- N. S. Vishnevetskaya, V. Hildebrand, A. Laschewsky, P. Müller-Buschbaum, C. M. Papadakis
  Schizophrenic Micelles from Doubly and Orthogonally Switchable Block Copolymers
  European Polymer Congress (EPF 2019), Heraklion Crete, Greece, 9 - 14 June 2019

- N. S. Vishnevetskaya, V. Hildebrand, N. M. Nizardo, C.-H. Ko, P. Müller-Buschbaum, A. Laschewsky, C. M. Papadakis
  All-in-one schizophrenic self-assembly of orthogonally tuned thermoresponsive diblock copolymers
  Kolloid-Tagung ”Complex Fluids/49th Conference of the German Colloid Society, Stuttgart, 23 – 25 Sep 2019

- N. S. Vishnevetskaya, V. Hildebrand, N. M. Nizardo, C.-H. Ko, P. Müller-Buschbaum, A. Laschewsky, C. M. Papadakis
  All-in-one schizophrenic self-assembly of orthogonally tuned thermoresponsive diblock copolymers
  MLZ User Meeting 2019, München, 10/11 Dec 2019

- T. Widmann, L. Kreuzer, N. Hohn, K. Wang, G. Mangiapia, Y. Hertle, T. Hellweg, P. Müller-Buschbaum
  GISANS sample environment for the investigation of thin polymer films
  DPG-Frühjahrstagung, Regensburg, 31 Mar – 5 Apr 2019

- T. Widmann, L. P. Kreuzer, P. Müller-Buschbaum
  Flexible sample environment for the investigation of soft matter for implementation at the ESS
  FlexiProb Meeting, Lund, Sweden, 27 – 28 May 2019

- C. L. Weindl, M. A. Giebel, T. F. Fässler, P. Müller-Buschbaum
  Germanium-based nanostructure synthesis guided by amphiphilic diblock copolymer templating
  Annual ATUMS meeting, Canmore, Canada, 10 – 15 Nov 2019

- K. S. Wienhold, V. Körstgens, S. Grott, X. Jiang, M. Schwartzkopf, S.V. Roth, P. Müller-Buschbaum
  In-situ study of printed films of PBDB-T-SF:IT-4F for application in organic solar cells
  DPG-Frühjahrstagung, Regensburg, 31 Mar – 5 Apr 2019

- D. Yang, F.C. Löhrer, V. Körstgens, A. Schreiber, S. Bernstorff, J. Buriak, P. Müller-Buschbaum
  Investigating in-operando the effects of solvent additives on the stability of organic solar cells based on PTB7-Th:PC71BM
  DPG-Frühjahrstagung, Regensburg, 31 Mar – 5 Apr 2019

9.3 Posters

- S. Aeschbach, S. Grott, P. Müller-Buschbaum
  Morphological investigations of fullerene-free bulk heterojunction blends for photovoltaic applications cast on curved surfaces
  DPG-Frühjahrstagung, Regensburg, 31 Mar – 5 Apr 2019

- N. Aslan, K. Pranzas, C. Horstmann, O. Kotlyar, O. Metz, S. Busch, C. Pistidda, M. Dornheim, M. Müller and W. Lohstroh
  High-Pressure cell for in-situ characterization of hydrogen storage materials
  MML Workshop, Dresden, 13 – 15 Feb 2019

- N. Aslan, W. Lohstroh, S. Busch, C. Pistidda, K. Pranzas, M. Müller
  Molecular dynamics and hydrogen diffusion in (NH2)-and (BH4)-based hydrogen storage materials
  IFF Spring School 2019, Jülich, 10 – 22 Mar 2019

- N. Aslan, W. Lohstroh, S. Busch, C. Pistidda, K. Pranzas, M. Müller
  Characterisation of complex hydrides with neutron scattering
  Gordon Research Seminar and Conference, Castelldefels Spain, 29 Jun – 5 Jul 2019

- N. Aslan, W. Lohstroh, S. Busch, C. Pistidda, K. Pranzas, M. Müller
  QENS and in situ SANS investigation of complex hydrides
  MLZ User Meeting 2019, München, 10/11 Dec 2019

- A. Baccari, P. Müller-Buschbaum
  Thermo-mechanical behavior of silver-filled thermoplastic polymers
  DPG-Frühjahrstagung, Regensburg, 31 Mar – 5 Apr 2019

- A. V. Berezkin, F. Jung, D. Posselt, D.-M. Smilgies, C. M. Papadakis
  Morphologies and solvent distribution during solvothermal vapor annealing of block copolymer thin films: in situ, real-time GISAXS investigations
  GISAXS 2019, Hamburg, 20 – 22 Nov 2019

- W. Cao, S. Xia, X. Jiang, M. Appold, M. Opel, M. Gallei, M. Schwartzkopf, S. V. Roth, P. Müller-Buschbaum
  Self-assembly of large nanoparticles in ultrahigh molecular weight linear diblock copolymer films
  DPG-Frühjahrstagung, Regensburg, 31 Mar – 5 Apr 2019

- W. Cao, S.Xia, X. Jiang, M. Appold, M. Opel, M. Gallei, M. Schwartzkopf, S.V. Roth, P. Müller-Buschbaum
  Self-assembly of large iron oxide nanoparticles in ultrahigh molecular weight linear diblock copolymer films
  4th internal biennial science meeting of the MLZ, Grainau, 24 – 27 Jun 2019

- W. Cao, S. Xia, X. Jiang, M. Appold, M. Opel, M. Gallei, M. Schwartzkopf, S. V. Roth, P. Müller-Buschbaum
  Magnetic films based on ultrahigh molecular weight diblock copolymer
  MLZ User Meeting 2019, München, 10/11 Dec 2019

- W. Chen, P. Müller-Buschbaum
  Quantum dot solids for photo-devices
  4th internal biennial science meeting of the MLZ, Grainau, 24 – 27 Jun 2019

- L. Diaz Piola, V. Körstgens, P. Müller-Buschbaum
  Water-processed active layers for hybrid photovoltaics using spray deposition techniques
  DPG-Frühjahrstagung, Regensburg, 31 Mar – 5 Apr 2019

- L. Díaz Piola, V. Körstgens, K. Stallhofer, H. Iglev, R. Kienberger and P. Müller-Buschbaum
  Water-processed active layers for hybrid photovoltaics using spray and slot-die coating techniques
  9th Energy Colloquium of the Munich School of Engineering, Garching, 1 Aug 2019

- C. Geiger, C. Henschel, A. Laschewsky, C.M. Papadakis, P. Müller-Buschbaum
  Co-nonsolvency induced self-organization of thermo-responsive block copolymers in thin films
  DPG-Frühjahrstagung, Regensburg, 31 Mar – 5 Apr 2019

- C. Geiger, T. Widmann, L. P. Kreuzer, G. Mangiapia, C. Henschel, A. Laschewsky, C. M. Papadakis, P. Müller-Buschbaum
  TOF-NR investigation of the co-nonsolvency behavior of thermo-responsive block copolymer thin films
  Emerging Neutronic Approaches for Advanced Materials Study and Innovation in Energy, the Environment, Health and Infrastructure, Hong Kong, China, 5 – 10 May 2019

- C. Geiger, C. Henschel, L.P. Kreuzer, T. Widmann, G. Mangiapia, V. Körstgens, A. Laschewsky, C.M. Papadakis, P. Müller-Buschbaum
  Investigating vapor-induced co-nonsolvency in thin films by TOF-NR
  4th internal biennial science meeting of the MLZ, Grainau, 24 – 27 Jun 2019

- C. Geiger, T. Widmann, L. P. Kreuzer, G. Mangiapia, C. Henschel, A. Laschewsky, C. M. Papadakis, P. Müller-Buschbaum
  Cononsolvency in PNIPAM-based block copolymer thin films
  MLZ User Meeting 2019, München, 10/11 Dec 2019

- M. Gensch, M. Schwartzkopf, W. Ohm, C. J. Brett, P. Pandit, L. Bießmann, L. P. Kreuzer, J. Drewes, O. Polonskyi, F. Faupel, A. Stierle, Peter-Müller-Buschbaum, S. V. Roth
  Optoelectronic properties of nanogranular silver layers during polymer-template assisted sputter deposition
  SAXS/WAXS user meeting 2019, Hamburg, 24 – 25 Jan 2019

- M. Gensch, M. Schwartzkopf, W. Ohm, C. J. Brett, P. Pandit, L. Bießmann, L. P. Kreuzer, J. Drewes, O. Polonskyi, F. Faupel, A. Stierle, Peter-Müller-Buschbaum, S. V. Roth
  Optoelectronic properties of nanogranular silver layers during polymer-template assisted sputter deposition
  MLL Workshop 2019, Dresden, 13 – 15 Feb 2019

- M. Gensch, M. Schwartzkopf, W. Ohm, C. J. Brett, P. Pandit, L. Bießmann, L. P. Kreuzer, J. Drewes, O. Polonskyi, F. Faupel, A. Stierle, Peter-Müller-Buschbaum, S. V. Roth
  Optoelectronic properties of nanogranular silver layers during polymer-template assisted sputter deposition
  Food and Energy Winterschool 2019, Raitenhaslach, 18 – 22 Feb 2019

- M. Gensch, M. Schwartzkopf, J. Drewes, O. Polonskyi, T. Strunskus, F. Faupel, P. Müller-Buschbaum, S.V. Roth
  Sputter deposition of Al & Ag on nanostructured PMMA-b-P3HT and PS-b-PMMA copolymer thin films
  4th internal biennial science meeting of the MLZ, Grainau, 24 – 27 Jun 2019

- M. Gensch, M. Schwartzkopf, S. Schaper, L. P. Kreuzer, A.-L. Oechsle, N. Li, J. Drewes, O. Polonskyi, T. Strunskus, F. Faupel, P. Müller-Buschbaum, S. V. Roth
  Sputter deposition of Ag on nanostructured PMMA-b-P3HT and PS-b-PMMA copolymer thin films
  GISAXS 2019, Hamburg, 20 – 22 Nov 2019
- G. Glänzer, Z. Siebers, R. Streng, S. J. Schaper, P. Müller-Buschbaum
  Interfaces in polymer based thin-film Lithium-Ion batteries
  8th MSE Energy Kolloquium, Nürnberg, 8 Jul 2019
- G. Glänzer, Z. Siebers, R. Streng, S. J. Schaper, P. Müller-Buschbaum
  Interfaces in polymer based thin-film Lithium-Ion batteries
  MLZ User Meeting 2019, München, 10/11 Dec 2019
- S. Grott, R. Delgado, V. Körstgens, K. Wienhold, X. Jiang, M. Schwartzkopf, S. V. Roth, P. Müller-Buschbaum
  Printed fullerene free organic thin films for photovoltaic applcations
  DESY Photo Science Users' Meeting, Hamburg, 23 – 25 Jan 2019
- S. Grott, X. Jiang, V. Körstgens, K. Wienhold, M. Schwartzkopf, S.V. Roth, P. Müller-Buschbaum
  In-situ study of printed active layers of conjugated polymers and small acceptor molecules for application in high-efficiency organic solar cells
  4th internal biennial science meeting of the MLZ, Grainau, 24 – 27 Jun 2019
- S. Grott, R. Delgado, V. Körstgens, K. Wienhold, X. Jiang, M. Schwartzkopf, S. V. Roth, P. Müller-Buschbaum
  Printing low-bandgap based bulk heterojunctions for photovoltaic applicationsy
  9th Energy Colloquium of the Munich School of Engineering, Garching, 1 Aug 2019
- S. Grott, R. Delgado, V. Körstgens, K. Wienhold, X. Jiang, M. Schwartzkopf, S. V. Roth, P. Müller-Buschbaum
  Printed bulk heterojunction blends for photovoltaic applications
  8th SolTech Conference, Nürnberg, 30 Sep – 2 Oct 2019
- S. Grott, R. Delgado, V. Körstgens, K. Wienhold, X. Jiang, M. Schwartzkopf, S. V. Roth, P. Müller-Buschbaum
  Printed organic thin films for photovoltaic applications – a morphology study
  MLZ User Meeting 2019, München, 10/11 Dec 2019
- R. Guo, W. Chen, L. K. Reb, S. Yin, K. Wienhold, B. Predeschly, M. A. Scheel, P. Müller-Buschbaum
  Do different device architectures of perovskite solar cells have different degradation mechanisms?
  4th internal biennial science meeting of the MLZ, Grainau, 24 – 27 Jun 2019
- R. Guo, W. Chen, L. K. Reb, S. Yin, K. Wienhold, B. Predeschly, M. A. Scheel, P. Müller-Buschbaum
  Do different device architectures of perovskite solar cells have different degradation mechanisms?
  9th Energy Colloquium of the Munich School of Engineering, Garching, 1 Aug 2019

- R. Guo, W. Chen, L. K. Reb, S. Yin, K. Wienhold, B. Predeschly, M. A. Scheel, P. Müller-Buschbaum
  Do different device architectures of perovskite solar cells have different degradation mechanisms?
  E-conversion conference, Sepr 9—13, 2019
- R. Guo, W. Chen, L. K. Reb, S. Yin, K. Wienhold, B. Predeschly, M. A. Scheel, P. Müller-Buschbaum
  What is the initial stage of degradation mechanism for perovskite solar cells?
  8th SolTech Conference, Nürnberg, 30 Sep – 2 Oct 2019
- R. Guo, W. Chen, L. K. Reb, S. Yin, K. Wienhold, B. Predeschly, M. A. Scheel, P. Müller-Buschbaum
  What is the initial stage of degradation mechanism for perovskite solar cells?
  Hot Carrier Dynamics in Advanced Concept Solar Cells, Garching, 28/29 October
- R. Guo, W. Chen, L. K. Reb, S. Yin, K. Wienhold, B. Predeschly, M. A. Scheel, P. Müller-Buschbaum
  What is the initial stage of degradation mechanism for perovskite solar cells?
  GISAXS 2019, Hamburg, 20 – 22 November
- R. Guo, W. Chen, L. K. Reb, S. Yin, K. Wienhold, B. Predeschly, M. A. Scheel, P. Müller-Buschbaum
  What is the initial stage of degradation mechanism for perovskite solar cells?
  MLZ User Meeting 2019, München, 11/12 Dec 2019
- J. E. Heger, W. Chen, S. Grott, X. Jiang, S. Bernstorff, P. Müller-Buschbaum
  Biopolymer templated titanium dioxide films prepared via spray coating
  DPG-Frühjahrstagung, Regensburg, 31 Mar – 5 Apr 2019
- J. E. Heger, W. Chen, A.-L. Oechsle, N. Li, S. Yin, C. J. Brett, W. Ohm, S. V. Roth, S. Bernstorff, P. Müller-Buschbaum
  Spray deposition of bio templated titania for hybrid solar cells
  9th Energy Colloquium of the Munich School of Engineering, Garching, 1 Aug 2019
- J. E. Heger, W. Chen, A.-L. Oechsle, N. Li, S. Yin, C. J. Brett, W. Ohm, S. V. Roth, S. Bernstorff, P. Müller-Buschbaum
  Bio-hybrid thin films for templating titania nanostructures
  MLZ User Meeting 2019, München, 10/11 Dec 2019
- C. Henschel, C.-H. Ko, A. Laschewsky, C. M. Papadakis
  Self-assembly and co-nonsolvency of hydrophobic/thermoresponsive block copolymers: influence of chemical structure and block lengths
  Macromolecular Colloquium Freiburg, Freiburg, 20 – 22 Feb 2019
- L. Huber, K. Wienhold, P. Müller-Buschbaum
  Influence of printing temperature on the effitiency of organic solar cells
  MLZ User Meeting 2019, München, 10/11 Dec 2019
- G.I. Ivandekiç, S. Grott, P. Müller-Buschbaum
  Investigation on the influence of morphological modifications on the power-conversion efficiency of fullerene-free organic solar cells
  DPG-Frühjahrstagung, Regensburg, 31 Mar – 5 Apr 2019

- X. Jiang, S. Grott, T. Riccitelli, V. Körstgens, K. Wienhold, M. Schwartzkopf, S.V. Roth, W. Cao, S. Yin, L. Song, P. Müller-Buschbaum
  Following the morphology formation of printed non-fullerene active layer for solar cells
  DPG-Frühjahrstagung, Regensburg, 31 Mar – 5 Apr 2019
- X. Jiang, S. Grott, T. Riccitelli, V. Körstgens, K. Wienhold, M. Schwartzkopf, S.V. Roth, P. Müller-Buschbaum
  Tracking the morphology formation of printed non-fullerene active layer for solar cells
  4th internal biennial science meeting of the MLZ, Grainau, 24 – 27 Jun 2019
- X. Jiang, S. Schaper, P. Müller-Buschbaum
  In-situ investigation of sputter deposition electrodes for organic solar cells
  9th Energy Colloquium of the Munich School of Engineering, Garching, 1 Aug 2019
- X. Jiang, S. Grott, W. Chen, P. Müller-Buschbaum
  Tracking the morphology formation of printed non-fullerene active layers for solar cells by using GISAXS technique
  8th SolTech Conference, Nürnberg, 30 Sep – 2 Oct 2019
- X. Jiang, S. Schaper, P. Müller-Buschbaum
  In-situ investigation of electrode sputter deposition for non-fullerene organic solar cell applications
  MLZ User Meeting 2019, München, 10/11 Dec 2019
- F. A. Jung, P. A. Panteli, C.-H. Ko, J.-J. Kang, L. C. Barnsley, C. Tsitsilianis, C. S. Patrickios, C. M. Papadakis
  Structural properties of a pH and temperature responsive telechelic pentablock quaterpolymer in dilute solution
  French-German Opportunities of Cooperation to Face the European Revolution in Neutron Science, Garching, Germany, 14 – 16 May 2019
- F. A. Jung, P. A. Panteli, D.-M. Smilgies, D. Posselt, C. Tsitsilianis, C. S. Patrickios, C. M. Papadakis
  In situ GISAXS investigations of multi-responsive block copolymer thin films during solvent vapor annealing
  GISAXS 2019, Hamburg, 20 – 22 Nov 2019
- J.-J. Kang, D. Gieseler, C.-H. Ko, L. C. Barnsley, R. Jordan, C. M. Papadakis
  PTX-loaded poly(2-oxazoline) molecular brushes: A structural investigation
  French-German Opportunities of Cooperation to Fact the European Revolution in Neutron Science, Garching, Germany, 14 – 16 May 2019
- J.-J. Kang, F. A. Jung, C.-H. Ko, K. Shehu, L. C. Barnsley, F. Kohler, H. Dietz, J. Zhao, S. Pispas, C. M. Papadakis
  Morpology of thermoresponsive molecular brushes with PPO-PEO copolymer side arms in aqueous solution
  European Polymer Congress, Crete, 9 – 14 June 2019
- J.-J. Kang, D. Gieseler, L.C. Barnsley, R. Jordan, C. M. Papadakis
  Morphological investigation on PTX-loaded poly(2-oxazoline) molecular brushes
  4th Internal Biennial Science Meeting of the MLZ, Grainau, 24 – 27 Jun 2019

- J.-J. Kang, D. Gieseler, C.-H. Ko, L. C. Barnsley, R. Jordan, C. M. Papadakis
  Drug-loaded poly(2-oxazoline) molecular brushes: A structural investigation
  Kolloid-Tagung "Complex Fluids/49th Conference of the German Colloid Society, Stuttgart, Germany, 23 – 25 Sep 2019

- J.-J. Kang, D. Gieseler, C.-H. Ko, L. C. Barnsley, R. Jordan, C. M. Papadakis
  Drug-loaded poly(2-oxazoline) molecular brushes: A structural investigation
  MLZ User Meeting 2019, Munich, Germany, 10 – 11 Dec 2019

- H. Kim, T. Riccitelli, X. Jiang, P. Müller-Buschbaum
  Determination of morphological evolution in bulk heterojunction polymer solar cells
  DPG-Frühjahrstagung, Regensburg, 31 Mar – 5 Apr 2019

- C.-H. Ko, K.-L. Claude, D. Schanzenbach, B.-J. Niebuur, F. A. Jung, J.-J. Kang, H. Frielinghaus, L. C. Barnsley, V. Pipich, B. Wu, A. Schulte, P. Müller-Buschbaum, A. Laschewsky, C. M. Papadakis
  The structural and thermal behavior of the thermoresponsive polymer Poly(N-isopropylmethacrylamide) in aqueous solution
  French-German Opportunities of Cooperation to Fact the European Revolution in Neutron Science, Garching, Germany, 14 – 16 May 2019

- C.-H. Ko, C. Henschel, L. Barnsley, J.-J. Kang, A. Laschewsky, P. Müller-Buschbaum, C. M. Papadakis
  Thermal behavior and cononsolvency of the amphiphilic diblock copolymers PMMA-b-PNIPAM and PMMA-b-PNIPMAM in aqueous solution
  European Polymer Congress (EPF 2019), Heraklion Crete, Greece, 9 – 14 Jun 2019

- C.-H. Ko, C. Henschel, L.C. Barnsley, J.-J. Kang, A. Laschewsky, P. Müller-Buschbaum, C. M. Papadakis
  Thermal behavior and cononsolvency of the thermoresponsive diblock copolymers PMMA-b-PNIPAM and PMMA-b-PNIPMAM in aqueous solution
  4th internal biennial science meeting of the MLZ, Grainau, 24 – 27 Jun 2019

- C.-H. Ko, C. Henschel, G. P. Meledam, M. Schroer, A. Laschewsky, P. Müller-Buschbaum, C. M. Papadakis
  Thermal behavior and cononsolvency of the amphiphilic diblock copolymer PMMA-b-PNIPAM in aqueous solution
  Kolloid-Tagung "Complex Fluids/49th Conference of the German Colloid Society, Stuttgart, Germany, 23 – 25 Sep 2019

- C.-H. Ko, K.-L. Claude, D. Schanzenbach, B.-J. Niebuur, F. A. Jung, J.-J. Kang, H. Frielinghaus, L. C. Barnsley, V. Pipich, B. Wu, A. Schulte, P. Müller-Buschbaum, A. Laschewsky, C. M. Papadakis
  The structural and thermal behavior of the thermoresponsive polymer poly(N-isopropylmethacrylamide) in aqueous solution
  MLZ User Meeting 2019, München 10/11 Dec 2019

- V. Körstgens, M. Schwartzkopf, H. Iglev, S. V. Roth, R. Kienberger, P. Müller-Buschbaum
  Hybrid solar cells with laser-ablated titania: in situ investigations of device processing
  SAXS/WAXS satellite workshop of DESY User Meeting, 24 January – 25 January 2019

- V. Körstgens, C. Mayr, M. Schwartzkopf, H. Iglev, S. V. Roth, R. Kienberger, P. Müller-Buschbaum
  Insights into the active layer of hybrid solar cells with x-ray and neutron scattering
  Gordon Research Conference on Neutron Scattering, Hong Kong, 6 May – 10 May 2019

- A. Kotobi, S. Grott, C. Ott, T. Nilges, P. Müller-Buschbaum
  Influencing the properties of fullerene-free bulk heterojunction blends for photovoltaic applications
  DPG-Frühjahrstagung, Regensburg, 31 Mar – 5 Apr 2019

- L. P. Kreuzer, T. Widmann, L. Bießmann, N. Aldosari, G. Mangiapia, V. Hildebrand, A. Laschewsky, C. M. Papadakis, P. Müller-Buschbaum
  Thermo-responsive polymers as self-cooling window surface coatings
  3rd interdisciplinary Winter School 2019 „Food and Energy", Raitenhaslach, 18 – 22 Feb 2019

- N. Li, L. Song, N. Saxena, W. Cao, X. Jiang, P. Müller-Buschbaum
  Nano-confinement on chain alignment and crystallization of conjugated polymers P3HT and PffBT4T-2OD by printed mesoporous TiO2 photoanodes
  DPG-Frühjahrstagung, Regensburg, 31 Mar – 5 Apr 2019

- N. Li, L. Song, N. Saxena, W. Cao, X. Jiang, P. Müller-Buschbaum
  Influence of nano-confinement on the crystallization of conjugated polymers P3HT and PffBT4T-2OD
  4th internal biennial science meeting of the MLZ, Grainau, 24 – 27 Jun 2019

- N. Li, L. Song, N. Hohn, N. Saxena, W. Cao, X. Jiang, P. Müller-buschbaum
  Nano-confinement on chain alighment and crystallization of conjugated polymers P3HT and PffBT4T-2OD by printed mesoporous TiO_2 *photoanodes*
  9th Energy Colloquium of the Munich School of Engineering, Garching, 1 Aug 2019

- N. Li, S. Yin, J. E. Heger, R. Schaffrinna, C. J. Brett, M. A. Hossain, J. Zheng, P. S. Deime, F. Allegretti, M. Schwartzkopf, G. Schmitz, J. V. Barth, J. G. C. Veinot, S. V. Roth, P. Müller-Buschbaum
  Highly ordered titania films with incorporated germanium nanoparticles calcined under different atmospheres
  MLZ User Meeting 2019, München, 10/11 Dec 2019

- S. Liang, P. Müller-Buschbaum
  Highly-regular porous antimony oxide thin film electrode for rechargeable batteries
  4th internal biennial science meeting of the MLZ, Grainau, 24 – 27 Jun 2019

- S. Liang, S. Yin, K. Wienhold, M. Schwartzkopf, S. V. Roth, P. Müller-Buschbaum
  Template oriented mesoporous Germanium dioxide thin film anodes for rechargeable batteries: synthesis and morphology evolution
  9th Energy Colloquium of the Munich School of Engineering, Garching, 1 Aug 2019

- S. Liang, W. Chen, S. Yin, M. Schwartzkopf, S. V. Roth, P. Müller-Buschbaum
  In-situ GISAXS observation of sputter depositing Au plasmonic nanoparticles on TiO_2 *templates*
  MLZ User Meeting 2019, München, 10/11 Dec 2019

- F. Löhrer, Volker Körstgens, S. Schaper, M. Schwartzkopf, A. Hinz, O. Polonskyi, T. Strunskus, F. Faupel, S.V. Roth, P. Müller-Buschbaum
  In-situ GISAXS investigation of the sputter deposition of metal contacts on photoactive polymer films
  4th internal biennial science meeting of the MLZ, Grainau, 24 – 27 Jun 2019

- F. C. Löhrer, C. Senfter, P. Müller-Buschbaum
  Solar cell aging on a nanoscale – why even small changes can hurt
  9th Energy Colloquium of the Munich School of Engineering, Garching, 1 Aug 2019

- R. Märkl, N. Hohn, E. Hupf, G. Mangiapia, M. Pomm, E. Rivard, P. Müller-Buschbaum
  Mesoporous titania backfilled with heavy element containing small molecules and high-efficiency polymer PTB7-Th for hybrid photovoltaics
  DPG-Frühjahrstagung, Regensburg, 31 Mar – 5 Apr 2019

- G. P. Meledam, B.-J. Niebuur, V. Pipich, M.-S. Appavou, A. Schulte, C. M. Papadakis
  Pressure-Dependence on Formation of Poly(N-isopropyl acrylamide) Mesoglobules above Cloud Point
  French-German Workshop on the Opportunities for Cooperation to Face the European Revolution in Neutron Science, Garching, May 14 – 16, 2019

- G. P. Meledam, B.-J. Niebuur, V. Pipich, M.-S. Appavou, A. Schulte, C. M. Papadakis
  Influence of Pressure on Poly(N-isopropylacrylamide) Mesoglobules above Cloud Point
  4th internal biennial science meeting of the MLZ, June 24 – 27, 2019

- G. P. Meledam, B.-J. Niebuur, V. Pipich, M.-S. Appavou, A. Schulte, C. M. Papadakis
  Structural Evolution of Poly(N-isopropylacrylamide) Mesoglobules under High Pressure
  RACIRI Summer School, August 4 – 11, 2019

- G. P. Meledam, B.-J. Niebuur, V. Pipich, M.-S. Appavou, A. Schulte, C. M. Papadakis
  Pressure Dependent Structural Evolution of Poly(N-isopropylacrylamide) Mesoglobules above Cloud Point
  Kolloid-Tagung ”Complex Fluids/49th Conference of the German Colloid Society, Stuttgart, Germany, 23 – 25 Sep 2019

- G. P. Meledam, C.-H. Ko, S.-H. Huang, B.-J. Niebuur, L. Chiappisi, C. Henschel, P. Müller-Buschbaum, A. Laschewsky, A. Schulte, C. M. Papadakis
  Tuning Hydrophobicity and Aggregation Kinetics in Block Copolymer Micelles by Rapid Pressure Jumps: A Time-Resolved Small-Angle Neutron Scattering Investigation
  CompFlu 2019, IISER Bhopal India, December 5 – 7, 2019.

- V. Munteanu, S. J. Schaper, V. Körstgens, M. Schwartzkopf, P. Pandit, A. Hinz, O. Polonskyi, T. Strunskus, F. Faupel, S.V. Roth, P. Müller-Buschbaum
  Analysis of metal nanostructure evolution on polymer surfaces by in-situ GISAXS during sputter deposition
  DPG-Frühjahrstagung, Regensburg, 31 Mar – 5 Apr 2019

- B.-J. Niebuur, G. P. Meledam, V. Pipich, M.-S. Appavou, A. Schulte, C. M. Papadakis
  Mesoglobules in PNIPAM solutions: influence of pressure
  DPG-Frühjahrstagung, Regensburg, 31 Mar – 5 Apr 2019

- B.-J. Niebuur, W. Lohstroh, M.-S. Appavou, A. Schulte, C.M. Papadakis
  Water dynamics in a concentrated poly(N-isopropylacrylamide) solution at high pressure
  DPG-Frühjahrstagung, Regensburg, 31 Mar – 5 Apr 2019

- B.-J. Niebuur, W. Lohstroh, M.-S. Appavou, A. Schulte, C. M. Papadakis
  Water dynamics in a concentrated poly(N-isopropylacrylamide) solution at high pressure
  French-German Opportunities of Cooperation to Fact the European Revolution in Neutron Science, Garching, Germany, 14 – 16 May 2019

- B.-J. Niebuur, G.P. Meledam, V. Pipich, M.-S. Appavou, A.Schulte, C.M.Papadakis
  Influence of pressure on poly(N-isopropylacrylamide) mesoglobules above cloud point
  4th Internal Biennial Science Meeting of the MLZ, Grainau, 24 – 27 Jun 2019

- A. L. Oechsle, N. Saxena, P. Müller-Buschbaum
  Preparation of semiconducting polymer thin films and methods of post-treatment to influence their thermoelectric properties
  3rd Winter School "Food and Energy" of the Graduate Center MSE, Raitenhaslach, 18 – 21 Feb 2019

- A.-L. Oechsle, N. Saxena, P. Müller-Buschbaum
  Post-treatment of thermoelectric polymer thin films to influence their thermoelectric properties
  DPG-Frühjahrstagung, Regensburg, 31 Mar – 5 Apr 2019

- A.-L. Oechsle, P. Müller-Buschbaum
  Post-treatment methods of semiconducting polymer films and investigation of the influence on thermoelectric properties
  4th internal biennial science meeting of the MLZ, Grainau, 24 – 27 Jun 2019

- A. L. Oechsle, J. Heger, N. Li, S. Yin, H. Stadler, S. Bernstorff, P. Müller-Buschbaum
  Investigation of different treatment methods on semi-conducting polymer thin films to improve their thermoelectric properties
  9th Energy Colloquium of the Munich School of Engineering, Garching, 1 Aug 2019

- A. L. Oechsle, J. Heger, N. Li, S. Yin, H. Stadler, S. Bernstorff, P. Müller-Buschbaum
  EMIM-DCA post-treatment of semi-conducting PEDOT:PSS polymer thin films to improve their thermoelectric properties
  MLZ User Meeting 2019, München, 10/11 Dec 2019

- D. Petz, V. Baran, M. Hofmann, M.J. Mühlbauer, A. Senyshyn
  Non-uniform capacity fading in lithium-ion batteries revealed by spatially resolved diffraction of neutrons and synchrotron radiation
  MLZ User Meeting 2019, München, 10/11 Dec 2019

- S. Pratap, N. Tamura, C. Stan, Z. Yuan, H. Gowdey, A. MacDowell, T. Song, N. Barchi, P. Müller-Buschbaum, C. Sutter-Fella, J. Slack
  Probing the in-situ dynamics of structure-property evolution in hybrid perovskite thin films spin-coated from complex fluids by a custom designed, beamline compatible multimodal measurement chamber
  40th International Conference on Vacuum Ultraviolet and X-ray Physics, San Francisco, USA, 1 – 5 Jul 2019

- B. Predeschly, L. Reb, P. Müller-Buschbaum
  Characterization and encapsulation of perovskite solar cells
  DPG-Frühjahrstagung, Regensburg, 31 Mar – 5 Apr 2019

- L. Reb, P. Müller-Buschbaum
  The 2-Step deposition method of mixed perovskites as a route to highly tunable optoelectronic properties
  DPG-Frühjahrstagung, Regensburg, 31 Mar – 5 Apr 2019

- L. Reb, P. Müller-Buschbaum
  Tailoring optoelectronic properties of mixed halide perovskites via the versatile 2-Step deposition method
  4th internal biennial science meeting of the MLZ, Grainau, 24 – 27 Jun 2019

- R. Schaffrinna, M. Schwager, P. Müller-Buschbaum
  Thiophene based semiconductors and graphene oxide for organic solar cells
  3th Winter School of the Graduate Center MSE, Raitenhaslach, 18 – 21 Feb 2019

- R. Schaffrinna, M. Schwager, P. Müller-Buschbaum
  Thiophene based semiconductors and graphene oxide for organic solar cells
  DPG-Frühjahrstagung, Regensburg, 31 Mar – 5 Apr 2019

- R. Schaffrinna, M. Schwager, P. Müller-Buschbaum
  Thiophene based semiconductors and graphene oxide for organic solar cells
  4th internal biennial science meeting of the MLZ, Grainau, 24 – 27 Jun 2019

- R. Schaffrinna, M. Schwager, P. Müller-Buschbaum
  Thiophene based semiconductors for organic solar cells
  9th Energy Colloquium of the Munich School of Engineering, Garching, 1 Aug 2019

- R. Schaffrinna, M. Schwager, P. Müller-Buschbaum
  Thiophene based semiconductors for organic solar cells
  MLZ User Meeting, München, 10/11 Dec 2019

- S. J. Schaper, F. C. Löhrer, S. Xia, M. Schwartzkopf, P. Pandit, A. Hinz, O. Polonskyi, T. Strunskus, F. Faupel, S. V. Roth, P. Müller-Buschbaum
  Revealing the growth of copper as contacts for polymer thin film lithium-ion batteries
  9th Energy Colloquium of the Munich School of Engineering, Garching, 1 Aug 2019

- S. J. Schaper, F. C. Löhrer, S. Xia, M. Schwartzkopf, P. Pandit, A. Hinz, O. Polonskyi, T. Strunskus, F. Faupel, S. V. Roth, P. Müller-Buschbaum
  Revealing the formation of sputter deposited metal nanolayers on functional polymer thin films for lithium-ion batteries
  GISAXS 2019, Hamburg, 20 – 22 Nov 2019

- S. J. Schaper, F. C. Löhrer, S. Xia, M. Schwartzkopf, P. Pandit, A. Hinz, O. Polonskyi, T. Strunskus, F. Faupel, S. V. Roth, P. Müller-Buschbaum
  Revealing the formation of sputter deposited metal nanolayers on functional polymer thin films for lithium-ion batteries
  MLZ User Meeting 2019, Munich, Germany, 10 – 11 Dec 2019

- M. A. Scheel, P. Müller-Buschbaum
  Non-destructive in-situ slot-die coating x-ray and neutron scattering experiments on perovskite thin films for photovoltaic application
  4th internal biennial science meeting of the MLZ, Grainau, 24 – 27 Jun 2019

- M. A. Scheel, L. K. Reb, R. Guo, S. Grott, M. Schwartzkopf,
  S. V. Roth, P. Müller-Buschbaum
  In-situ annealing GIWAXS studies of 2-step printed MAPI for large area PSCs
  e-conversion Conference, Venice, 9 – 13 Sep 2019

- M. A. Scheel, L. K. Reb, R. Guo, S. Grott, V. K örstgens, W. Chen, N. Li, M. Schwartzkopf,
  S. V. Roth, P. Müller-Buschbaum
  In-situ GISAXS/GIWAXS measurements on slot-die printed thin-film perovskite layers for solar cell application
  SolTech Conference, Nuremberg, 30 Sep – 02 Oct 2019

- M. A. Scheel, L. K. Reb, R. Guo, S. Grott, M. Schwartzkopf, S. V. Roth, P. Müller-Buschbaum
  In-situ annealing GIWAXS studies of 2-step printed MAPI for large area PSCs
  TUM-IAS Focus Workshop, Munich, 28 – 29 Oct 2019

- M. A. Scheel, L. K. Reb, R. Guo, S. Grott, M. Schwartzkopf, L. Polavarapu, S. V. Roth,
  P. Müller-Buschbaum
  GISAXS and GIWAXS studies of 2-step printed MAPI films and templated Perovskite Quantum Dots
  GISAXS 2019, Hamburg, 20 – 22 Nov 2019

- M. A. Scheel, L. K. Reb, R. Guo, S. Grott, M. Schwartzkopf, L. Polavarapu, S. V. Roth,
  P. Müller-Buschbaum
  GISAXS and GIWAXS studies of 2-step printed MAPI films and templated Perovskite Quantum Dots
  MLZ User Meeting 2019, München, 10/11 Dec 2019

- D. Schwaiger, M. Golub, I. Seuffert, A. Zouni, W. Lohstroh, P. Müller-Buschbaum, J. Pieper
  Protein dynamics of a thermophile photosystem
  DPG-Frühjahrstagung, Regensburg, 31 Mar – 5 Apr 2019

- D. Schwaiger, M. Golub, I. Seuffert, A. Zouni, W. Lohstroh, J. Pieper, P. Müller-Buschbaum
  Protein dynamics of a thermophile photosystem
  4th internal biennial science meeting of the MLZ, Grainau, 24 – 27 Jun 2019

- D. Schwaiger, W. Lohstroh, P. Müller-Buschbaum
  Investigation of molecular dynamics of a PTB7:PCBM polymer blend with quasielastic neutron scattering
  9th Energy Colloquium of the Munich School of Engineering, Garching, 1 Aug 2019

- D. Schwaiger, W. Lohstroh, P. Müller-Buschbaum
  Investigation of molecular dynamics of a PTB7:PCBM polymer blend with quasielastic neutron scattering
  MLZ User Meeting 2019, München, 10/11 Dec 2019

- M. Spyranti, N. Li, S. J. Schaper, S. Grott, P. Müller-Buschbaum
  Synthesis of Mesoporous titania films by using PS-b-P$_4$VP as template block co-polimer: Fabrication and Analysis
  MLZ User Meeting 2019, München, 10/11 Dec 2019

- D. M. Steger, K. S. Wienhold, P. Müller-Buschbaum
  Influence of solvent on the morphology and optical properties of printed active layers based on PBDB-TSF:IT-4F for application in organic solar cells
  MLZ User Meeting 2019, München, 10/11 Dec 2019

- R. E. Stene, T. Chemnitz, F. Kraus, W. Petry
  Non-aqueous separation of Molybdenum from Uranium
  GDCh - Wissenschaftsforum Chemie, Aachen, 15 – 18 Sep 2019

- S. Szabò, F. Yang, D. Holland-Moritz, T. Voigtmann, Z. Evenson and W. Petry
  The short-range order in Zr-Ti melts
  2019 Sino-German Symposium, Münster, 18 – 22 Mar 2019

- S. Szabò, F. Yang, W. Lohstroh and W. Petry
  Self-diffusion in Mercury investigated with quasi-elastic neutron scattering
  MLZ User Meeting 2019, München, 10/11 Dec 2019

- C. Telescu, S.J. Schaper, P. Müller-Buschbaum
  Polymers for lithium ion batteries - investigating composite electrodes
  DPG-Frühjahrstagung, Regensburg, 31 Mar – 5 Apr 2019

- T. Tian, P. Müller-Buschbaum
  Morphology tuning of ZnO nanostructures for hybrid solar cells
  4th internal biennial science meeting of the MLZ, Grainau, 24 – 27 Jun 2019

- T. Tian, P. Müller-Buschbaum
  Morphology Tailoring of ZnO for Application in Solid-state Dye-sensitized Solar Cells
  9th Energy Colloquium of the Munich School of Engineering, Garching, 1 Aug 2019

- T. Tian, P. Müller-Buschbaum
  Morphology Tailoring of ZnO for Application in Solid-state Dye-sensitized Solar Cells
  MLZ User Meeting 2019, München, 10/11 Dec 2019

- S. Tu, N. Saxena, P. Müller-Buschbaum
  Thermoelectric thin hybrid films based on PEDOT:PSS and inorganic nanoparticles
  MLZ User Meeting 2019, München, 10/11 Dec 2019

- A. Vagias, S. J. Schaper, L. P. Kreuzer, W. Chen, S. Liang, M. Gensch, P. Pandit, M. Schwartzkopf, S. V. Roth, B. J. Drewes, N. Carstens, T. Strunskus, F. Faupel, A. Laschewsky, P. Müller-Buschbaum
  Monitoring selectivity of gold cluster growth/formation on antifouling-relevant zwitterionic thin block copolymer coatings
  MLZ User Meeting 2019, München, 10/11 Dec 2019

- A. Vagias, S. J. Schaper, L. P. Kreuzer, W. Chen, S. Liang, M. Gensch, P. Pandit, M. Schwartzkopf, S. V. Roth, B. J. Drewes, N. Carstens, T. Strunskus, F. Faupel, A. Laschewsky, P. Müller-Buschbaum
  Monitoring selectivity of gold cluster growth/formation on antifouling-relevant zwitterionic thin block copolymer coatings
  GISAXS 2019, Hamburg, 20 – 22 Nov 2019
- P. Wang, L. P. Kreuzer, C. Geiger, T. Widmann, S. Liang, P. Müller-Buschbaum
  Effect on conformational transformation of methyl side group in Poly(sulfobetaine)-based thermo-responsive block copolymer thin films
  MLZ User Meeting 2019, München, 10/11 Dec 2019
- C. L. Weindl, P. Müller-Buschbaum
  Germanium-based nanostructure synthesis guided by amphiphilic diblock copolymer templating
  4th internal biennial science meeting of the MLZ, Grainau, 24 – 27 Jun 2019
- C. L. Weindl, M. A. Giebel, T. F. Fässler, P. Müller-Buschbaum
  Germanium-based nanostructure synthesis guided by amphiphilic diblock copolymer templating
  MSE Kolloquium, Garching, 1 Aug 2019
- C. L. Weindl, M. A. Giebel, T. F. Fässler, P. Müller-Buschbaum
  Germanium-based nanostructue synthesis guided by amphiphilic diblock copolymer templating
  8th SolTech Conference 2019, Nürnberg, 30 Sep – 2 Oct 2019
- C. L. Weindl, M. A. Giebel, T. F. Fässler, P. Müller-Buschbaum
  Germanium-based nanostructure synthesis guided by amphiphilic diblock copolymer templating
  MLZ User Meeting 2019, München, 10/11 Dec 2019
- T. Widmann, L. Kreuzer, P. Müller-Buschbaum
  Humidity chamber for grazing incidence neutron scattering
  4th internal biennial science meeting of the MLZ, Grainau, 24 – 27 Jun 2019
- T. Widmann, L. P. Kreuzer, P. Müller-Buschbaum
  3D-printed humidity chamber for neutron diffraction experiments on thin films
  European Conference on Neutron Scattering, St. Petersburg, Russia, 30 Jun – 5 Jul 2019
- T. Widmann, L. P. Kreuzer, P. Müller-Buschbaum
  3D-printed humidity chamber for neutron diffraction experiments on thin films
  MLZ User Meeting 2019, München, 10/11 Dec 2019
- K. S. Wienhold, V. Körstgens, S. Grott, X. Jiang, M. Schwartzkopf, S. V. Roth and P. Müller-Buschbaum
  In situ printing of active layers of PBDB-T-SF:IT-4F for application in high efficiency organic solar cells
  8th SolTech Conference, Nürnberg, 30 Sep – 2 Oct 2019
- K. S. Wienhold, V. K örstgens, S. Grott, X. Jiang, M. Schwartzkopf, S. V. Roth and P. Müller-Buschbaum
  In-situ printing of PBDB-T-SF:IT-4F for application in high-efficiency organic solar cells
  MLZ User Meeting 2019, München, 10/11 Dec 2019

- T. Xiao, P. Müller-Buschbaum
  Wearable electronic skin based on triboelectric and luminescent effect for pressure and tensile sensing
  4th internal biennial science meeting of the MLZ, Grainau, 24 – 27 Jun 2019

- T. Xiao, W. Chen, P. Müller-Buschbaum
  Wearable electronic skin based on triboelectric and luminescent effect for pressure and tensile sensing
  9th Energy Colloquium of the Munich School of Engineering, Garching, 1 Aug 2019

- T. Xiao, W. Cao, W. Chen, S. -J. Wöhnert, S. V. Roth, P. Müller-Buschbaum
  Hybrid energy harvester based on solar cell and triboelectric nanogenerator
  GISAXS 2019, Hamburg, 20 – 22 Nov 2019

- T. Xiao, W. Cao, W. Chen, S. -J. Wöhnert, S. V. Roth, P. Müller-Buschbaum
  Hybrid energy harvester based on solar cell and triboelectric nanogenerator
  MLZ User Meeting 2019, München, 10/11 Dec 2019

- D. Yang, B. Cao, T. Hauger, E.J. Luber, P. Müller-Buschbaum, J. M. Buriak
  How to rationally select an interfacial modifier for high performance organic photovoltaics
  4th internal biennial science meeting of the MLZ, Grainau, 24 – 27 Jun 2019

- S. Yin, P. Müller-Buschbaum
  Key factors in the synthesis of template-oriented porous ordered titanium dioxide: solvents and catalysts
  DPG-Frühjahrstagung, Regensburg, 31 Mar – 5 Apr 2019

- S. Yin, P. Müller-Buschbaum
  Nanostructured SnO2 templated by amphiphilic block copolymer for Lithium-Ion battery anodes
  4th internal biennial science meeting of the MLZ, Grainau, 24 – 27 Jun 2019

- S. Yin, P. Müller-Buschbaum
  TiO_2 and SnO_2 anode material for lithium ion battery
  9th Energy Colloquium of the Munich School of Engineering, Garching, 1 Aug 2019

- S. Yin, P. Müller-Buschbaum
  Preparation of porous SnO_2 thin films by tuning the precursor category, precursor content and HCl content
  MLZ User Meeting 2019, München, 10/11 Dec 2019

9.4 Invited Talks at the Institute of Functional Materials/Soft Matter Physics Group

- Manuel Scheel, Fraunhofer ISE Freiburg
  Solvent Vapor Annealing and In-situ Photoluminescence Measurements of MAPbI3 Perovskite Layers
  9 Jan 2019

- Michaela Würbser, TUM
  Influence of chiral BINOL-Box Ligands on the Yttrium-mediated in situ Ring-Opening Polymerization of racemic β-Butyrolactone
  30 Jan 2019

- Maximilian Röhrl, Universiät Regensburg
  Directional, hierarchical films via spray deposition
  26 Apr 2019

- Dr. Simon Titmuss, University of Edinburgh
  Thin film physics in bacterial biofilms and chocolate
  8 Jul 2019

- Prof. Dr. U-Ser Jeng, National Synchrotron Radiation Research Center, Taiwan
  Tracing the Structural Evolution during Spin-coating of Polymer/Fullerene Thin Films
  10 Jul 2019

- Prof. Dr. Uli Wiesner, Cornell University, Ithaca, USA
  From Soft Macromolecular Self-Assembly to Quantum Materials and Energy Storage Devices
  21 Oct 2019

9.5 Funding

Deutsche Forschungsgesellschaft:

- *In-situ Untersuchungen zu Kondensation, Nukleation und Wachstum von Metallfilmen und Nanostrukturen auf organischen Oberflächen während Sputterbeschichtung*
  Grant Number: MU 1487/18-2
  Project Leader: Prof. Dr. Peter Müller-Buschbaum

- *Transport und Morphologie, Einfluss auf nichtgeminale Rekombination in Organischen Solarzellen*
  Grant Number: MU 1487/22-1
  Project Leader: Prof. Dr. Peter Müller-Buschbaum

- *Rheologie und Grenzflächenstrukturen von Protein- und Partikelstabilisierten Schäumen - ein Multiskalenansatz*
  Grant Number: MU 1487/32-1
  Project Leader: Prof. Dr. Peter Müller-Buschbaum

- Teilprojekt *Inorganic-organic hybrid photovoltaic solar cells using novel hybrid materials* im GRK 2022: University of Alberta / Technische Universität München Internationale Graduiertenschule für Funktionelle Hybridmaterialien (ATUMS) der DFG
  IRTG-2022
  Project Leader: Prof. Dr. Peter Müller-Buschbaum

- *Cononsolvency-induzierte Selbstorganisation thermoresponsiver Blockcopolymere in Lösung und im dünnen Film*
  Grant Number: MU 1487/29-1, Project Leader: Prof. Dr. Peter Müller-Buschbaum
  Grant Number: PA 771/20-1, Project Leader: Prof. Dr. Christine Papadakis

- *Kinetik der Aggregation in thermoresponsiven Polymerlösungen bei Drucksprüngen*
  Grant Number: PA 771/22-1, Project Leader: Prof. Dr. Christine Papadakis

- *Dünne Filme aus pH und thermoresponsiven Triblockcopolymeren: von der Netzwerkdynamik zum defektfreien Film*
  Grant Number: PA 771/19-1
  Project Leader: Prof. Dr. Christine Papadakis

Bundesministerium für Bildung und Forschung:

- *FlexiProb: Flexible Probenumgebungen für die Untersuchung weicher Materie zur Implementierung an der ESS*
  Teilprojekt: 3
  Project Leader: Prof. Dr. Peter Müller-Buschbaum

- *Optische In-situ Methoden für das Flugzeitspektrometer TOFTOF*
  Project Leader: Prof. Dr. Peter Müller-Buschbaum

Bayerisches Staatsministerium für Wissenschaft und Kunst:

- Im Rahmen der Munich School of Engineering (MSE):
  Solar Technologies Go Hybrid (SolTech) - Forschungsnetzwerk TUM.solar
  Project Leader: Prof. Dr. Peter Müller-Buschbaum
- Im Rahmen der Munich School of Engineering (MSE): Netzwerk Regenerative Energien
  Aufbau eines interdisziplinären Netzwerks aus Lehrstühlen der Technischen Universität München und anderen Forschungseinrichtungen zur Förderung der Forschungsaktivitäten im Bereich der regenerativen Energien
  Project Leader: Prof. Dr. Peter Müller-Buschbaum

Others:

- Im Rahmen des Exzellenzclusters Nanosystems Initiative Munich (NIM)
  e-conversion
  Principal Investigator: Prof. Dr. Peter Müller-Buschbaum

10 The chair

10.1 Staff

Chair:

Prof. Dr. Peter Müller-Buschbaum

Professor:

Prof. Dr. Christine Papadakis

Emerited Professor:

Prof. Dr. Winfried Petry

Fellows:

Dr. Volker Körstgens
Dr. Michael Leitner
Dr. Wiebke Lohstroh
Dr. Geethu Pathirassery Meledam

Dr. Jürgen Neuhaus
Dr. Neelima Paul
Dr. Apostolos Vagias
Dr. Marcell Wolf

PhD Students:

Neslihan Aslan
Bruno Baumeister
Lorenz Bießmann
Wei Cao
Tobias Chemnitz
Wei Chen
Mihael Coric
Oliver Filonik
Sandra Geara
Christina Geiger
Sebastian Grott
Tianfu Guan
Renjun Guo
Julian Eliah Heger
Alexander Ewin Heldmann
Nuri Hohn
Xinyu Jiang
Florian Jung
Jia-Jhen Kang
Chia-Hsin Ko
Lucas Philipp Kreuzer
Nian Li
Yanan Li
Suzhe Liang
Franziska Carina Löhrer
Bart-Jan Niebuur
Anna-Lena Oechsle
Shambhavi Pratap
Lennart K. Reb
Christian Reiter
Nitin Saxena
Roy Schaffrinna
Simon Jakob Schaper
Manuel Andree Scheel
Dominik Mathias Schwaiger
Christian Schwarz
Kaltrina Shehu
Jingyi Shi
Riane Elizabeth Stene
Christian Steyer
Sandro Szabò
Ting Tian
Suo Tu
Kun Wang
Peixi Wang
Christian Ludwig Weindl
Tobias Widmann
Kerstin Sabrina Wienhold
Senlin Xia
Tianxiao Xiao
Dan Yang
Shanshan Yin
Yuqin Zou
Ulrike Zweck

Master Students:

Seraphin Aeschbach
Nawarah Aldosari
Amira Baccari
Kalyan Biswas
Johannes Costa
Lautaro Dìaz Piola
Ali Doaa
Korbinian Faust
Johannes Gallitscher
Georg Glänzer
Naifei Guo
Shu Hasegawa
Shu Hsien Huang
Linus Huber
Goran Ivkovic Ivandekiç
Hongwon Kim
Amir Kotobi
Sabine Matuschik
Raphael Märkl
Valentin Munteanu
Dominik Petz
Benjamin Predeschly
Julija Reitenbach
Ronja Schönecker
Magdalini Spyranti
Daniel Steger
Cristian Telescu
Rika Unkelbach
Rui Wang
Christian Weindl

Bachelor Students:

Johannes Allwang
Laura Bauer
Judith Brenner
Lukas Bührend
Luka Gaetani
Adrian Jurjevic
David Machenschalk
Dominik Mayer
Dorian-David Percheron
Cristian Schott
Zoe Siebers
Raphael Streng
Nicola Taffertshofer
Hagen Übele
Florian Wietschorke

Students Assistants:

Safwan Uddin Ahmed
Hendrik Hegels
Michele Lecis

Internships/Exchange Students:

Samah Akel
Hossain Asjad
Aaron Kirkey
Shih-Ho Lin
Zeyuan Ma
Eric Rende
Tommaso Riccitelli

Technical/Administrative Staff:

Reinhold Funer
Josef Huber
Josef Kaplonski
Carola Kappauf
Dieter Müller
Marion Waletzki

10.2 Graduations

- **Accomplished PhD Theses**

  Lorenz Bießmann
  Functional layers for enhanced photon extraction in ITO-free OLEDs

  Nuri Hohn
  Polymer templated nanostructures for application in hybrid photovoltaics and Li Ion batteries

  Bart-Jan Niebuur
  Thermoresponsive polymers under high pressure

  Christian Reiter
  A model system for transient calculations for research reactors with a compact core

  Nitin Saxena
  Thermoelectric thin films based on conducting polymers

  Christian Steyer
  Plasma and solid-state physics-based optimization of a coating process for monolithic UMo nuclear fuels

  Kun Wang
  Morphology control of zinc oxide nanostructures for application in hybrid solar cells"

  Senlin Xia
  Investigation of nanostructured magnetic thin polymer films

- **Accomplished Master Theses**

  Nawarah Aldosari
  Smart nano-sensors made of stimuli-responsive polymers in thin films

  Amira Baccari
  Physics-based characterization and modeling oft he thermo-mechanical behavior of a highly silver-filled thermoplastic die attach adhesive

  Kalyan Biswas
  Magnetic nanoparticles in polymer matrix

  Johannes Costa
  Inelastic neutron scattering on FeNiCo high-entropy alloys

  Ali Doaa
  Sub-picosecond dynamics of water studied by neutron scattering and molecular dynamics simulations

  Korbinian Faust
  Serpent 2 and openFOAM models for coupled calculations of research reactors with a compact core

  Johannes Gallitscher
  Formation of UMo-Al interdiffusion layers through cracks in the ZrN coating

  Shu Hsien Huang
  Temperature-pressure dependent phase behavior of polystyrene-b-poly(N-isopropylacrylamide) diblock copolymer in aqueous solution

  Hongwon Kim
  Morphology evaluation of non-fullerene organic photovoltaics

  Amir Kotobi
  Influencing the properties of fullerene-free bulk heterojunction blends for photovoltaic applications

Raphael Märkl
High-performance polymer and novel small molecule for Titania-based hybrid photovoltaics

Valentin Munteanu
Analysis of metal nanostructure evolution on polymer surfaces

Benjamin Predeschly
Design and realization of a measuring setup for characterizing organic and hybrid solar cells in space

Michael Trimpl
Charge-carrier recombination and trapping mechanisms in metal halide perovskite semiconductors

Christian Weindl
Investigation of novel material systems for increasing the efficiency of organic solar cells

- **Accomplished Bachelor Theses**

Johannes Allwang
Poly(oxazoline)-based bottlebrush polymers in ethanol solution: A light scattering study

Laura Bauer
Investigation of the morphology of printed organic solar cells

Judith Brenner
Quell- und Gelierverhalten dünner Filme aus pH-responsiven telechelischen Blockcopolymeren

Lukas Bührend
Protonation and microphase separation of dual pH-responsive pentablock terpolymer thin films

Adrian Jurjevic
High efficiency organic solar cells

David Machenschalk
Biopolymer templated hierarchical structures for hybrid solar cells

Dorian-David Percheron
Optimizing the compact TiO2 electron transport layer for high efficiency perovskite xolar cells

Christian Schott
Analysis and improvement of the thermoelectric properties of water-soluble P3P6T derivatives

Zoe Siebers
Block copolymer membranes for thin-film lithium-ion batteries

Raphael Streng
Composite electrodes for Lithium-Ion microbatteries

Nicola Taffertshofer
Improving the efficiency of perovskite solar cells by blocking layer optimization

Hagen Übele
Analysis and improvement of the thermoelectric properties of water-soluble P3P6T through acid-doping

Florian Wietschorke
Printing conductive paper

Florian Vögl
In situ dynamic light scattering at the Jülich Neutron Spin Echo Spectrometer and first investigation on Poly-L-Glutamic Acid as a potential sample

10.3 Guests

Prof. Dr. Stephan V. Roth, DESY Hamburg
7 – 9 Jan, 29 Jan, 12 Feb, 29 Jul, 5 Nov. 2019

Samah Akel, University of Jordan
7 Jan – 30 Jun 2019

Hossain Asjad, University of Alberta, Canada
14 Jan – 31 Mar 2019

Aaron Kirkey, University of Alberta, Canada
22 Jan – 10 Apr 2019 2019

Dr. Pallavi Pandit, DESY Hamburg
12 Feb 2019

Prof. Alfons Schulte, University of Central Florida, USA
15 May – 20 Jul 2019

Zeyuan Ma, University of Wisconsin, Madison, USA
4 Jun – 13 Aug 2019

Shih-Ho Lin, University of Taiwan
28 Jun – 31 Jul 2019 2019

Dr. Simon Titmuss, University of Edinburgh
8 Jul 2019

Prof. Dr. André Laschewsky, Universität Potsdam/IAP and Cristiane Hentschel, Universität Potsdam
17 Jul 2019

Calvin Brett, DESY Hamburg
30 Jul 2019

Delegation of 3 professors and 50 students of Beihang University, Beijing, China
16 Aug 2019

Eric Rende, University of Central Florida, USA
14 – 18 Oct 2019

Prof. Dr. Uli Wiesner, Cornell University, Ithaca, USA
21 Okt 2019

Delegation of 16 Chinese executives from different institutes researching photovoltaics materials
21 Nov 2019

Prof. Dr. Wanli Ma, FUNSOM, Soochow University, China
12 Dec 2019

Dr. Olaf Soltwedel/Matthias Kühnhammer, TU Darmstadt, Prof. Dr. Thomas Hellweg/Dr. Andreas Schmid, University of Bielefeld, Dr. Arno Hiess/Harald Schneider, ESS Sweden, Dr. Judith Houston/Dr. Sebastian Jaksch, JCNS Jülich
12/13 Dec 2019